The Influence of Loading on the Corrosion of Steel in Cracked Ordinary Portland Cement and High Performance Concretes

by

Shahzma Jafferali Jaffer

A thesis
presented to the University of Waterloo
in fulfilment of the
thesis requirement for the degree of
Doctor of Philosophy
in
Mechanical Engineering

Waterloo, Ontario, Canada, 2007

AUTHOR'S DECLARATION

I hereby declare that I am the sole author of this thesis. This is a true copy of the thesis, including any required final revisions, as accepted by my examiners.

I understand that my thesis may be made electronically available to the public.

Abstract

Most studies that have examined chloride-induced corrosion of steel in concrete have focused on sound concrete. However, reinforced concrete is seldom uncracked and very few studies have investigated the influence of cracked concrete on rebar corrosion. Furthermore, the studies that have examined the relationship between cracks and corrosion have focused on unloaded or statically loaded cracks. However, in practice, reinforced concrete structures (e.g. bridges) are often dynamically loaded. Hence, the cracks in such structures open and close which could influence the corrosion of the reinforcing steel. Consequently, the objectives of this project were (i) to examine the effect of different types of loading on the corrosion of reinforcing steel, (ii) the influence of concrete mixture design on the corrosion behaviour and (iii) to provide data that can be used in service-life modelling of cracked reinforced concretes.

In this project, cracked reinforced concrete beams made with ordinary Portland cement concrete (OPCC) and high performance concrete (HPC) were subjected to no load, static loading and dynamic loading. They were immersed in salt solution to just above the crack level at their mid-point for two weeks out of every four (wet cycle) and, for the remaining two weeks, were left in ambient laboratory conditions to dry (dry cycle). The wet cycle led to three conditions of exposure for each beam: (i) the non-submerged region, (ii) the sound, submerged region and (ii) the cracked mid-section, which was also immersed in the solution. Linear polarization resistance and galvanostatic pulse techniques were used to monitor the corrosion in the three regions. Potentiodynamic polarization, electrochemical current noise and concrete electrical resistance measurements were also performed. These measurements illustrated that (i) rebar corroded faster at cracks than in sound concrete, (ii) HPC was more protective towards the rebar than OPCC even at cracks and (iii) there was a minor effect of the type of loading on rebar corrosion within the period of the project. These measurements also highlighted the problems associated with corrosion measurements, for example, identifying the actual corroding area and the influence of the length of rebar.

The numbers of cracks and crack-widths in each beam were measured after the beam's initial exposure to salt solution and, again, after the final corrosion measurements. HPC beams had more cracks than the OPCC. Also, final measurements illustrated increased crack-widths in dynamically loaded beams, regardless of the concrete type. The cracks in both statically and dynamically loaded OPCC and HPC beams bifurcated at the rebar level and propagated parallel to the rebar.

This project also examined the extent of corrosion on the rebars and the distribution of corrosion

products in the concrete and on the concrete walls of the cracks. Corrosion occurred only at cracks in the concrete and was spread over a larger area on the rebars in HPC than those in OPCC. The damage due to corrosion was superficial in HPC and crater-like in OPCC. Regardless of the concrete type, there was a larger distribution of corrosion products on the crack walls of the dynamically loaded beams. Corrosion products diffused into the cement paste and the paste-aggregate interface in OPCC but remained in the crack in HPC. The most voluminous corrosion product identified was ferric hydroxide.

Elemental analysis of mill-scale on rebar which was not embedded in concrete or exposed to chlorides was compared to that of the bars that had been embedded in uncontaminated concrete and in cracked concrete exposed to chlorides. In uncontaminated concrete, mill-scale absorbed calcium and silicon. At a crack, a layer, composed of a mixture of cement paste and corrosion products, developed between the mill-scale and the substrate steel.

Based on the results, it was concluded that (i) corrosion occurred on the rebar only at cracks in the concrete, (ii) corrosion was initiated at the cracks immediately upon exposure to salt solution, (ii) the type of loading had a minor influence on the corrosion rates of reinforcing steel and (iv) the use of polarized area led to a significant underestimation of the current density at the crack.

It is recommended that the effect of cover-depth on (i) the time to initiation of corrosion and (ii) the corrosion current density in cracked concrete be investigated.

Acknowledgements

I would like to express my gratitude to Prof. Carolyn M. Hansson for choosing to be my supervisor. Prof. Hansson was the perfect supervisor for me because she understood my personality, my strengths and my weaknesses. When I came to the University of Waterloo, I knew very little about materials science. She taught me everything I know and it is because of her that I am able to teach materials science. I was raised in a small town in Tanzania and had to leave home when I was very young to pursue education. Most people in my situation only get school-based education but I have been fortunate because Prof. Hansson has taught me a lot more. I really admire her values, intelligence and 'out of the box' thinking.

I appreciate the help extended to me by Prof. J. West (a member of my PhD examining committee) in coming up with a design for my beams. He has an amazing ability to explain things and the University of Waterloo is very fortunate to have him educate its students.

I would like to thank other members of my PhD examining committee: Prof. H. Peemoeller, Prof. S. Corbin, Prof. E. Reardon and Prof. W.J. Weiss for their time and assistance.

This project would have been extremely difficult without the help of the remarkable technical staff at the University of Waterloo. In particular, I would like to thank Doug Hirst, Norval Wilhelm, Richard Morrison, Jim Baleshta, Dr. Yuquan Ding, John Potzold, John Boldt, Fred Bakker, Jorge Cruz, Juan Ulloa, Kwai Chan, Andy Barber, Martha Morales, Steve Hitchman, Ken Bowman and Terry Ridgway.

Thank you to Dr. Amirreza Esmaeilpoursaee, Dr. Laura Mammoliti, Brad Bergsma, Kyle Anders, Ramtin Movassaghi, Khanh Tran, Quan Tan, Irene Wijoyo, Ken Su, Greg MacNeill and Katherine Olsen for being such wonderful colleagues. I have learnt a lot from them and I appreciate their help.

I would like to thank Mr. Frank Pianca from MTO for teaching me how to conduct condition analyses of bridges and Prof. J. Medley for supporting me during my terms as the Graduate Student Representative on the Engineering Graduate Studies Committee and President of the Mechanical and Mechatronics Engineering Graduate Students Association (MMEGA).

I appreciate the support of my extended family. In particular, I would like to thank my parents: Farida and Jafferali, my aunts: Dilshad and Gulzar, my uncle: Amirali, my sister: Neilin, my brothers: Feizal and Jamil and my cousins: Alykhan, Sheliza, Nadia and Fatima.

Finally, I want to thank my wonderful friends: Amir Reza Baserinia, Gregory Mayer, Mona Mojdeh, Amin Mobasher, Salima Jetha, Salimeh Karim, Shareen Somani and Antoanela Palasanu for

being there for me.

This project was funded by the Natural Sciences and Engineering Research Council of Canada (NSERC).

Table of Contents

AUTHOR'S DECLARATION ii
Abstract iii
Acknowledgements v
Table of Contents vii
List of Tables x
List of Figures xi
Chapter 1 - Introduction 1
Chapter 2 - Background 2
2.1 CORROSION OF STEEL IN CONCRETE 2
2.2 POROSITY IN CONCRETE 4
2.3 SUPPLEMENTARY CEMENTING MATERIALS IN CONCRETE 6
2.3.1 Silica Fume 6
2.3.2 Granulated blast furnace slag 7
2.4 ORDINARY PORTLAND CEMENT AND HIGH PERFORMANCE CONCRETES 8
2.5 CRACKS IN CONCRETE 9
2.5.1 Sources of Cracks in Concrete 10
2.5.1.1 Shrinkage 10
2.5.1.2 Chemical Reactions 12
2.5.1.3 Weathering Processes 13
2.5.1.4 Corrosion of Reinforcement 14
2.5.1.5 Loading 15
2.6 CHLORIDE INGRESS IN REINFORCED CONCRETE 17
2.7 THE EFFECT OF CRACKING ON CORROSION 19
2.8 PRODUCTS OF CHLORIDE INDUCED CORROSION 20
2.9 THE IMPACT OF DYNAMIC LOADING ON THE CORROSION OF STEEL 21
2.10 CORROSION MEASURING TECHNIQUES 21
2.10.1 Half-cell Potential Measurements 22
2.10.2 Potentiostatic Linear Polarization Resistance 22
2.10.3 Galvanostatic Pulse Technique 24
2.10.4 Electrochemical Noise 24
2.10.5 Potentiodynamic Polarization 24

Chapter 3 - Experimental Procedures 26
3.1 DESIGN OF REINFORCED CONCRETE BEAMS 26
3.2 COMPRESSIVE TESTING 28
3.3 LOADING PROCEDURES 29
3.4 EXPOSURE CONDITIONS AND CORROSION MEASUREMENT LOCATIONS 31
3.5 CRACK-WIDTH MEASUREMENTS 32
3.6 DESIGN OF ELECTRODE HOLDER 33
3.7 CORROSION MEASUREMENTS 35
3.8 CHLORIDE PROFILE DETERMINATION 39
3.9 CHLORIDE ANALYSES 40
3.10 RAMAN SPECTROSCOPY 42
3.11 OBSERVATIONS OF MACROCRACK PROFILES IN CONCRETE 43
3.12 CHANGES IN MILL-SCALE 44
Chapter 4 - Results and Discussion 45
4.1 COMPRESSIVE TESTS 45
4.2 MACROCRACKS 45
4.3 CHLORIDE PROFILES 51
4.4 CORROSION MEASUREMENTS 55
4.4.1 LPR and Galvanostatic Pulse Measurements 55
4.4.1.1 Corrosion Current Densities 55
4.4.1.2 Corrosion potentials 64
4.4.2 Potentiodynamic Polarization Measurements 79
4.4.3 Electrochemical Noise 84
4.4.4 Concrete Electrical Resistance 91
4.5 CORROSION PRODUCTS 95
4.5.1 Extent of Corrosion on Rebar 95
4.5.2 Distribution of Corrosion Products in Concrete 101
4.5.3 Identification of Corrosion Products 105
4.5.4 Mill-Scale 124
Chapter 5 - Conclusions 132
Chapter 6 - Recommendations 134
Appendix A - Initial calculations for beam design 135

Appendix B - Crack-widths in OPCC and HPC beams 139
Appendix C - Current density data from LPR and galvanostatic pulse techniques 144
Appendix D - Corroding areas on rebar matched with cracks in the concrete 162
References 172

List of Tables

Table 1: Mixture proportions for OPCC and HPC. 28
Table 2: Compressive strengths of OPCC and HPC cylinders. 45
Table 3: Number of beams with additional visible cracks and increased crack-widths observed in the final measurements. 46
Table 4: Average number of cracks and crack-widths in the beams. 47
Table 5: Average i_{corr} in OPCC and HPC beams measured using the LPR technique. 63
Table 6: The interpretation of half-cell potential measurements according to ASTM C876. 64
Table 7: Corrosion current densities in the cracked region of OPCC determined from cyclic polarization measurements. 83
Table 8: The resistance of concrete in statically and dynamically loaded OPCC beams 92
Table 9: The resistance of concrete in statically and dynamically loaded HPC beams. 93
Table 10: Average and standard deviations of resistances measured in the different sections of the dynamically and statically loaded OPCC and HPC beams. 94
Table 11: Numbers of cracks in the beams and corroded areas on the rebar. 96
Table 12: Surface areas of corrosion damage and the areas covered by corrosion products in OPCC. 98
Table 13: Surface areas of corrosion damage and the areas covered by corrosion products in HPC. 99
Table 14: Nomenclature for the compounds identified in Figure 67-Figure 70. 107
Table 15: Literature sources used in the identification of peaks in Figure 67-Figure 70. 112
Table 16: Sources used for identification of Raman peaks in Figure 72-Figure 78. 121
Table 17: Corrosion products in the concrete beams. 122
Table 18: EDS analysis in atomic % for SE image in Figure 81 128

List of Figures

Figure 1: The E-pH diagram for iron. 2
Figure 2: Schematic illustration of C-S-H in cement paste. 5
Figure 3: A crack in (a) OPCC and (b) HPC 9
Figure 4: Corrosion products of iron. 15
Figure 5: The Pourbaix diagram for iron 25
Figure 6: The cross-section dimensions of the concrete samples. 27
Figure 7: The number of beams of each concrete type subjected to different loading conditions. 29
Figure 8: Schematic illustration of the beams for static and dynamic loading. 30
Figure 9: Beams under static loading. 30
Figure 10: Beams under dynamic loading. 31
Figure 11: A schematic illustration showing the level of salt solution in the wet cycle. 32
Figure 12: A crack comparator. 33
Figure 13: Photographs showing a crack comparator placed on a dynamically loaded OPCC beam when the macrocrack is (a) open and (b) closed 33
Figure 14: (a) and (b) show the two sides of the electrode holder. 34
Figure 15: The holder used to hold (a) the Galvapulse™ electrode assembly and (b) the calomel and counter electrodes for LPR measurements. 35
Figure 16: The current response to LPR potential applied. 36
Figure 17: The Galvapulse™ electrode assembly 38
Figure 18: Showing the locations of the ground hole and segment used for Raman spectroscopy. 40
Figure 19: Illustration of (a) the cracked mid-section with a ground hole through which spurr epoxy was introduced into the sample and (b) the sectioned sample showing the surface to be examined 44
Figure 20: Crack path in concrete (a) in OPCC and (b) in HPC. 48
Figure 21: Epoxy impregnated sections from (a) dynamically loaded OPCC, (b) statically loaded OPCC (c) dynamically loaded HPC and (d) statically loaded HPC photographed in UV light. 50
Figure 22: Photograph of OPCC statically loaded sample 2 in Figure 21(b) prior to impregnation. 50
Figure 23: Example of crack morphology along the edge of the sample in (a) statically loaded beams, (b) dynamically loaded OPCC beams and (c) dynamically loaded HPC beams 51
Figure 24: Chloride profiles in the cracked and submerged regions of OPCC and HPCC beams that were statically loaded. 51

Figure 25: Chloride profiles in the cracked and submerged regions of OPCC and HPCC beams that were dynamically loaded. 52
Figure 26: Networks of cracks observed on the tensile surface in (a) the submerged region of the HPC concrete and (b) the non-submerged region of the OPCC concrete. 54
Figure 27: (a) and (b) show the same crack at different locations on the tensile side in the submerged region of statically loaded OPCC beam 7 where the concrete for chloride concentration measurements was obtained from. 54
Figure 28: Curves illustrating the average chloride content in the beams which have been fitted with trendlines. 55
Figure 29: Corrosion current densities in the OPCC beams obtained using LPR measurements. 56
Figure 30: Corrosion current densities in the OPCC beams obtained using galvanostatic pulse measurements. 56
Figure 31: Corrosion current densities in the HPC beams obtained using LPR measurements. 57
Figure 32: Corrosion current densities in the HPC beams obtained using galvanostatic pulse measurements. 57
Figure 33: Corrosion current densities in the cracked region of the OPCC beams based on polarized areas and actual corroding areas measured using (a) LPR and (b) galvanostatic pulse techniques 61
Figure 34: Corrosion current densities in the cracked region of the HPC beams based on polarized areas and actual corroding areas measured using (a) LPR and (b) galvanostatic pulse techniques. 62
Figure 35: Corroding area A was used for calculation of corrosion current density in the cracked region of HPC1UF. 63
Figure 36: The corrosion potentials in the (a) non-submerged, (b) submerged and (c) cracked regions of the dynamically loaded OPCC beams measured during LPR measurements. 65
Figure 37: The corrosion potentials in the (a) non-submerged, (b) submerged and (c) cracked regions of the statically loaded OPCC beams measured during LPR measurements 66
Figure 38: The corrosion potentials in the (a) non-submerged, (b) submerged and (c) cracked regions of the unloaded OPCC beams measured during LPR measurements. 67
Figure 39: The corrosion potentials in the (a) non-submerged, (b) submerged and (c) cracked regions of the dynamically loaded HPC beams measured during LPR measurements. 68

Figure 40: The corrosion potentials in the (a) non-submerged, (b) submerged and (c) cracked regions of the statically loaded HPC beams measured during LPR measurements. 69
Figure 41: The corrosion potentials in the (a) non-submerged, (b) submerged and (c) cracked regions of the unloaded HPC beams measured during LPR measurements..... 70
Figure 42: The corrosion potentials in the (a) non-submerged, (b) submerged and (c) cracked regions of the dynamically loaded OPCC beams measured using the GalvaPulse™ 71
Figure 43: The corrosion potentials in the (a) non-submerged, (b) submerged and (c) cracked regions of the statically loaded OPCC beams measured using the GalvaPulse™ 72
Figure 44: The corrosion potentials in the (a) non-submerged, (b) submerged and (c) cracked regions of the unloaded OPCC beams measured using the GalvaPulse™ 73
Figure 45: The corrosion potentials in the (a) non-submerged, (b) submerged and (c) cracked regions of the dynamically loaded HPC beams measured using the GalvaPulse™ 74
Figure 46: The corrosion potentials in the (a) non-submerged, (b) submerged and (c) cracked regions of the statically loaded HPC beams measured using the GalvaPulse™ 75
Figure 47: The corrosion potentials in the (a) non-submerged, (b) submerged and (c) cracked regions of the unloaded HPC beams measured using the GalvaPulse™..... 76
Figure 48: i_{corr} in the cracked region of the OPCC static beams..... 79
Figure 49: Currents resulting from the applied over-potentials in the OPCC sections. 80
Figure 50: Rebar sections from the OPCC beams: (a) OPC1DCB (b) OPC7SBB and (c) OPC2DBB. 81
Figure 51: Polarization curves for the (a) OPCC and (b) HPC sections obtained after 9 months of exposure..... 82
Figure 52: Potentiodynamic polarization in OPCC and HPC beams after 18 months of exposure to salt solution 84
Figure 53: ECN measurements on dynamically loaded beams. 87
Figure 54: Encircled area shows corrosion products coming out of the casting defect in the submerged region of the dynamically loaded HPC beam 3. 88
Figure 55: ECN measurements on unloaded and statically loaded beams. 90
Figure 56: The number of cracks in a beam vs the number of corroding areas on the rebars. 96
Figure 57: The number of submerged cracks in the beams vs the number of corroding areas on the rebars. 97
Figure 58: A section of rebar (a) after removal from the beam and (b) after pickling.. 100

Figure 59: Examples of the type of damage encountered in (a) dynamically loaded OPCC (b) statically loaded OPCC (c) dynamically loaded HPC and (d) statically loaded HPC. 101
Figure 60: Corrosion products in the statically loaded OPCC beams 102
Figure 61: Distribution of corrosion products in the dynamically loaded OPCC concretes. 103
Figure 62: Cracks in statically loaded HPC beams with no corrosion products..... 103
Figure 63: Distribution of corrosion products in the dynamically loaded HPC beam 104
Figure 64: (a) A photograph of a section of OPCC dynamically loaded beam showing the macrocrack and the location of the rebar and (b) shows the section labelled X in (a)..... 105
Figure 65: The distribution of corrosion products on the 5 cm section of rebar surfaces from the cracked region in (a) statically loaded OPCC and (b) statically loaded HPC beams. 106
Figure 66: The distribution of corrosion products on the 5 cm section of rebar surfaces from the cracked region in (a) dynamically loaded OPCC and (b) dynamically loaded HPC beams..... 106
Figure 67: Raman spectra obtained from the rebar surface in the statically loaded OPCC beam..... 108
Figure 68: Raman spectra obtained from rebar surface in the dynamically loaded OPCC beam. 109
Figure 69: Raman spectra obtained from rebar surface in the statically loaded HPC beam 110
Figure 70: Raman spectra obtained from rebar surface in the dynamically loaded HPC beam 111
Figure 71: A photograph showing the distribution of corrosion products at a crack in the statically loaded OPCC beam 114
Figure 72: (a), (b) and (c) show the Raman spectra of the locations denoted by numbers in Figure 71. 115
Figure 73: A photograph showing the distribution of corrosion products at a crack in the dynamically loaded OPCC beam 116
Figure 74: (a), (b) and (c) show the Raman spectra of the locations denoted by numbers in Figure 73. 117
Figure 75: A photograph showing the distribution of corrosion products at a crack in the statically loaded HPC beam 118
Figure 76: Shows the Raman spectra of the locations denoted by numbers in Figure 75. 118
Figure 77: A photograph showing the distribution of corrosion products at a crack in the dynamically loaded HPC beam 119
Figure 78: (a), (b) and (c) show the Raman spectra of the locations denoted by numbers in Figure 77. 120

Figure 79: SE image and EDS analysis (weight %) of a cross-section of rebar not embedded in concrete or exposed to chlorides. 126
Figure 80: SE image and EDS analysis (weight %) of a cross-section of rebar embedded concrete but not exposed to chlorides 127
Figure 81: SE image and EDS analysis (weight %) of a cross-section of corroding rebar at a crack in concrete and the concrete adhered to it 128
Figure 82: An SE image of mill-scale on a cross-section of corroding rebar at a crack in concrete.. 129
Figure 83: SE image and EDS analysis (weight %) of mill-scale in the corroding bar..... 130
Figure 84: A BSE image of the image shown in Figure 83..... 131

Chapter 1 - Introduction

Driving on or under steel-reinforced concrete infrastructure in Canada can be a worrying experience. The presence of corrosion cannot be ignored in structures exposed to de-icing salts or marine environments. Many overpasses on Highway 401, for example, contain areas where concrete has cracked and spalled off under pressure from expansive iron corrosion products. This, in turn, leaves steel reinforcement (rebar) directly exposed to de-icing salts, enabling further corrosion. The cost of repairing such structures is immense. The Concrete Canada 1997 Annual Report [1] suggested a cost of $20 billion for rehabilitating existing structures; however, only $3 billion is assigned annually to maintain them and build new ones.

Concrete is the ideal environment for steel; however, chloride ions from de-icing salts penetrate into the concrete through cracks and pores causing corrosion when they reach the surface of the rebar. Considerable work has been done to examine chloride diffusion through the concrete pore network and its effect on the corrosion of rebar, but the role of cracking on corrosion has not been as thoroughly examined. Those studies that do exist have involved unloaded or statically loaded cracks, whereby cracks are kept open to maintain specific crack-widths throughout the experiment time. In real structures, however, cracks may open and close as a result of varying loads. This behaviour of cracks could significantly affect the dynamics of steel corrosion by influencing the ingress of aggressive species such as chloride ions and oxygen, and the perseverance of corrosion products in and around the cracks.

The objectives of this project were (i) to observe the effect of loading on reinforcement corrosion and the influence of the type of concrete, and (ii) to provide data that can be used for service-life modelling of cracked reinforced concretes. This thesis focuses on the effect of different loading types (i.e. no load, static and dynamic loading) on visible cracking (macrocracking) in concrete and the influence of these cracks on corrosion of the reinforcing steel. Other types of cracks such as those induced by freezing and thawing and alkali-aggregate reactions are not considered in this study.

Chapter 2 - Background

2.1 CORROSION OF STEEL IN CONCRETE

The potential-pH (E-pH) diagram for iron, shown in Figure 1 [2], illustrates the regions of thermodynamic stability for iron and its corrosion products, and indicates that concrete is the perfect environment for steel. The pH of pore solution in good quality concrete, which ranges for 12.5-13.5 [3], allows the steel to form a passive layer on its surface, which significantly reduces its corrosion rate.

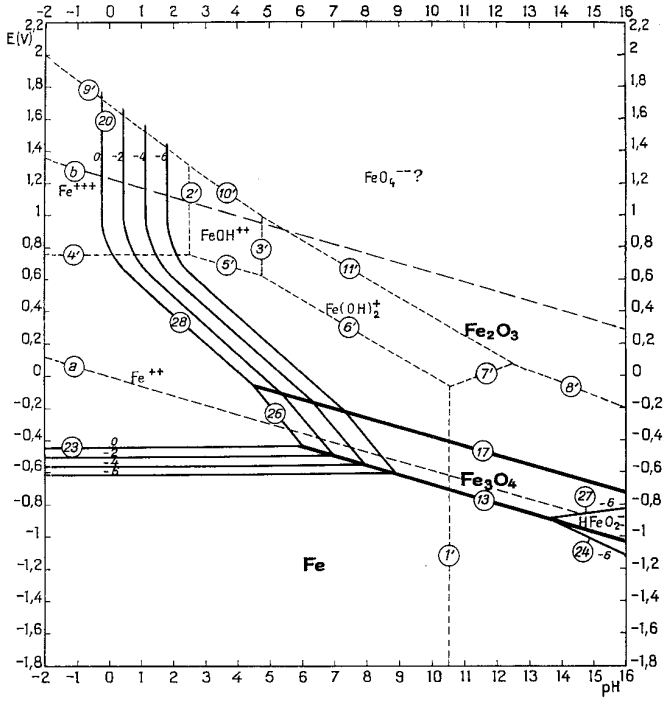

Figure 1: The E-pH diagram for iron [2]. Note the potentials on the y-axis are versus standard hydrogen electrode (SHE).

Two factors that cause active corrosion of reinforcing steel are carbonation of concrete and chloride ions [4]. During carbonation, carbon dioxide (CO_2) from the atmosphere dissolves in the pore solution of cement paste and reacts with potassium, sodium and calcium hydroxides, reducing the pH of pore solution to 8.3 [5, 6]. The oxide film that is formed on steel at this pH is not protective. Verbeck [7] states that it is easiest for CO_2 to penetrate into concrete in its gaseous form but, if the concrete is completely dry, it does not carbonate. CO_2 must dissolve in water before it reacts with

calcium hydroxide (CH[1]) to form calcium carbonate ($CaCO_3$), which precipitates as a solid in the pores of the concrete and reduces the rate of further penetration of CO_2. However, carbonation of concrete in cold climates takes a long time to occur as the concrete seldom dries out. Hence, carbonation as the cause of corrosion is not investigated further in this thesis.

Chloride ions can be introduced into concrete via a number of ways including through the addition of calcium chloride as a set accelerator (no longer permitted in most jurisdictions), contaminated water or aggregates [4]. Presently, the environment is the most common source of chlorides in concrete: concrete structures in marine environments and in coastal areas are highly susceptible to chloride ingress and, in cold climates, the use of de-icing salts, which contain chlorides, is prevalent.

De-icing salts are an immense threat to steel in reinforced concrete. Chloride ions from de-icing salts penetrate to the reinforcing steel (rebar) causing localized corrosion [8]. This could cause the steel to be completely severed without any visible signs of corrosion. However, a more common consequence is damage to concrete by expansive corrosion products. The cations of de-icing salts may also adversely affect concrete and prevent it from adequately protecting the steel. Magnesium ions react with CH and calcium silicate hydrate (C-S-H), the major phase in cement paste, to form brucite ($Mg(OH)_2$) and magnesium silicate hydrate (M-S-H). Brucite is formed at the expense of CH and its formation lowers the pH of pore solution thereby increasing corrosion rates of steel while M-S-H is non-cohesive and leads to disintegration of the paste [9]. On the other hand, calcium chloride de-icing salt leads to crystallization of expansive complex salts containing CH and $CaCl_2$ [10]. Cody et al. [11] determined that magnesium chloride was the most damaging to concrete followed by calcium chloride. Sodium chloride had an insignificant detrimental effect on the concrete. Sutter et al. [12] observed expansion and cracking in concrete samples exposed to $CaCl_2$ and $MgCl_2$ solutions which were attributed to the formation of calcium oxychloride and brucite.

Chlorides in concrete are present in two forms: bound by the hydrated phases of cement paste and as free ions in the paste pore solution. Since, the latter are the primary cause of rebar corrosion [13], the tricalcium aluminate (C_3A) content of the cement is important in this case because it can bind chloride ions to form Friedel's salt ($Ca_2Al(OH)_6Cl.2H_2O$) thereby removing some of the chloride ions

---

[1] Cement chemistry abbreviates oxides as follows: C = CaO, S = SiO_2, A = Al_2O_3, F = Fe_2O_3, $\bar{S}$ = SO_3 and H = H_2O

from solution. According to Suryavanshi et al. [14], Friedel's salt can be formed in two separate ways. The first involves absorption of chloride ions from the pore solution into the aluminate ferrite mono (AFm) phases such as monosulphate. The second method involves ion exchange between the pore solution and the AFm phases, whereby the AFm uptake chloride ions from and release hydroxyl ions into the pore solution. However, the influence of the above mechanisms on the sulphate ions in the AFm structure has not been discussed by the authors. Calcium oxychloride formation in concrete also binds free chlorides; however, the stability of this compound is temperature dependent and rising temperatures cause its dissociation, releasing chloride ions into pore solution [15]. The calcium silicate hydrate (C-S-H) phase in cement paste is also able to bind chlorides [16, 17] . Ramachandran [18] determined that chlorides can be bound by C-S-H in three ways: (i) a chemisorbed layer on C-S-H which is held in place by electrostatic and van der Waals forces, (ii) trapped in the interlayer spaces between C-S-H particles and (iii) integrated in the lattice of C-S-H. Chlorides that are admixed in the concrete at the time of casting are more likely to be trapped or combined in the C-S-H compared to the ones that enter the concrete after it has hardened.

Corrosion products observed on steel in concrete are oxides or hydroxides. Whether or not chlorides participate in these reactions that lead to the formation of the corrosion products is not known. However, it is thought that, initially, the following reaction takes place leading to the formation of iron chloride in the pits formed due to corrosion [19]:

$$Fe^{2+}_{(aq)} + 2Cl^{-}_{(aq)} \rightarrow FeCl_{2(aq).}$$

Iron chloride is considered to be stable in the pits because of acidic conditions. However, when it diffuses into the concrete where the pH is higher, it is no longer stable and decomposes into iron and chloride ions. The chloride ions are attracted back into the pits while the iron ions react with the hydroxyl ions and precipitates as ferrous hydroxide. This reaction is represented below. Ferrous hydroxide may further oxidize to form other hydroxides / oxides.

$$Fe^{2+}_{(aq)} + 2OH^{-}_{(aq)} \rightarrow Fe(OH)_{2(s)}$$

2.2 POROSITY IN CONCRETE

Porosity is an integral component of cement paste. Capillary pores are remnants of originally water filled spaces that have not been occupied by products of hydration [20]. Jehng et al. [21] have detected small and large capillary pores that have an average radius of 7.5 nm and 160 nm in white

cement pastes, respectively. However, their conclusion seems to be oversimplified. There is bound to be a broad range of pore sizes in paste, which will vary depending on the cementing materials and water to cement (w/c) ratio used. The interconnectivity of capillary pores can have advantages and disadvantages in cement paste. In pastes made with w/c < 0.42, which is the w/c ratio theoretically required for the complete hydration of cement [22], the interconnectivity of such pores may be limited but, if they are interconnected, the pores could aid hydration by acting as sites where water from external sources (e.g. precipitation) can be held. However, connected capillary pores also allow deleterious species such as chloride ions into the concrete. Figure 2 shows a schematic illustration of capillary pores in cement paste.

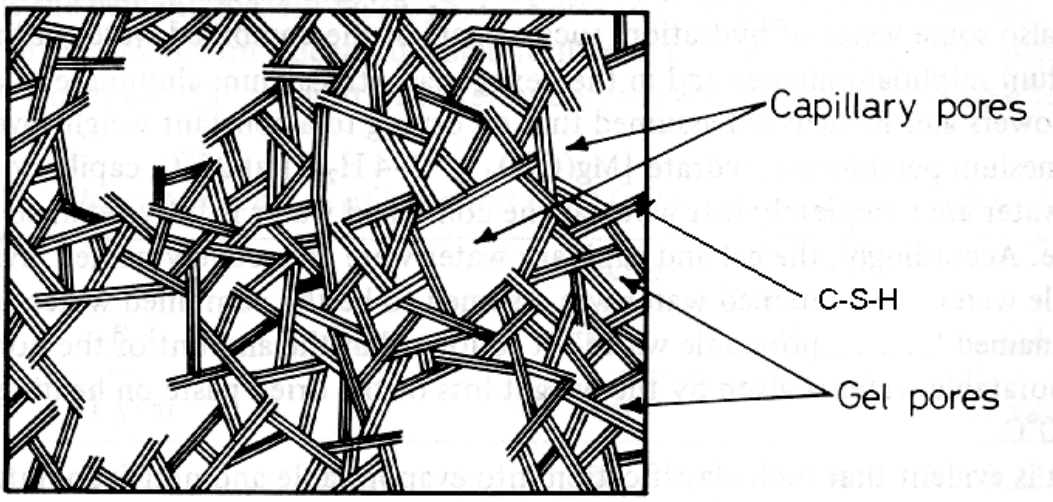

Figure 2: Schematic illustration of C-S-H in cement paste [23].

The pores between C-S-H particles are known as gel pores and are also illustrated in Figure 2. Power's model [20], which is the original model for porosity in cement pastes, gives an average diameter of 1.8 nm for gel pores. However, the existence of gel pores has been questioned by Diamond [24] who argues that such pores are not detectable by transmission electron microscopy (TEM) and mercury intrusion porosimetry (MIP). However, Jehng et al. [21] have detected pores with sizes 2 nm and 1 nm using the NMR technique.

The amount and interconnectivity of capillary porosity present in concrete influence the corrosion rates of steel. Interconnected capillary pores allow chloride ions to diffuse from the environment and current (ions) to migrate between cathodic and anodic sites in concrete. Therefore, reducing the amount of interconnected capillary porosity increases resistance to corrosion.

2.3 SUPPLEMENTARY CEMENTING MATERIALS IN CONCRETE

Supplementary cementing materials (SCMs) are often by-products of industrial processes; hence, their use in concrete (a) saves the cost of disposing them and (b) reduces the amount of cement required, which, in turn, decreases the amount of fuel used and carbon dioxide (formed during cement production) per volume of concrete. When used appropriately in concrete, they provide beneficial contributions to its properties such as lower permeability [25]. Their use in concrete is also desirable because they are less costly than cement.

ASTM C 595 [26] defines a pozzolan as "a siliceous or siliceous and aluminous material, which itself possesses little or no cementitious value but will, in finely divided form and in the presence of moisture, chemically react with CH to form compounds (C-S-H) possessing cementitious properties." Pozzolanic reactions in concrete may occur slowly with time because they depend on the availability of CH; hence, the rate of strength development in concretes containing pozzolans may be slow relative to those with no pozzolans [27]. Most of the SCMs, such as fly ash and silica fume, have pozzolanic properties. Blast furnace slag, however, has both pozzolanic and cementitious properties. Silica fume and ground granulated blast furnace slag are described in detail below because they have been used in this experimental program.

2.3.1 Silica Fume

Silica fume is a by-product of the production of silicon or ferro-silicon alloys [28]. It contains more than 85 % amorphous silicon dioxide (SiO_2) [27]. Silica fume particles are spherical in shape and have an average diameter of 0.1-0.3 μm which is about a hundred times smaller than an average cement particle [29]. This allows silica fume to be highly reactive but its addition to concrete increases water requirements because of its large surface area. Nehdi et al. [30] suggest that silica fume particles may also have the affinity to adsorb multiple layers of superplasticizer molecules increasing water demand in low water to cementitious material (w/cm) ratio concretes compared to other ultrafine particles such as ground silica and limestone. However, their observation was based on experimentation with one type of superplasticizer (naphthalene-sulphonate formaldehyde) and may not be extendable to other types.

In concrete (w/cm = 0.35) containing 10 % silica fume by weight of cement, the silica fume starts to contribute to the strength of the concrete from as early as 3 days after mixing [31]. In fact, infrared spectra have shown that, in similar pastes, silica fume starts reacting with CH from the first hour of

hydration [32] to form C-S-H. This reaction consumes most of the CH produced for up to 12 hours of hydration. Silica fume continues to contribute to the increasing compressive strength of cement pastes at all ages [31], but mostly at early ages [33]. However, Feldman et al. [34] have shown that compressive strengths of cement pastes with w/cm = 0.25 decrease as the silica fume content increases. They tested 0 %, 10 % and 30 % silica fume by weight of cement but details on how they made the concrete with such a low w/c ratio could not be found. The decrease in strength in the lower w/cm pastes could be due to the continuous network of microcracks formed as a result of autogenous shrinkage, which was observed by Igarashi et al [35].

The high rate of pozzolanic reaction of silica fume, which is enhanced by its high surface area to volume ratio, leads to a lower CH content in concretes containing silica fume. Page et al. [36] documented that 30 % silica fume content by weight of cement (w/c = 0.5) led to a drop in the pH of cement paste pore solution to below 12.5 indicating that all the CH had been consumed in the reaction with silica fume. Silica fume improves the microstructure of cement pastes by filling pores and densifying the paste [37]. Mehta and Gjørv [27] state that cement pastes containing 30 % silica fume are dense structures that do not have large pores (> 0.1μm). Igarashi et al. [38] found that concretes containing silica fume had fewer coarse pores (diameter > 0.2 mm) than those that did not contain any SCMs.

The amount of silica fume used in concrete should reduce the porosity without eliminating CH. Standards such as ASTM C 1240 [39] and AASHTO M 307 [40] specify the use of 10 % silica fume by mass of cementitious materials for most tests examining the properties of mortar and concretes containing silica fume. In Canada, Portland cement with 8-9 % silica fume is commonly available [41].

2.3.2 Granulated blast furnace slag

Granulated blast furnace slag (slag) is formed by rapidly cooling molten blast furnace slag [42]. The ground product consists of angular glassy particles less than 45 μm in size. To obtain a given consistency in concretes containing slag, lower amounts of water are required than for Portland cement concrete due to the deflocculation and dispersion of cement particles by slag particles in the former [43].

Aldea et al. [44] have shown that 25 % slag replacement of Portland cement in concrete (w/cm = 0.45) gives the highest compressive strength compared to other replacement values while 50 % slag

replacement gives the same strength as ordinary Portland cement concrete (OPCC). Jau et al. [45] illustrate that, at 20 % cement replacement with slag, the pore volume in concrete (w/cm = 0.6) is minimum compared to other replacement amounts. While Aldea et al.[44] did not test 20 % replacement of cement with slag, Jau et al.[45] have not examined 25 % replacement. However, the reason for high compressive strengths observed by the former is probably the reduced porosity formed in concrete when there is a 20-25 % replacement of cement with slag (depending on the w/cm used). This reduction in porosity may be because of the optimal amounts and characteristics of hydration products being formed which fill up large sized pores. This could also be the reason why the partial substitution of cement with slag also reduces the chloride penetration into concrete compared to OPCC [46-48]. Leng et al. [46] indicate that slag contains high C_3A contents, which may increase the ability to bind chlorides in concrete. Scaling, however, has been a problem reported in warm climates where concrete structures, containing slag, are subjected to drying at early ages which results in large pores [47] that cause a decrease in the strength of the concrete. However, this phenomenon should be true for all concretes containing low w/c ratios and pozzolans that react slowly.

2.4 ORDINARY PORTLAND CEMENT AND HIGH PERFORMANCE CONCRETES

The water to cementing materials (w/cm) ratio has an immense impact on durability because it governs (a) the porosity in concrete which, in turn, controls the ingress of chloride ions and (b) cracking as a result of freeze-thaw cycles. Ordinary Portland cement concretes (OPCCs) are typically made with w/c ratios of 0.40 or higher. As stated in Section 2.2, a w/c ratio of 0.42 is theoretically required for the complete hydration of cement in concrete. However, hydration is a gradual process and, as a result, the unused mixing water in OPCCs is retained in the capillary pores. The existence of water-filled pores causes OPCCs to have a low resistance to the ingress of chloride ions and to cracking as a result of freezing and thawing.

High performance concretes (HPCs) were developed to resolve the durability problems encountered in OPCCs. They are low w/cm ratio concretes containing SCMs that receive adequate curing and exhibit higher strength and greater abrasion resistance than OPCCs [49]. HPCs have lower capillary porosity [50] because they are typically made with w/cm ratios of 0.35 or lower. A workable high performance concrete (HPC) mix is obtained with the aid of superplasticizers containing

surfactants (e.g. sulphonated melamine formaldehyde, sulphonated naphthalene formaldehyde or polycarboxylates) that adhere to the surface of the cement particles, dispersing them in the fluid concrete mix [51]. HPCs also contain SCMs which help reduce porosity even further by producing C-S-H that grows into the pores. In HPCs, the paste is often as strong as the aggregates because of the low porosity and large amount of C-S-H present in it. Therefore, cracks in HPCs tend to propagate in straight paths cutting through the aggregates [52]. This is not the case in OPCCs, in which aggregates act as obstacles to cracks which propagate through the soft paste around the aggregates. Figure 3 shows crack propagation in OPCC and HPC. Hence, more energy is required to propagate cracks in OPCC than in HPC. As a result, HPCs tend to be more brittle than OPCCs [53] and are more prone to shrinkage cracking [54].

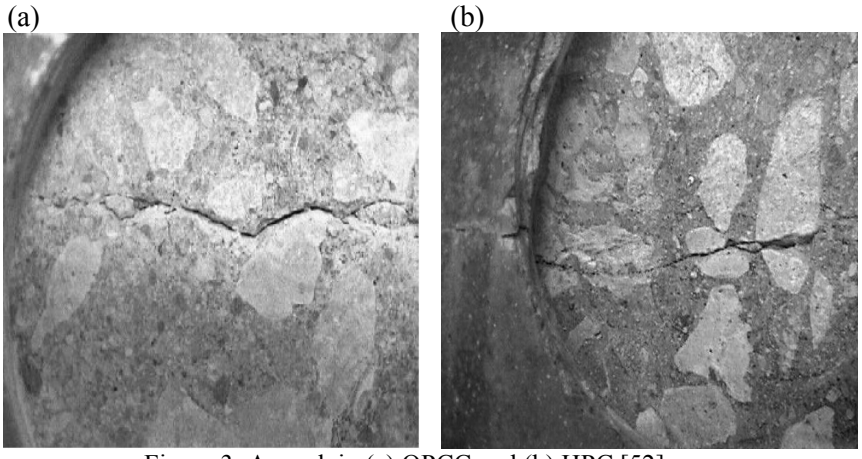

Figure 3: A crack in (a) OPCC and (b) HPC [52].

2.5 CRACKS IN CONCRETE

Although this study focuses on macroscopic loading cracks, a crack network exists in concrete with contributions from many sources. Therefore, cracks of all types are reviewed here.

Cracks are usually classified in two types: microcracks and macrocracks. There are various definitions in the literature that distinguish microcracks from macrocracks, which are either based on crack morphology or means of formation.

A literature search pertaining to crack morphology revealed that crack-widths were important in distinguishing between macrocracks and microcracks. Bisschop and van Mier [55], and Shiotani et al. [56] define microcracks as those with widths less than 50 μm, whereas Slate and Hover [57] define

them as cracks with a width less than 100 μm. Kjellsen and Jennings [58] define an upper limit of 10 μm for microcrack widths.

A number of studies distinguish between macrocracks and microcracks based on their formation. Mehta [59] reports that macrocracks are formed from irregularities in the concrete microstructure when the concrete is subjected to loading and weathering. Hauwaert et al. [60] have shown that loading of concrete can result in both macro- and microcracking. Burrows [61] claims that macrocracks result from the various types of shrinkage mechanisms discussed in Section 2.5.1.1, while microcracking is caused by freeze-thaw cycles, wetting-drying of concrete and may also be formed when concrete undergoes drying shrinkage. Gerwick [62] proposes that microcracks are formed initially in highly porous and weak cement pastes in concrete due to water concentration at the aggregate-paste interface, as well as under reinforcement. Other causes of microcracking include thermal incompatibility between the reinforcement, paste and aggregates, and alternate wetting and drying of concrete.

While the distinction between macrocracks and microcracks may be necessary to interpret data from laboratory tests that usually last for a short time, this distinction may not be appropriate for long lasting structures. In the latter, a crack network may develop with the crack sizes changing over time (i.e. microcracks developing into macrocracks) because the causes (discussed above) will have an impact on already existing cracks. However, for the purpose of this laboratory project, cracks in concrete are classified into visible by the eye, or macrocracks, and invisible, or microcracks.

2.5.1 Sources of Cracks in Concrete

There are various mechanisms that cause cracking in concrete. These mechanisms are discussed in the sections below.

2.5.1.1 Shrinkage

Shrinkage is defined as the “contraction of cement paste or concrete” [22] due to one of five causes: plastic shrinkage, drying shrinkage, autogenous shrinkage, thermal shrinkage and carbonation shrinkage. Shrinkage usually occurs in two stages designated as early and later [63]. The early stage takes place up to the point where the cement paste sets and starts to harden. This is usually in the first twenty-four hours after the cement paste is mixed. The later stage shrinkage begins after the first

twenty-four hours. Holt and Leivo [63] suggest that early stage shrinkage consists of drying, autogenous and thermal shrinkage, whereas long-term shrinkage includes these types and carbonation shrinkage.

Even though shrinkage is a three-dimensional phenomenon, most studies such as [64] and [65] have examined it in terms of uniaxial strain as opposed to observing its effect on the microstructure of concrete. This is because dimensional changes are easier to measure and, in concrete, since one of the dimensions is usually longer than the others, the effects of shrinkage are greatest in this direction.

Plastic shrinkage is said to occur in fresh concretes when the rate of evaporation of water from the surface of the concrete is higher than the rate at which concrete bleeds (i.e. when particles in freshly mixed concrete settle resulting in higher w/cm ratio near the top surface of the concrete compared to the bulk) [66]. In such cases, the surface of the concrete does not flow and hence, is too stiff and weak to resist tensile stresses that are caused by restraint. This results in the development of cracks at the surface. These cracks are almost straight and result in the weakening of concrete structure [67] and they allow the ingress of aggressive species into the concrete. Plastic shrinkage can be due to the reduction in bleeding as a result of absorption of water by forms or aggregates and/or the use of low w/c ratios [66]. Al-Amoudi et al. [68] observed an increase in plastic shrinkage cracking with an increase in the silica fume content in concretes exposed to hot weather conditions. This is probably because evaporation in concretes is also complimented by hydration of the cementing materials. The cements containing large amounts of silica fume are likely to hydrate more initially compared to those without, which further decreases the amount of water in the concrete (i.e. even less water bleeding).

Autogenous shrinkage occurs as a consequence of hydration of cement [22]. It is also called self-desiccation shrinkage, which basically means that the cement paste is drying itself out and there is no moisture movement to and from it [69]. For hydration to occur there must be sufficient water present for chemical reactions to occur and for filling of gel pores [22]. In the case of OPCC, if the w/c is 0.42 or greater, the cement can (theoretically) hydrate fully. If a lower w/c ratio is used, there will not be enough water to saturate the surfaces of capillary pores. Hydration is at its lowest rate if the water vapour pressure in the capillary pores falls below 0.8 of the saturation pressure [22]. This is known as self-desiccation and it only applies to cases where concrete is completely isolated from an external moisture source. Setter et al. [70] describe self-desiccation as the drying out of pores as a result of hydration. In HPC, early and prolonged wet curing reduces autogenous shrinkage and decreases the pore volume. Water from curing is used to hydrate particles of unhydrated cement, which results in the decrease in porosity. Continuous hydration from curing practices creates very fine porosity in the

HPC. However, when this porosity becomes filled with products of hydration, self-desiccation can occur in concrete even though it may be exposed to an external source of water [71].

Drying shrinkage is shrinkage that is caused by moisture loss after concrete is hardened [65, 72]. The water in the pores is held by strong forces and the strength of these forces decrease as the diameter of the pores increases [22]. Thus drying is caused by the evaporation of water from the capillary pores that are exposed to air, which has a lower relative humidity than the pores. Water loss is progressive and occurs at a decreasing rate with increasing hydration time.

There is very limited information in the literature that actually relates autogenous and drying shrinkage to the morphology and interconnectivity of cracks produced as a result. The studies that exist, such as [55, 73, 74], are aimed at describing how to prepare samples for observation.

Carbonation causes decalcification of cement pastes [75]. Apart from reacting with CH to form $CaCO_3$, it changes the structure of C-S-H by depleting calcium and leaving behind silicate structures [76, 77]. It is difficult to imagine how carbonation leads to shrinkage particularly since it results in the formation of $CaCO_3$. A literature search on how carbonation leads to volume changes (shrinkage) in concrete revealed only one explanation. Powers [78] hypothesized that the cause of shrinkage is the dissolution of CH crystals that are under pressure. This causes stresses to develop in the remaining paste leading to a volume decrease. Even though $CaCO_3$ is produced as a result of the carbonation, it fails to prevent this volume change because it is precipitated in sites that are not under pressure.

Thermal shrinkage usually occurs in mass concretes where the heat of hydration cannot easily escape and causes the temperature gradient of the concrete to increase. The expansion of warm inner layers of concrete results in the development of stresses on the cooler outer layers. This causes the formation of cracks in the latter. Also, as warm concrete cools off over time, it starts contracting. If there is any restraint on the contraction then cracking develops [79].

2.5.1.2 Chemical Reactions

Chemical reactions that lead to cracking in concrete include alkali-silica, alkali carbonate and carbonation reactions. Carbonation has been discussed in Sections 2.1 and 2.5.1.1

Aggregates in concrete rarely change with time unless affected by deleterious reactions such as alkali-silica and alkali carbonate reactions. In the alkali-silica reactions (ASR), the highly alkaline pore solution in cement reacts with acidic rocks (containing silica and siliceous materials) [80]. The alkali-silicate gels produced as a result of this reaction absorb water and expand, creating cracks in

the concrete. In the alkali-carbonate reaction (ACR), the alkaline pore solution reacts with aggregates composed of carbonates such as dolomitic limestone ($CaMg(CO_3)_2$) producing brucite ($Mg(OH_2)$, calcium carbonate ($CaCO_3$) and alkali carbonates ($(K,Na)_2CO_3$) [81]. The reason for cracking due to ACR include: (i) pressures caused by water molecules and alkali ions and (ii) production and re-distribution of ACR products [82].

2.5.1.3 Weathering Processes

Freezing and thawing and wetting and drying are weathering processes that cause cracking in concrete [83]. The theory behind how concrete undergoes freeze-thaw cycles was based on observations in soils [84], in which it was noticed that, when water in one section turned into ice, ions were forced out of this water. These ions caused water to be drawn out of unfrozen sections and attracted into regions where ice was formed. This process occurred at macroscopic levels in soils. Powers [85] claimed that this theory could not be applied at the macroscopic level to hardened cement pastes of average quality because the strength of the concrete would resist ice formation at the macroscopic level. However, he considered that it was possible for this process to occur at the microscopic level. It was later found that Powers' idea did account, in part, for the freeze-thaw phenomenon observed in concretes [84]. It was also determined that ice formation in water filled capillary pores exerted stresses in the surrounding cement paste causing the cracking of the paste. Entrained air voids prevent the build up of these stresses in concrete by providing room for water to flow into as ice expands, thereby preventing concrete from cracking. Powers [20] also found that the freezing of solution in the pores of the cement paste was a function of the pores' surface area and the ion content of the solution. Freezing and thawing has a limited effect on HPC because it has a low moisture transport coefficient and small moisture capacity [86] due to the absence of large number of capillary pores.

While there has been a lot of research on freezing and thawing in concretes, only two studies have examined the characteristics of cracks formed in concrete subjected to freeze-thaw cycles. In one of the studies, Jacobsen et al. [87] observed 10 μm-wide cracks in OPCCs that were subjected to seventy freeze-thaw cycles. They also found that the distance between these cracks was 400-500 μm. In another study, Jacobsen et al. [88] observed cracks with widths between 1-10 μm in concrete samples that had undergone freezing and thawing. Cracks with widths less than 5 μm healed when the samples were immersed in water for three months. The difference between the two studies is that the former

examined the effect of freezing and thawing on the microstructure of high strength concrete using an optical microscope, while the latter focused on the differences in microstructure between frost affected and self-healed concretes using a scanning electron microscope (SEM). This is probably why smaller crack sizes were observed in the latter.

A considerable number of studies (e.g. [89, 90]) exists which examine the corrosion of reinforcement in concrete that was exposed to cycles of wetting and drying in salt water to simulate marine environment. However, most of these studies focus on the corrosion of the reinforcement and neglect the effect of such exposure on concrete. Wetting and drying of concrete is particularly important if the concrete is exposed to de-icing salts. The wetting phase allows the penetration of the dissolved salts into the concrete. Excessive drying of concrete could lead to crystallization pressures in the pores [91] which could result in cracks being formed. However, in regions with cold climates, infrastructure concrete seldom dries out completely. Hence, wetting and drying may not be a significant problem in these regions.

2.5.1.4 Corrosion of Reinforcement

The corrosion of reinforcing steel has an immense impact on cracking in concrete. The corrosion products of iron are expansive as shown in Figure 4. The unit volumes of the products presented in this figure are based on theoretical considerations and the actual volumes might be greater due to the inclusion of porous and water-filled spaces. The formation of these products induces stresses in the concrete, which can result in cracking. In this section, the studies that have examined the effect of corrosion on cracking in concrete will be discussed. The studies that have researched the effect of cracking on corrosion are reviewed in Section 2.7.

Very few studies have actually examined the effect of corrosion on cracking. Cabrera [92] observed that corrosion caused cracks parallel to the reinforcement when reinforcement was corroded using an impressed current. Andrade et al. [93] found that only a few micrometers of rebar corrosion induced visible cracks (~ 0.1 mm width) in reinforced concrete also corroded with an impressed current. However, studies that use impressed currents to cause corrosion of the steel in concrete are not realistic representations of what happens in actual concrete structure because (i) corrosion is not initiated by aggressive species such as chloride ions (ii) corrosion is uniform and not localized (iii) oxygen may be evolved at the anode and hydrogen at the cathode, and (iv) very little time is given for corrosion products to form and disperse into the concrete [94].

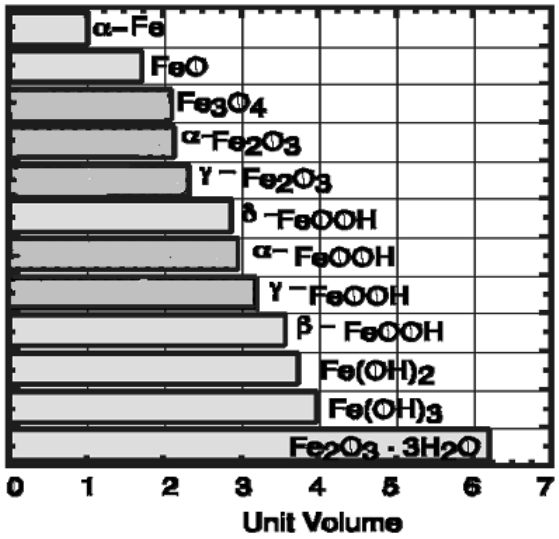

Figure 4: Corrosion products of iron [95].

A few studies have also tried to examine the effect of corrosion on cracking by means of simulation. Allan [96] applied hydraulic pressures through the reinforcing bars to simulate the cracking of concrete from localized formation of corrosion products. Uddin et al. [97] claim that cracks in concrete propagate by mode I fracture (opening mode) with small contributions from mixed mode and mode II fracture (in-plane shear). This study also relied on hydrostatic pressures from expansive agents to simulate cracks in reinforced concrete. Ohtsu and Shinichi [98] modelled crack initiation and crack propagation in concrete due to reinforcement corrosion. They took into account various types of cracks (surface, spalling, internal, vertical and diagonal cracks) based on location or outcome of their formation and the effect of hydrostatic and vertical pressures from corrosion products on these cracks.

All the studies listed in this section assume that cracking is initiated from the rebar-concrete interface due to pressures from corrosion products in the interface. None of these studies, except that of Allan [96], consider the possibility of corrosion products diffusing into the concrete without cracking it. Allan [96] suggests that the time to cracking in concrete will be extended if concrete is porous or has air voids and microcracks which can act as storage sites for corrosion products.

2.5.1.5 Loading

Cracking in concrete is strongly influenced by the interfacial transition zone (ITZ) between the aggregates and the cement paste and Nemati et al. [99] observed more interconnected porosity at the

ITZ in unloaded normal strength concrete than in unloaded high strength concrete because the bond between the aggregates and cement paste in latter was stronger. Thus, they observed less cracking in loaded high strength concrete than unloaded normal strength concrete.

When concrete is subjected to external tensile loading, microcracks are found to develop at the aggregate-paste interface or at any defects in concrete [100]. As the tensile load increases, the microcracks increase in size and join to form macrocracks. Gopalaratnam and Shah [101] reported that a single visible crack developed at peak tensile load in concrete. However, Otsuka and Date [102] determined that the propagation of a large crack in concrete is preceded by the formation of numerous microcracks at the tip of the large crack.

Goto [103] demonstrated that various types of cracks developed when reinforced concrete was subjected to uniaxial tension parallel to the reinforcement. Primary cracks developed perpendicular to the reinforcement at the surface of the concrete at low load levels (1050 kg/cm^3) and propagated to the level of the rebar. At higher load levels (3000 kg/cm^3), secondary cracks developed and propagate from the rebar level to the surface of the concrete. At the rebar level, a comb like structure developed which led to de-bonding between the rebar and the concrete. The (internal) cracks in this comb-like structure were formed due to shearing action between the rebar lugs and the concrete.

Raju [104] found that microcracks also form in concrete under compression because of localized tensile stresses in concrete particularly in regions of high aggregate density and at the paste-aggregate interface. He also found that more microcracks develop when concrete is subjected to cyclic loading than when it is under static loading. Nemati et al. [99] also observed microcracks initiating in the ITZ under compressive loads. According to Shah and Chandra [105], these cracks develop at about 50 % of the ultimate load. At 70 % of ultimate load, cracks form in the mortar surrounding the aggregates. A region of localized damage forms at the ultimate load [106], which has a different post peak stress-strain response than the bulk concrete [107]. Puri and Weiss [108] examined the development of the localized damaged zone by studying the acoustic emissions that are released during crack formation. Their research revealed that the axial damage zone was 1.2 times the diameter of the cylindrical concrete sample at the ultimate load.

Shah and Chandra [109] examined the effect of sustained compressive loads and cyclic compressive loads on cracking in concretes. They concluded that sustained loading strengthened the concretes; however, the presence of water caused crack formation in concretes under sustained load. On the other hand, cyclic loading did not allow the strengthening of concretes and caused additional cracking, which was not witnessed in concretes under sustained loads, to develop. In fact, concretes

subjected to cyclic loading illustrated fracture striations and the numbers of striations were equal to the numbers of loading cycles applied to the concretes.

2.6 CHLORIDE INGRESS IN REINFORCED CONCRETE

Chloride ions cause the corrosion of reinforcing steel in concrete as discussed in Section 2.1. There are two ways by which chloride ions from external sources can reach the reinforcing steel: via the porosity in the paste or via interconnected cracks, which offer a more direct path.

The diffusion and/or absorption of chloride ions into uncracked concrete occurs mainly through the interconnected capillary pores in the concrete [110]. Low w/cm ratios and the presence of SCMs reduce the interconnectivity of capillary pores and therefore limit the penetration of chloride ions. At early ages, 5-10 % silica fume content in the cement significantly reduces chloride ingress into concrete compared to other pozzolans such as fly ash [111] because the higher surface area to volume ratio of the silica fume particles causes them to react and fill up the pores faster than the other pozzolans. Jensen et al. [112] found that, in concretes with w/cm ratio of 0.7, chloride ingress occurred through continuous capillary pores. Hansson and Okulaja [113] found after the same exposure, that OPCC contained significantly more chlorides than HPC at greater penetration depths from the surface. Hobbs [114] claims that aggregates in concrete should not be completely neglected when considering the diffusion of chlorides into concrete: the permeability of the aggregates and the amount present in concrete could influence diffusion.

A significant number of studies, including [115] and [116], has examined the ingress of chloride ions into concrete using the “rapid chloride permeability test” [117]. This test actually measures the migration of ions, not the diffusion or the sorption of chloride ions which would be the case in concrete in service [118]. Castellote et al. [119] claim that the determination of “diffusion” coefficients from these tests (using potentials recommended for such tests) match those of actual diffusion of chloride ions into concrete. However, Feldman et al. [120] conclude that this test may be used to obtain a relative comparison of concretes’ permeabilities rather than give the actual values, but the relative comparison can also be achieved more easily by measuring the resistivity of the concretes.

Wetting and drying of concrete has an immense affect on the ingress of chloride ions into concrete compared to continuous saturation. In wet concrete, chloride ions ingress by diffusion;

however, when dry concrete is wetted, chloride ions penetrate into the concrete by capillary absorption which is a much faster process than diffusion [118].

As stated in Section 2.1 whether chloride ions are bound or free has a significant impact on the risk of reinforcement corrosion. Many studies have been published which refer to the "chloride threshold values" in concrete. This term does not have a sound definition and has been defined as the amount of free chlorides (e.g. [121]), total chlorides (e.g. [122]) or Cl^-/OH^- ratio at the surface of the steel (e.g. [123]) at the initiation of active corrosion. Glass and Buenfeld [124] claim that threshold values should be stated as the total amount of chlorides; stating these values as the amount of free chlorides and Cl^-/OH^- ions offers no advantage and ignores factors that influence corrosion initiation such as the moisture content and precipitated CH (which maintains the pH of pore solution at 12.6). Also, bound chlorides may become free if the pH falls below 11.5 [125]. The threshold values depend on several factors including w/cm ratio, cement type, C_3A content, SCMs content and exposure conditions [126] and, of course, type of rebar.

Cracks significantly increase the penetration rate of chloride ions into concrete [127]. Jacobsen et al. [128] measured the migration of chloride ions in OPCC (w/c 0.4) subjected to freeze-thaw cycles. They found that cracks which formed as a result of freezing and thawing increased the chloride penetration depth and decreased the chloride penetration time. They also found that crack healing in concretes, which were submerged in water for three months, significantly reduced the penetration of chlorides into concrete. Also, crack-widths less than 50 μm may have an insignificant effect on the penetration of chlorides into concrete [129, 130]. Gowripalan et al. [131] examined the effect of the ratio of crack-width to cover depth on the ingress of chloride ions into concrete (w/cm = 0.6) under flexure. They found that more chlorides diffused through the region of concrete that was under tension compared to that in compression because compression resulted in reduced porosity. Win et al. [132] found that, in concretes with w/c ratios of 0.45 and 0.60, the penetration of chloride ions from the surface of a crack is equal to or higher than that from the surface of the concrete. Gagné et al. [133] also detected chloride profiles similar to the above in mortar samples where chloride ingress occurred via the sample surface or through cracks with widths greater than 125 μm.

2.7 THE EFFECT OF CRACKING ON CORROSION

Aggressive species, such as chloride ions, oxygen and water, penetrate uncracked portions of concrete by diffusing through the porosity in the cement paste. However, concrete is always cracked. Structural design codes and guidelines contain provisions to control cracks in concrete structures primarily for aesthetic reasons, but also to limit the penetration of moisture and aggressive species. The Canadian Highway Bridge Design Code [134] provides maximum allowable crack-widths as a function of exposure condition. The code requirements for concrete buildings [135] control cracking indirectly through reinforcement detailing, also as a function of exposure conditions. Further guidance on tolerable crack-widths as a function of exposure condition is provided by ACI Committee 224 [136].

Very few studies have examined the corrosion of steel in cracked concrete. Suzuki et al. [137] observed the effect of single crack versus multiple cracks on the corrosion of steel in concrete. They concluded, based on half-cell potential measurements and observation of rust stains on concrete that, in concrete containing many cracks, steel corroded earlier at one of the cracks than at the other cracks. This difference was attributed to the low availability of moisture and oxygen in the latter cracks. However, this study relied only on half-cell corrosion potential measuring technique which addresses only the probability of corrosion and not the corrosion rates, and the results are, therefore, open to interpretation. Arya and Ofori-Darko [138] observed that, in samples with synthetic cracks (made by inserting plastic shims at the time of casting), a small number of such cracks resulted in lower corrosion than a large number. Weiermair et al. [139] studied the effect on steel of cracks in different types of concrete mixes (Class C-4 concrete with a w/cm ratio =0.55, a class C-2 concrete with a w/cm = 0.43, HPC containing silica fume and w/cm of 0.25 and HPC without silica fume with a w/cm ratio of 0.28) which were subjected to tidal conditions in seawater. Initial corrosion measurements indicated active corrosion rates of rebar at the cracks in HPC with and without silica fume but, after three months, the steel was passive, while corrosion rates of steel in other types of concrete increased. Preliminary results of this study indicated higher corrosion activity at cracked areas than in uncracked areas. The higher corrosion rates were measured when the tide rose higher or dropped below the crack level. This was attributed to increased water and oxygen levels at cracks. Schiessl and Raupach [140] found the corrosion in cracked OPCC increased when the cover depths was reduced or when the w/cm ratio and/or cracked widths were increased. They concluded that the cover depth and w/cm ratio had a more significant influence on corrosion than the crack-width. Hansson and Okulaja [113] found that cracked HPC offered higher corrosion protection to embedded steel than cracked OPCC

but the difference was significantly less than that in the sound HPC and OPCC.

It can be inferred from the above that cracks are more detrimental to rebar corrosion than interconnected porosity. However, the interaction between cracking and porosity in concrete has an influence on corrosion.

2.8 PRODUCTS OF CHLORIDE INDUCED CORROSION

The examination of corrosion products of steel in concrete has been a recent development. Hence, literature in this area is limited. Belaïd et al. [141] examined the corrosion products on galvanized steel in chloride contaminated concrete and found that the type of products formed depend on the amount of chlorides and the thickness of the zinc coating. A more comprehensive study of the corrosion of carbon-steel in concrete has been conducted by Marcotte and Hansson [142]. This study related the distribution and composition of corrosion products formed to the environment in the same concretes as those investigated by Weiermair et al. [139] An important finding was that the corrosion products were distributed in the concrete up to 5 mm from the rebar in HPC without silica fume while in HPC with silica fume the corrosion products were concentrated in the cracks in concrete intersecting the steel. This difference was attributed to the less porous structure of HPC with silica fume and its superior bonding to the rebar. The corrosion products in HPC without silica fume caused cracking in the concrete surrounding them; however, such cracks were not observed in HPC with silica fume because the corrosion products were confined. Moreover, akaganeite (β-FeOOH) and goethite (α-FeOOH), which are more oxidized and expansive forms of iron corrosion products (Figure 4), were found in the former while the latter contained only magnetite (Fe_3O_4). These authors [143] also compared the corrosion products of steel in cracked Class C-2 (w/c = 0.41) with those in HPC (w/cm = 0.27). They detected maghemite (γ-Fe_2O_3), a form of hæmatite deficient in oxygen, in the class C-2 concrete which was not found in the HPC suggesting that less oxygen was available in the former. The absence of maghemite was attributed to cracks present in HPC which enabled corrosion products to move away from the steel/concrete aggregate where the oxygen supply was considered to be higher and resulted in the formation of akaganeite and goethite.

According to the above, the most expansive corrosion product observed in the crack is akaganeite, which is about 3.5 times the original volume of iron. More expansive corrosion products (see Figure 4) were not witnessed in these statically loaded cracks probably because of the limited supply of

oxygen available inside the crack due to the build-up of the products.

2.9 THE IMPACT OF DYNAMIC LOADING ON THE CORROSION OF STEEL

The term “dynamic loading” implies the application of variable stresses on reinforced concrete structures over time. Examples of such loading in service structures include traffic loading on bridge decks and parking garage slabs, and deflections of buildings and long bridges by winds. Although dynamic loading is common in concrete structures, a literature search has uncovered only two studies that examined the effect of dynamic loading on the corrosion of steel in concrete.

Using half-cell potential measurements and visual observation of samples, Espelid and Nielsen [144] found that, in reinforced concrete beams under both static (constant load over time) and dynamic loading that were completely submerged in seawater, corrosion was insignificant even in cracked regions. This was attributed to the lack of oxygen in the seawater. They also observed that, when the beams were exposed to tidal conditions, the current demand for cathodic protection increased significantly. They concluded that the type of loading (static or dynamic) had no influence on the corrosion behaviour of the beams.

Ahn et al. [145] found that corroding reinforced beams deteriorated more rapidly under dynamic loading than under static loading. However, this study does not replicate corrosion in “real” environments as an impressed current was used to corrode reinforcement in the beams.

2.10 CORROSION MEASURING TECHNIQUES

Techniques for monitoring corrosion that have been applied in this project include half-cell potential measurements, galvanostatic pulse technique, linear polarization resistance, electrochemical noise and cyclic polarization. Each of these techniques uses the same method for measuring potential; however, not all of them measure corrosion rates. This section will focus on research pertaining to the application of these techniques to reinforced concrete. The instruments implementing these techniques have been investigated to determine their accuracy by comparing the results with gravimetric measurements [146].

2.10.1 Half-cell Potential Measurements

Half-cell potential (E_{corr}) measurement is the simplest and the most commonly used technique for detecting active corrosion in reinforced concrete structures. It involves measuring the potential difference between the reference electrode and the rebar. This technique was first used by Stratfull [147] on the San Mateo-Hayward Bridge in California. ASTM C 876 [148] provides directions on conducting half-cell measurements on reinforced concrete structures and guidelines for the interpretation of the potential values for carbon-steel in reinforced concrete.

The advantages of the half-cell technique are that it is not as time consuming as other corrosion monitoring techniques and it does not require an external power source for perturbation of the rebar. The disadvantage of this method is that it gives only the probability of corrosion rather than the actual corrosion rates. Other than corrosion, concrete cover, concrete resistivity and oxygen availability also influence the measured potentials [149]. A large cover depth makes it difficult for the localized corroding area to be determined by means of potential measurements. A decrease in the resistivity of the concrete (i.e. an increase in the moisture content of the concrete) renders more negative potentials from the embedded rebar because it allows better electrical contact between the rebar and the reference electrode. Depletion of oxygen in the concrete also leads to very negative potentials (-900 to -1000 mV Vs $Cu/CuSO_4$ electrode). Due to the above effects, Elsener et al. [149] recommend the use of potential gradients rather than single measurements to determine areas of active corrosion. Some of the studies that have relied on half-cell measurements to determine active corrosion of embedded steel include [144, 150, 151].

2.10.2 Potentiostatic Linear Polarization Resistance

The linear polarization resistance (LPR) method has been used by a number of researchers (e.g. [152-155]) to determine the corrosion rates of reinforcement in laboratory testing. Gowers and Millard [156] have also used this monitoring method on concrete structures in service. This technique originates from the work of Stern and Geary [157] who determined that at small over-voltages (~ 20 mV) from E_{corr}, current and potential have a linear relationship i.e. follow Ohm's law. There are four common ways of conducting LPR: potentiodynamically, potentiostatically, galvanodynamically and galvanostatically. In potentiodynamic LPR, the potential is changed at a steady rate and the resulting current is monitored. The slope of the applied potential and the resulting current curve renders the polarization resistance (R_p). Galvanodynamic LPR is conducted similarly; the difference is that

current is applied and the change in potential is monitored. Potentiostatic LPR involves applying a constant potential of ± 10-20 mV vs E_{corr} to the rebar and measuring the resulting steady state currents. R_p is then determined by Ohm's law using the applied potential difference (ΔE) and difference in the steady state currents (ΔI). Galvanostatic LPR is conducted in a similar manner; current is applied and the resulting steady state potentials are measured. The corrosion current density (i_{corr}) is calculated using Equation 1.

$$i_{corr} = \frac{B}{R_p A} \qquad \text{Equation 1}$$

where:
B is the Stern-Geary constant: generally considered to be 26 mV for actively corroding steel and 52 mV for passive steel [158]; and A is the corroding surface area of the rebar.

Potentiostatic LPR is more appropriate for use in concrete then potentiodynamic LPR because dynamics such as movement of ions and diffusion of corrosion products, which influence corrosion rates, occur slowly [8]. Applying a constant over-potential until current reaches steady state allows these processes to reach their equilibrium state at that over-potential. If potendiodynamic LPR is used for determining corrosion rates in reinforced concrete, the rate of change of potential with time (scan rate) should be slow enough to allow the resulting current at each over-potential to reach steady state.

Unlike half-cell potential measurements, LPR enables the determination of corrosion rates. Gowers and Millard [156] recommend the use of LPR where half-cell measurements indicate active corrosion. However, the corrosion current densities determined using Equation 1 are not precise. This is because the corroding area of the rebar in concrete is difficult to determine [159] and incorrect areas are often used to determine the current densities. For example, in small laboratory samples, the whole surface area of the exposed steel may be used to calculate the current density. In large samples and in-service structures, polarizing the rebar and determining the length over which the polarization has an influence may lead to an estimate of this area. Also, the value of B used was determined for steel in alkaline solutions rather than in concrete [8].

2.10.3 Galvanostatic Pulse Technique

The galvanostatic pulse technique involves application of a constant current perturbation (typically between 5 – 400 mA) to the rebar [160]. The idea behind this is to maintain anodic polarization of the rebar within 20 mV of E_{corr} and the electrical response is sampled over the period of the application of the current (typically 25-100s) [161]. The advantage of the galvanostatic pulse technique is that the application of a current pulse, as opposed to the administering of continuous current or large voltages, minimizes the changes to the rebar due to polarization.

Newton and Sykes [162], and Elsener et al. [163] have examined this technique and its application to reinforcement. According to Gowers and Millard [159], the practical use of the galvanostatic pulse technique has two difficulties. First, the potential response to the current pulse must have stabilized to give an accurate corrosion current. Second, as discussed in Section 2.10.2, the actual corroding area of rebar is unknown; hence, the i_{corr} calculated may not be accurate.

2.10.4 Electrochemical Noise

Electrochemical noise (ECN) involves measurement of current and/or potential fluctuations generated by corrosion reactions [164]. Important advantages of this technique are that it does not require perturbation from an external source and it can easily detect small changes in the corrosion dynamics [165].

Hardon et al. [166] found a correlation between the standard deviation of the noise potential and the corrosion rate of reinforcing steel obtained by LPR. Mariaca et al. [167] used electrochemical noise to observe active and passive corrosion in dry and wet concrete. In dry concrete, they found no difference in the current oscillations of actively corroding and passive reinforcements. However, in wet concrete, actively corroding rebars rendered more oscillations than the passive ones. Electrochemical noise potential seemed to be unaffected by the wetness of the concrete. Katwan et al. [168] found that measurements of reinforced concrete under static and dynamic loading gave identical standard deviations implying that the corrosion rate is identical under both conditions.

2.10.5 Potentiodynamic Polarization

Potentiodynamic (cyclic) polarization involves changing the potential of rebar from E_{corr} to several hundred millivolts away from E_{corr} and concurrently measuring the current [8]. The potentials

are usually brought back to E_{corr} at the end of the measurement to reduce the impact that over-potentials have on the corrosion of the rebar if they are allowed, without perturbation, to return to E_{corr} over time.

The potentiodynamic polarization curves are important because: (i) they convey information on the condition of the steel i.e. whether it is passive or corroding [8], (ii) the susceptibility of rebar to localized forms of corrosion such as pitting, and (iii) diffusion limitations. Studies that have examined pitting of rebar using potentiodynamic polarization curves include [169, 170].

Choosing an appropriate scan rate is important in potentiodynamic polarization. If the potential is changed too fast, the resulting current does not reach steady state producing incorrect polarization curves which do not reflect the true corrosion behaviour of the rebar [171].

The range of potential over which the passive film is stable for steel in concrete is schematically shown on the Pourbaix diagram for iron in Figure 5. Applying cathodic polarization to steel causes the reduction of passive film. However, cathodic polarization may be necessary to determine the availability of oxygen at the rebar. In order to observe the effect of passive film on the corrosion behaviour of steel in concrete, potentials are scanned from E_{corr} to about 500 mV vs SCE (~ 260 mV vs SHE). In this potential range, the passive film lies within the span indicated in Figure 5 and may even increase in thickness. The application of potentials above this range could lead to a breakdown of the passive film.

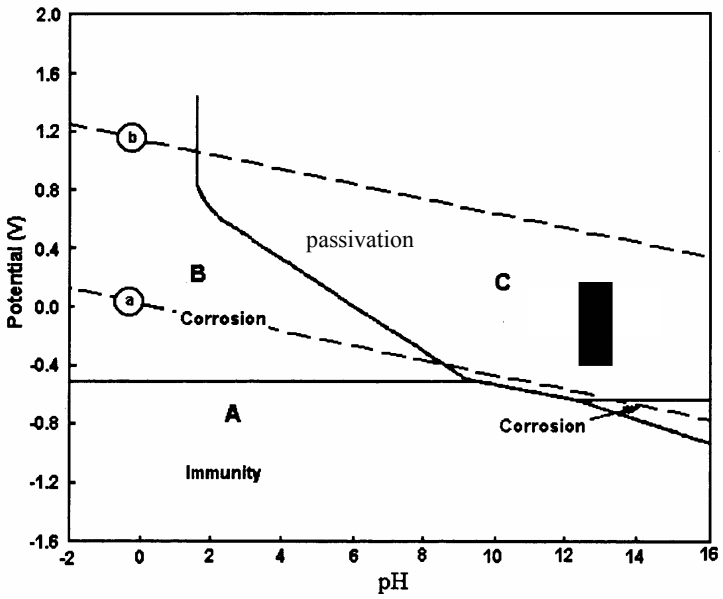

Figure 5: The Pourbaix diagram for iron [2]. The potential on the y-axis is vs SHE. The black rectangle denotes the approximate range of potentials over which the passive film is stable for steel in concrete.

Chapter 3 - Experimental Procedures

3.1 DESIGN OF REINFORCED CONCRETE BEAMS

The following considerations were taken into account in deciding the dimensions of the concrete beams:

1. The combination of readily available compressed air and the capacity of cylinders for applying dynamic loading to the beams; a maximum load of 2.1 kN was realized;
2. The 28-day compressive strength of the concrete to be used for calculation purposes was 35 MPa, which is the minimum requirement for Class C-1 concretes i.e. structurally reinforced concretes exposed to chlorides [172];
3. The beams had to be at least 1 m in length in order to be able to maintain a distinguishable difference between submerged and non-submerged regions of the concrete;
4. Two 10 M carbon steel reinforcing bars were to be embedded in each beam in order to be able to perform electrochemical noise measurements (which require at least two identical working electrodes);
5. The cover depth had to be at least twice the size of the maximum aggregate used in the concrete to reduce the probability of two aggregates stacking on top of each other, which would make it easy for them to scale off as the amount of paste holding them in place would be insufficient. The stacked aggregates would also allow easy passage of chloride ions through a continuous interfacial transition zone (ITZ). The maximum aggregate size was ~ 12.5 mm;
6. The width of the samples had to be at least 120 mm to enable corrosion measurements using the GalvaPulse^{TM}, galvanostatic pulse instrument.

A 120 mm x 70 mm cross-section, illustrated in Figure 6, was chosen based on conditions 5 and 6. The length of the beams was 1.2 m: a working length of 1 m was allocated for corrosion

measurements and the additional 0.2 m was for attaching brackets to load the samples in three-point bending. Calculations, given in Appendix A, were performed to determine the maximum load that can be applied before the beams would start cracking immediately upon loading and to examine if this load would cause the beams to fail in shear because it was initially planned to let cracks appear in the beams over time. However, the amount of time required for cracks intersecting the steel to develop into the samples could not be predicted and because of the amount of time allocated to this project, the development of such cracks could not be depended on. Hence, the beams were loaded under three-point bending such that they cracked immediately at their midsection.

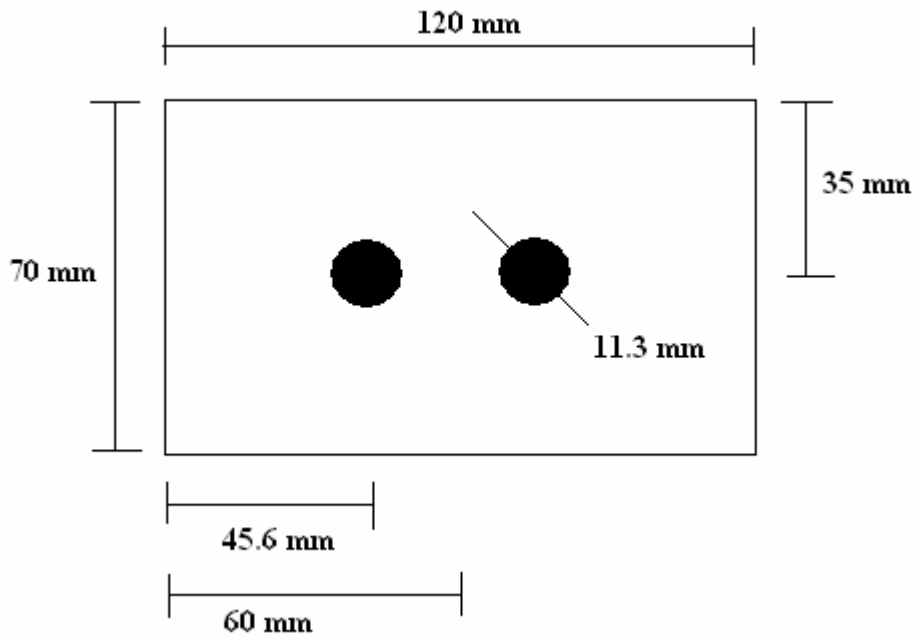

Figure 6: The cross-section dimensions of the concrete samples.

Initially, a pair of trial beams was made with OPCC to determine if they could endure dynamic loading. The beams were subjected to the loading, as described in Section 3.3, for two weeks continuously and each developed cracks at the mid-level.

Thereafter, two sets of beams were cast: one a Class C-3 OPC concrete and the other a Class C-XL concrete (the CSA classification for HPC). These designs are designated OPCC and HPC, respectively. The concretes with w/cm ratio of 0.46 (slump 76 mm) and 0.35 (slump 82 mm), respectively, were cast using the mixture proportions given in Table 1. The HPC contained Type 10ESF cement (containing 8 % silica fume) with 25 % of this cement replaced by slag. The latter was based on the Ministry of Transportation of Ontario (MTO) [173] recommendations of up to 25 %

replacement of cement by slag. Eighteen beams (120 mm X 70 mm X 1200 mm) and fourteen cylinders (100 mm ϕ X 120 mm) of each type of concrete were cast. The cylinders were for compressive strength testing.The OPCC specimens were subjected to two days of wet curing while the HPC specimens were wet cured for seven days as per the MTO requirements [174].

Table 1: Mixture proportions for OPCC and HPC.

Component	**OPCC**	**HPC**
Type 10 Portland Cement, kg	355	0
Type 10ESF (containing 8% Silica fume), kg	0	337
Ground granulated blast furnace slag, kg	0	113
Sand, kg	770	718
Stone, <12.5 mm, kg	1070	1065
Water, L	165	158
Air Entrainer	40 ml /100 kg of cementitious material	65 ml / 100 kg of cementitious material
Water Reducer	250 ml / 100 kg of cementitious material	250 ml / 100 kg of cementitious material
Superplasticizer		635 ml – 1271 ml /100 kg cementitious material
w/cm ratio	0.46	0.35

3.2 COMPRESSIVE TESTING

Compressive tests were performed, as per ASTM C 39 [175] on three or four cylinders of each type of concrete at 28 days, 22 and 27 months after casting. Those that were tested at 28 days were capped a day before the test with Saureisen Bosolit Sulphur Cement No. 600, which conformed to ASTM C 617 [176]. For those tested at 22 months, the cylinders' ends were ground with Hi-Kenma Tsuru Tsuru Model MIT-196-1-30 End Grinder to make them smooth and parallel so that the compressive load could be applied evenly across them. The compression tests at 28 days and 22 months were performed in a Forney Incorporated Compression Test Machine. Those tested at 27 months were also subjected to end grinding before being tested in an ELE Compression Tester.

3.3 LOADING PROCEDURES

Brackets were installed on the beams for the application of static and dynamic loading about 12 weeks after casting and the beams were exposed to chloride solution 12 weeks thereafter. The number of beams under each of the loading conditions is shown in Figure 7. A small number of beams were under no load because (a) very limited space was available for the storage of the beams and (b) minimal damage was expected for the beams in this condition compared to those under static and dynamic loading.

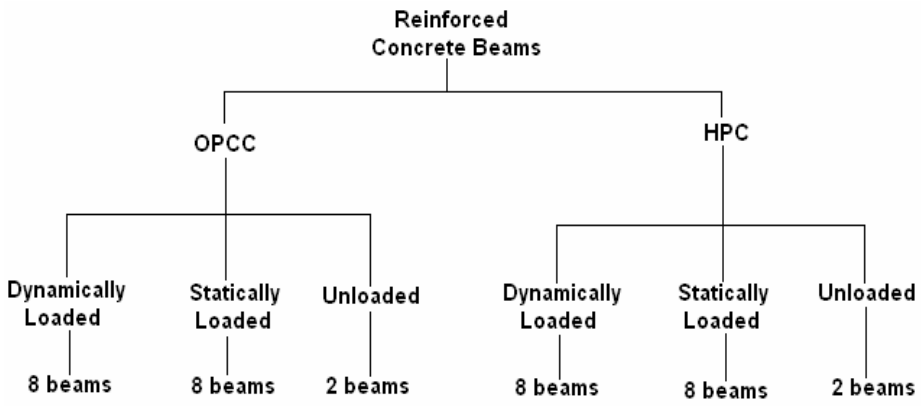

Figure 7: The number of beams of each concrete type subjected to different loading conditions.

The beams in the statically loaded conditions were subjected to three-point bending by coupling in pairs and using the bracket and fulcrum set-up shown in Figure 8. Static loading was applied to each pair of beams by tightening the nuts on the threaded rod indicated in Figure 8. Figure 9 shows beams under static loading.

Dynamically loaded beams were coupled in a similar manner to the statically loaded beams but an air cylinder and a piston were mounted at the top bracket and connected to a square wave generator to control the frequency of the pulsed load. Applying compressed air to the cylinder, load was applied at a 0.5 Hz frequency. Figure 10 shows beams subjected to dynamic loading.

Each beam in the loaded conditions (i.e. static and dynamic) was initially subjected to a load of 2.1 kN at the top bracket for 70 hours after exposure to chloride solution and, because of the nature of the set-up, the same load was applied at the bottom bracket. The value of 2.1 kN was chosen because this was the maximum load that could be applied using the combination of air cylinder and air pressure supply. This load caused a large deflection at the top end of the beams (~ 10 mm). It was thought that this deflection in the dynamically loaded beams would cause them to fail prior to the

completion of the experimental testing. Therefore, the loads were reduced to about 0.68 kN thereafter on both the statically and dynamically loaded beams to maintain a maximum deflection of 3 mm at the top end of the beams. The beams subjected to dynamic loading were subsequently exposed to the new load for 1-2.5 hours per day.

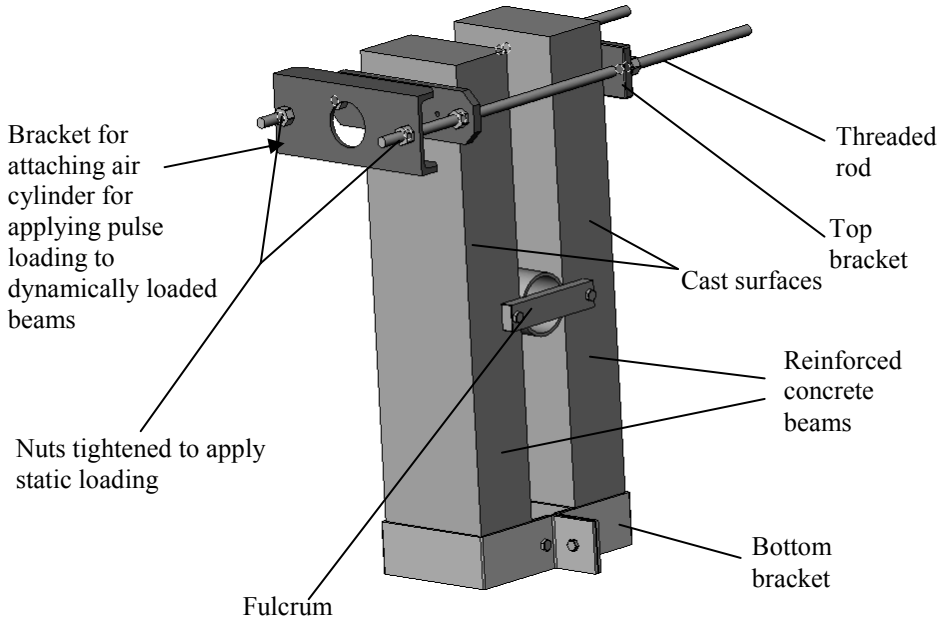

Figure 8: Schematic illustration of the beams for static and dynamic loading.

Figure 9: Beams under static loading.

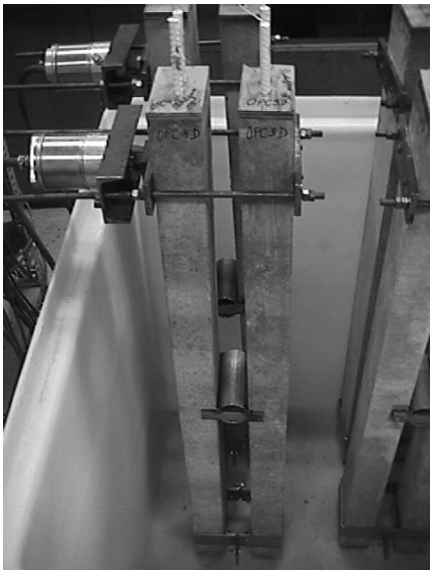

Figure 10: Beams under dynamic loading.

3.4 EXPOSURE CONDITIONS AND CORROSION MEASUREMENT LOCATIONS

All the beams were cracked one day prior to their exposure in salt solutions. The static or dynamic loading was applied to the beams for an hour on the day before their exposure to salt solution to initiate cracking in the concrete. The load applied at each end of the beams was 2.1 kN. The unloaded beams were also cracked under three-point bending using the same load.

The beams were placed upright in a container of 3 % rock salt solution such that the solution reached slightly above the midpoint level of the beams, i.e. just above the central crack as shown in Figure 11. The chloride content of the salt solution was checked when the beams were immersed in the solution, after nine months of exposure and towards the end of the project. These measurements revealed a variation of chloride content between 2.7 % and 3%. The decrease in chloride content was corrected by adding an appropriate amount of salt to the solution. Corrosion measurements were conducted at three locations in each beam: in the non-submerged region (A in Figure 11), in the submerged uncracked region (C in Figure 11) and in the submerged cracked region (B in Figure 11).

To increase the amount of chlorides entering the concrete through the pore network, the beams were submerged in the salt solution (on the average) for two out of four weeks and, for the remaining two weeks, they were left in the ambient laboratory conditions to dry.

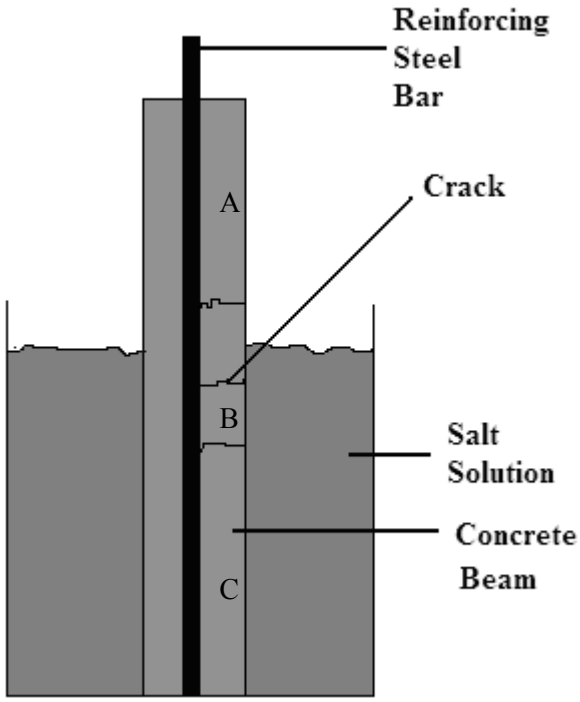

Figure 11: A schematic illustration showing the level of salt solution in the wet cycle.

3.5 CRACK-WIDTH MEASUREMENTS

Initial widths of the macrocracks in the beams were measured using a crack comparator (Figure 12) and their morphology was noted after subjecting the beams to the load change at 70 hours of exposure to salt solution. Crack-widths prior to exposure were not noted, as most cracks were difficult to observe. After exposure to chloride solution, the cracks became easier to detect because salt crystallized in the cracks. Examples of the cracks are shown Figure 13. The actual crack-widths were determined by comparing an actual line width on the comparator to the crack-width and a comparator line width in the photographs.

After nine months of exposure to salt solution, two beams of each concrete type and each loading type (static and dynamic) were autopsied. Prior to this, the crack-widths were again documented. The crack-widths on the remaining beams were measured after the final corrosion measurements at eighteen months of exposure.

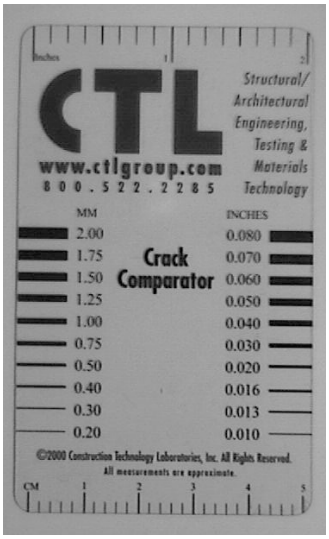

Figure 12: A crack comparator.

(a) (b)

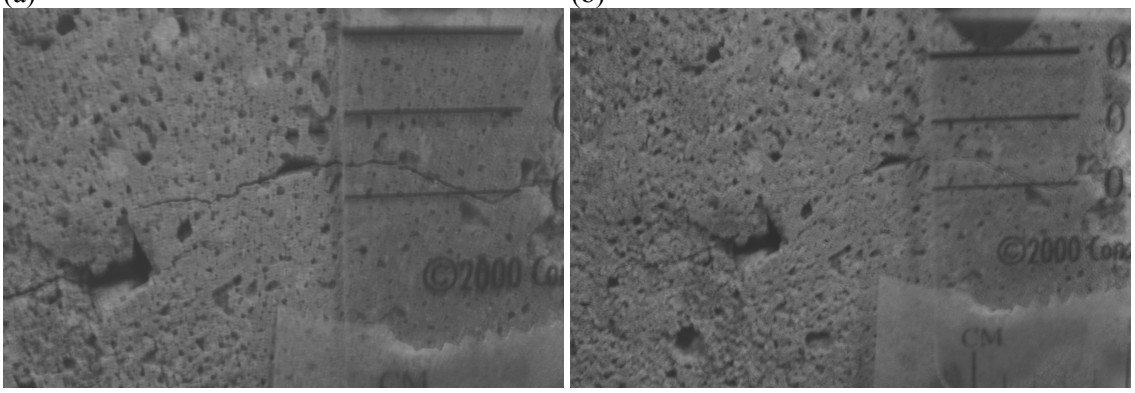

Figure 13: Photographs showing a crack comparator placed on a dynamically loaded OPCC beam when the macrocrack is (a) open and (b) closed.

3.6 DESIGN OF ELECTRODE HOLDER

A plastic holder was designed and constructed to accommodate the various electrodes for corrosion measurements. Figure 14 shows the holder which can be held at the three different measurement locations on the beams (i.e. non-submerged, submerged and crack level) by attaching plastic chains of different lengths on its side. Figure 15 shows the holder in use.

(a)

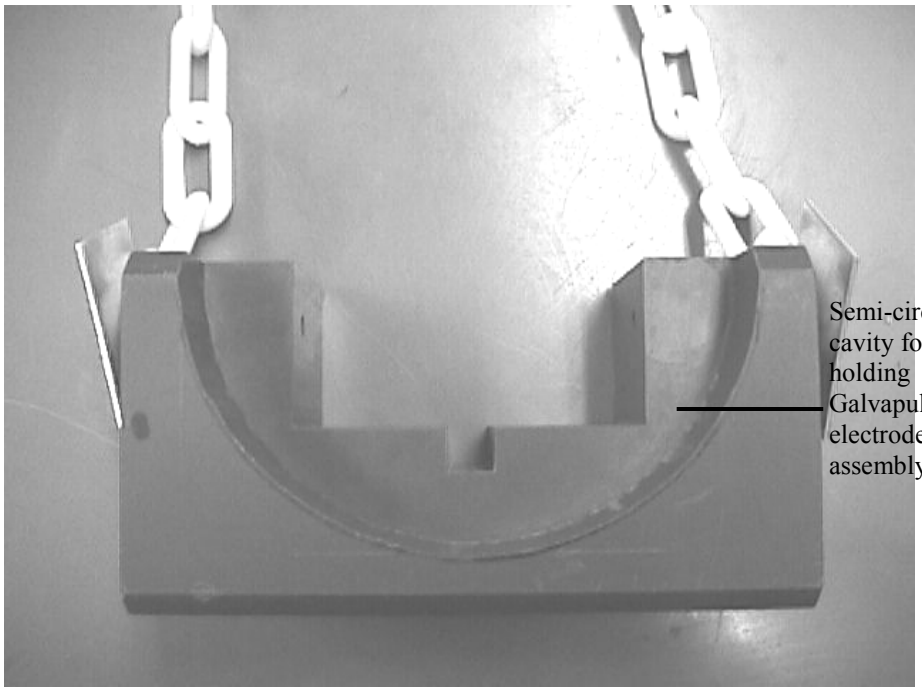

(b)

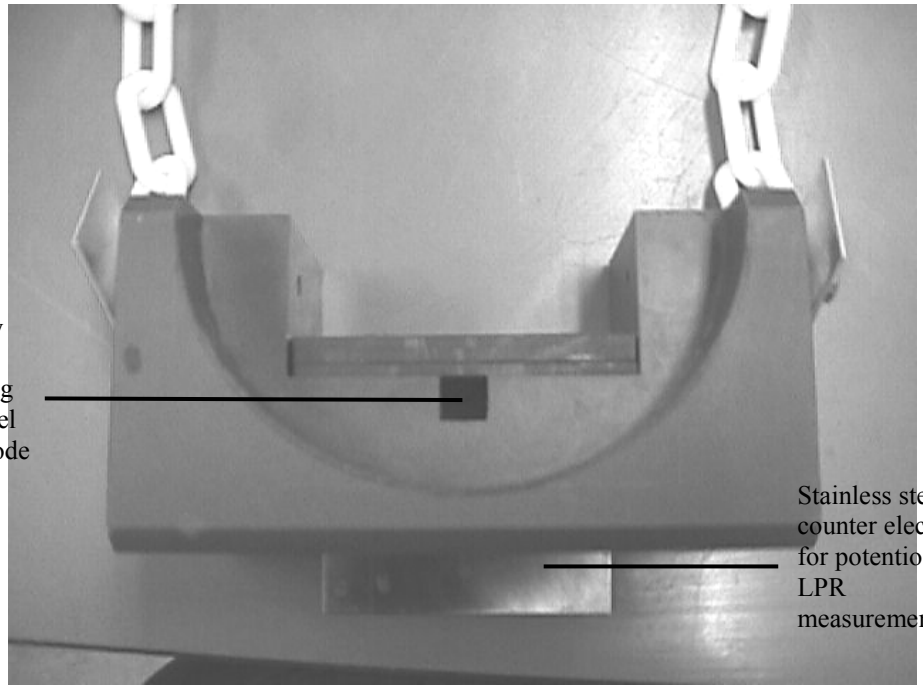

Figure 14: (a) and (b) show the two sides of the electrode holder.

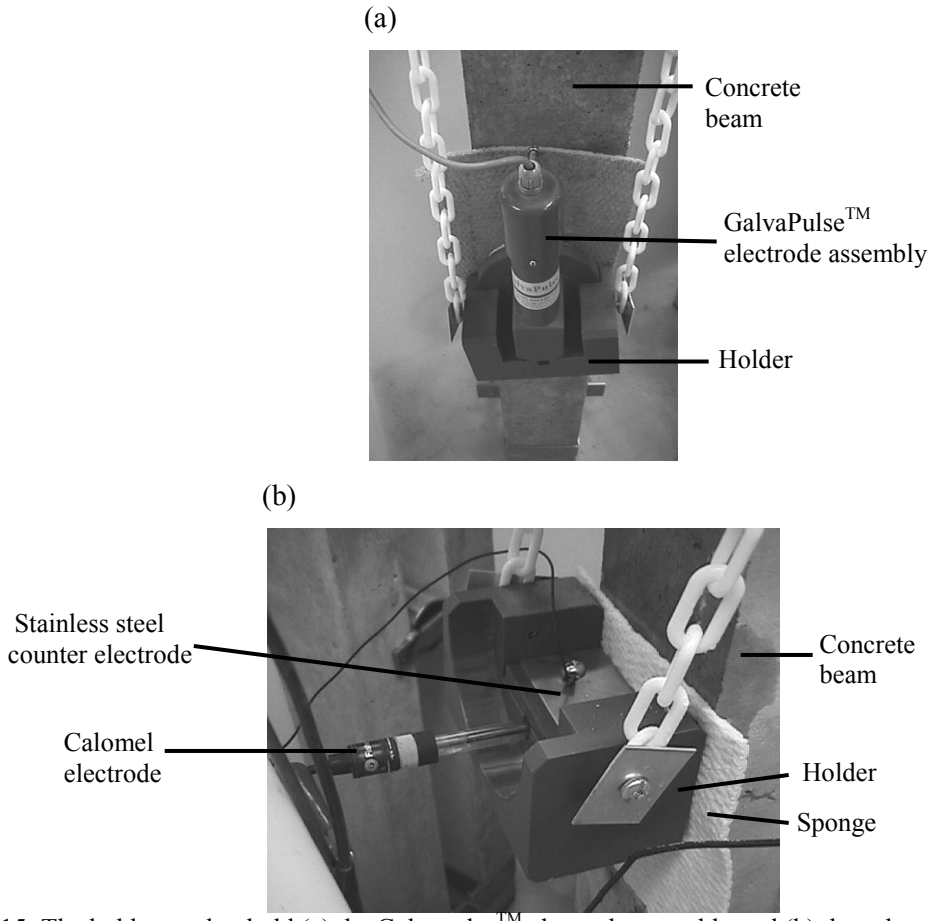

Figure 15: The holder used to hold (a) the Galvapulse™ electrode assembly and (b) the calomel and counter electrodes for LPR measurements.

3.7 CORROSION MEASUREMENTS

Several different electrochemical techniques were used to characterize the corrosion behaviour of the embedded steel. These included LPR, galvanostatic pulse, cyclic polarization and electrochemical noise.

LPR and galvanostatic pulse measurements were regularly conducted on the reinforcements in the beam. LPR measurements were conducted using a Parstat®2263 potentiostat. Saturated calomel (SCE) and 70 mm x 75 mm stainless steel were used as reference and counter electrodes, respectively. Initially, LPR measurements in OPCC and dynamically loaded HPC beams were conducted at the beginning of the dry cycle using a wet sponge between the reference/counter electrodes and the concrete surface; however, it took considerable time to establish an electrical

contact between the electrodes and the steel via the concrete when the concrete was not saturated. Thus, measurements in the submerged and cracked regions of the beams were later performed before switching from wet cycle to dry cycle. Measurements in the cracked and submerged regions of the statically loaded and unloaded HPC beams were conducted before switching from wet cycle to dry cycle from the very beginning.

In an LPR measurement, a scan consisted of two parts as shown in Figure 16. The first part of the scan consisted of applying a potential (E), 20 mV more positive than the corrosion potential (E_{corr}) for 150 - 240 s while the second part consisted of applying a potential, 20 mV more negative than E_{corr} for an additional 150 - 240 s. The steady state current (I) at the end of each part was noted. The potential values of ± 20 mV with respect to E_{corr} were chosen because it was assumed that, within this range of potential, the current response is linear and Ohm's law can be applied to calculate the polarization resistance (R_p). Hence, R_p is given by $\Delta E/\Delta I$ (= 40 mV/ΔI). The value of R_p can be substituted in Equation 1 (previously mentioned in Section 2.10.2) to determine the corrosion current density (i_{corr}).

$$i_{corr} = \frac{B}{R_p A} \qquad \text{Equation 1}$$

where B is the Stern-Geary constant: generally considered to be 26 mV for actively corroding steel and 52 mV for passive steel [158] and A is the surface area of the working electrode.

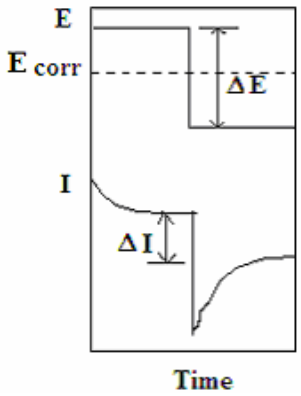

Figure 16: The current response to LPR potential applied.

In this project, a B value of 26 mV was used to determine LPR current densities at all three regions of the reinforced concrete beams described in Section 3.4 because the difference in i_{corr}

obtained when using the two values of B is negligible compared to the actual difference in i_{corr} expected between passive and active steel.

The area A, used to convert corrosion currents obtained from the LPR measurements to current densities, varied depending on the section of the beam. This area was determined by polarization measurements. Potentials were monitored at 5 cm intervals along the length of an unloaded OPCC beam. 20 mV potential more positive than E_{corr} was then applied to each location, A, B and C of the beam and, during this application, the potential measurements were repeated over the previously measured locations. The polarized length of the rebar was determined to be the length over which there was a noticeable potential change between the two potential measurements and the polarized area was calculated to be the surface area of the rebar along this length. For the non-submerged, cracked and submerged sections of the beams this length was 300 mm, 150 mm and 300 mm, respectively. For the final LPR measurements, the actual corroding/ passive areas were determined by visual observations of the autopsied rebars and used in the calculations to compare the actual i_{corr} obtained to the i_{corr} determined using the polarized area.

Galvanostatic pulse measurements were conducted using the GalvaPulse^{TM} [177]. Details about galvanostatic pulse measurement technique can be found in [160-163, 178]. The electrode assembly, shown in Figure 17, contained a silver-silver chloride reference electrode, a zinc counter electrode and a zinc guard ring. The purpose of the guard ring was to provide a uniformly polarized area over which the measurement was being conducted and limit the applied current outside the area. The input parameters for the measurements were: the current applied, the period of the current pulse, the polarized length and diameter of the rebar. For the cracked region and the submerged region, a current of 100 μA was applied for 10 seconds as this combination resulted in potential change that reached steady state in the initial measurements on OPCC beams. For the non-submerged region, a current of 48 μA for 48 s gave the best results. The guard ring was intended to limit the polarized area to 7 cm along the surface of rebar. However, during the course of this project, Esmaeilpoursaee [146] determined that it was unable to do this. Hence, the polarized lengths of the rebar that were used in the calculation of current densities were the same as in LPR. After each measurement, the GalvaPulse^{TM} displayed E_{corr}, i_{corr} and concrete resistance values. All GalvaPulse^{TM} measurements were conducted in the dry cycle because the electrode assembly could not be submerged in salt solution. Galvapulse^{TM} measurements were used as secondary measurements to verify the trend of LPR measurements and were not conducted as regularly as the latter.

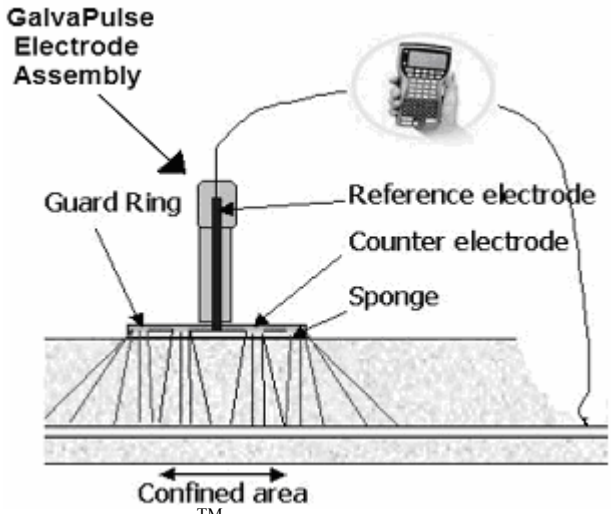

Figure 17: The Galvapulse™ electrode assembly (Modified from [177]).

Potentiodynamic (cyclic) polarization measurements were conducted after exposing the beams to salt solution for nine months and after removal of most of the cover for chloride profile determination, as described below (Section 3.8), in the cracked and submerged regions. These measurements were conducted in the cracked region of two beams for each concrete and loading type (excluding unloaded beams) and, as a control, in one beam in the submerged region of each concrete type under dynamic loading. The ground hole, which was used as a well into which the reference (calomel) and counter electrodes (30 mm x 40 mm stainless steel) were placed, was filled with distilled water. The combination of distilled water, chloride and other ions present in the concrete was expected to provide the necessary conductivity of the electrochemical cells during the measurement. Initially, a 1 mV/s scan rate was used for cyclic polarization measurements which took 45 minutes per scan; however, the polarization curves obtained were not accurate because this scan rate did not allow corrosion currents resulting from the applied change in potential to reach steady state [146]. A slower scan rate of 0.01 mV/s was later used which took approximately 3.5 days per measurement and gave more accurate results [146]. The slow scan rate measurements were initiated at 50 mV more negative than E_{corr}. The potential was increased to +500 mV vs SCE and then reversed to -500 mV vs SCE. The potential drop due to the resistance of the concrete (IR drop) was automatically compensated for by the Solartron 1286 potentiostat. After about 18 months of exposure, a cyclic polarization scan was conducted at the midsection of one of the remaining OPCC and HPC beams to determine the oxygen availability at the rebar in the cracked region. An 8 mm deep hole (70 mm in diameter) was ground in each of the beams, which was used to host water and the reference and counter electrodes. These

scans were started at E_{corr}. The potential was scanned to -300 mV vs E_{corr} before being raised to +500 mV vs the reference and was then returned to E_{corr}. The scan rate was kept at 0.01 mV/s.

Electrochemical noise (ECN) refers to current and or potential fluctuations generated by corrosion reactions [164]. ECN current measurements were performed on the beams after eight months of exposure. These measurements were non-perturbative [179], meaning that no current or potential was applied to the rebar from an external source and there was no polarization of the rebar. One of the rebars in each beam was used as the working electrode while the other was used as the counter electrode. An assumption that was made was that both rebars in each beam were under identical conditions. Electrochemical potential noise measurements were not conducted on the beams because (a) the beams did not have a third rebar and (b) trial measurements on a beam in salt solution did not reveal any data that could be interpreted by means of spectral analysis.

The electrical resistance of the concrete under different loading conditions was determined in each of the three sections of some beams at 3 and 9 months of exposure in salt solution using three techniques: alternating current (AC) impedance using the Parstat® 2263, galvanostatic pulse using Galvapulse™ and galvanostatic pulse using Parstat® 2263. Concrete resistance can be determined from an AC impedance Nyquist plot of imaginary impedance (Z") vs. real impedance (Z') as discussed in [180]. The applied frequencies for AC impedance in this project ranged from 2 MHz to 100 mHz. Galvanostatic pulse measurement using Parstat® 2263 was conducted by applying a current of 100 μA for a maximum time of 100 s. The resistance of concrete was determined from the resulting initial rapid potential change as indicated in [163].

The notation used in this work to denote the locations of measurements on the beams is as follows: OPC2DAF, where the first three letters denote the type of concrete (e.g. OPC or HPC), the number denotes the beam number, which is followed by the type of loading applied to the beam (e.g. D for dynamic, S for static, U for unloaded). The letter after this represents the location of measurement (A for the non-submerged region, B for the cracked mid-section, C for the submerged region). F (front) or B (back) denote the two rebars inside each beam.

3.8 CHLORIDE PROFILE DETERMINATION

After 9 months of exposure, two beams for each concrete and loading type, excluding unloaded beams, were cut into three sections: the non-submerged, submerged and cracked regions. The

concrete in the submerged section and cracked mid-section was ground in 2 or 3 mm intervals from the tensile surface inwards towards the reinforcing bar and centred over one of the rebars in each section as illustrated in Figure 18. The concrete over the other section was left intact for corrosion product analyses and will be discussed in Section 3.10. The maximum depth of grinding was 21 mm from the surface of the concrete, i.e. 9 mm from the reinforcing steel. The grinding was performed using the PF 1101 Profile Grinder from Germann Instruments. The diameter of the ground hole was 70 mm giving a representative sample of the concrete. At every grinding step (2 or 3 mm deep) the concrete powder was collected for chloride analysis. While grinding at the cracked mid-section, the surface of the ground hole was moistened at every grinding step to distinguish between the paste and the aggregates and the crack was photographed.

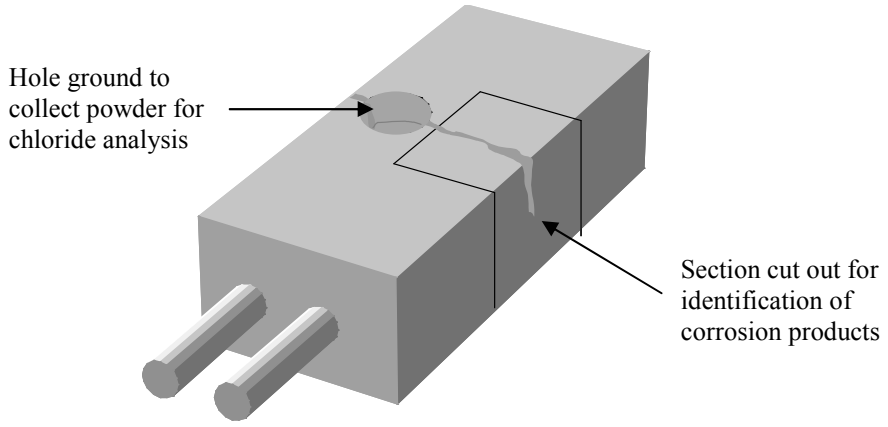

Figure 18: Showing the locations of the ground hole and segment used for Raman spectroscopy.

3.9 CHLORIDE ANALYSES

The acid soluble chloride content of concrete powders collected at each step during the above grinding (Section 3.8) was determined by titration against silver nitrate ($AgNO_3$) solution.

For titration, ASTM Standards C 114 [181] and C 1152 [182] were followed with some modifications, as outlined:

1. A known amount of concrete powder (W) from each step was poured into a clean 250 ml beaker containing 120 ml dilute nitric acid (1:10 acid to distilled water volume);
2. The mixture was covered and boiled for 5 minutes after which it was filtered through a

Whatman No 4 filter paper (retaining particles sizes between 20-25 μm) into a clean 400 ml beaker;

3. The 250 ml beaker was rinsed three times using hot distilled water to collect all the chlorides. The solution and residue from the rinsing were filtered into the 400 ml beaker;
4. Hot distilled water was poured onto the filter paper and the retained particles at least 6 times to remove any chlorides attached. The filtrate was collected in the 400 ml beaker;
5. Distilled water was added to the 400 ml beaker containing the solution with chlorides to increase its volume to 250 ml;
6. 40 ml of this solution was titrated against 0.011178 eq/l (0.011 M)$AgNO_3$ solution using the Radiometer TIM800 semi-automatic titrator. For powders with lower amounts of chlorides, a more dilute $AgNO_3$ solution (0.004409 eq/l or 0.0045 M) was used. When the $AgNO_3$ with the latter concentration was not able to detect chlorides in the powders, 10 ml of 0.0036 M NaCl solution was added to 30 ml concrete powder solution before titration. The titrator added $AgNO_3$ solution to the chloride solution in increments of 0.2 ml until the equivalence point was reached (i.e. a rapid large change in the potential difference between the reference and silver electrodes the titrator was observed);
7. The volume of titrant ($AgNO_3$ solution) used to reach the equivalence point and the volume of the concrete solution used in the titration were used to calculate the concentration of the chlorides in a litre of solution (*Y*);
8. For samples with added chloride solution, the concentration of the chloride solution was measured and subtracted from the above.
9. From concentrations (Y in moles/litre) obtained, the moles of chloride in 120 ml (*X*) of the original solution (step 1) were determined using Equation 2 :

$$X = \frac{Y \times 250}{1000}$$ Equation 2

10. The weight of chlorides (W_{cl}) in the concrete powder dissolved in step 1 (in grams) was calculated by multiplying the answer from step 9 by the molecular weight of chlorine (35.453).

11. The percent of chloride in the powder was calculated using Equation 3.

$$\%Cl = \frac{W_{cl}}{W} \times 100$$ Equation 3

The titration was repeated three times with 40 ml aliquots of the solution and the average value is given in the results.

3.10 RAMAN SPECTROSCOPY

Raman spectroscopy was used to identify corrosion products on the reinforcing steel at the crack and on the concrete walls constituting the crack. The parts of the cracked sections of the beams containing the second rebar with the concrete and rebar intact (Figure 18) were used for this purpose. Cuboid pieces (approximately 70 mm x 60 mm x 50 mm) of the portions with the steel and crack intact were cut out using a diamond saw. Notches were introduced in these pieces on all four surfaces, to facilitate removal of the steel from the concrete in an inert atmosphere. The pieces were introduced into a sealed glove box purged with nitrogen. Inside the glove box, concrete was detached using a hammer and a chisel, and the steel was placed in an airtight chamber containing an optical quality glass window. The chamber was sealed before being taken out of the glove box. The remaining concrete was left in the glove box with the crack surfaces of the concrete still in place i.e. the crack was still intact. The sealed chamber containing the steel was then taken to the Raman spectrometer for analysis in situ. After analysis of the steel, the chamber was reintroduced inside the glove box and the steel was removed. The crack surfaces of the concrete were opened and placed inside the chamber before it was sealed again and taken out of the glove box. The corrosion products on the surface of the concrete were then analysed using Raman spectroscopy. In addition to analysing the concrete and

the steel, the glass window on the sealed chamber was also analysed to determine if it interfered with the analysis of the steel and the concrete.

Raman spectroscopy was conducted using a Renishaw 1000 system. This system included an Olympus optical microscope, a Peltier-cooled charge couple device (CCD) detector and a spectrograph. The source used for excitation was a 35 mW HeNe laser with a wavelength of 632.8 nm; however, this was reduced to 3 mW on the surface of the sample by the optics present in the Renishaw system to prevent the products from being altered. The samples to be studied were placed on the stage of the optical microscope and were focused under 50 times magnification using white light. A photograph of the area under focus was obtained before changing to laser lighting. The area was then scanned using five accumulations with each accumulation covering a frequency range of 70 cm^{-1} to 1800 cm^{-1}. The results of the accumulations were obtained and averaged by the Renishaw Wire software.

3.11 OBSERVATIONS OF MACROCRACK PROFILES IN CONCRETE

To determine the effect of loading on macrocrack profiles in concrete, a dynamically loaded OPCC beam was sectioned into three parts: non-submerged, submerged and cracked mid-section. A 70 mm diameter hole (8 mm deep) was ground at a crack in the mid-section (Figure 19 (a)). Spurr epoxy containing EpoDye, a fluorescent dye, was introduced into the sample via this hole using solvent exchange with alcohol as described in [183] and, at every step, the sample was placed in the vacuum for 3 hours to allow the epoxy to penetrate into the sample. The sample was kept in the ambient laboratory conditions during the day and in the refrigerator at night for about a week. This was done to extend the pot-life of the epoxy. The sample was then heated at 70 ^{o}C for 24 hours to allow the epoxy to harden. The sample was then sectioned parallel to the rebars (Figure 19 (b)) to determine the depth of penetration of the epoxy. The epoxy had only penetrated concrete about 20 mm from the surface and failed to ingress into regions of the crack that were filled with corrosion products. As a result, some parts of the crack were difficult to distinguish from the components of the concrete even when viewed under ultra-violet (UV) light.

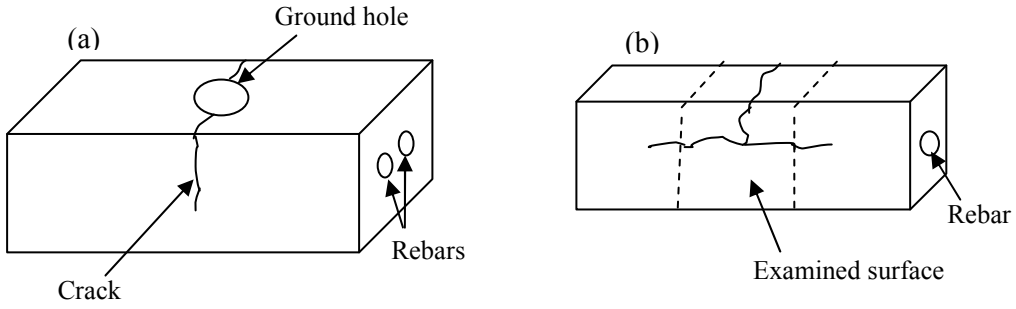

Figure 19: Illustration of (a) the cracked mid-section with a ground hole through which spurr epoxy was introduced into the sample and (b) the sectioned sample showing the surface to be examined.

The surface to be examined (Figure 19 (b)) from the above cut sample was then ground to make it even. This surface was impregnated by placing it face down in fluid epoxy, Specifix 20 containing EpoDye. After the epoxy had hardened the sample was re-ground and polished. The surface was then examined under UV light and, this time, the epoxy had filled a significant portion of the crack. This process was then repeated for the other samples.

3.12 CHANGES IN MILL-SCALE

Mill-scale on rebars exposed to three conditions, (i) not embedded in concrete, (ii) embedded in uncontaminated concrete and (iii) exposed to chlorides at a crack in concrete, was observed in a JEOL JSM-6460 scanning electron microscope (SEM) under the secondary electron (SE) and backscattered electron (BSE) modes. The elemental analysis of mill-scale was obtained using an Oxford Instruments IncaX-sight energy dispersive spectroscopy (EDS) detector (model 7573) with an ATW2 window, which was attached to the SEM.

Prior to the SEM observations, small sections of rebar (approximately 15 mm long) were mounted in a hot mounting material. These samples were then ground and polished to obtain smooth and flat surfaces for observation. They were then coated in gold to enable the discharge of electron build-up in the SEM.

Chapter 4 - Results and Discussion

4.1 COMPRESSIVE TESTS

The compressive strengths of OPCC and HPC cylinders at 28 days, and 22 and 27 months after casting are shown in Table 2. Experimental problems were encountered at 28 days and 22 months and, therefore, these data have been discounted.

Table 2: Compressive strengths of OPCC and HPC cylinders.

Concrete	Test Number	Compressive Strength (MPa)		
		28 days	22 months	27 months
OPCC	1	40.9	35	39.2
	2	42	34.4	41.5
	3	44.6	33.1	48.2
		-	-	42.0
	Average	**42.5 ± 1.9**	**34.2 ± 1.0**	**42.7 ± 3.8**
HPC	1	45.8	54.7	63.2
	2	34.4	53.5	61.9
	3	38.2	50.9	62.3
	Average	**39.5 ± 5.8**	**53.0 ± 1.9**	**62.5 ± 0.7**

4.2 MACROCRACKS

All the beams were pre-cracked prior to their exposure to salt solution and the macrocrack widths were measured after 70 hours of exposure to salt solution. All these initial crack-widths are shown in Appendix B (Table B1 and Table B2). The tables in Appendix B also provide the surface crack-widths measured after nine months of exposure on two beams (beam names in italics) of each type of concrete subjected to static and dynamic loading. The final widths on the remaining beams were obtained after eighteen months of exposure and are also presented in the tables. Some beams had more visible cracks (crack number in bold) during final measurements, which were not observed in the initial measurements. Also, in the unloaded beams, the cracks were not readily visible initially. To observe the number of cracks initially in the unloaded beams, the tensile surfaces were sprayed with water. The water penetrated much faster into the cracks than in the rest of the concrete, making the cracks visible from the side of the beam. However, when final measurements were conducted, the cracks, which had become filled with crystallized salt, could be observed in the region of the HPC beams that was submerged in solution but not in the OPCC. The porous nature of the OPCC would

have allowed less salt to crystallize in the crack than in the HPC because the salt would attract water from the pores (particularly in the dry cycle) and combine with it to form solution.

Based on the information from Appendix B, Table 3 summarizes the number of beams for each concrete and loading type that had additional visible cracks in the final measurements. These cracks could have existed when the initial measurements were conducted but were not observed because the widths were small and could not be detected by the eye even when wet. In the dynamically loaded beams, the cracks could have formed or grown as a result of the loading because they were typically wider than those of the additional cracks observed in the statically and unloaded loaded beams. According to Raju [104], more microcracks were observed in concrete that was subjected to cyclic loading than that under static loading implying that dynamic loading does have an effect on crack formation and growth.

Table 3: Number of beams with additional visible cracks and increased crack widths observed in the final measurements.

Beams	**Number of beams with increased number of visible cracks**	**Number of beams with increased crack-widths**
OPCC Dynamic	6 out of 8	7 out of 8
OPCC Static	1 out of 8	0 out of 8
OPCC Unloaded	0 out of 2	N/A
HPC Dynamic	5 out of 8	7 out of 8
HPC Static	3 out of 8	2 out of 8
HPC Unloaded	2 out of 2	N/A

The tables in Appendix B indicate that most of the surface cracks increased in widths in the dynamically loaded beams while, in the statically loaded beams, the widths remained more or less constant. However, this behaviour was not evident from the average values that are presented in Table 4 because the averages were based on the sum of the crack-widths and the total number of cracks for each concrete and loading type, both of which varied (variation not consistent between them) from initial to final measurements. The increase in crack-widths observed in the dynamically loaded beams can be attributed to the fact that cracks continued to propagate parallel to the rebar as described below. When the beams were under tension, the concrete in the vicinity of the crack became de-bonded from the rebar. The resulting gap would have grown over time and led to the observation of increased crack-widths. Also, the accumulation of salt crystals and corrosion products in this space may have prevented the cracks from closing to their initial widths when the tensile load was removed. In contrast, the cracks in the statically loaded beams, once formed on the initial application of load, remained unaffected by further application of the load.

Table 4: Average number of cracks and crack-widths in the beams. The average number of cracks was rounded to the closest integer value that was less than the actual average, while the average crack-width was round to the nearest 0.05 mm.

Beams	Average Number of Cracks		Average Crack Width (mm) - Loaded		Average Crack Width (mm) - Unloaded	
	Beginning	End	Beginning	End	Beginning	End
OPCC Dynamic	3	4	0.15	0.2	0.05	0.1
OPCC Static	3	3	0.1	0.1	N/A	N/A
OPCC Unloaded	3	3	N/A	N/A	Not visible	Not visible
HPC Dynamic	3	4	0.15	0.15	0.05	0.1
HPC Static	4	4	0.1	0.15	N/A	N/A
HPC Unloaded	5	6	N/A	N/A	Not visible	0.05

The difference in the average crack-widths observed in the OPCC and HPC beams under the different loading conditions, given in Table 4, was not significant. The average numbers of cracks (observed initially and finally) in both sets of dynamically loaded beams are the same whereas the unloaded and statically loaded HPC beams had higher averages for the number of cracks than their equivalent in the OPCC. HPC is known to be more brittle than OPCC and, therefore, more prone to cracking. When the crack propagates into concrete by growing through the paste and avoiding the aggregates, more energy is required to propagate it (less brittle) in comparison to a crack that propagates in the concrete without circumventing the aggregates (more brittle). However, observations of crack paths in the beams revealed no difference between the OPCC and HPC. In fact, as shown in Figure 20, there were some instances when the cracks propagated through the paste and around the aggregates and there were also cases when the cracks cut through the aggregates in both concretes. However, the aggregates (gravel) used in this project had varying strengths and were responsible for these crack morphologies. Thus, the cement paste in HPC could still be more brittle than that in the OPCC because it contained reduced porosity and a more uniform distribution of C-S-H.

The fact that the average number of cracks in the unloaded and statically loaded HPC beams was higher initially than in the dynamically loaded beams despite being subjected to similar deflections is probably because the cyclic tensile loading applied to the HPC beams prior to initial crack measurement caused existing flaw/cracks to grow before developing new ones over time, while constant tensile loading caused cracks to form from the very beginning. This was also why the average number of cracks increased with time in the dynamically loaded beams and remained more or less constant (not taking into account cracks with widths < 0.05) in the statically and unloaded ones.

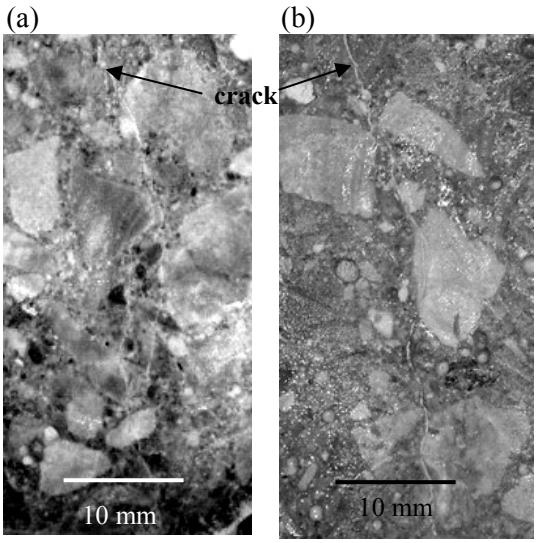

Figure 20: Crack path in concrete (a) in OPCC and (b) in HPC.

In contrast to the HPC, the average number of cracks in the unloaded and statically loaded OPCC beams was similar to that under dynamic load. This could again be because the paste in OPCC was less brittle than that in HPC.

Two beams of each concrete type under static and dynamic loading were sectioned after eighteen months of exposure to salt solution, to determine the morphology of the cracks at the rebar-concrete interface in the vicinity of the region where the maximum bending moment was applied. As illustrated in Figure 21 (a) and (c), in the dynamically loaded beams of both concretes, the cracks reached the rebar and propagated parallel to the rebar along the rebar-concrete interface. This behaviour was also evident in the statically loaded HPC beams (Figure 21 (d)) and one of the statically loaded OPCC (Figure 21 (b) sample 1). In the other statically loaded OPCC, Figure 21 (b) sample 2, there was only a slight excursion of the crack parallel to the rebar along the rebar-concrete interface as shown in Figure 22.

Figure 23 illustrates the profile of the cracks along the edge of the beams after nine months of exposure. For both types of concrete, the cracks in the statically loaded beams propagated on the side face of the beam to the level of the rebar and no further as shown in Figure 23 (a). In the dynamically loaded beams, on the other hand, the cracks propagated past the position of the rebar and continued to grow into the concrete. In the dynamically loaded OPCC beams, Figure 23 (b), the absence of rebar close to the edge of the concrete, allowed the repeated loading to grow the crack from the tensile surface to a point past the rebar. This is also the case in the dynamically loaded HPC beams (Figure 23 (c)) but, in this case, the crack bifurcates beyond the rebar.

(a) Dynamically loaded OPCC

(i)

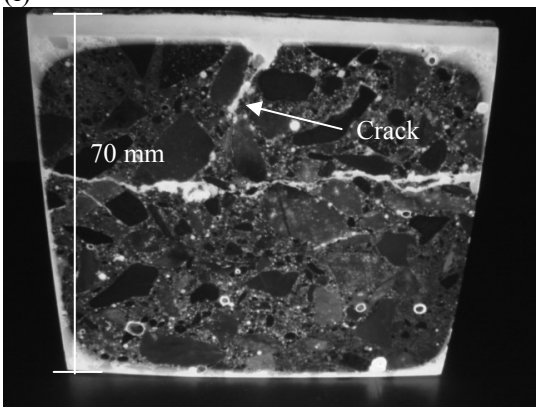

(ii)

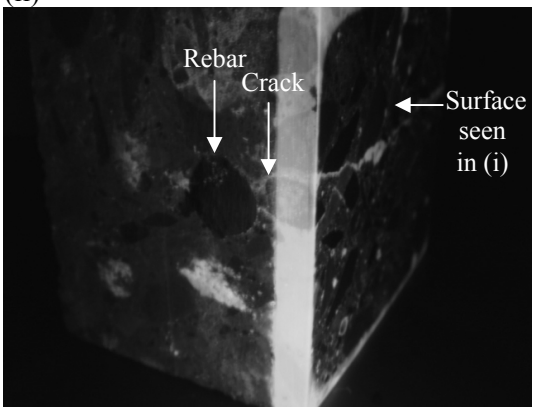

(b)

Statically loaded OPCC (sample 1)

(i)

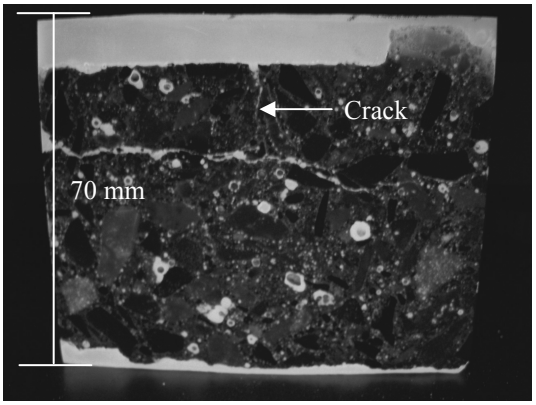

(ii)

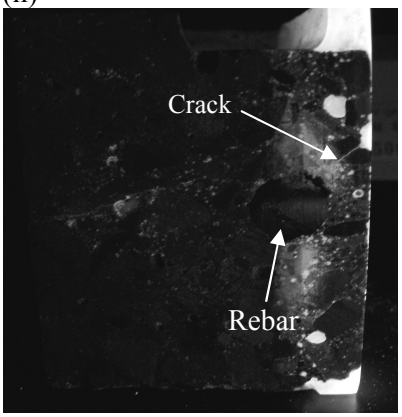

Statically loaded OPCC (sample 2)

(i)

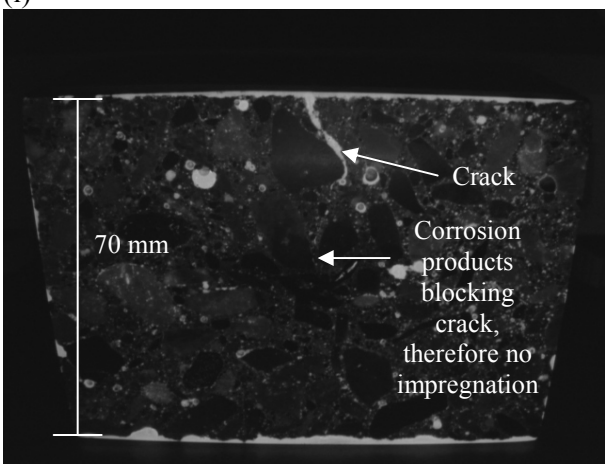

(ii)

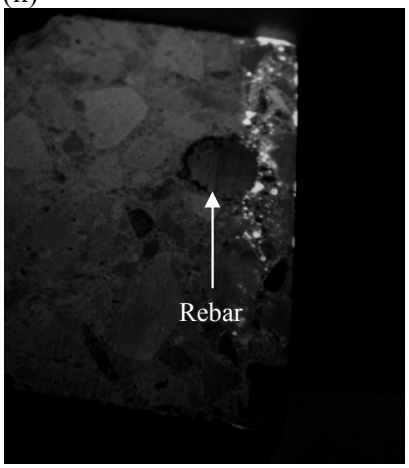

(c) Dynamically loaded HPC

(i) (ii)

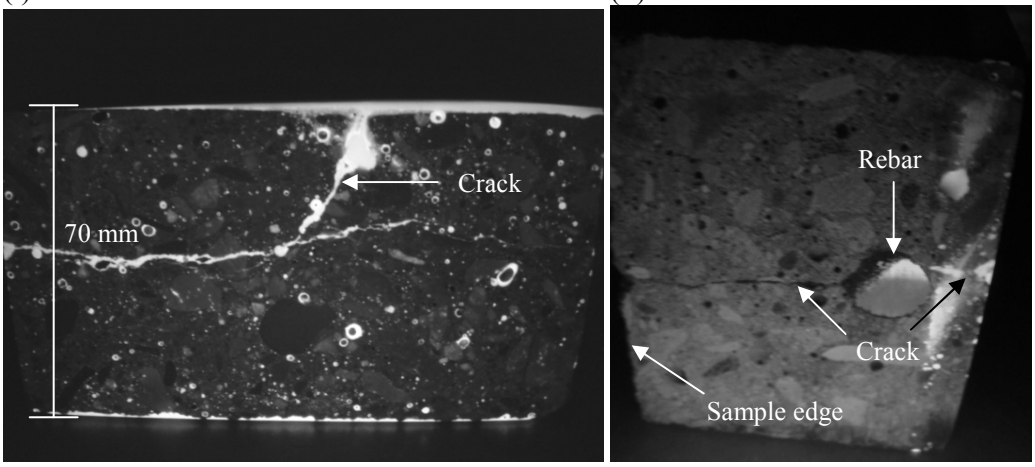

(d) Statically loaded HPC

(i) (ii)

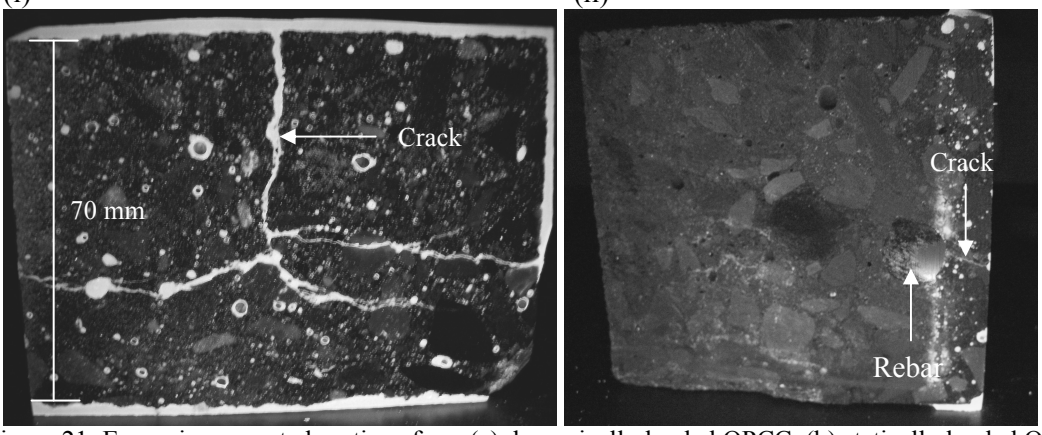

Figure 21: Epoxy impregnated sections from (a) dynamically loaded OPCC, (b) statically loaded OPCC (c) dynamically loaded HPC and (d) statically loaded HPC photographed in UV light. Figures labelled (i) illustrate the face of the section that is parallel to the rebar contained in this section and those labelled (ii) show the face that is perpendicular to the rebar.

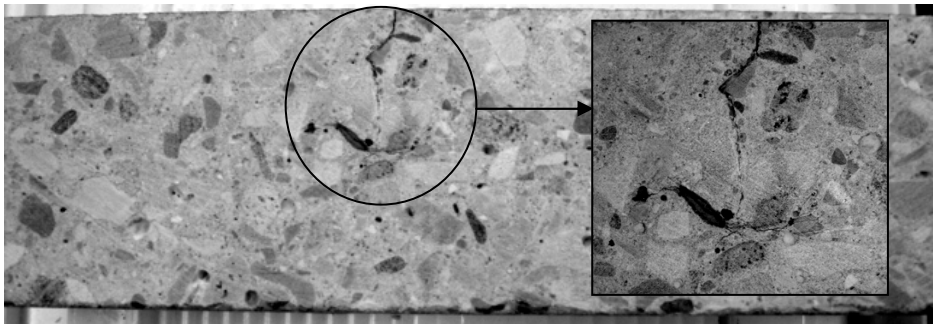

Figure 22: Photograph of OPCC statically loaded sample 2 in Figure 21(b) prior to impregnation. Note the height of the section (as shown) is 70 mm.

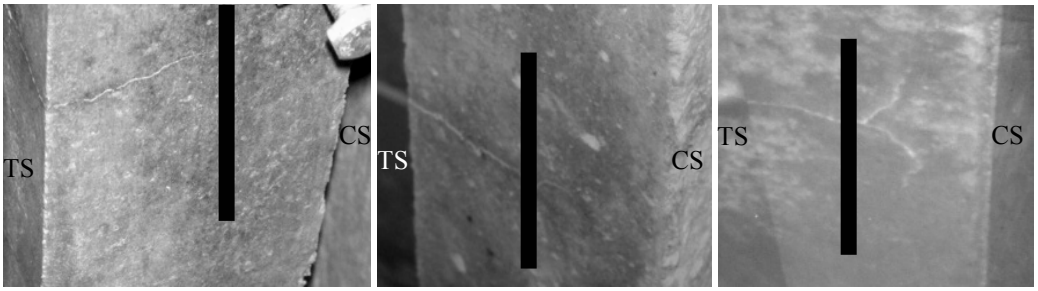

Figure 23: Example of crack morphology along the edge of the sample in (a) statically loaded beams, (b) dynamically loaded OPCC beams and (c) dynamically loaded HPC beams. CS and TS denote compressive and tensile surfaces, respectively, on the beam. Black line illustrates the location of the rebar.

4.3 CHLORIDE PROFILES

The chloride concentration profiles from the cracked and submerged regions of two each of OPCC and HPC beams subjected to static and dynamic loading are presented in Figure 24 and Figure 25. It should be noted that the profiles are not smooth curves because the amount of paste and aggregate varied at the crack, and influenced chloride penetration from the crack into the concrete.

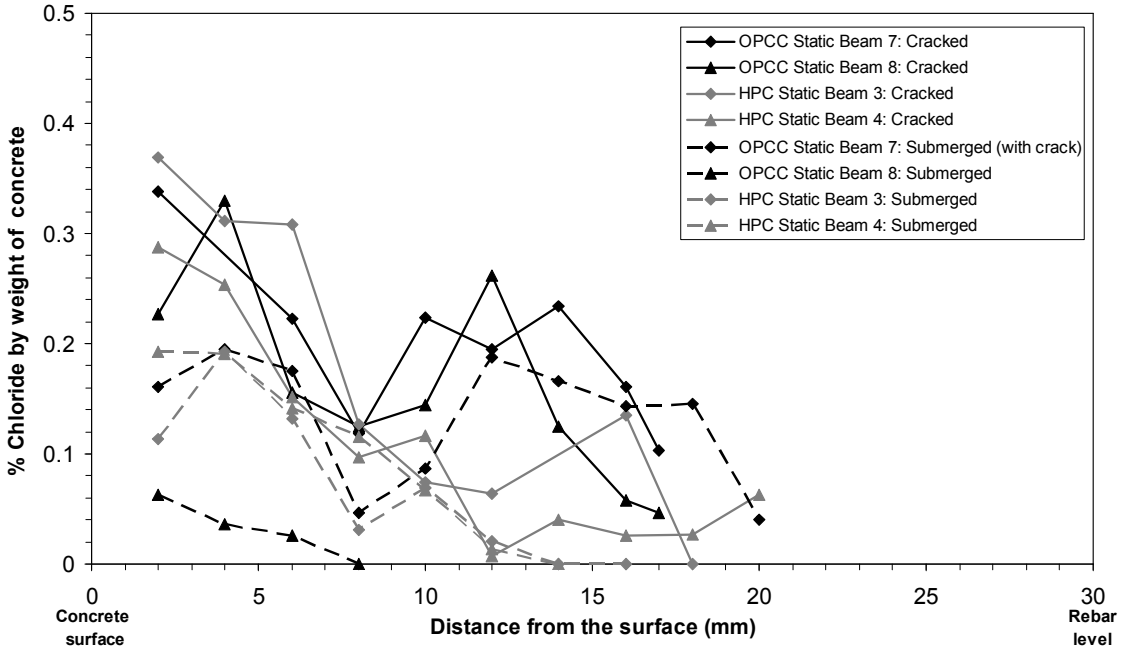

Figure 24: Chloride profiles in the cracked and submerged regions of OPCC and HPCC beams that were statically loaded.

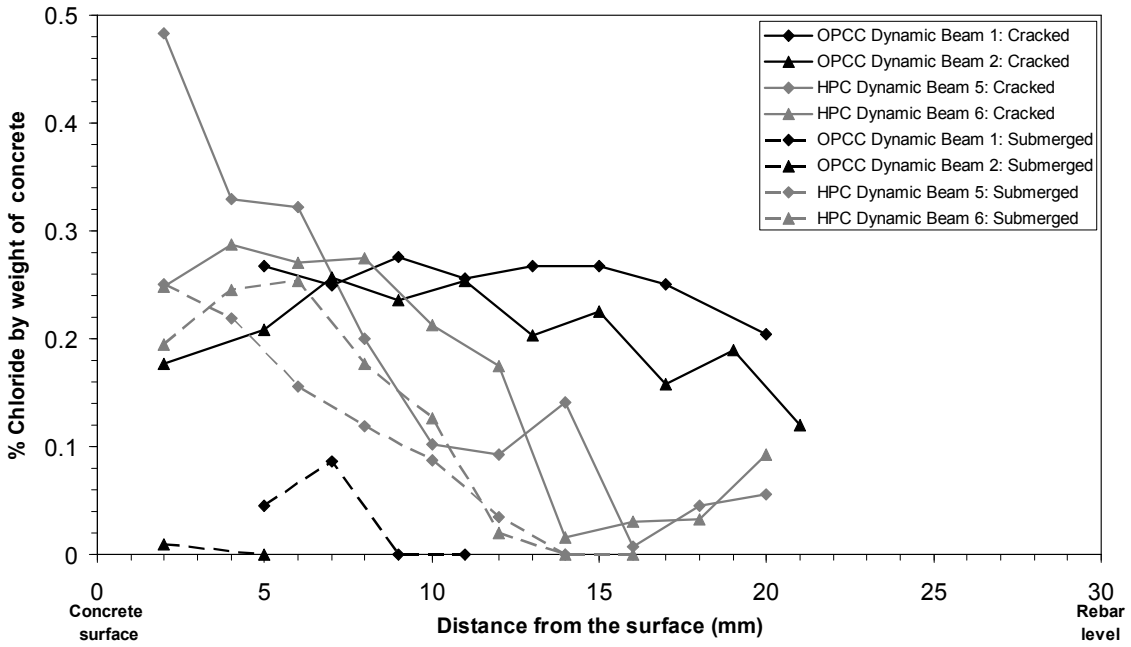

Figure 25: Chloride profiles in the cracked and submerged regions of OPCC and HPCC beams that were dynamically loaded.

The chloride content in the cracked region of the dynamically loaded OPCC beams remained more or less constant from the surface into the interior of the concrete while, in the corresponding HPC beams, the chloride content decreased from the surface into the interior of the concrete. The portion of the concrete closest to the surface had chlorides penetrating from the surface as well as from the crack walls; however, in the interior of the concrete, the ingress was mainly from the crack walls. This results in the descending profiles observed in the dynamically loaded HPC. The difference between the dynamically loaded beams can be attributed to the fact that the OPCC was more porous than the HPC and chloride ions penetrated more easily into it from the crack. The amount of chlorides also decreased in the cracked region of the statically loaded HPC beams for the same reason.

Generally, the chloride profiles decreased from the surface into the interior at a crack in the statically loaded OPCC beams; however, there was a region between 10 and 15 mm from the surface where there was a higher chloride concentration. Photographs of the concrete obtained at different penetration depths from the surface at a magnification of three times (shown in Section 4.5.2) did not reveal any distinguishable differences between this region and the ones before or after it. A possible explanation for the increased chloride content in this region (which is at ~ half the cover depth) was that the walls of the cracks were subjected to bending under tension caused by the interaction of the applied stress on the beam and the bond between the concrete and rebar. The maximum bending

occurred at the mid-region (10 - 15 mm from the surface of the concrete) along the length of the crack into the concrete. Hence, more opening of microcracks perpendicular to the original crack would have occurred in this region, aiding in penetration of chloride ions into the concrete. These cracks may also have occurred in the statically loaded HPC; however, because HPC was less porous than OPCC, the chloride ingress was not as significant.

The difference in the profiles of the dynamically and statically loaded OPCC can be attributed to the opening and closing of the crack in the former which renewed the supply of salt solution in the crack and pushed the solution into the pores and microcracks. It could also be that the application of dynamic loading on the beams caused microcracks to grow and branch, resulting in increased chloride penetration.

The type of loading did not influence chloride ingress in the submerged region of the concrete. In both the dynamically and statically loaded beams, HPC had higher chloride content than OPCC in the submerged region. This was contrary to what was expected since HPC was less porous than OPC. However, networks of cracks were observed on the HPC concrete in the submerged region, as shown in Figure 26, and were not observed in the OPCC. These cracks may have been responsible for the higher chloride content in the HPC. On the contrary, OPCC displayed a network of cracks in the non-submerged region while HPC did not. Similar observations have not been reported in the literature. Therefore, it is hypothesized that the cracks probably occurred in HPC when salt was present and attracted water to it; however, due to the decreased porosity in this concrete compared to in OPCC there were no space for this water to be accommodated in. Hence, the water caused expansive stresses in the concrete causing cracks to form. Further investigation is needed, but this topic lies beyond the scope of the present study. However, in the OPCC the networks of cracks were likely caused by drying shrinkage because it received only two days of curing compared to the seven days that was applied to the HPC.

In Figure 24, one of the statically loaded OPCC beams showed a higher chloride content in the submerged region than its counterpart. The profile obtained indicated that there was a crack present in this region. However, a visual examination of the beam in this region did not reveal such a crack. The area was then examined via a fifteen times magnification lens which did reveal a crack, as shown in Figure 27.

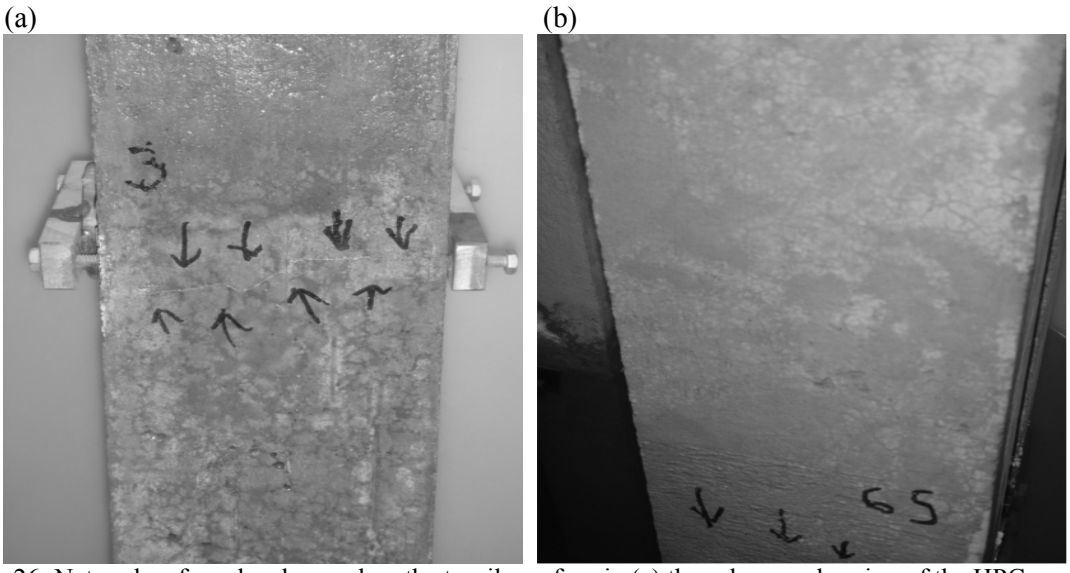

Figure 26: Networks of cracks observed on the tensile surface in (a) the submerged region of the HPC concrete and (b) the non-submerged region of the OPCC concrete.

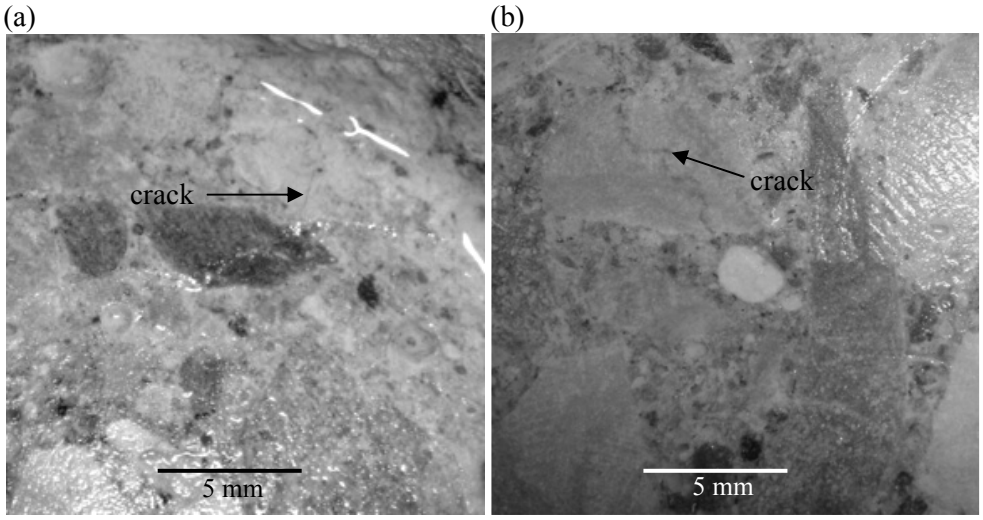

Figure 27: (a) and (b) show the same crack at different locations on the tensile side in the submerged region of statically loaded OPCC beam 7 where the concrete for chloride concentration measurements was obtained from.

In order to establish quantitative data that can be used in service life prediction models, the chloride content values at different depths from the surface for the two beams of each concrete and loading type were averaged and plotted against the distance from the surface as shown in Figure 28. The curves were fitted with trendlines (dashed lines) and the equations of the latter are given in Figure 28. The equations are used to provide a way of quantifying the effect of cracks on chloride contents in concrete and are not intended to represent any physical aspects. The equations can be used

to predict the approximate chloride content at cracks in concretes which constitute similar compositions and have been exposed to similar conditions as the beams. However, further testing is needed to verify if this behaviour extends to concretes with varying w/cm and containing different types and amounts of SCMs and, which have been exposed, for longer times, to loading and salt.

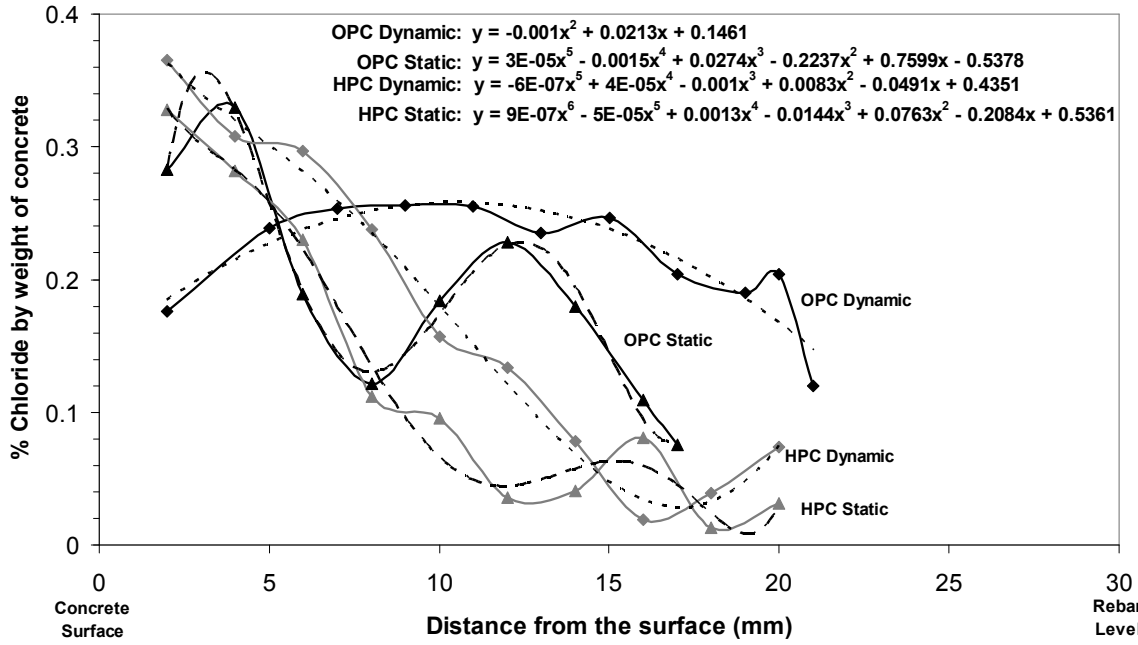

Figure 28: Curves illustrating the average chloride content in the beams which have been fitted with trendlines.

4.4 CORROSION MEASUREMENTS

4.4.1 LPR and Galvanostatic Pulse Measurements

4.4.1.1 Corrosion Current Densities

Corrosion current densities (i_{corr}) in the non-submerged, submerged and cracked regions of all the beams were obtained from LPR and galvanostatic pulse measurements and the individual results are given in Appendix C (Figures C1-C12). The average values for each concrete and loading type are given in Figure 29-Figure 32.The current densities are based on the polarized area rather than the

actual corroding area. The impact of the actual actively corroding area on the current densities is discussed below.

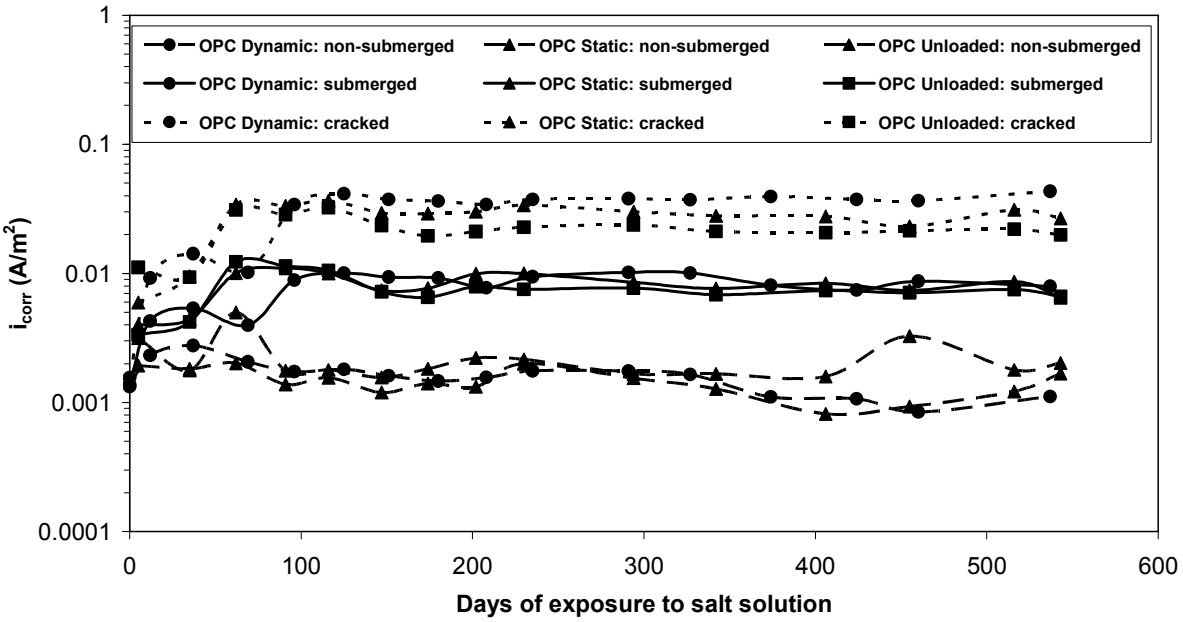

Figure 29: Corrosion current densities in the OPCC beams obtained using LPR measurements.

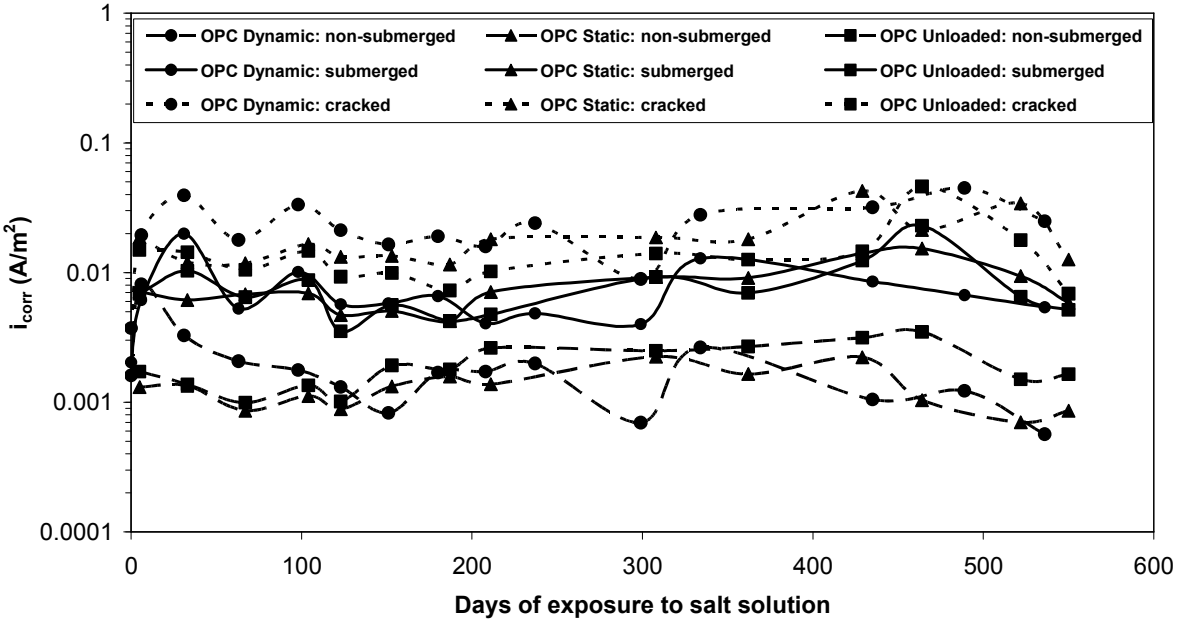

Figure 30: Corrosion current densities in the OPCC beams obtained using galvanostatic pulse measurements.

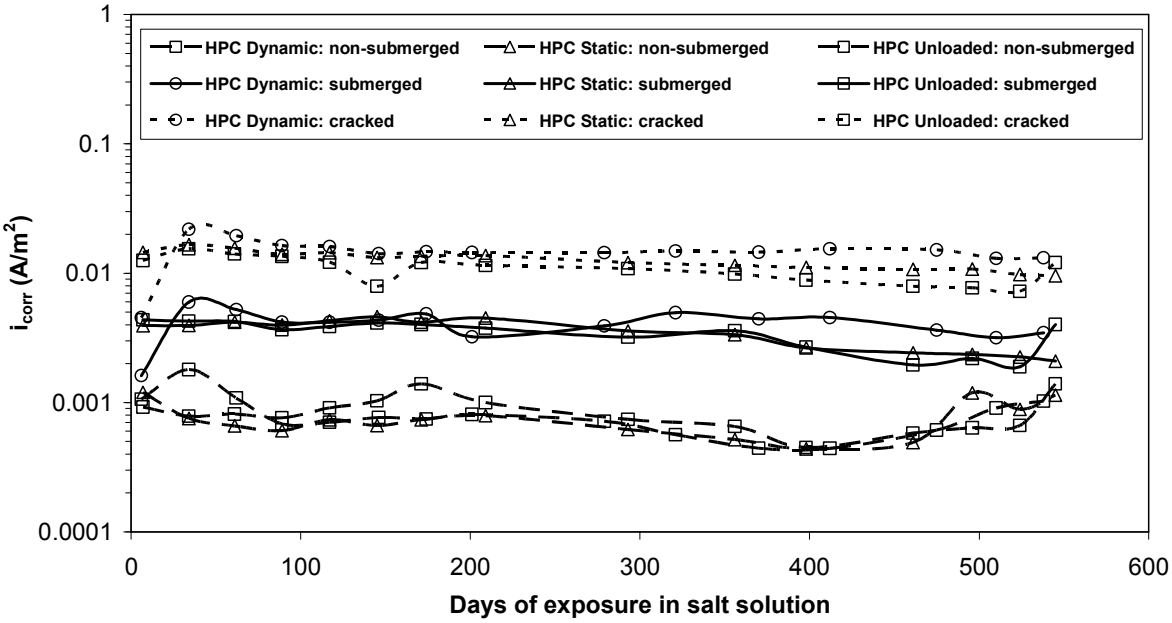

Figure 31: Corrosion current densities in the HPC beams obtained using LPR measurements.

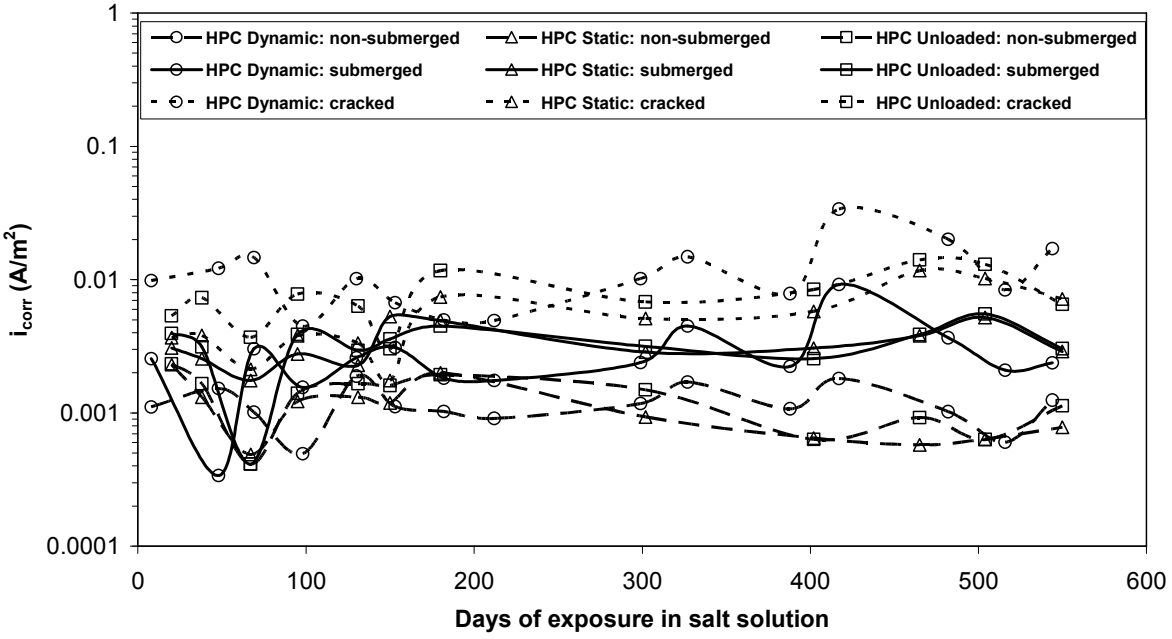

Figure 32: Corrosion current densities in the HPC beams obtained using galvanostatic pulse measurements.

It should be noted that the initial increase in the LPR current density in the cracked and submerged regions of all the OPCC beams and the dynamically loaded HPC beams occurred because

the conditions under which the measurements were conducted were changed (i.e. from dry to wet cycle). This increase was not observed in the data from galvanostatic pulse measurements because these were always conducted in the dry cycle. The fact that the corrosion rates in the three regions of the beams remained more or less constant from the beginning to the end is an indication that the cracks in the mid-section were influencing the rebars from the very beginning. Also, the current densities obtained using the galvanostatic pulse technique exhibited greater fluctuation than those obtained using LPR because they were conducted at different intervals in the dry cycle and, as a result, the dryness of the concrete could have been influencing the corrosion rates.

According to Figure 29-Figure 32, the highest current densities were obtained in the cracked regions of the beams and the lowest in the non-submerged regions, as expected. This difference in the i_{corr} between the submerged and cracked regions was more pronounced in the LPR measurements that were conducted in the wet cycle than the galvanostatic pulse in the dry cycle. This was probably because the presence of solution inside the crack increased the corrosion activity on the rebar at the crack and also provided an easier path for ionic currents. In fact, the i_{corr} (based on polarized area) in the cracked regions of the OPCC and HPC varied between $6x10^{-3}$ - $5x10^{-2}$ A/m^2, which indicated (based on experience) active corrosion. The i_{corr} obtained in the non-submerged regions of the beams were between $4x10^{-4}$ - $3x10^{-3}$ A/m^2, typical of passive currents for steel in concrete. It was very difficult to obtain electrical connection between the rebar and the counter electrode in this region of the beams because of the high resistance of the concrete. In the submerged regions, the i_{corr} varied between $2x10^{-3}$ -$1x10^{-2}$ A/m^2. The higher current density observed in this region compared to the non-submerged region could have been because of (a) decreased resistance of the concrete due to exposure in salt solution (particularly in the porous OPCC concrete), (b) the galvanic coupling between the rebar in the submerged and the cracked sections and (c) the measurements performed in the submerged region could be detecting currents from the cracked region due to lower electrical resistance (i.e. lower concrete and polarization resistances) to current flow at a crack than in the sound concrete. However, the coupling between the non-submerged and cracked regions of the beams did not affect the corrosion rates of rebar in the former because (a) the concrete was dry and (b) the crystallization of salt in the concrete pores between the two regions could have prevented wicking of the salt solution into the non-submerged region.

Both LPR and galvanostatic pulse measurements indicated that, in the submerged and cracked regions, the current density is higher in the OPCC than in the HPC. However, there was a minor effect of the loading type on the i_{corr}. The difference between the current densities of rebar in OPCC

and HPC were higher when measured using LPR than with galvanostatic pulse because of the fluctuations in the latter measurements; however, the order of magnitude of the current densities was the same for the two techniques.

The corrosion current densities based on polarized area do not reveal accurate corrosion rates but they are useful when differentiating between actively corroding and passive rebars. This is an important point to bear in mind when current densities may be relied on to predict the remaining service life of a structure. Normally, the polarized area is used for calculation of the corrosion current density because there is currently not any technique which can non-destructively determine the actual actively corroding area.

In this project, rebars in four each of the statically and dynamically loaded beams and two unloaded beams of each type of concrete were removed from the concrete to determine the actual corroding areas at the end of the measurements. In the non-submerged region, the rebars were passive; hence, the actual current densities were assumed to be the same as those calculated using the polarized area.

In the submerged region some of the rebars had superficial corrosion in the epoxy-coated ends. However, there was no visible corrosion of the rebar away from these ends and cyclic polarization measurements (Section 4.4.2) showed that the corrosion in these ends had a negligible influence on measurements in the passive region of the submerged region. Therefore, the actual current densities in the submerged region were considered to be the same as those based on the polarized area except in one beam (HPC3D) which had a casting defect in the submerged region and the rebar B was actively corroding.

In the cracked region, the surface area used for the calculation of current density was larger than the actual corroding area. When a potential is applied to passive bars in concrete, it spreads over a large distance on the surface of the bars. As described in Section 3.7, this distance was assumed to be 300 mm in the non-submerged and submerged regions and 150 mm in the cracked region based on polarization measurements. However, when a reinforcing bar containing an area of active corrosion is polarized in the vicinity of this area, the current is attracted to the corroding area. Hence, the resulting potential and currents changes are actually from the corroding area, rather then the whole polarized area. In some of the beams, however, more than one actively corroding area existed in the cracked region due to the presence of multiple cracks. Therefore, the area that was used for the calculation of the actual current density was the sum of all these areas within the ‘polarized’ 150 mm length of the rebar in the cracked region where the corrosion rate measurements were performed.

Figure 33 and Figure 34 present final current densities based on the polarized areas and on the actual corroding areas in the cracked regions of the beams. The actual current density in the cracked region of the HPC beams is typically lower than in the OPCC. In the HPC, the damage due to corrosion was more superficial and was spread over a large area on the rebar, while, in the OPCC, corrosion occurred over a smaller area and induced crater-like damage on the rebar.

The average corrosion rates obtained in OPCC and HPC using the LPR technique are presented in Table 5. For the non-submerged and submerged regions, the current densities based on polarized and actual corroding areas are the same because the actual corroding area was considered to be the same as the polarized area. In the cracked region, the current densities based on actual corroding areas are higher than those obtained based on polarized areas because the actual corroding area was smaller than the polarized area. As can be seen in Figure 34 (b) there was a large variation in corrosion rates in the cracked region of the HPC unloaded beams giving a very large coefficient of variation. This was due to a very small corroding area within the 15 cm length of rebar HPC1UF that was polarized. However, there was another corroding area outside this length (Figure 35) which could have been affecting the currents measured in the cracked section of this beam.

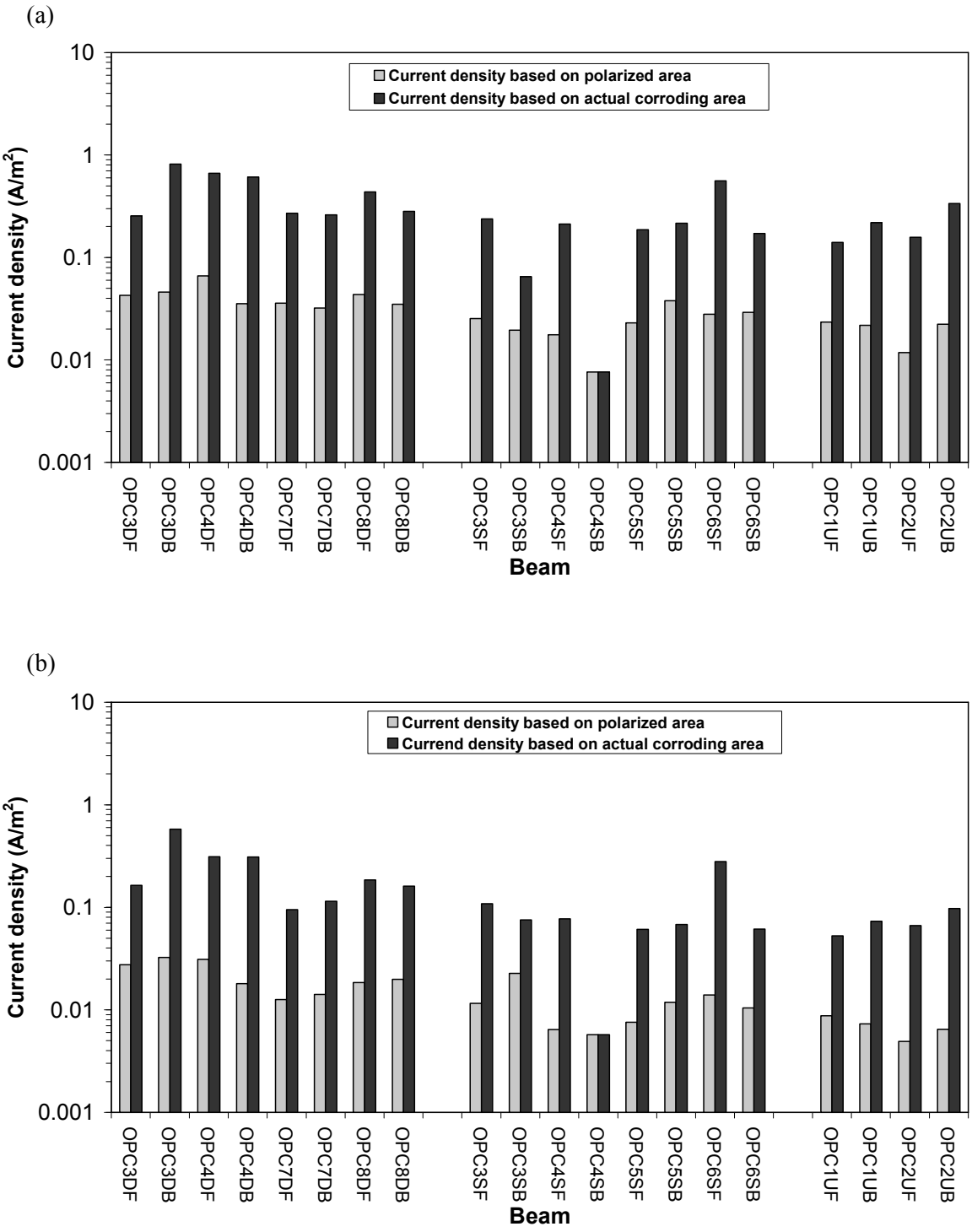

Figure 33: Corrosion current densities in the cracked region of the OPCC beams based on polarized areas and actual corroding areas measured using (a) LPR and (b) galvanostatic pulse techniques. The notation used for naming the beams is described in Section 3.7.

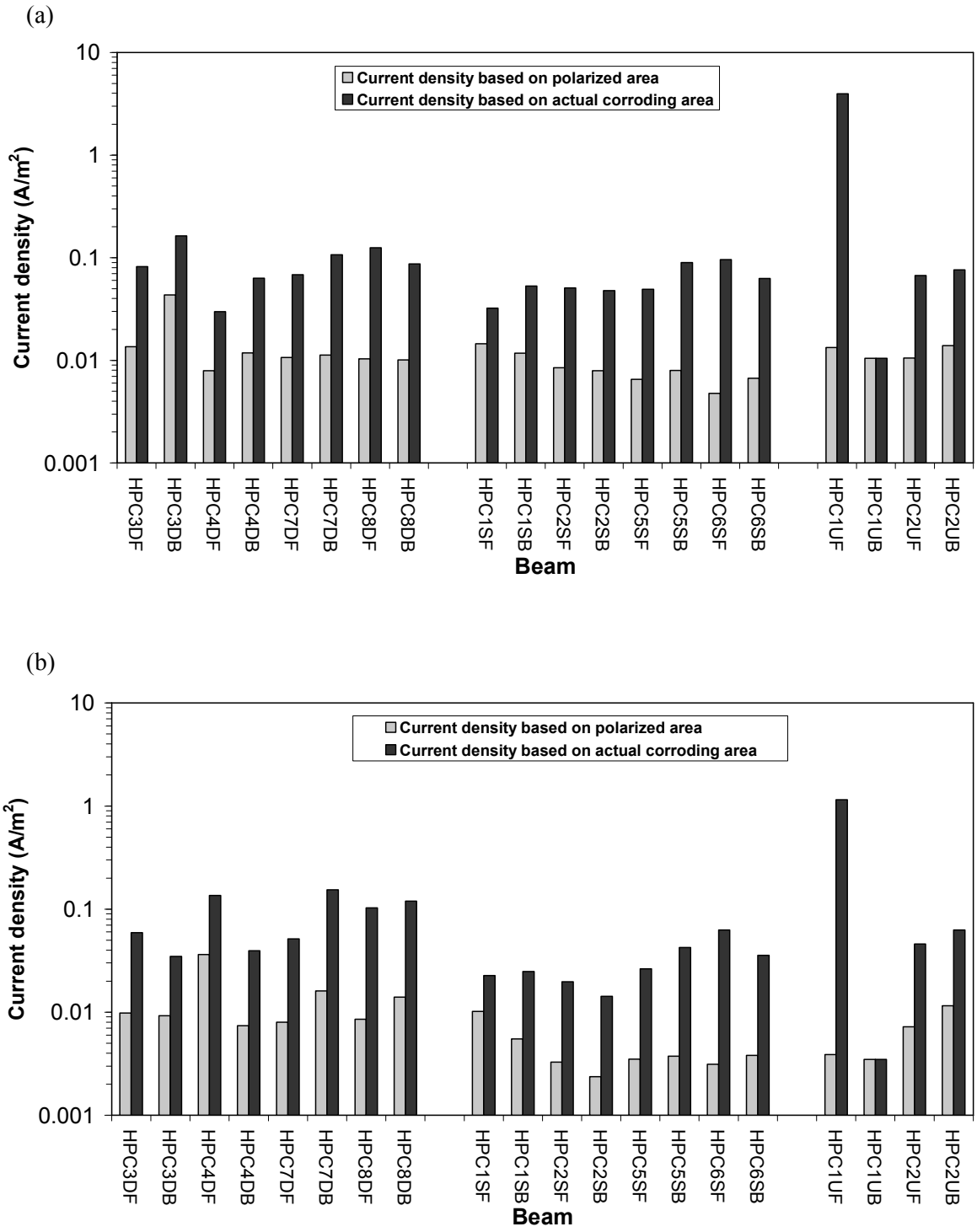

Figure 34: Corrosion current densities in the cracked region of the HPC beams based on polarized areas and actual corroding areas measured using (a) LPR and (b) galvanostatic pulse techniques. The notation used for naming the beams is described in Section 3.7.

Table 5: Average i_{corr} in OPCC and HPC beams measured using the LPR technique.

Beam Section	Loading	Average I_{corr} (A/m^2) Based on polarized area	Coefficient of Variation (%) Based on polarized area	Average I_{corr} (A/m^2) Based on corroding area	Coefficient of Variation (%) Based on corroding area
OPCC Non-submerged	Dynamic	1.11×10^{-3}	76	1.11×10^{-3}	76
	Static	1.68×10^{-3}	24	1.68×10^{-3}	24
	Unloaded	2.03×10^{-3}	5	2.03×10^{-3}	5
OPCC Cracked	Dynamic	4.33×10^{-2}	22	4.49×10^{-1}	49
	Static	$2.67x\ 10^{-2}$	34	2.07×10^{-1}	79
	Unloaded	1.99×10^{-2}	27	2.13×10^{-1}	42
OPCC submerged	Dynamic	7.95×10^{-3}	13	7.95×10^{-3}	13
	Static	6.46×10^{-3}	29	6.46×10^{-3}	29
	Unloaded	6.63×10^{-3}	10	6.63×10^{-3}	10
HPC Non-submerged	Dynamic	1.03×10^{-3}	46	1.03×10^{-3}	46
	Static	1.14×10^{-3}	36	1.14×10^{-3}	36
	Unloaded	1.39×10^{-3}	17	1.39×10^{-3}	17
HPC Cracked	Dynamic	1.31×10^{-2}	74	9.06×10^{-2}	45
	Static	9.56×10^{-3}	31	6.02×10^{-2}	36
	Unloaded	1.21×10^{-2}	15	1.03×10^{0}	149
HPC Submerged	Dynamic	1.86×10^{-3}	21	1.86×10^{-3}	21
	Static	2.09×10^{-3}	20	2.09×10^{-3}	20
	Unloaded	4.01×10^{-3}	7	4.01×10^{-3}	7

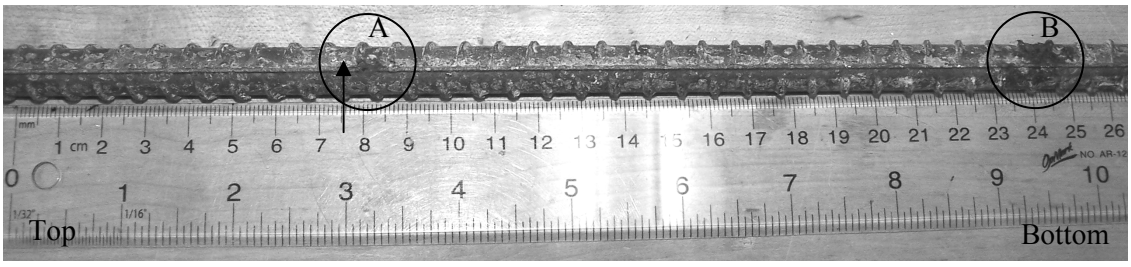

Figure 35: Corroding area A was used for calculation of corrosion current density in the cracked region of HPC1UF. However, area B could be influencing the corrosion currents. The arrow denotes the measurement location.

4.4.1.2 Corrosion potentials

Half-cell (E_{corr}) potential measurements are commonly used in reinforced concrete structures to determine the condition of the rebar. E_{corr} measurements are rarely accompanied by i_{corr} measurements in the evaluation of such structures. Hence, even though the corrosion potential measurements in this project were conducted in combination with current density measurements, the data from the potential measurements has been presented as a separate section from the current density data (Section 4.4.1.1) to illustrate the difficulties encountered when relying on E_{corr} (half-cell) measurements alone to detect active corrosion.

Corrosion (half-cell) potentials obtained, over the exposure period, using (i) a calomel reference electrode at the onset of LPR measurements and (ii) a Ag/AgCl reference electrode before beginning galvanostatic pulse measurements have been converted to corresponding values with respect to a $Cu/CuSO_4$ reference electrode and are presented in Figure 36-Figure 47. These figures also contain two dashed lines at -200 and -350 mV vs $Cu/CuSO_4$ to delineate the regions identified by the guidelines of ASTM C876 [148], which are presented in Table 6. The potentials have not been presented as averages because they exhibit large variations for certain sections of the beams. For example, in the non-submerged region of the statically loaded OPCC beams (Figure 37 (a)) the potentials span across the three regions defined by ASTM C876 [148].

Table 6: The interpretation of half-cell potential measurements according to ASTM C876[148].

Half-cell potential reading versus $Cu/CuSO_4$	**Corrosion activity**
More positive than -200 mV	90 % probability of no Corrosion
between -200 mV and -350 mV	an increased probability of corrosion
More negative than -350 mV	90 % probability of corrosion

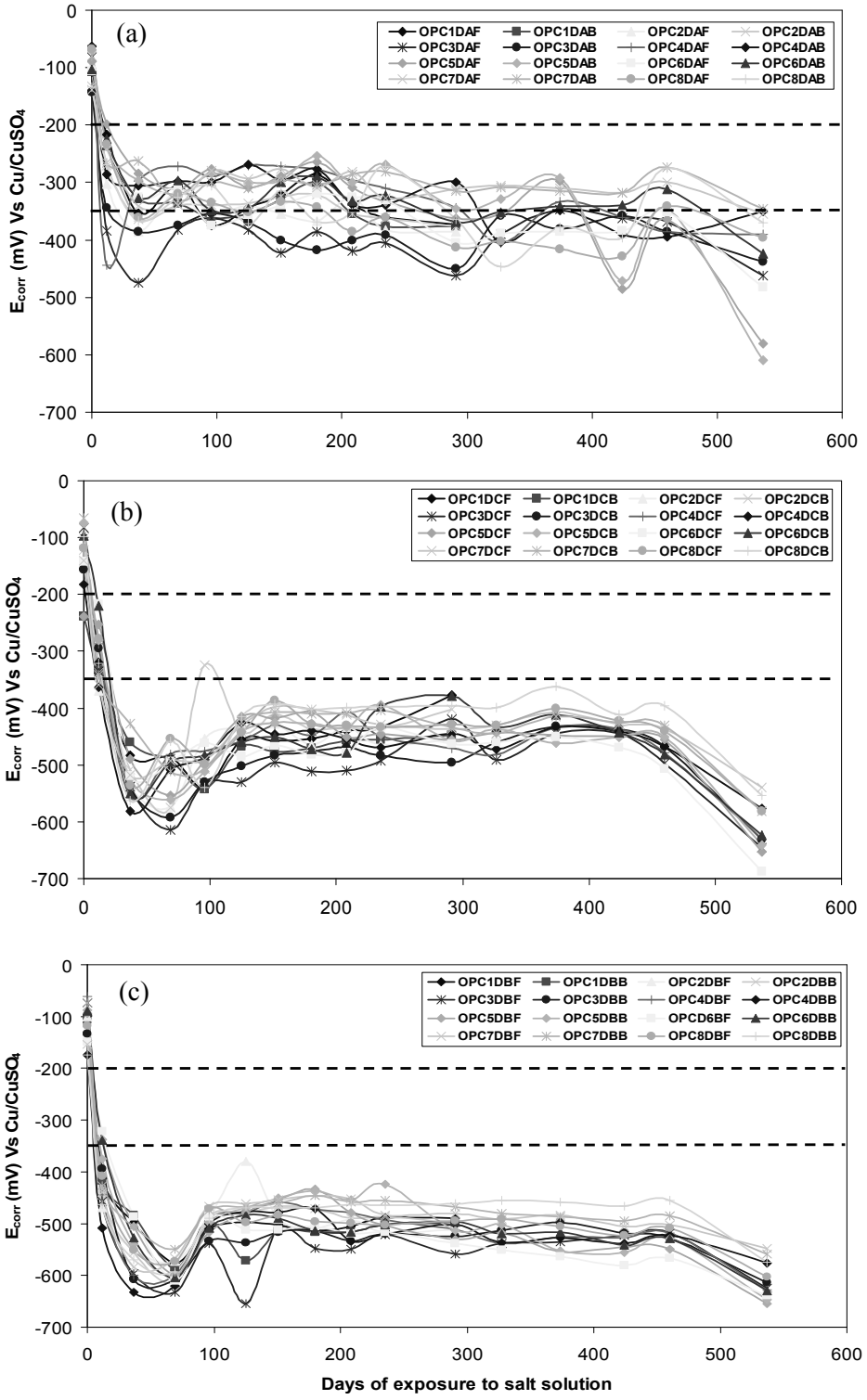

Figure 36: The corrosion potentials in the (a) non-submerged, (b) submerged and (c) cracked regions of the dynamically loaded OPCC beams measured during LPR measurements. Dashed lines represent limits designated by ASTM C876 [148].

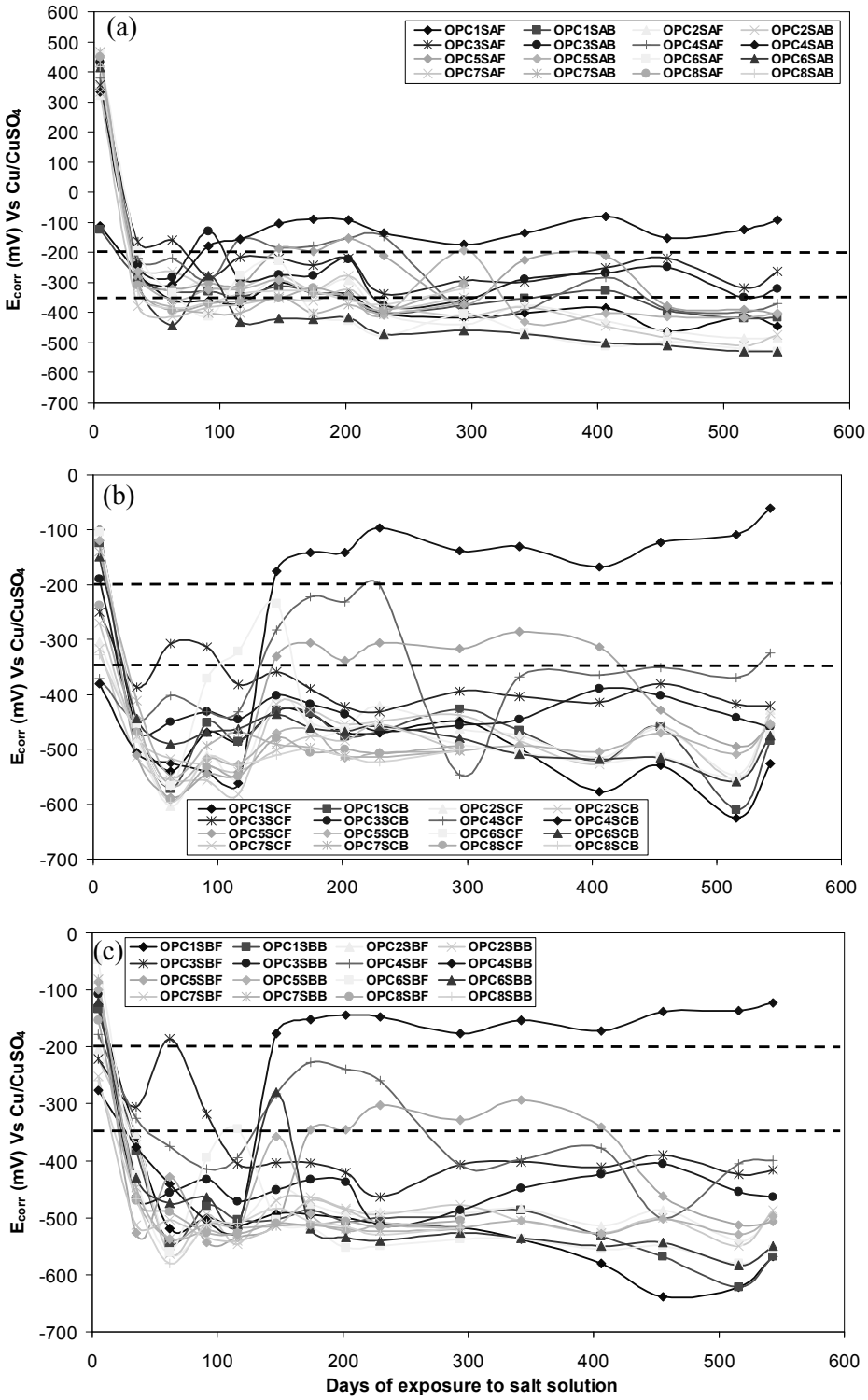

Figure 37: The corrosion potentials in the (a) non-submerged, (b) submerged and (c) cracked regions of the statically loaded OPCC beams measured during LPR measurements. Dashed lines represent limits designated by ASTM C876 [148].

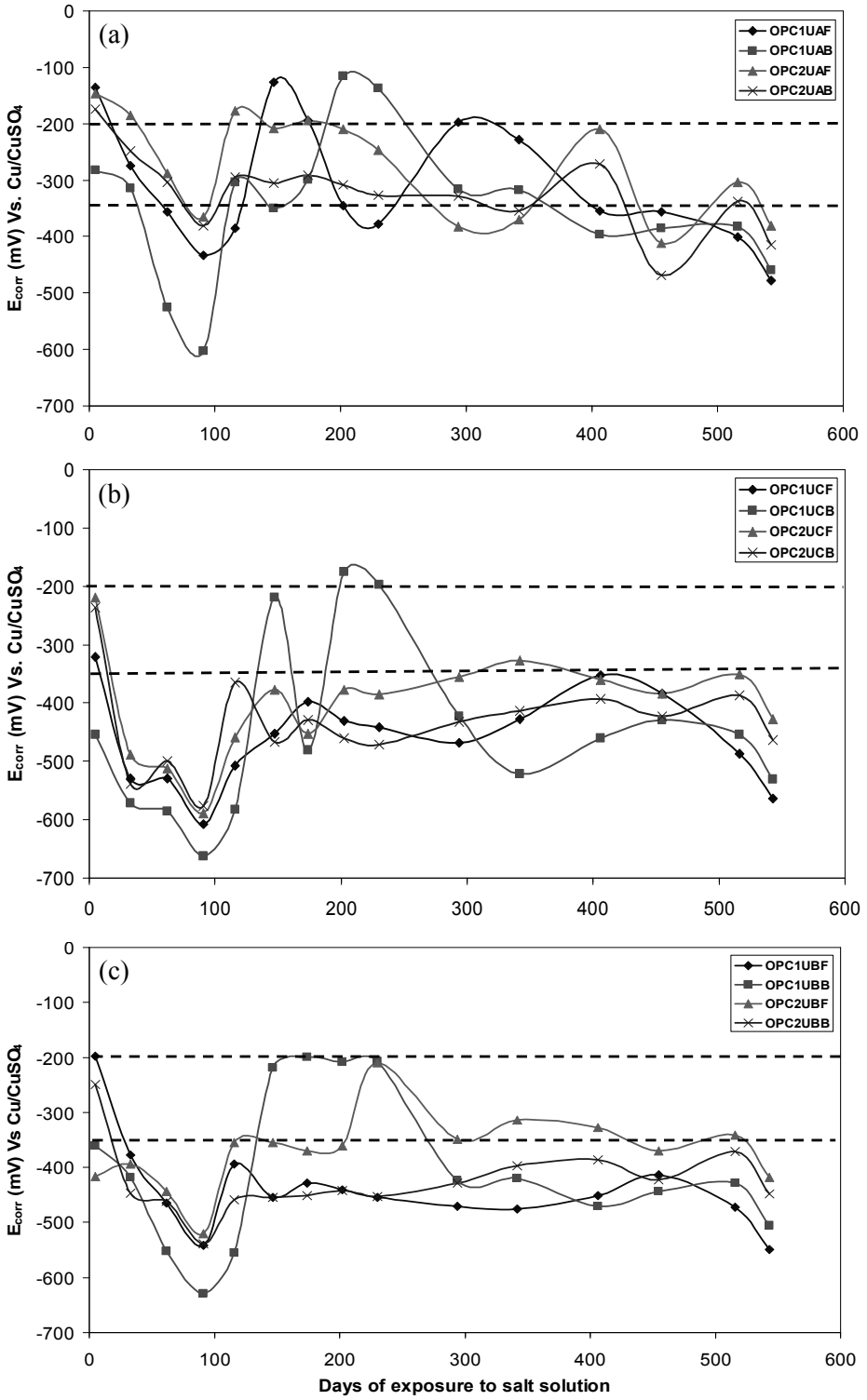

Figure 38: The corrosion potentials in the (a) non-submerged, (b) submerged and (c) cracked regions of the unloaded OPCC beams measured during LPR measurements. Dashed lines represent limits designated by ASTM C876 [148].

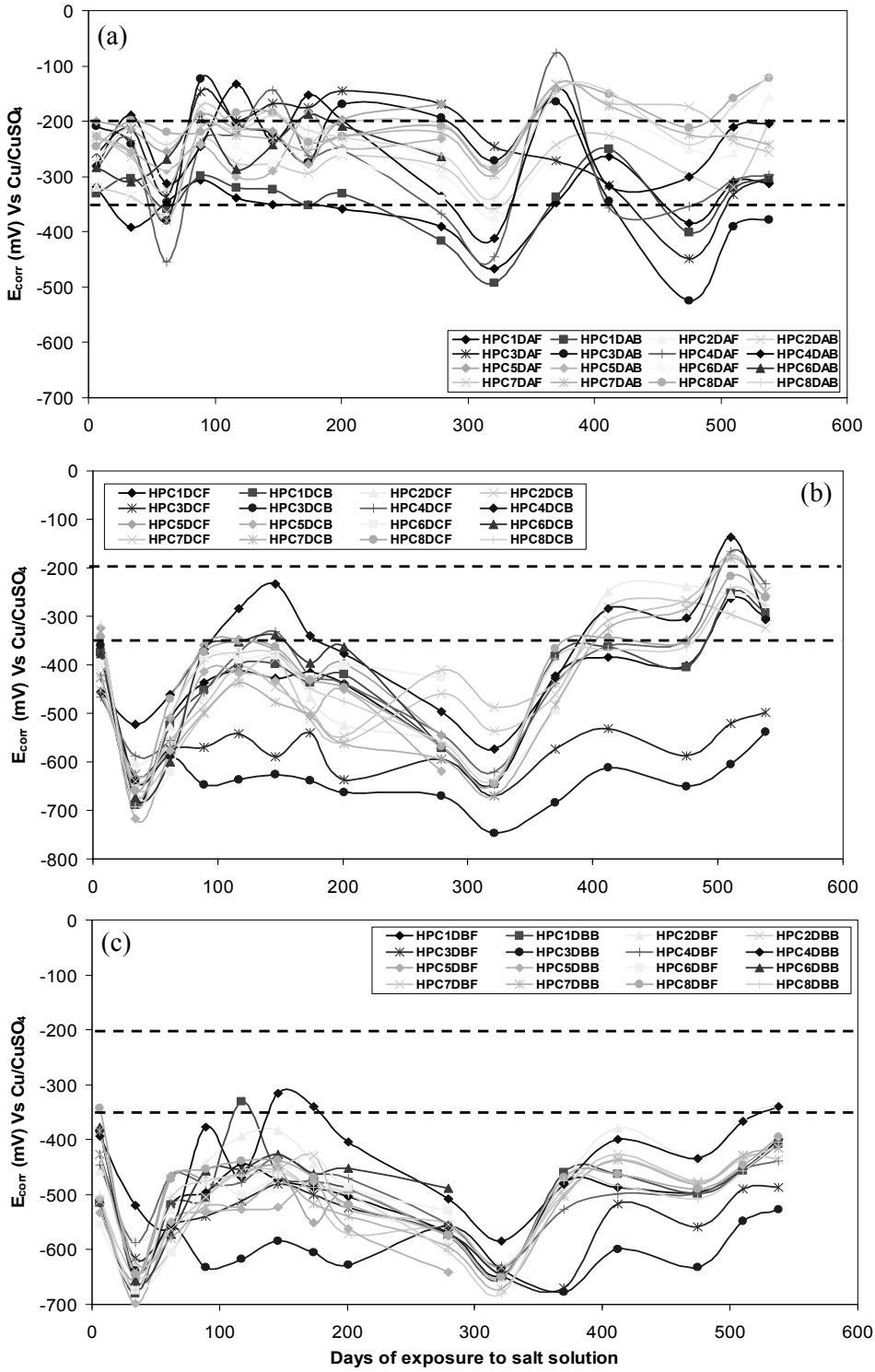

Figure 39: The corrosion potentials in the (a) non-submerged, (b) submerged and (c) cracked regions of the dynamically loaded HPC beams measured during LPR measurements. Dashed lines represent limits designated by ASTM C876 [148].

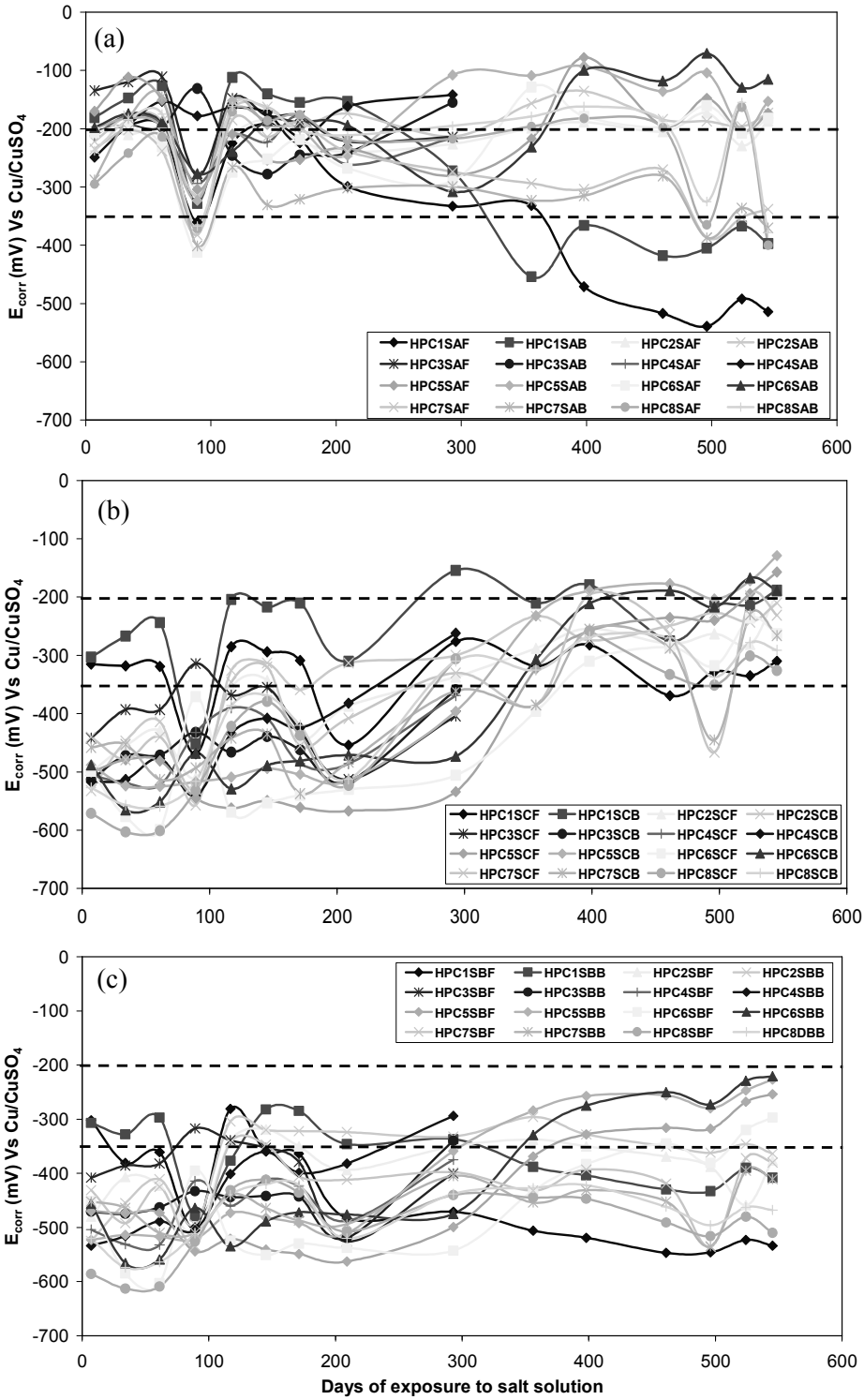

Figure 40: The corrosion potentials in the (a) non-submerged, (b) submerged and (c) cracked regions of the statically loaded HPC beams measured during LPR measurements. Dashed lines represent limits designated by ASTM C876 [148].

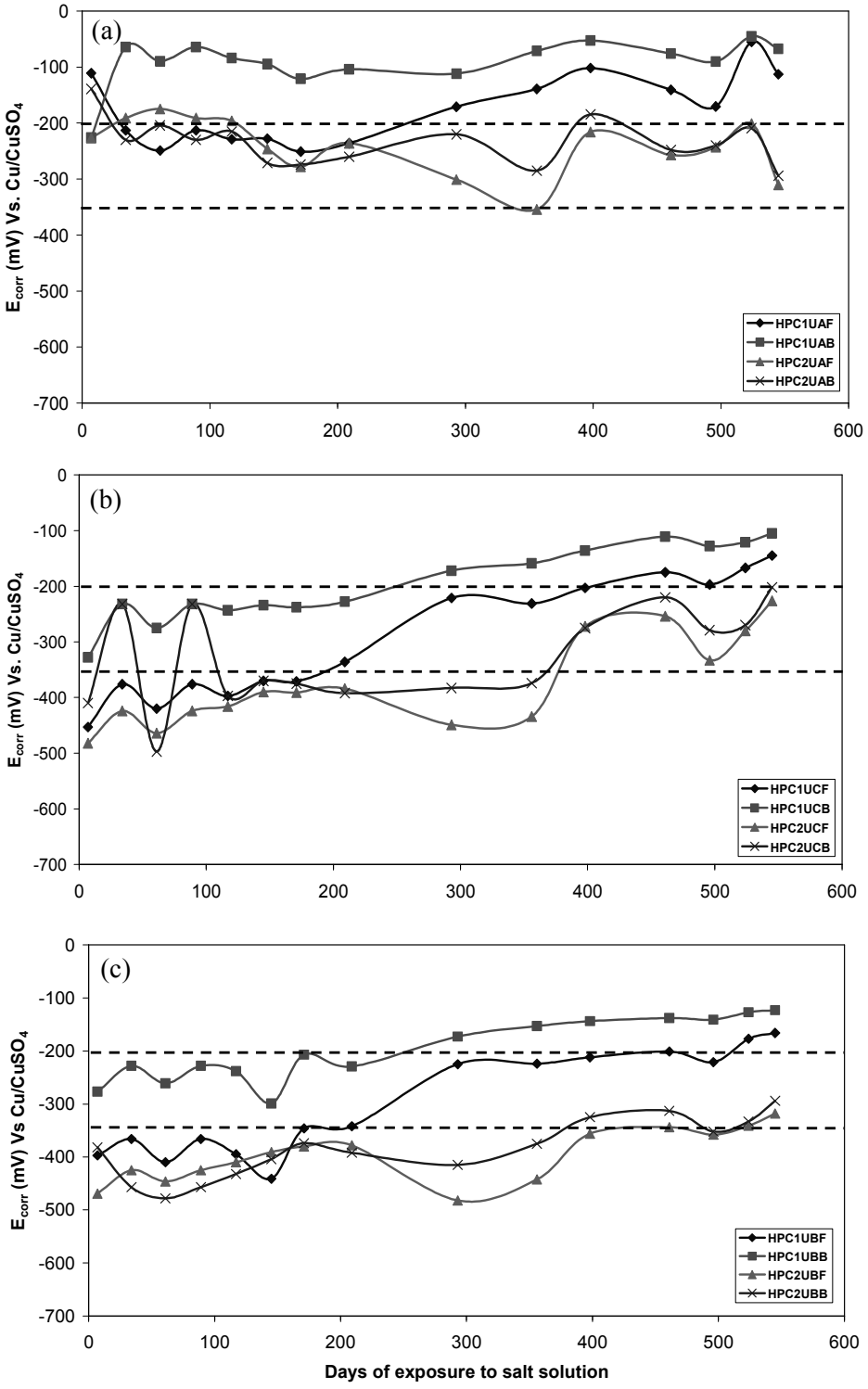

Figure 41: The corrosion potentials in the (a) non-submerged, (b) submerged and (c) cracked regions of the unloaded HPC beams measured during LPR measurements. Dashed lines represent limits designated by ASTM C876 [148].

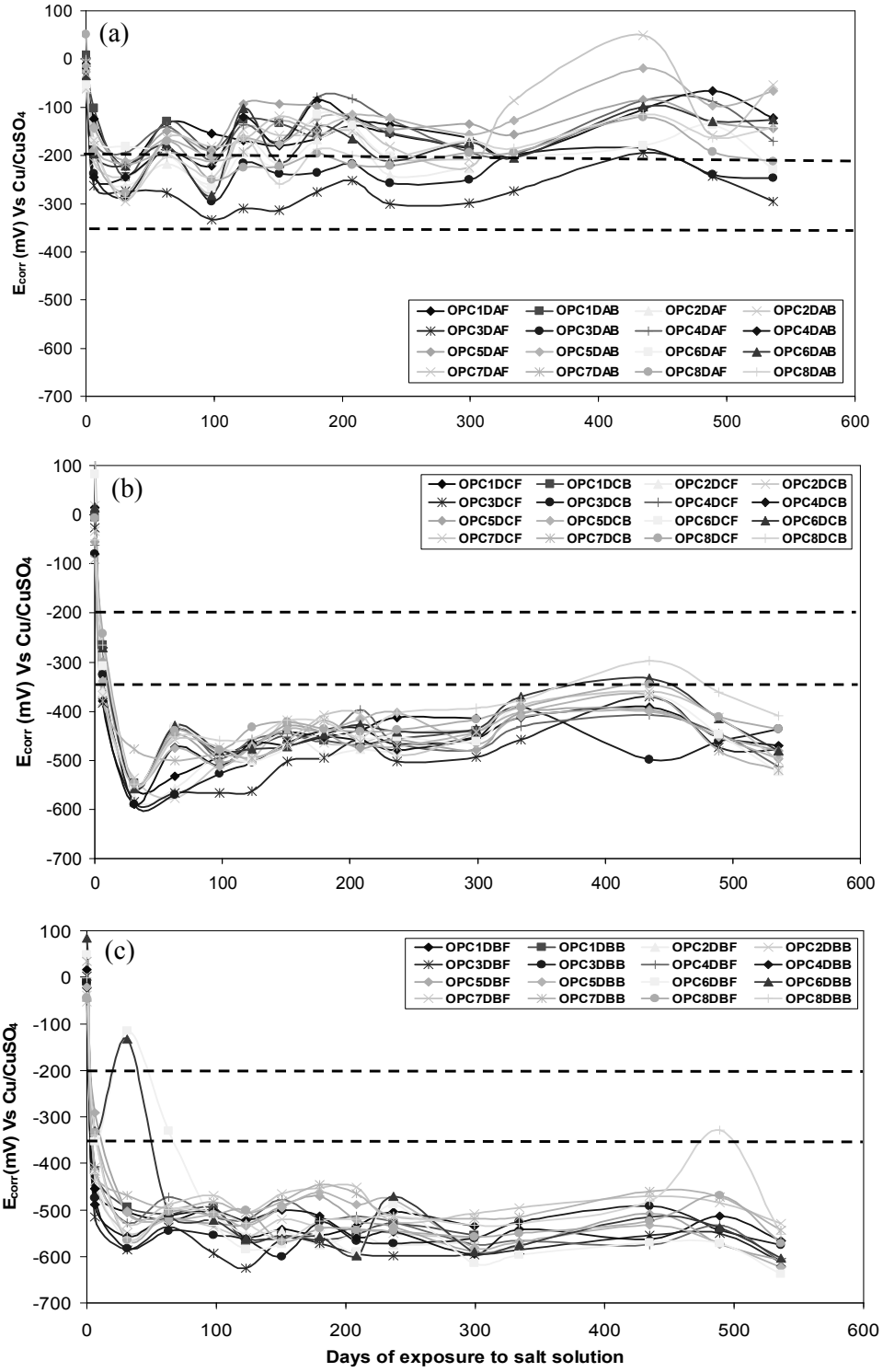

Figure 42: The corrosion potentials in the (a) non-submerged, (b) submerged and (c) cracked regions of the dynamically loaded OPCC beams measured using the GalvaPulse^{TM}. Dashed lines represent limits designated by ASTM C876 [148].

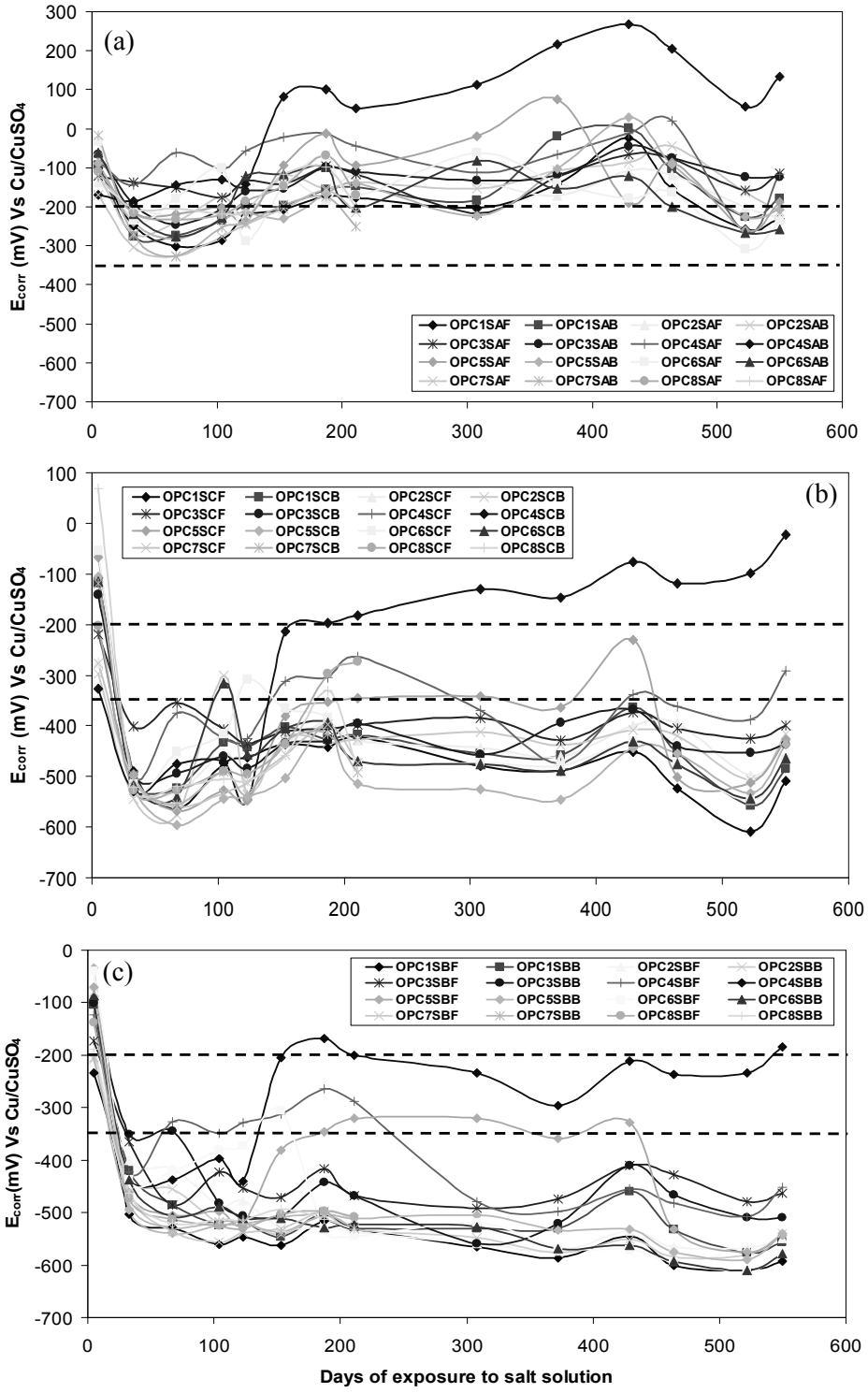

Figure 43: The corrosion potentials in the (a) non-submerged, (b) submerged and (c) cracked regions of the statically loaded OPCC beams measured using the GalvaPulse^{TM}. Dashed lines represent limits designated by ASTM C876 [148].

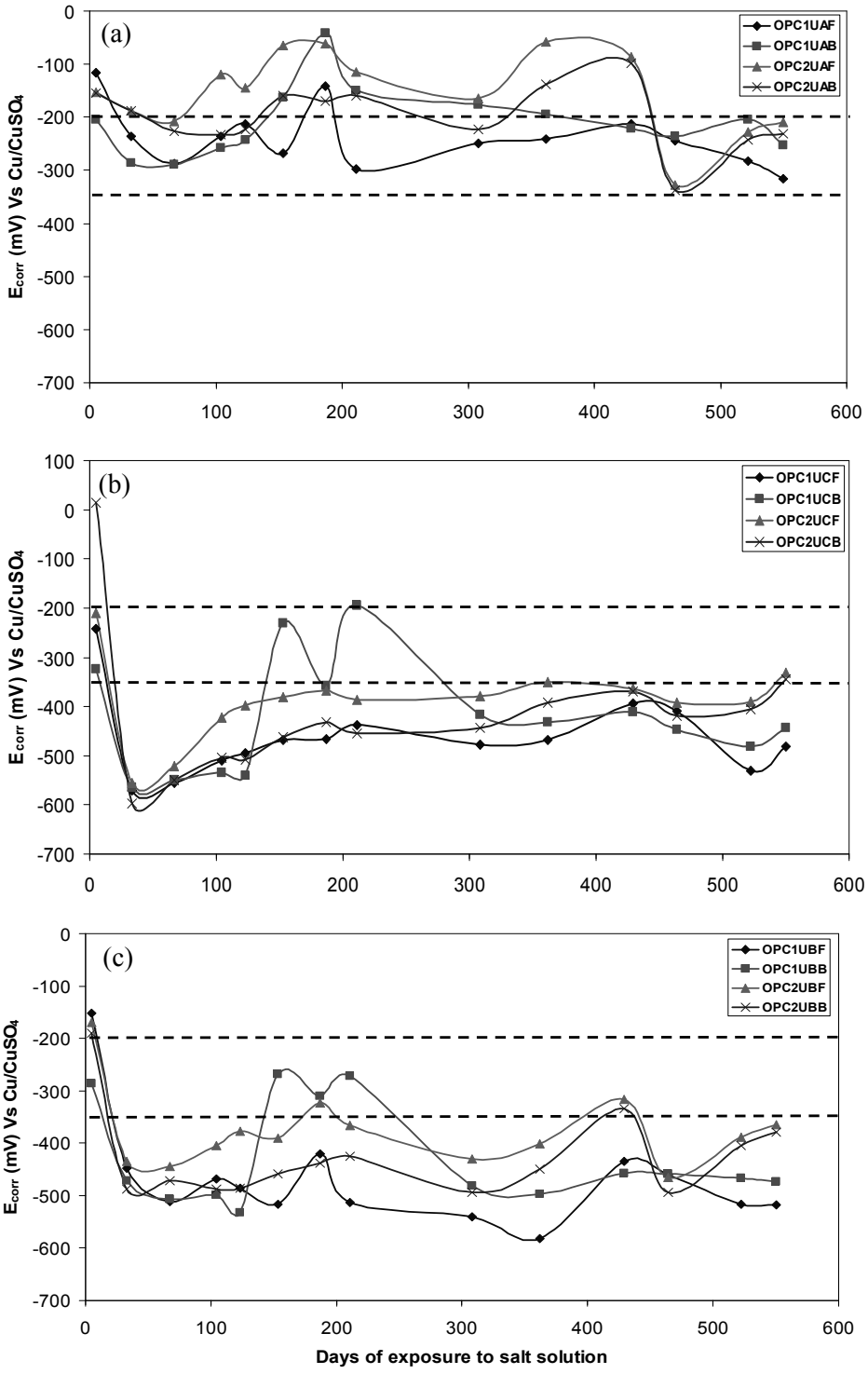

Figure 44: The corrosion potentials in the (a) non-submerged, (b) submerged and (c) cracked regions of the unloaded OPCC beams measured using the GalvaPulse^{TM}. Dashed lines represent limits designated by ASTM C876 [148].

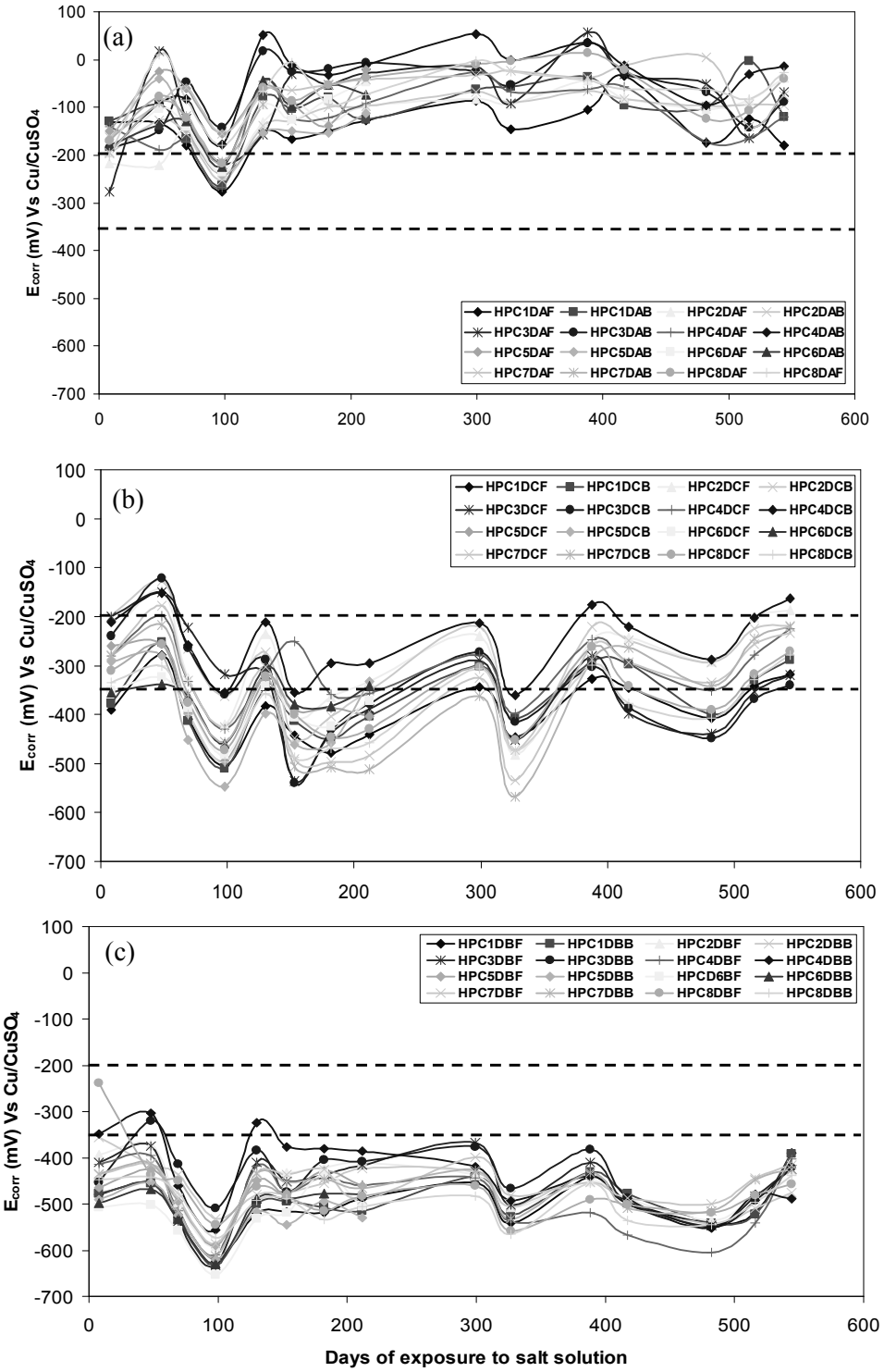

Figure 45: The corrosion potentials in the (a) non-submerged, (b) submerged and (c) cracked regions of the dynamically loaded HPC beams measured using the GalvaPulse™. Dashed lines represent limits designated by ASTM C876 [148].

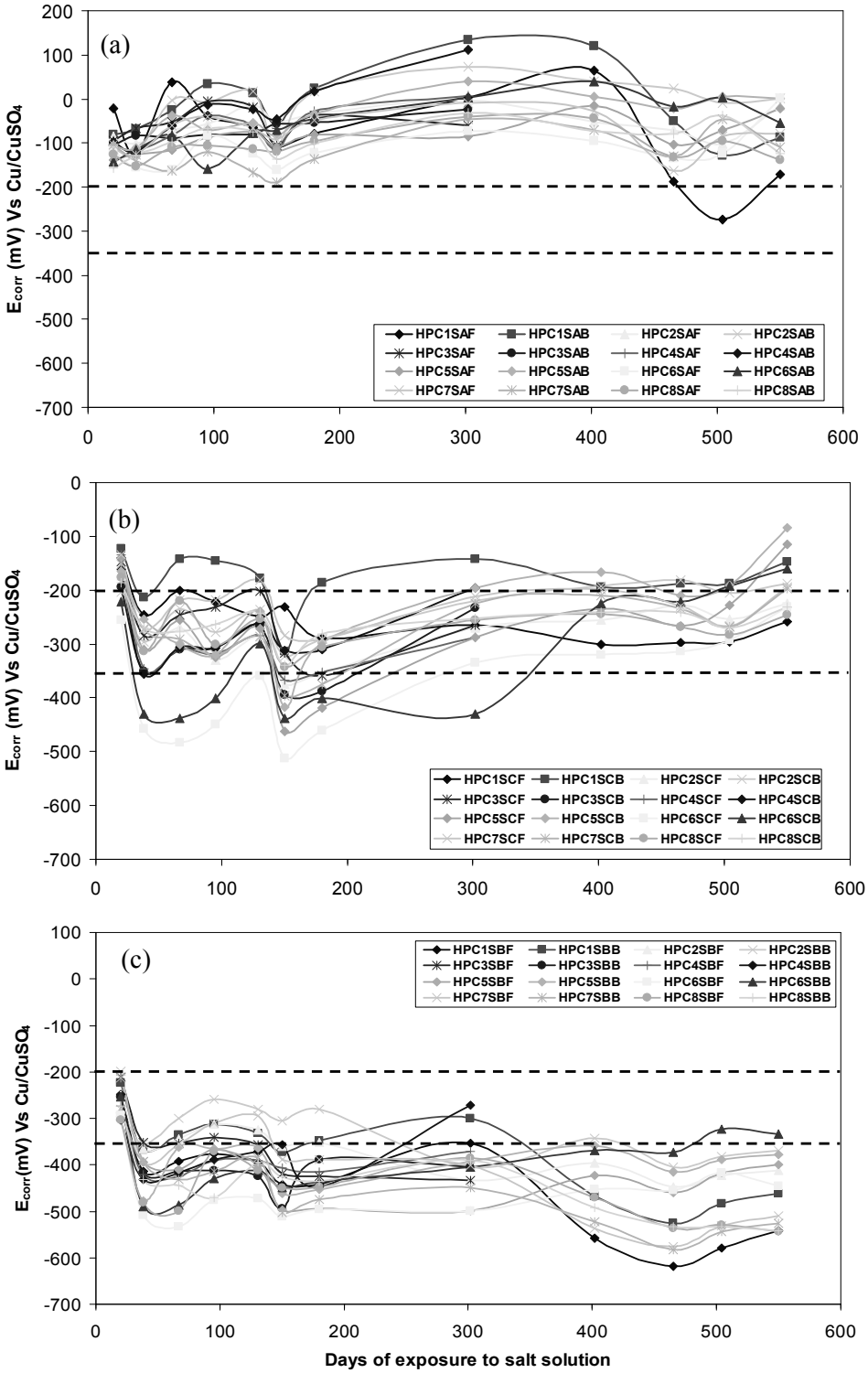

Figure 46: The corrosion potentials in the (a) non-submerged, (b) submerged and (c) cracked regions of the statically loaded HPC beams measured using the GalvaPulse^{TM}. Dashed lines represent limits designated by ASTM C876 [148].

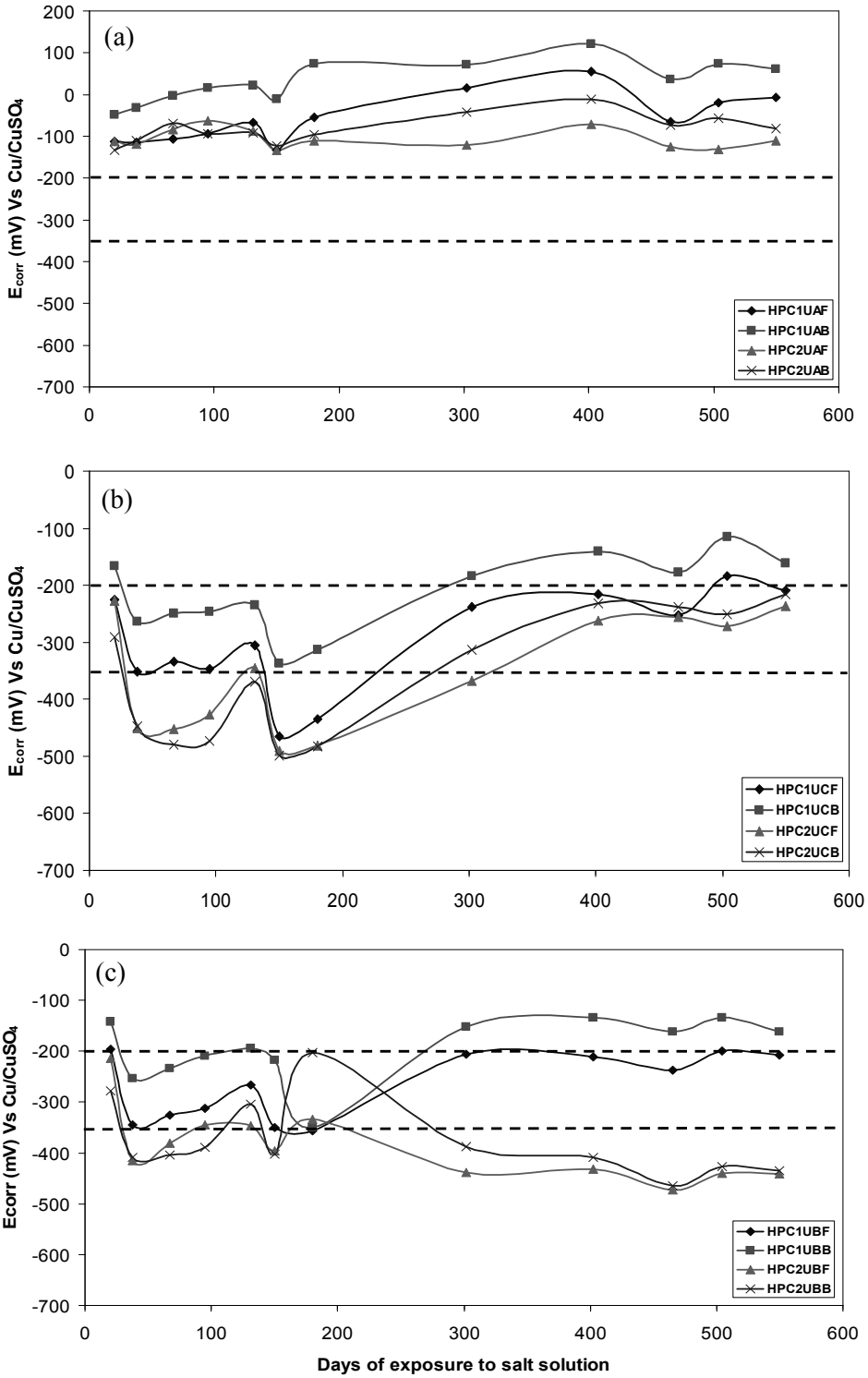

Figure 47: The corrosion potentials in the (a) non-submerged, (b) submerged and (c) cracked regions of the unloaded HPC beams measured using the GalvaPulse^{TM}. Dashed lines represent limits designated by ASTM C876 [148].

The corrosion potentials measured at the onset of LPR measurements in the OPCC beams (Figure 36-Figure 38) illustrated similar trends and values between the cracked and submerged regions of the concrete. The behaviour of the potentials in the non-submerged region was similar to that in the other two regions but the actual values were more positive. The potentials measured before galvanostatic pulse measurements (Figure 42-Figure 44) showed different values between the cracked and submerged regions but similar trends. Also, as in the LPR measurements, more positive potentials were observed in the non-submerged region than in the other two regions. A possible reason for similar potentials being observed at the onset of LPR measurements in the submerged and cracked regions of the beams was that the two regions were galvanically coupled and had established a couple potential. However, it is not known why the potentials differed in the two regions when measured before galvanostatic pulse. One reason could be that the dryness of the concrete was affecting the potential readings. During galvanostatic pulse measurements, the different sections of the beams were wetted with a sponge for 3-15 minutes before measurements were conducted. This meant that the amount of water received by each section varied along with the depth of the concrete the water had penetrated. The dryness of the concrete along with the crystallization of salt in the pores of the concrete may also have been responsible for the more positive potentials observed in the non-submerged regions.

Most rebars in the OPCC (Figure 36-Figure 38 and Figure 42-Figure 44) beams exhibited potentials below -350 mV vs $Cu/CuSO_4$ in the cracked and submerged regions, indicating a 90 % probability of corrosion according to ASTM C876. However, most of the rebars that were removed from the concrete had no signs of corrosion in the submerged region. There were some exceptions like OPC4SB (Figure 37 and Figure 43), which exhibited potentials that indicated a 10 % probability of corrosion after 120 days and 90 % probability of corrosion prior to this time. When this rebar was removed from the beam, it had no visible damage from corrosion. The reason for this behaviour of the OPC4SB is unclear and was not due to poor electrical connections or fluctuations in temperature. Hence, interpreting corrosion potentials according to ASTM C876 may not be a reliable method for predicting whether or not a rebar is actively corroding, particularly in the instances when passive bars are connected to actively corroding ones.

Potentials measured in the non-submerged region of the OPCC beams using the galvanostatic pulse technique (Figure 42-Figure 44) were more positive than -350 mV vs $Cu/CuSO_4$, while those measured using LPR (Figure 36-Figure 38) were mostly more negative than -350 mV vs $Cu/CuSO_4$. The differences in measurements were not due to the improper calibration of reference electrodes

used because they showed similar values for the cracked region. When some of the concrete beams were autopsied, no corrosion was observed in the non-submerged region. Both measurements seemed to be reasonable depending on how they were interpreted. One could argue that the potentials measured prior to LPR are more negative in the non-submerged region than those measured before galvanostatic pulse measurements because of galvanic coupling of this region to the cracked region. On the other hand, potentials measured before the initiation of galvanostatic pulse measurements were more positive because they were from the passive region. This further illustrated the complexities involved with half-cell measurements. In this project, potential measurements were accompanied by corrosion current measurements (Section 4.4.1.1) which enabled a more accurate prediction of the condition of the rebar in the three regions.

In HPC concrete beams, potentials of the steel measured before both LPR (Figure 39-Figure 41) and galvanostatc pulse measurements (Figure 45-Figure 47) in the submerged and cracked regions exhibited similar trends; however, the values were not always similar. The similar trends could be attributed to galvanic coupling between the two regions. However, the concrete, containing low porosity, may have had an influence on the potentials measured in the submerged region. As in the measurements for the OPCC, potentials measured before LPR measurements in the non-submerged region are higher than those measured prior to galvanostatic pulse measurements. However, as in the OPCC, half-cell potential measurements were supplemented by corrosion current measurements which illustrated a better prediction of the condition of the rebar in the three regions.

As expected, there was a correlation between the i_{corr} and E_{corr} in the beams. For example, in OPC4SBB, when E_{corr} became more positive (Figure 37(c)), the i_{corr} decreased as illustrated in Figure 48. In this project, a mathematical relationship between variations in i_{corr} with changing E_{corr} was not determined. However, in the future, it would be interesting to determine if such a correlation exists between the two.

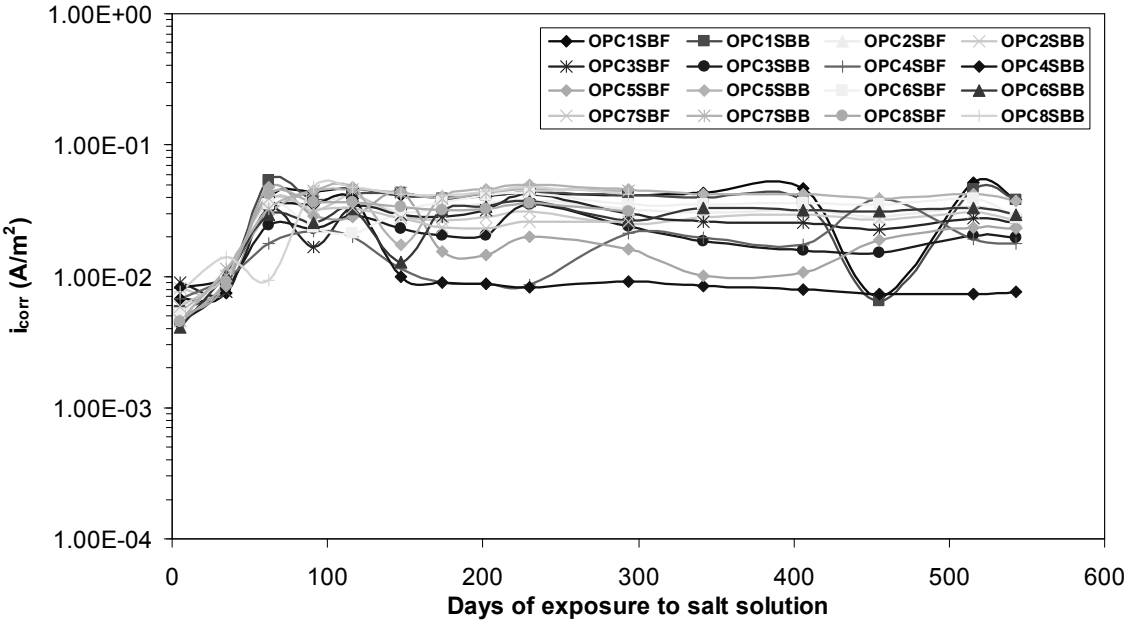

Figure 48: i_{corr} in the cracked region of the OPCC static beams.

4.4.2 Potentiodynamic Polarization Measurements

Because potentiodynamic (cyclic) polarization measurements took considerable time (~3.5 days) and the measuring equipment was available for a limited number of days, they were performed on five sections of each type of concrete after nine months of exposure: two each in the cracked sections of statically and dynamically loaded beams and one in the submerged region of a dynamically loaded beam. The measurements were made after the beams had been cut into three sections i.e. non-submerged, submerged and cracked. The notation used to denote the steel bars in the different sections of the beams has been described in Section 3.7 and is repeated here to make this section easier to follow: e.g. OPC2DCF, where the first three letters denote the type of concrete (e.g. OPC or HPC), the number denotes the beam number, which is followed by the type of loading applied to the beam (e.g. D for dynamic and S for static). The final letters represent the location of measurement (B for the cracked mid-section and C for the submerged region) and F (front) or B (back) denote the two rebars inside each beam.

Figure 49 illustrates the polarization curves for the rebar sections in the OPCC beams. It should be noted that the x-axis on this figure denotes current rather than current density in order to illustrate the negligible effect of corrosion observed in the epoxy-coated ends of some of the rebars on the measurements performed in the submerged region. According to the figure, OPC7SBB and

OPC1DCB portrayed lower currents than the other sections (OPC8SBF, OPC2DBB and OPC1DBF) when subjected to the same over-potentials. When the bars were removed from the beams, OPC7SBB, i.e. the cracked region of beam OPC7S, showed no signs of active corrosion (Figure 50) confirming the electrochemical measurements. On the other hand, OPC1DCB (i.e. the submerged region of beam OPC1D) had two regions of active corrosion: at the epoxy coated end and further along the rebar away from the measurement location but it is apparent that these areas did not contribute to the polarization curves. OPC2DBB, which is taken as a representative of the remaining sections, also illustrated a region of active corrosion where the measurement was performed. This region was the source of higher current observed in the cyclic polarization measurement.

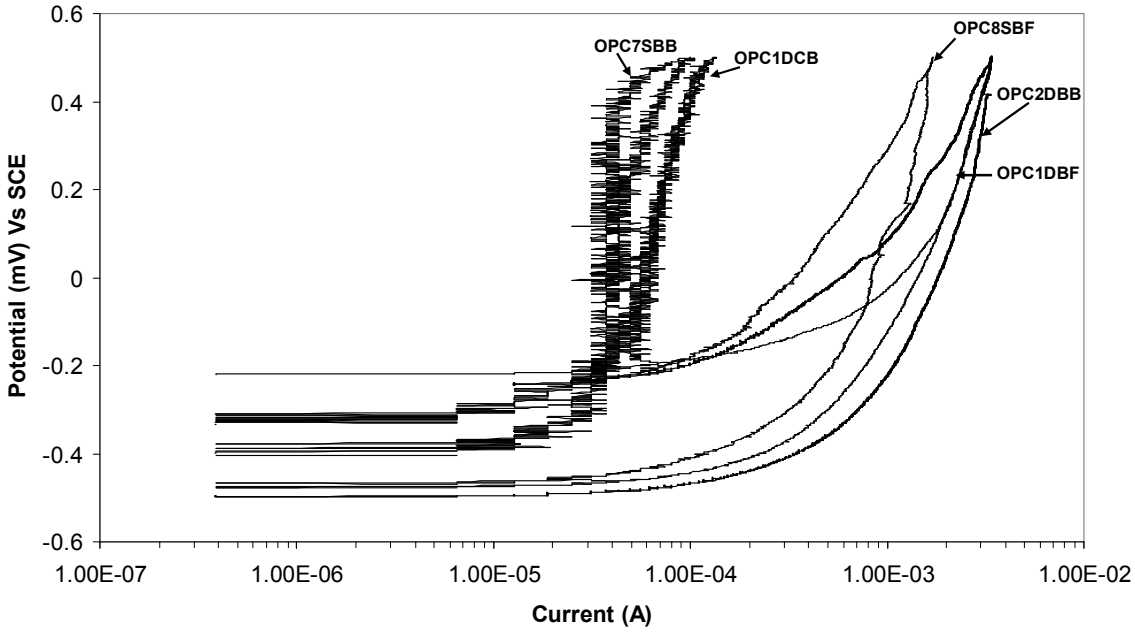

Figure 49: Currents resulting from the applied over-potentials in the OPCC sections.

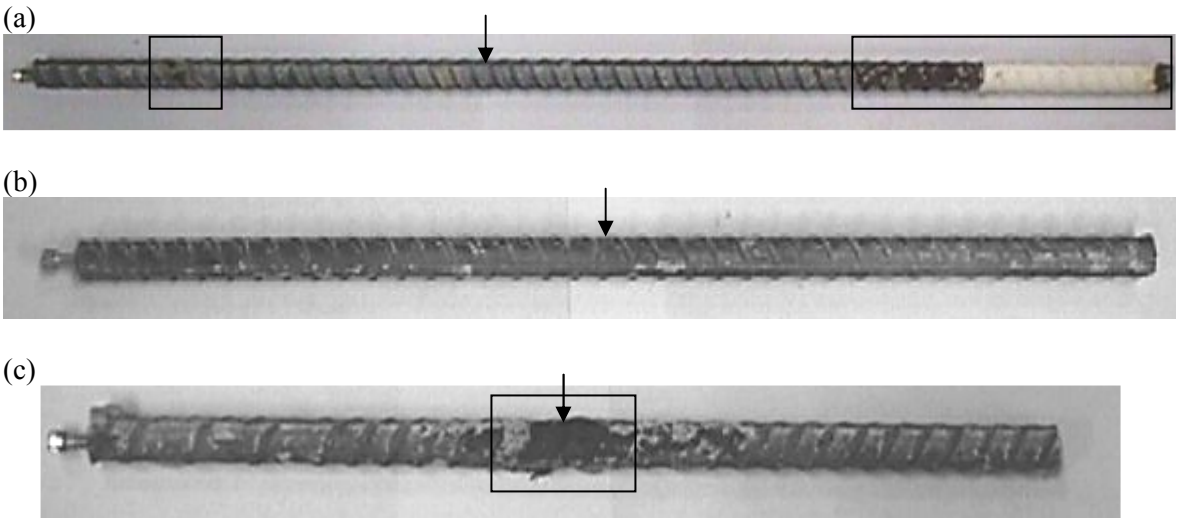

Figure 50: Rebar sections from the OPCC beams: (a) OPC1DCB (b) OPC7SBB and (c) OPC2DBB. Arrows illustrate the measurement locations and rectangles mark the corroding areas. Screws were inserted to make electrical connection with the bars easier.

The polarization curves for steel in OPCC and HPC, based on the actual corroding areas, are shown in Figure 51. An interesting thing to note is that, unlike in the OPCC, the curves for the actively corroding bars in HPC (HPC3SBB, HPC4SBF, HPC5DBB, HPC6DBB) do not exhibit a drop in current density at E_{corr}. This was probably because the high resistance of HPC did not allow the actual corrosion potential of the rebar to be determined on the concrete surface even in the cracked region. Hence, the range of potentials over which the rebar in HPC was polarized did not pass through the actual E_{corr} of the rebar, which was anticipated to be more negative than the starting potentials of the polarization curves. Even though the potentials were compensated for the IR drop through the concrete, the compensation would not have helped in determining the actual E_{corr} of the section. It may be argued that the presence of a crack filled with water would allow a more direct electrical contact for the actual potentials to be measured in HPC; however, potential field lines omitted by an actively corroding area on the rebar, which were detected during half-cell measurements, were not restricted to the crack and also passed through the concrete. Therefore, even in the cracked regions of the HPC, the concrete influenced the corrosion potentials. The OPCC did not exhibit the same effect because the concrete was more porous and the pores contained solution which conducted the potential field lines.

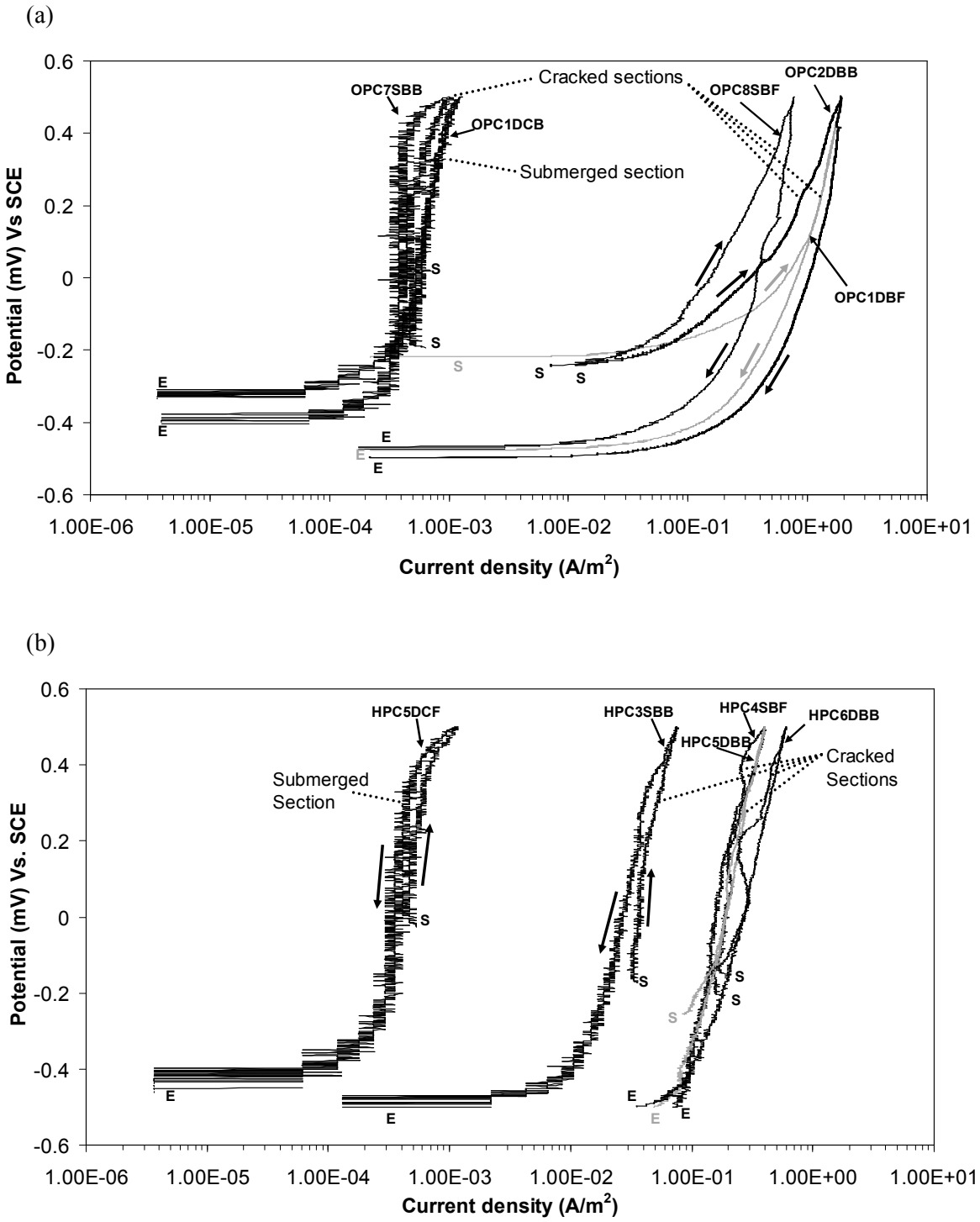

Figure 51: Polarization curves for the (a) OPCC and (b) HPC sections obtained after 9 months of exposure. S and E denote start and end points on the curves.

Figure 51 illustrates that, the steel in all the cracked sections except one, is undergoing active corrosion while that in the submerged sections is passive. The polarization curves for steel in the cracked OPCC sections show higher currents in the negative potential sweeps than in the positive ones while those for the steel in the cracked HPC exhibit the similar currents in both directions. This difference could be due to the higher porosity in the OPCC concrete than in the HPC, which would assist the crack in conducting ionic current. Also, in the cracked region, the current densities in the OPCC are slightly higher than in the HPC. This implies that HPC is more protective towards the rebar than the OPCC, which could be because of (a) higher resistance of the HPC concrete at the cracks and (b) accumulation of corrosion products along the rebar surface in HPC (as discussed in Section 4.5.1).

Approximate corrosion current densities (actual densities) for OPCC beams were determined by means of Tafel extrapolation from Figure 51(a) and are shown in Table 7. The current densities were not determined for the HPC beams because they did not exhibit actual E_{corr} of the reinforcing steel. The current densities obtained for cracked regions of OPCC by potentiodynamic polarization were lower than those obtained by LPR and galvanostatic pulse techniques (Section 4.4.1.1, Table 5). This is due to cyclic polarization having been performed after nine months of exposure in salt solution while the actual current densities using LPR and galvanostatic pulse techniques were obtained after eighteen months of exposure. The conditions in the beams would have changed over this time. In fact, the corrosion was superficial over the surface of the rebars at nine months, which was different from LPR and galvanostatic pulse measurements where the actual loss of rebar was observed.

Table 7: Corrosion current densities in the cracked region of OPCC determined from cyclic polarization measurements.

Beam Section	**Current Density (A/m^2)**
OPC1DBF	$2x10^{-2}$
OPC2DBB	$3x10^{-2}$
OPC7SBB	$3x10^{-4}$
OPC8SBF	$4x10^{-2}$

Cyclic potentiodynamic polarization curves obtained in the cracked region of an OPCC beam and an HPC beam after eighteen months of exposure are shown in Figure 52. It should be noted that the currents obtained from the polarization measurements were converted to current density using the polarized area determined for the LPR measurements (i.e. the surface area of 150 mm of rebar) because the rebars were not removed from the reinforced sections to determine the actual corroding area since the sections were used to examine the crack morphologies presented in Section 4.2. Also, the reverse scan on the HPC was not completed due to interruptions to the measurement by electrical

power surges. Figure 52 illustrates that that HPC was significantly more protective to steel than the OPCC even in the region of a major crack. Also, there was no concentration polarization observed in the scans, implying that the corrosion products were not affecting the supply of aggressive species to the steel. This figure also demonstrates that, for the HPC beam, the measurement starts at the half-cell potential of the beam i.e. the potential does not occur later on in the scan as explained for the curves in Figure 51. In Figure 51, the curves for HPC start out at more positive values than -350 mV vs $Cu/CuSO_4$, while, in Figure 21, the starting potential is more negative than -350 mV vs $Cu/CuSO_4$. This difference could be due to the change in the resistance of the concrete at the crack between nine and eighteen months due to the dynamic loading and exposure to salt solution.

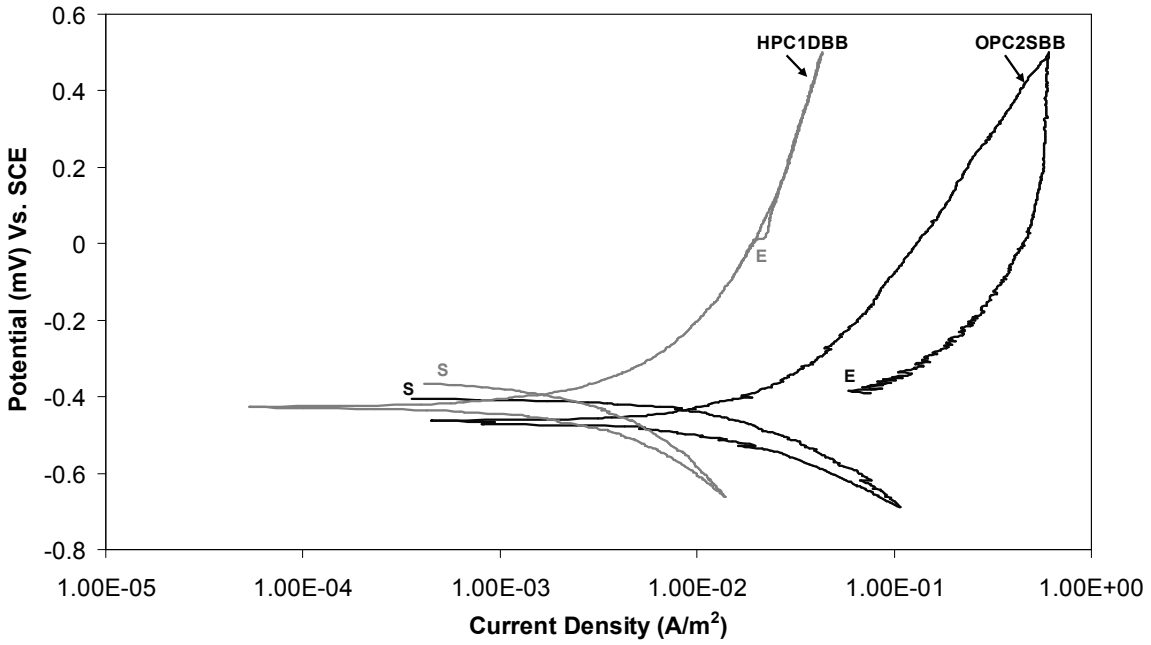

Figure 52: Potentiodynamic polarization in OPCC and HPC beams after 18 months of exposure to salt solution. S and E denote start and end points on the curves.

4.4.3 Electrochemical Noise

Electrochemical noise (ECN) measurements were conducted on the rebars in the beams after eight months of exposure to the salt solution. They involved measuring the current fluctuations between two rebars in the same beam. The bars were not polarized in ECN measurements. Also, the whole length of rebar was involved in the ECN measurement, which was not the case in LPR and

galvanostatic pulse measurements. Hence, electronic and ionic currents would flow from one bar to the other via the external electrical connection and the concrete, respectively.

Figure 53 illustrates the electrochemical current noise (ECN current) as a function of time for the dynamically loaded beams in the wet cycle and in the dry cycle over an 11 hour period. The measurements were initiated on the first day of the cycle. In Figure 53 (c), the application of dynamic loading can be observed in the ECN current measurements as noise in the data. This application of load was not captured in the other beams as it occurred after the data accumulation time. The wetting and drying of beams had a more significant impact on the dynamically loaded OPCC beams than HPC. In the former, the currents were generally higher in the wet cycle than in the dry cycle and curves also included more peaks. The peaks, whether in the direction of increasing current or decreasing current, indicated pit initiation and repassivation in the rebars. The direction of the peak indicated which of the two rebars in the beams was pitting. The wetting of concrete caused a higher macrocell current (the offset of the curve from zero) between the bars in the dynamically loaded OPCC beams than drying because the presence of solution enabled the ions to move easily from one bar to another, in the crack and in the concrete. This may also explain why the LPR measurements, that were carried out in the wet cycle, revealed higher corrosion currents particularly in the cracked region than the galvanostatic pulse measurements, which were made in the dry cycle. The higher overall current in the wet cycle could be due to the unprotected rebar at the cracks being submerged in solution and undergoing rapid corrosion while peaks could be caused by pitting in the rebar that was protected by the concrete (e.g. in the areas close to the crack which may have contained chlorides).

Higher ECN currents were also observed in the dynamically loaded HPC in the wet cycle than in the dry. However, the overall difference in currents was much lower than in the OPCC because of its higher resistance. Also peaks were not observed in the ECN current measurements in the HPC because, in the areas away from the crack, the concrete had low porosity and was resistant to the ingress of chlorides. Hence, it was highly protective towards the steel. The dynamically loaded HPC beam D-3 illustrated higher currents than the other beams because it had a casting defect in the submerged region which allowed the salt solution to penetrate into the concrete. This is shown in Figure 54.

(a) OPCC beams: wet cycle

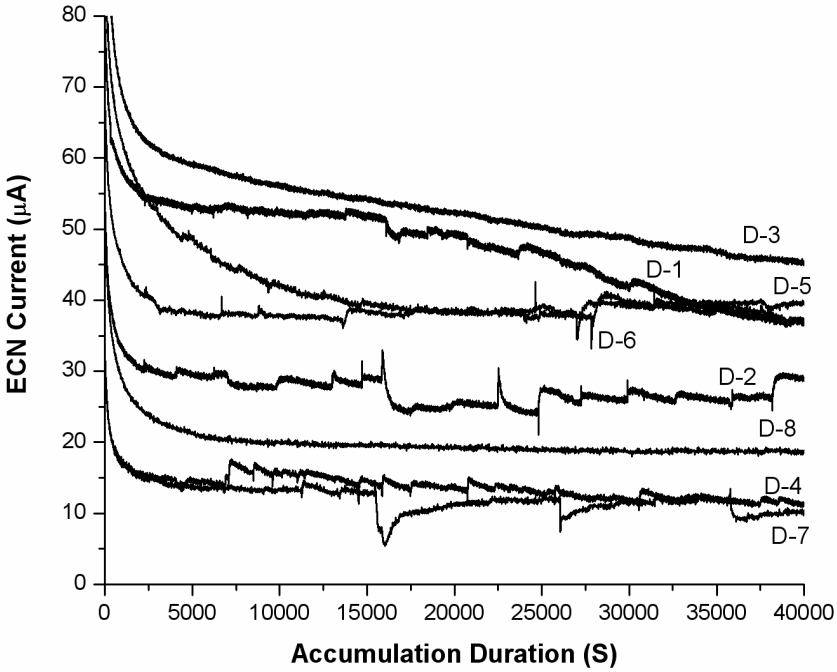

(b) OPCC beams: dry cycle

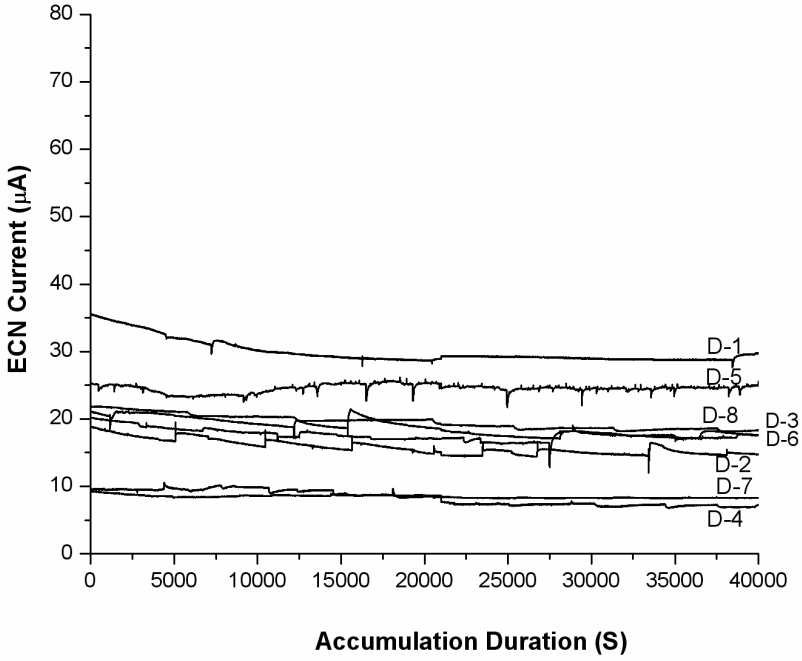

(c) HPC beams: wet cycle

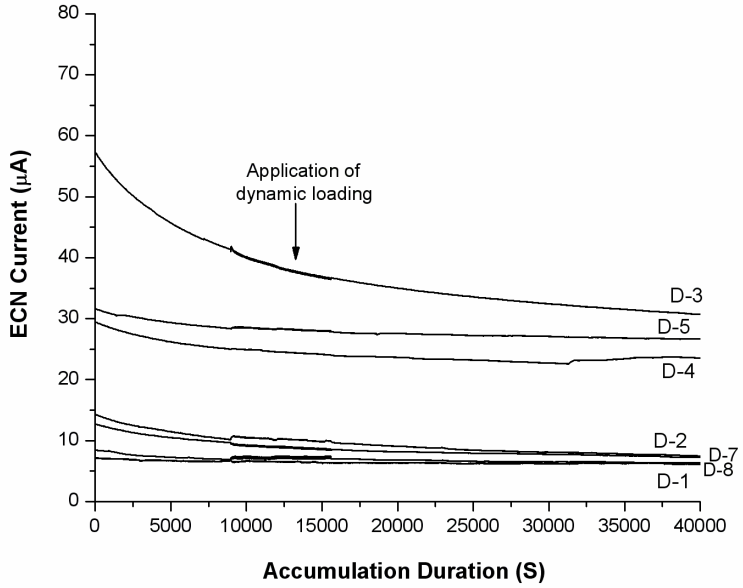

(d) HPC beams: dry cycle

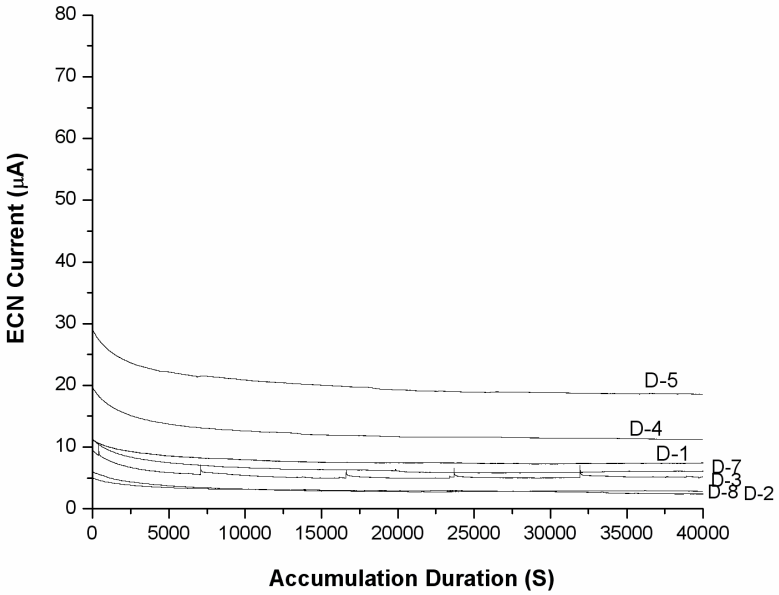

Figure 53: ECN measurements on dynamically loaded beams. (a) and (b) are for the OPCC beams in the wet and dry cycle, respectively and (c) and (d) illustrate the corresponding data for the HPC. Note that the beam numbers are indicated in the Figures as D-1 (i.e. dynamically loaded beam 1).

Figure 54: Encircled area shows corrosion products coming out of the casting defect in the submerged region of the dynamically loaded HPC beam 3.

With a few exceptions, there was very little difference in the ECN currents between the steel in the unloaded and statically loaded OPCC and HPC beams exposed to wetting and drying cycles (Figure 55). Wetting did have an influence on the macrocell currents but the effect was not as significant as in the dynamically loaded beams. The opening and closing of the cracks in the latter may have prevented corrosion products from blocking the path between the two rebars allowing easier current flow between the bars but the crack may have been blocked by the corrosion products in the unloaded and statically loaded beams. There is also less pitting of the steel in the unloaded and statically loaded OPCC than in the steel in the dynamically loaded OPCC because of the lower salt content at the steel in the former. As in the dynamically loaded HPC, pitting was not observed in the statically and unloaded HPC indicating that the concrete was protecting the steel where it was bonded to it

A comparison of the ECN data from the bars in OPCC and HPC beams, revealed that, regardless of the type of loading, the HPC was more protective when dealing with macrocell corrosion. In fact, the combination of dynamic loading and OPCC concrete was the most detrimental for macrocell corrosion of steel in cracked concrete while static loading applied to HPC concrete illustrated the lowest macrocell currents. Also, HPC beams under dynamic loading better protected the steel than OPCC beams subjected to no loading and static loading. These differences between static and dynamically loaded beams were not evident in LPR and galvanostatic pulse measurements because

(a) they were not as sensitive as ECN and (b) they were used to measure microcell currents, i.e. the resistance of the concrete did not play as large a role.

(a) OPCC beams: wet cycle

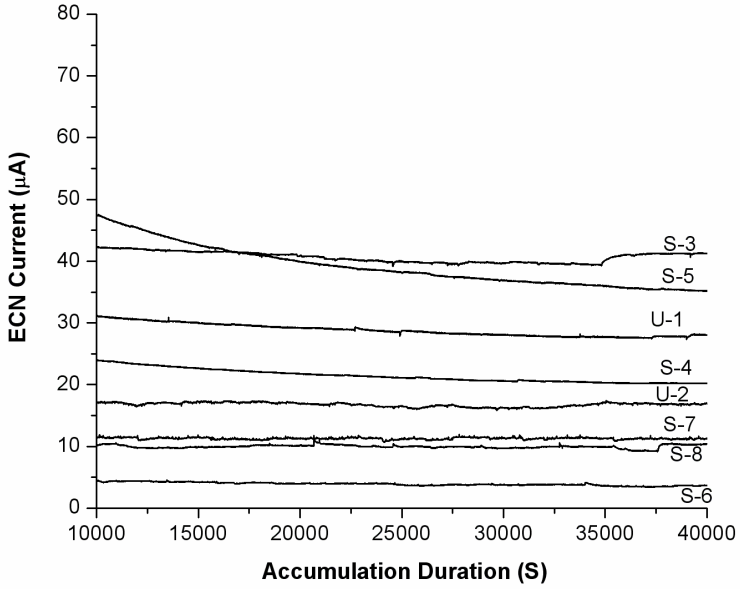

OPCC beams: dry cycle

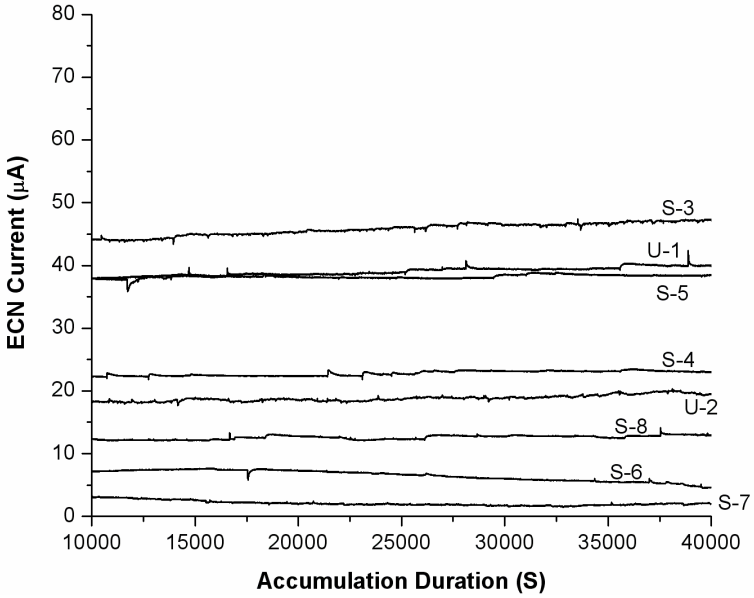

(c) HPC beams: wet cycle

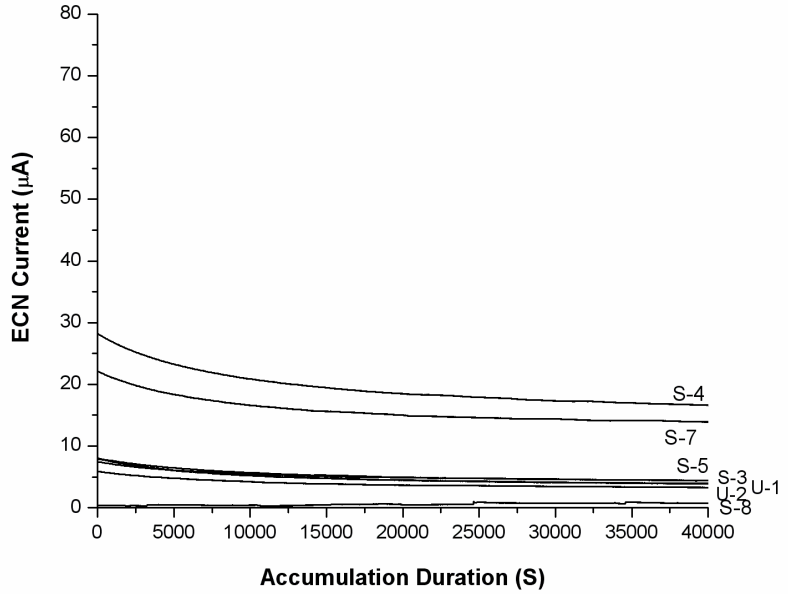

(d) HPC beams: dry cycle

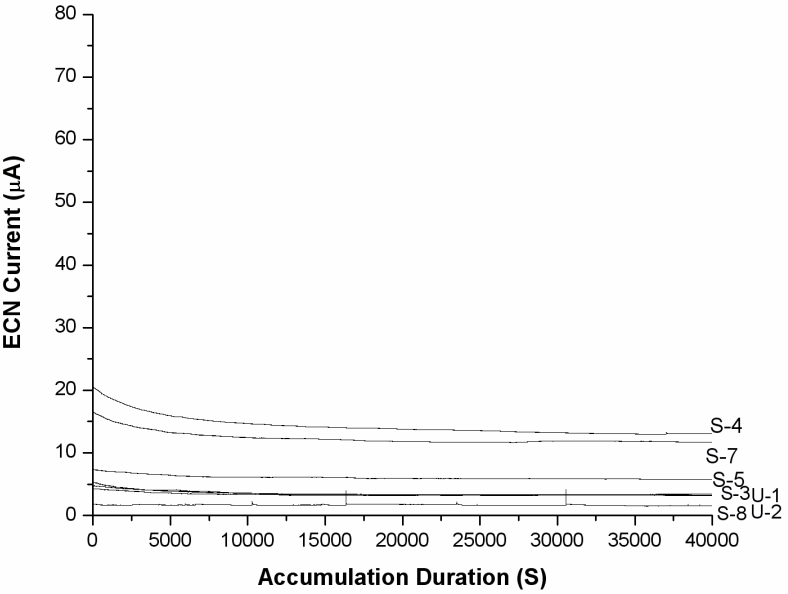

Figure 55: ECN measurements on unloaded and statically loaded beams. (a) and (b) are for the OPCC beams in the wet and dry cycle, respectively and (c) and (d) illustrate the corresponding data for the HPC. Note that the beam numbers are indicated in the Figures as S-3 (i.e. Statically loaded beam 3) and U-1 (i.e. unloaded beam 1).

4.4.4 Concrete Electrical Resistance

The concretes' electrical resistances in the non-submerged, cracked and submerged regions of some of the statically and dynamically loaded OPCC and HPC at three and nine months of exposure are presented in Table 8 and Table 9. The resistances were measured using various methods as described in Section 3.7. It is evident from the tables that the galvanostatic pulse technique performed using GalvaPulse™ gave higher values of resistance than when executed with Parstat 2263®. AC impedance, which was also implemented using Parstat 2263® gave similar results to the latter. The difference in resistances between the GalvaPulse™ and Parstat 2263® could be because of the use of the guard ring with the GalvaPulse™ [146]. This difference could be further enhanced by the condition of the concrete when the measurements were made. All GalvaPulse™ measurements and Parstat 2263® measurements in the non-submerged region were conducted in the dry cycle by (a) wetting the concrete with a sponge and (b) placing a wet sponge between the electrodes and the concrete during the measurements. The Parstat 2263® measurements in the cracked and submerged regions of the beams were performed in solution in the wet cycle.

As anticipated, all three measurement techniques showed that the resistances measured in the three sections of the OPCC beams were lower than those in their counterparts in HPC. Cracks were expected to have a negligible electrical resistance because they offer a direct path for ion migration between the reinforcing steel and the counter electrode. However, the resistance measurements were conducted over an extended area which included the crack. Hence, concrete surrounding the crack influenced resistance measurements and affected current and potential measurements.

Since the measurements in the non-submerged regions of the beams were conducted after wetting the concrete with a sponge, the resistances measured could be a function of the amount of wetting and the time after the wetting that the measurements were performed. This could be the reason why the measurements conducted in the non-submerged region of the OPCC beams with Parstat 2263® portrayed (in a majority of the cases) an increase in resistance from three to nine months for the dynamically loaded beams and a decrease for the statically loaded beams. A majority of resistance measurements in the non-submerged region of the HPC beams with the Parstat 2263® showed an increase from three to nine months of exposure. The porosity in HPC was expected to decrease with time in the HPC due to the inclusion of SCMs and the low w/cm which would have prevented complete hydration from occurring early on and, therefore, allowing for additional hydration later. This decrease in porosity could have had a more pronounced influence on the resistance measurements in HPC than the wetness of the concrete. The GalvaPulse™, on the other hand, showed

that the resistances in the non-submerged region of both concretes increased with exposure time. This behaviour was more intuitive for the HPC concretes as they were expected to harden (reduced porosity) over time, while the OPCC seemed to have reached their maximum hardening capacity at 28 days as illustrated in Section 4.1.

Table 8: The resistance of concrete in statically and dynamically loaded OPCC beams. NM denotes not measured.

	3 months of exposure			After 9 months of exposure		
Beam	**GalvaPulse™ Ω**	**Galvanostatic (Parstat) Ω**	**AC Imp. Ω**	**GalvaPulse™ Ω**	**Galvanostatic (Parstat) Ω**	**AC Imp. Ω**
OPC2DAF	1900	919	803	5700	1544	1292
OPC2DAB	2000	946	NM	5700	1483	1218
OPC3DAF	2100	879	817	4500	1019	879
OPC3DAB	2100	878	700	4500	NM	NM
OPC6DAF	2600	1486	1770	11000	1975	1692
OPC6DAB	2500	1468	1750	11000	NM	NM
OPC2DBF	1000	131	100	1200	92	80
OPC2DBB	1100	141	105	1300	94	80
OPC3DBF	1400	147	120	1300	101	82
OPC3DBB	1400	153	120	1300	94	80
OPC6DBF	1100	152	120	2600	101	88
OPC6DBB	1100	152	110	2500	110	97
OPC2DCF	2300	168	140	4700	155	124
OPC2DCB	2400	174	133	4700	152	127
OPC3DCF	2900	177	150	3900	174	138
OPC3DCB	3000	189	150	3900	168	134
OPC6DCF	1900	189	140	5200	189	146
OPC6DCB	1800	186	120	5100	196	151
OPC2SAF	8600	2270	2000	13000	1569	1380
OPC2SAB	8900	1880	1600	14000	1370	1086
OPC3SAF	3100	1338	1250	8900	1098	946
OPC3SAB	3100	NM	NM	8600	NM	NM
OPC8SAF	4900	NM	1000	10000	1319	3092
OPC8SAB	4900	1480	NM	10000	2578	2359
OPC2SBF	1400	170	90	3400	128	104
OPC2SBB	1500	200	100	3400	134	104
OPC3SBF	1300	230	85	2400	128	110
OPC3SBB	1300	190	100	2400	122	115
OPC8SBF	1500	140	110	2100	122	94
OPC8SBB	1500	170	100	2200	106	93
OPC2SCF	3900	220	160	5000	250	209
OPC2SCB	4100	190	160	4600	259	205
OPC3SCF	2300	260	190	4800	287	251
OPC3SCB	2200	270	200	5400	299	250
OPC8SCF	2300	240	160	4600	211	173
OPC8SCB	2400	210	160	4000	226	173

Table 9: The resistance of concrete in statically and dynamically loaded HPC beams. NM denotes not measured.

	After 3 months of exposure			After 9 months of exposure		
Beam	**GalvaPulse™ Ω**	**Galvanostatic (Parstat) Ω**	**AC Imp. Ω**	**GalvaPulse™ Ω**	**Galvanostatic (Parstat) Ω**	**AC Imp. Ω**
HPC2DAF	8900	4510	4500	15000	3080	2841
HPC2DAB	8900	NM	NM	16000	NM	NM
HPC6DAF	15000	4340	4100	NM	5429	6197
HPC6DAB	14000	4780	5500	NM	NM	NM
HPC7DAF	15000	5640	5200	18000	5359	5312
HPC7DAB	15000	7920	5500	18000	6390	6127
HPC2DBF	5500	450	440	5300	537	514
HPC2DBB	5700	480	460	5500	579	558
HPC6DBF	3700	400	370	NM	463	440
HPC6DBB	3600	390	360	NM	476	449
HPC7DBF	5100	490	480	7000	613	587
HPC7DBB	5000	480	450	6900	580	559
HPC2DCF	6500	860	800	9000	940	887
HPC2DCB	6700	910	830	9300	1080	1024
HPC6DCF	5500	980	730	NM	897	808
HPC6DCB	5100	770	700	NM	860	796
HPC7DCF	7300	800	860	13000	1169	1098
HPC7DCB	7200	920	900	13000	1093	1026
HPC2SAF	11000	1328	4000	36000	9216	8505
HPC2SAB	11000	7803	7300	38000	8262	8009
HPC3SAF	12000	5304	5300	18000	6378	6273
HPC3SAB	12000	NM	NM	18000	6201	6007
HPC4SAF	19000	4166	4700	30000	7394	7166
HPC4SAB	20000	NM	NM	30000	7181	7084
HPC2SBF	6000	520	498	7600	664	612
HPC2SBB	6200	560	516	8000	683	652
HPC3SBF	3500	461	442	5100	571	573
HPC3SBB	3200	470	444	4900	592	548
HPC4SBF	5900	483	455	6800	604	575
HPC4SBB	5500	463	436	6100	586	552
HPC2SCF	7600	522	487	8900	857	800
HPC2SCB	7900	544	508	9200	919	873
HPC3SCF	7000	458	440	10000	845	820
HPC3SCB	6800	455	429	9900	843	809
HPC4SCF	8200	476	350	8600	876	832
HPC4SCB	7900	409	350	8900	880	848

In the cracked and submerged regions of the OPCC beams, GalvaPulse™ demonstrated an increase in resistance from three to nine months of exposure, while measurements conducted using Parstat 2263® showed a decrease in the resistance for the dynamically loaded OPCC and a variable change (depending on whether AC impedance or galvanostatic pulse technique was used) in resistance for the statically loaded OPCC. It was difficult to determine which of the above was accurate because there were plausible explanations for both. It may be argued that the GalvaPulse™

gave an increase in resistance because the OPCC concrete had undergone further hardening over time due to being exposed to solution which decreased its porosity. However, it could also be that the concrete in the dynamically loaded OPCC had developed more cracking in which case the resistances from Parstat 2263® were accurate. Both types of equipments, however, illustrated that the cracked region in OPCC had lower resistance than the submerged region.

All the techniques showed that the resistances of the cracked and submerged regions of the HPC increased from three to nine months of exposure due to the increased hydration.

Based on the above, the values obtained for concrete resistances in reinforced structures should be analysed with caution and should be interpreted based on additional knowledge of the structure. Table 10 shows the averages and standard deviations of concrete resistances from the different techniques which can be used for the purpose of service life modelling.

Table 10: Average and standard deviations of resistances measured in the different sections of the dynamically and statically loaded OPCC and HPC beams. The numbers preceded by (3) and (9) denote values obtained after three and nine months of exposure, respectively.

	GalvaPule™ Ω		**Galvanostatic (Parstat) Ω**		**EIS Ω**	
Beam Section	**Average**	**Std Dev**	**Average**	**Std Dev**	**Average**	**Std Dev**
OPCC dynamic non-submerged	(3) 2200 (9) 7067	(3) 283 (9) 3094	(3) 1096 (9) 1505	(3) 296 (9) 391	(3) 1168 (9) 1270	(3) 542 (9) 334
OPCC dynamic cracked	(3) 1183 (9) 1700	(3) 172 (9) 660	(3) 146 (9) 99	(3) 9 (9) 7	(3) 113 (9) 85	(3) 9 (9) 7
OPCC dynamic submerged	(3) 2383 (9) 4583	(3) 469 (9) 567	(3) 181 (9) 172	(3) 9 (9) 18	(3) 139 (9) 137	(3) 11 (9) 11
OPCC static non-submerged	(3) 5583 (9) 10750	(3) 2583 (9) 2227	(3) 1742 (9) 1587	(3) 420 (9) 579	(3) 1463 (9) 1773	(3) 435 (9) 921
OPCC static cracked	(3) 1417 (9) 2650	(3) 98 (9) 592	(3) 183 (9) 123	(3) 31 (9) 10	(3) 98 (9) 103	(3) 9 (9) 9
OPCC static submerged	(3) 2867 (9) 4733	(3) 882 (9) 468	(3) 232 (9) 255	(3) 31 (9) 34	(3) 172 (9) 210	(3) 18 (9) 35
HPC dynamic non-submerged	(3) 12800 (9) 16750	(3) 3046 (9) 1500	(3) 5438 (9) 5064	(3) 1475 (9) 1404	(3) 4960 (9) 5119	(3) 631 (9) 1571
HPC dynamic cracked	(3) 4767 (9) 6175	(3) 903 (9) 900	(3) 448 (9) 541	(3) 44 (9) 61	(3) 427 (9) 518	(3) 50 (9) 61
HPC dynamic submerged	(3) 6383 (9) 11075	(3) 900 (9) 2226	(3) 873 (9) 1007	(3) 79 (9) 124	(3) 803 (9) 940	(3) 77 (9) 127
HPC static non-submerged	(3) 14167 (9) 28333	(3) 4167 (9) 8618	(3) 4650 (9) 7439	(3) 2686 (9) 1146	(3) 5325 (9) 7174	(3) 1420 (9) 964
HPC static cracked	(3) 5050 (9) 6417	(3) 1340 (9) 1280	(3) 493 (9) 617	(3) 39 (9) 46	(3) 465 (9) 585	(3) 33 (9) 40
HPC static submerged	(3) 7567 (9) 9250	(3) 554 (9) 575	(3) 477 (9) 870	(3) 49 (9) 28	(3) 427 (9) 830	(3) 67 (9) 27

4.5 CORROSION PRODUCTS

4.5.1 Extent of Corrosion on Rebar

Corrosion products were only found on the rebars at cracks in the concrete. The corroding spots on the rebars from some of the beams have been matched with the corresponding cracks in the concrete and are presented in Appendix D. The corroding areas were predominantly found at cracks below the solution level which provided easy access for the salt solution to reach the rebar. However, corrosion did not occur at all the submerged cracks. Based on the distribution of corrosion products on the rebar surface in Appendix D, it was deduced that corrosion initially started at one of the cracks before initiating at other cracks. In most cases, this crack was closest to where the maximum bending moment occurred due to the loading. It may be that the bifurcation / branching of the crack at this location had caused larger amounts of rebar to become unprotected compared to that in the remaining parts of the beams. Also, the bending could have induced cracking in the mill-scale which would have made it easier for the salt solution to reach the un-oxidized iron. There were some locations where the corrosion products were found on the steel at the non-submerged crack that was closest to the solution level. This was induced by salt solution which had reached this crack either by capillary suction through the pores of the concrete from the submerged region or by the meniscus effect in the gap at the de-bonded rebar-concrete interface.

Table 11 details the numbers of cracks in each beam and the corroded areas on each of the rebars contained in the beams. Figure 56 shows the number of corroded areas on beams containing different amounts of visible cracking. It should be noted that all the beams of the same concrete, regardless of the loading, have been attributed the same symbol in this plot. This means that there are over-lapping symbols in the figure. According to this figure, if the number of cracks in a beam was three or fewer for OPCC and four or fewer for HPC, the corrosion was usually confined to one crack. Similarly, Figure 57 shows that in OPCC and HPC concretes, the presence of two or more submerged cracks were likely to cause more than one corrosion spot on the rebar.

In the OPCC concretes, there was a tendency for the corrosion products at the rebar-concrete interface to remain in the vicinity of the crack (see Appendix D) while in the HPC the products tended to spread along the rebar away from the crack. This was due to the differences in the porosity of the concretes. Both OPCC and HPC beams had cracks bifurcating at the rebar-concrete interface and propagating parallel to the rebar; however, because OPCC was more porous than HPC, the corrosion products in the former accumulated in the concrete rather than spreading across the rebar

surface. In both concretes, the corrosion products were observed along the side of the rebar that was subjected to tensile loading and their accumulation may have led to further de-bonding at the interface.

Table 11: Numbers of cracks in the beams and corroded areas on the rebar. F and B denote front and back bars, respectively, in each beam.

Beam	Total number of visible (macro) cracks	Number of submerged cracks	Corroded areas on rebar	
OPC3D	5	3	F:2	B:2
OPC4D	5	3	F:1	B:3
OPC7D	4	2	F:1	B:1
OPC8D	5	2	F:2	B:2
OPC3S	3	2	F:1	B:1
OPC4S	1	1	F:1	B:0
OPC5S	5	3	F:1	B:3
OPC6S	2	1	F:1	B:1
OPC1U	2	2	F:1	B:1
OPC2U	4	3	F:4	B:2
HPC3D	2	2	F:1	B:1
HPC4D	2	2	F:2	B:2
HPC7D	5	3	F:4	B:4
HPC8D	5	3	F:4	B:4
HPC1S	3	2	F:1	B:1
HPC2S	4	3	F:1	B:1
HPC5S	8	5	F:1	B:3
HPC6S	5	3	F:2	B:2
HPC1U	6	5	F:3	B:2
HPC2U	6	4	F:2	B:2

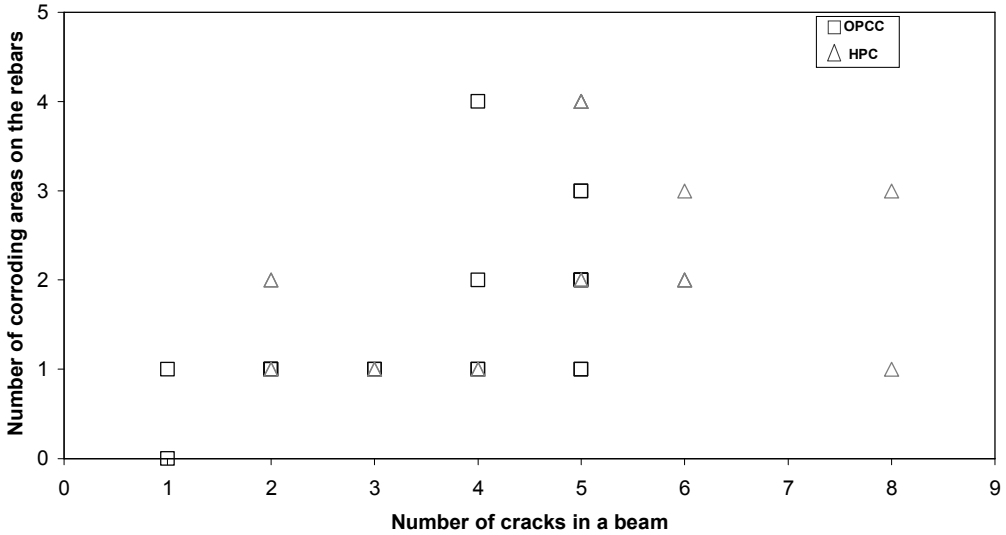

Figure 56: The number of cracks in a beam vs the number of corroding areas on the rebars.

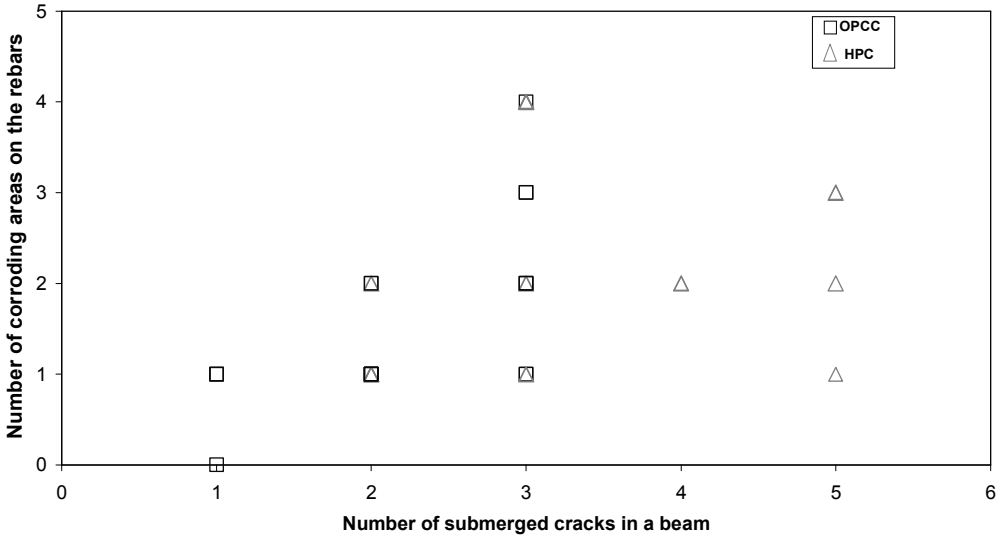

Figure 57: The number of submerged cracks in the beams vs the number of corroding areas on the rebars.

The surface areas of the portions of the rebar with a decreased cross-section (visible decrease prior to removing corrosion products) and the area over which the corrosion products spread (including the areas with decreased cross-sections) were measured and are presented in Table 12 and Table 13. In some cases it was relatively easy to distinguish between the two areas; however, this was not always the case, particularly in HPC, where the damage was very superficial i.e. the depth of corrosion was small. In this case, the damaged area was considered to be the same as the area over which the corrosion products had spread. The corroding sections of some bars were pickled in inhibited acid as per ASTM G1 [184] to remove corrosion products without dissolving the metal. The pickled sections illustrated non-uniform metal loss under the areas that were covered by corrosion products (Figure 58). Hence, the surface areas that were used for calculation of the actual corrosion current density (Section 4.4.1.1) were those covered by corrosion products and, in many cases, these were larger than the actual corroded area revealed after pickling.

In most of the OPCC dynamically and statically loaded beams, the corrosion at the cracks close to where the maximum bending moment was applied was localized and led to a loss in the cross-section of the steel as shown in Figure 59. However, in their counterparts in the HPC, the damage was superficial as illustrated in Figure 59 and there was no observable loss in the rebar cross-sections prior to pickling. Further away from the point of maximum bending moment, the corrosion on both OPCC and HPC was predominantly superficial. The mill-scale (20-50 μm thick) on the rebar with superficial corrosion appeared to be cracked. These results differ from those of Marcotte and Hansson

[142] who observed deeper, narrower channels of corrosion on rebars at cracks in HPC with fly ash and silica fume than in those in HPC containing only fly ash. However, their samples had been exposed to synthetic seawater for about four years.

Table 12: Surface areas of corrosion damage and the areas covered by corrosion products in OPCC.

Rebar	**Surface area of damaged portion (mm^2)**	**Area covered by corrosion products (mm^2)**
OPC3DF	Spot 1: 128 Spot 2: 88	Spot 1: 896 Spot 2: 88
OPC3DB	Spot 1: 300 (superficial) Spot 2: 134 (superficial)	Spot 1: 300 Spot 2: 134
OPC4DF	Spot 1: 134	Spot 1:532
OPC4DB	Spot 1: 50 Spot 2: 88 Spot 3: 88 (superficial)	Spot 1: 310 Spot 2: 488 Spot 3: 88
OPC7DF	Spot 1: 710 (superficial)	Spot 1: 710
OPC7DB	Spot 1: 656 (superficial)	Spot 1: 656
OPC8DF	Spot 1:70 Spot 2: 150	Spot 1: 532 Spot 2: 610
OPC8DB	Spot 1: 80 Spot 2: 88 (superficial)	Spot 1: 661 Spot 2: 88
OPC3SF	Spot 1: 568 (superficial)	Spot 1: 568
OPC3SB	Spot 1: 260	Spot 1: 1596
OPC4SF	Spot 1: 154	Spot 2: 444
OPC4SB	No corrosion	No corrosion
OPC5SF	Spot 1: 88	Spot 1: 661
OPC5SB	Spot 1: 24 (superficial) Spot 2: 118 Spot 3: 134 (superficial)	Spot 1: 24 Spot 2: 932 Spot 3: 332
OPC6SF	Spot 1: 62	Spot 1: 266
OPC6SB	Spot 1: 606 (very deep)	Spot 1: 907
OPC1UF	Spot 1: 887 (superficial)	Spot 1: 887
OPC1UB	Spot 1: 532 (superficial)	Spot 1: 532
OPC2UF	Spot 1: 266 (superficial) Spot 2: 132 (superficial) Spot 3: 354 (superficial) Spot 4: 36 (superficial)	Spot 1: 266 Spot 2: 132 Spot 3: 354 Spot 4: 36
OPC2UB	Spot 1: 354 (superficial) Spot 2: 178 (superficial)	Spot 1: 354 Spot 2: 178

Table 13: Surface areas of corrosion damage and the areas covered by corrosion products in HPC.

Rebar	Surface area of damaged portion (mm^2)	Area covered by corrosion products (mm^2)
HPC3DF	Spot 1: 166	Spot 1: 886
HPC3DB	Spot 1: 70	Spot 1: 1418
HPC4DF	Spot 1: 1418 (superficial) Spot 2: 166 (superficial)	Spot 1: 1418 Spot 2: 166
HPC4DB	Spot 1: 998 (superficial) Spot 2: 354 (superficial)	Spot 1: 998 Spot 2: 354
HPC7DF	Spot 1: 166 (superficial) Spot 2: 666 (superficial) Spot 3: 488 (superficial) Spot 4: 20 (superficial)	Spot 1: 166 Spot 2: 666 Spot 3: 488 Spot 4: 20
HPC7DB	Spot 1: 70 (superficial) Spot 2: 488 (superficial) Spot 3: 496 (superficial) Spot 4: 106 (superficial	Spot 1: 70 Spot 2: 488 Spot 3: 496 Spot 4: 106
HPC8DF	Spot 1: 443(superficial) Spot 2: 976 (superficial) Spot 3: 178 (superficial) Spot 4: 178 (superficial)	Spot 1: 443 Spot 2: 976 Spot 3: 178 Spot 4: 178
HPC8DB	Spot 1: 620 (superficial) Spot 2: 887 (superficial) Spot 3: 132 (superficial) Spot 4: 42 (superficial)	Spot 1: 620 Spot 2: 887 Spot 3: 132 Spot 4: 42
HPC1SF	Spot 1: 2396 (superficial)	Spot 1: 2396
HPC1SB	Spot 1: 1182 (superficial)	Spot 1: 1182
HPC2SF	Spot 1: 886 (superficial)	Spot 1: 886
HPC2SB	Spot 1: 886 (superficial)	Spot 1: 886
HPC5SF	Spot 1: 708 (superficial)	Spot 1: 708
HPC5SB	Spot 1: 118 (superficial) Spot 2: 354 (superficial) Spot 3: 106 (superficial)	Spot 1: 118 Spot 2: 354 Spot 3: 106
HPC6SF	Spot 1: 177 (superficial) Spot 2: 88 (superficial)	Spot 1: 177 Spot 2: 88
HPC6SB	Spot 1: 248 (superficial) Spot 2: 319 (superficial)	Spot 1: 248 Spot 2: 319
HPC1UF	Spot 1: 18 (superficial) Spot 2: 106 (superficial) Spot 3: 44 (superficial)	Spot 1: 18 Spot 2:106 Spot 3: 44
HPC1UB	Spot 1: - Spot 2: -	Spot 1: few dots Spot 2: few dots
HPC2UF	Spot 1: 792 (superficial all around) Spot 2: 44 (superficial)	Spot 1: 792 Spot 2: 44
HPC2UB	Spot 1: 932 (superficial) Spot 2: 44 (superficial)	Spot 1: 932 Spot 2: 44

(a)

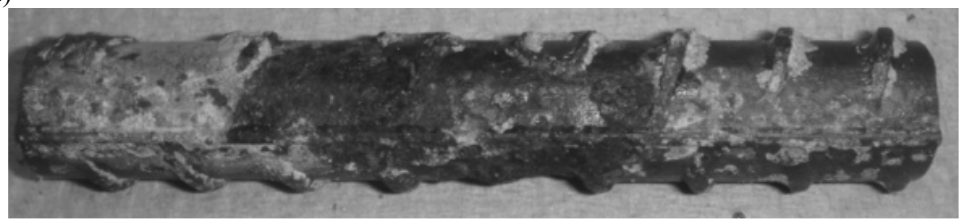

(b)

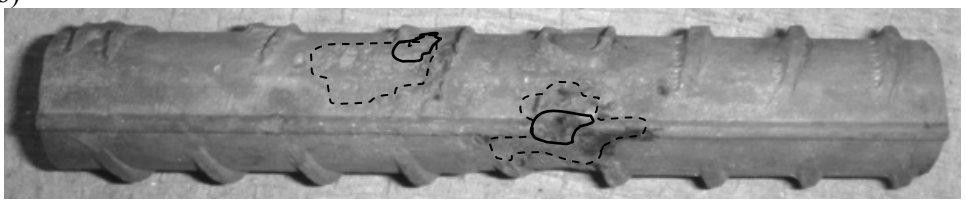

Figure 58: A section of rebar (a) after removal from the beam and (b) after pickling. The areas enclosed by the dashed line were 'shallow craters' (maximum depth of loss after pickling was 0.07 mm) whereas those in the solid lines were 'deep craters' (maximum depth of loss after pickling was 1.18 mm).

(a) Dynamically loaded OPCC:

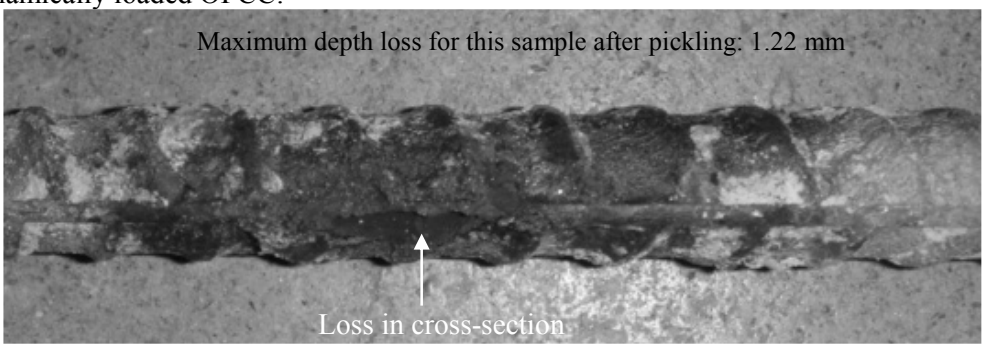

(b) Statically loaded OPCC:

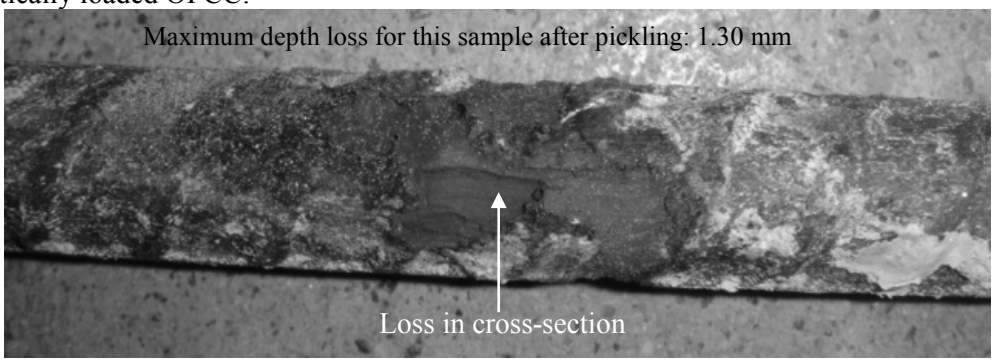

(c) Dynamically loaded HPC:

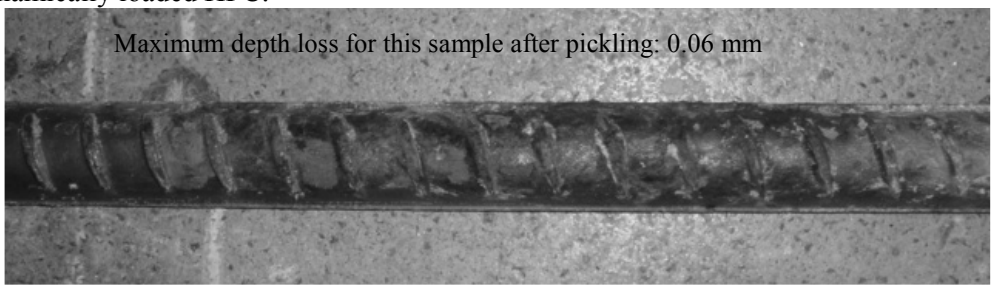

(d) Statically loaded HPC:

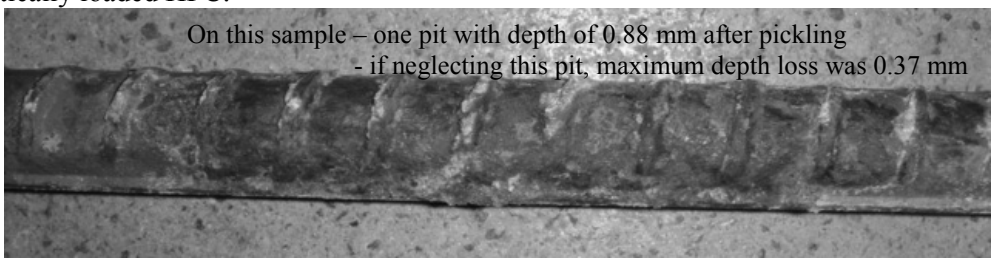

Figure 59: Examples of the type of damage encountered in (a) dynamically loaded OPCC (b) statically loaded OPCC (c) dynamically loaded HPC and (d) statically loaded HPC.

4.5.2 Distribution of Corrosion Products in Concrete

The distribution of corrosion products in the concrete in and around the mid-section cracks in the beams was visually inspected while grinding away layers in 2 to 3 mm increments. The maximum depth of penetration into the concrete by grinding was 21 mm, which was approximately 9 mm from the rebar surface; hence, the distribution of the corrosion products in the concrete close to the rebars was not examined.

Examples of the corrosion in the crack in the statically loaded OPCC are shown in Figure 60. Also, the corrosion products diffused from the crack into the aggregate-cement paste interface as indicated in Figure 60(b). This phenomenon may lead to detachment of the aggregate-paste bond. However, there were significantly fewer instances of this happening in the statically loaded OPCC beams than in the dynamically loaded OPCC beams. This is probably because, under dynamic loading, the loading would have opened up the interface and created free space for corrosion products to easily diffuse into. As a result, corrosion products in the statically loaded OPCC were generally confined to the crack, as shown in Figure 60. Multi-coloured aggregates (Figure 60(b)) were also observed at the cracks in the beams and should not be confused with corrosion products. In the dynamically loaded OPCC beams, the corrosion products not only diffused from the cracks into the

aggregate-paste interfaces, but also into the cement paste as illustrated in Figure 61. Where this occurred, cracking was also observed as indicated in Figure 61 (a). As will be illustrated in Section 4.5.3, the mid-section crack in OPCC dynamically loaded beams had a higher accumulation of corrosion products than in the other beams. The accumulation of products in the crack is likely to force them to penetrate into the interconnected porosity. However, the products cannot move easily through the bottle-necks of the capillary pores and result in accumulation of large amounts of corrosion products, exerting stresses on the pore walls causing the paste to crack. This situation is also likely to occur in the statically loaded OPCC if there are large amounts of corrosion products deposited in the cracks.

In the statically loaded HPC beams, corrosion products were not observed at any depth from the surface; however, there was crystallization of salt in the crack due to the evaporation of water from the salt solution contained in it. Figure 62 illustrates images of cracks from the statically loaded HPC concretes. The fact that corrosion products were not observed in these beams does not mean that they did not exist. As discussed in Section 4.5.1, the products in these beams tended to accumulate at the rebar-concrete interface.

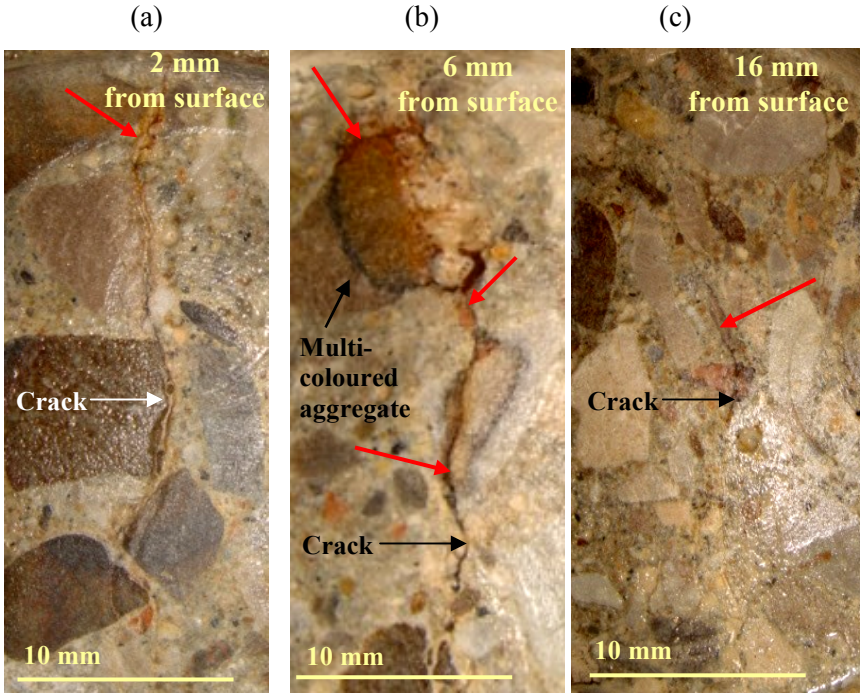

Figure 60: Corrosion products in the statically loaded OPCC beams. Note the multi-coloured aggregate in (c). Red arrows point to the location of visible products. Photographs (a) and (b) were obtained from OPC7S and photograph (c) was obtained from OPC8S

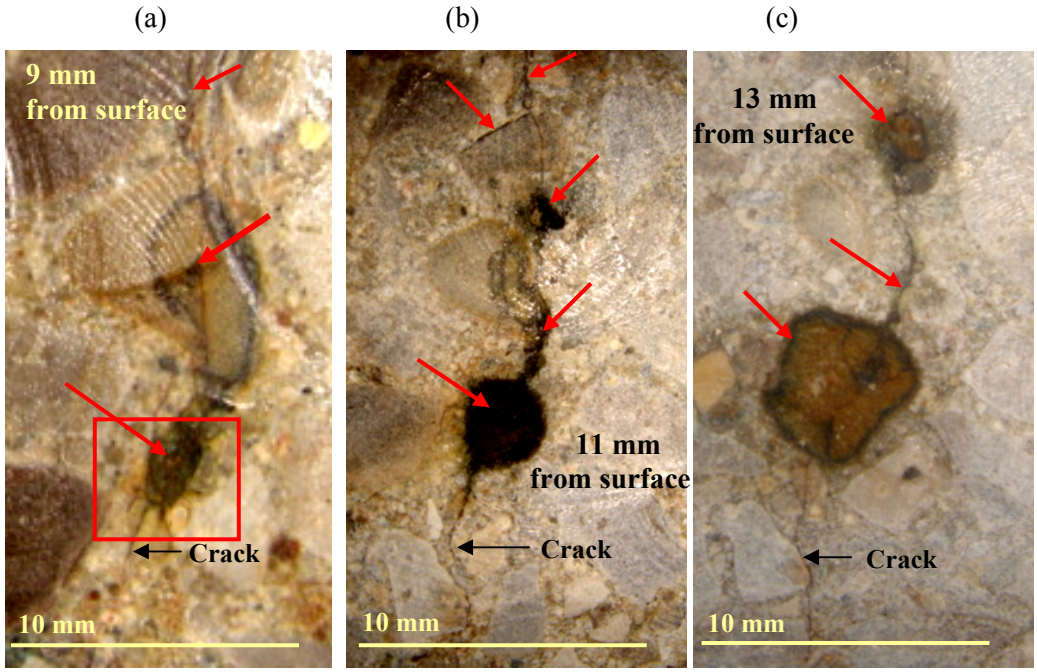

Figure 61: Distribution of corrosion products in the dynamically loaded OPCC concretes. Red arrows point to the location of visible products. The protruding cracks in the square region in (a) may have been formed because of the accumulation of corrosion products. Photographs shown are from OPC1D.

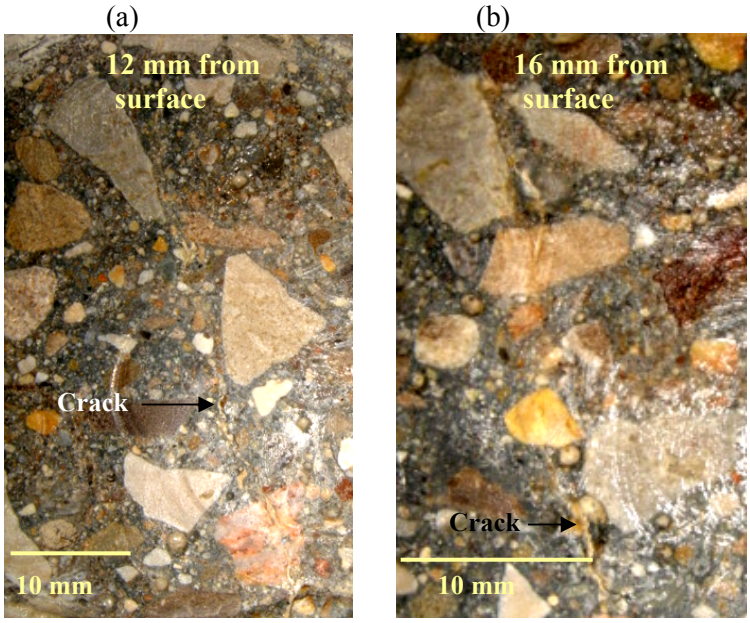

Figure 62: Cracks in statically loaded HPC beams with no corrosion products. Photographs were obtained from HPC3S.

In contrast, corrosion products were seen in the cracks in the dynamically loaded HPC beams as shown in Figure 63; however, unlike those in the OPCC, they did not penetrate into the adjacent concrete. In Figure 63(a), corrosion products can be observed inside an entrapped air void, which was intercepted by the crack. Figure 63(b) and (c) show branched cracks in which the products had accumulated. Dynamically loaded HPC beams have significantly more corrosion products at the cracks than the statically loaded HPC due to the opening and closing of the cracks which allows the solution to carry some of the products away from the rebar. Corrosion products tend to accumulate in the free space that is available to them. Hence, the low amount of interconnected capillary porosity in HPC can be both an advantage and a disadvantage when it comes to accommodating corrosion products. The advantage is that the products will not disperse into the concrete if empty spaces are available for them to diffuse into. However, the drawback is that, if such spaces are not available, the forces caused by the accumulation of these products can cause cracking in the concrete. The corrosion products are most likely responsible for the branched cracking shown in Figure 63(b) and (c).

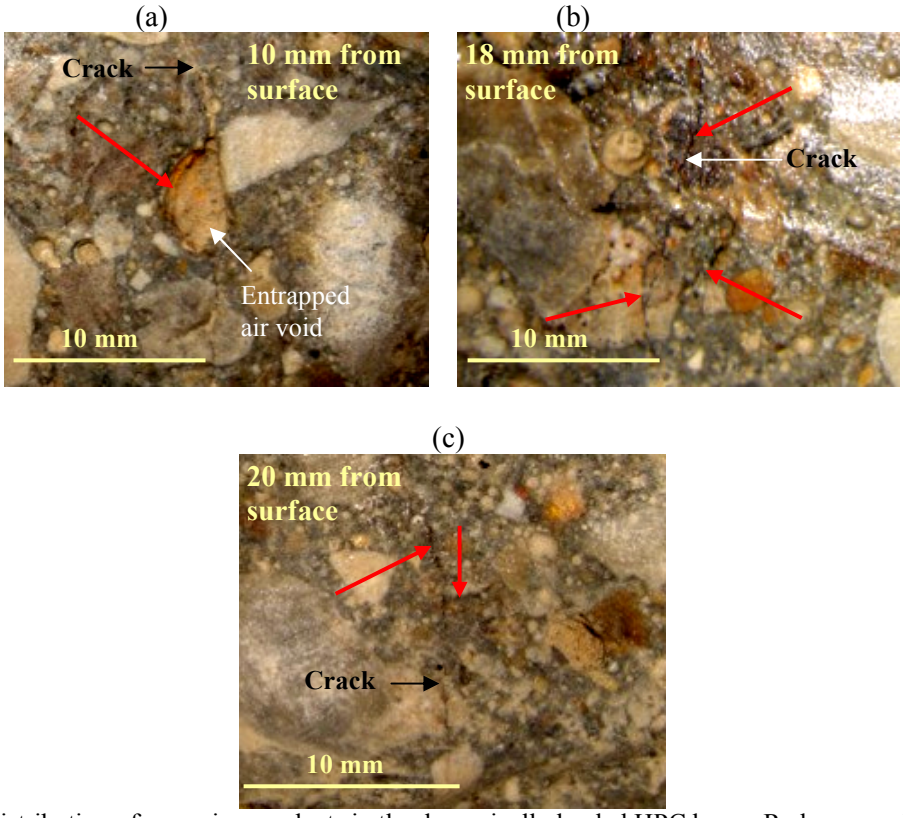

Figure 63: Distribution of corrosion products in the dynamically loaded HPC beam. Red arrows show the location of visible corrosion products. Photographs were obtained from HPC6D.

Based on these observations, HPC is less prone to cracking caused by corrosion products than OPCC because of its higher strength. However, if the stresses exerted by the corrosion products exceed this strength, then HPC will also crack. This situation will most likely be encountered at the rebar-concrete interface in the HPC where the products tend to accumulate as illustrated in Section 4.5.1.

4.5.3 Identification of Corrosion Products

The identification of the corrosion products on the rebar surfaces where they intersect macrocracks at the mid-section of the concrete beams and on the concrete surfaces that form the walls of the macrocracks (illustrated in Figure 64) is discussed in this section. Corrosion products on the rebar surface are presented first and are followed by corrosion products on the crack walls.

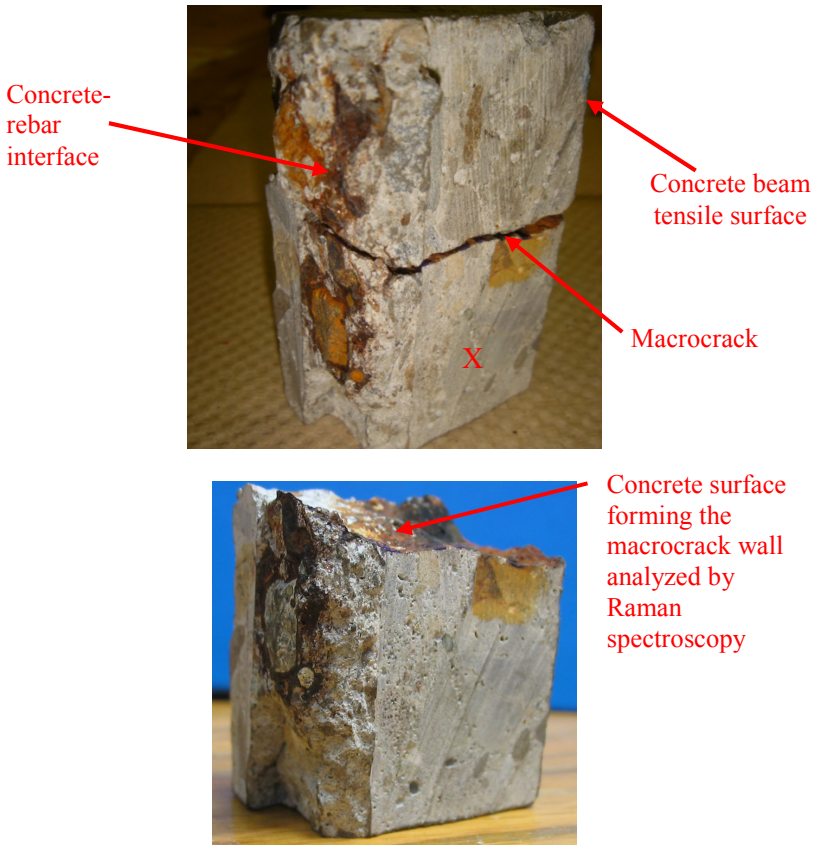

Figure 64: (a) A photograph of a section of dynamically loaded OPCC beam showing the macrocrack and the location of the rebar and (b) shows the section labelled X in (a). The concrete surface forming the crack wall is identified in (b).

The identification of corrosion products was conducted on the surfaces of the rebar that were directly intercepted by a crack i.e. on the rebar surfaces indicated by (i) in Figure 65 and Figure 66. The spatial extent of corrosion on the rebar surfaces was discussed in Section 4.5.1.

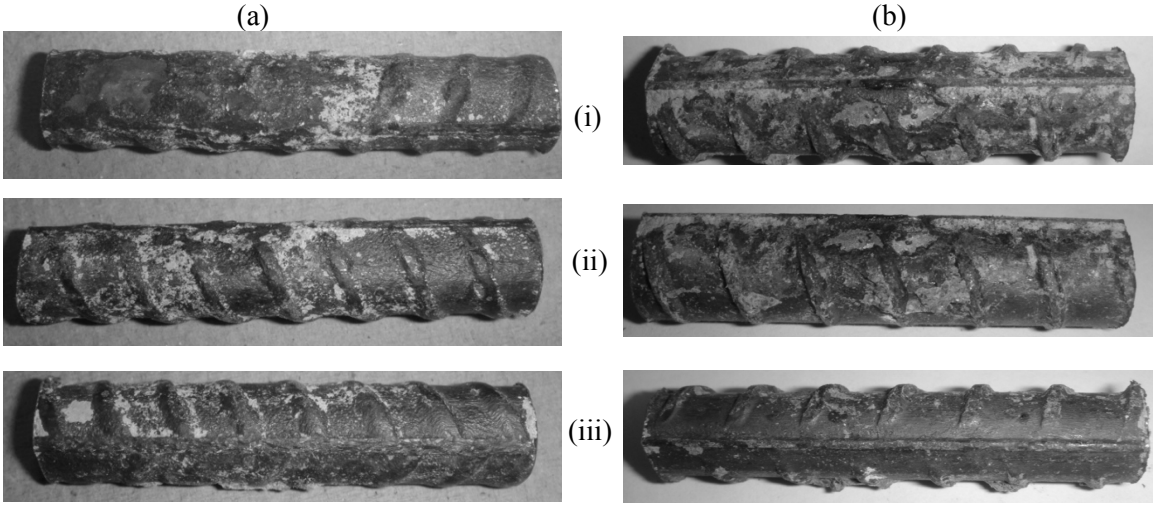

Figure 65: The distribution of corrosion products on the 5 cm section of rebar surfaces from the cracked region in (a) statically loaded OPCC and (b) statically loaded HPC beams. (i) shows the surface of rebar that was intersected by the crack (tensile side), (ii) illustrates the rebar surface 90^{o} away from where the crack intersected it and (iii) displays the surface on the reverse side of the rebar i.e. the side which is not in contact with the crack in this particular case.

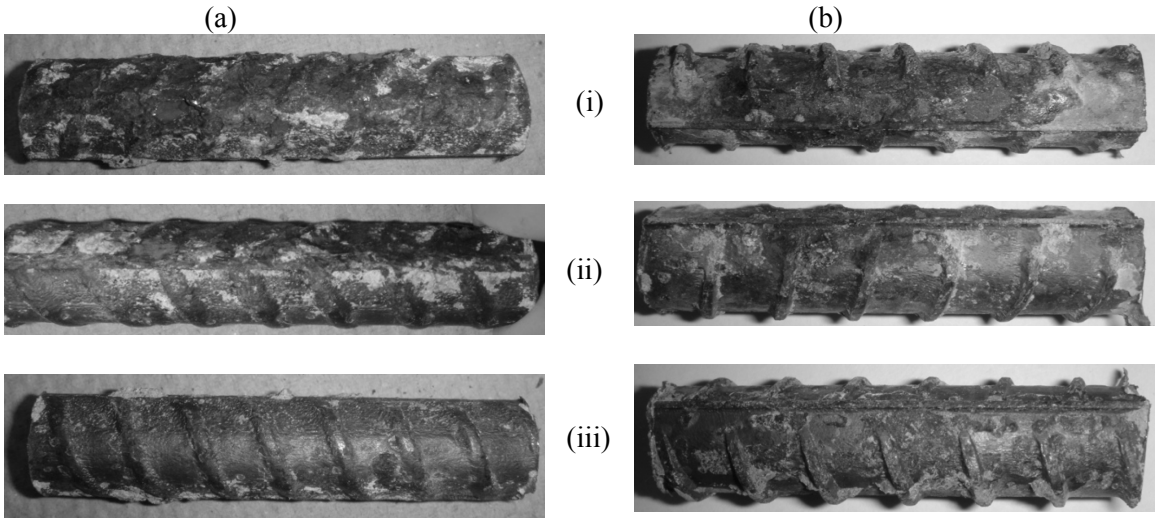

Figure 66: The distribution of corrosion products on the 5 cm section of rebar surfaces from the cracked region in (a) dynamically loaded OPCC and (b) dynamically loaded HPC beams. The (i), (ii) and (iii) denotations are the same as for Figure 5.

The area sampled by the Raman laser was approximately 5 μm in diameter and 3 μm in depth [185]. The Raman spectra for different locations on the surface of the rebars in the OPCC statically loaded beam and dynamically loaded beam are shown in Figure 67 and Figure 68, respectively. The spectra for the corresponding rebars in the HPC beams are given in Figure 69 and Figure 70. Each figure contains multiple plots corresponding to different locations on the same bar. Some of the plots have a logarithmic scale for the y-axes due to the large range of intensity. The peaks corresponding to corrosion products and concrete components have been identified in the figures by dashed, vertical lines. Each line has been attributed a letter which denotes the compound responsible for the peak. The nomenclature used is indicated in Table 14. It should be noted that, in some cases, two compounds had very close or even identical Raman shifts (e.g. 245 cm^{-1} for hematite and goethite [186]). In such cases, the compound for which there were other peaks in the spectrum, was attributed this shift and, if two compounds had other peaks in the spectrum, then both were assigned the peak. Table 15 identifies the literature sources that were used to characterize the peaks. It should be noted that most studies that have paired Raman peaks to the corresponding iron corrosion products have only examined Raman shifts between 200 and 800 cm^{-1}. This made it difficult to identify peaks with shifts outside this range.

Table 14: Nomenclature for the compounds identified in Figure 67-Figure 70.

Identification Letter	Compound (Chemical Formula)	Specific Volumes [95]
A	Akaganeite (β-FeOOH)	3.54
C	Calcium carbonate ($CaCO_3$)	-
CH	Calcium hydroxide ($Ca(OH)_3$)	-
F	Feroxyhite (δ-FeOOH)	2.87
F2	Ferrous Hydroxide ($Fe(OH)_2$)	3.75
F3	Ferric Hydroxide ($Fe(OH_3$)	4.00
G	Goethite (α-FeOOH)	2.93
H	Hæmatite (α-Fe_2O_3)	2.12
L	Lepidocrocite (γ-FeOOH)	3.14
m	Magnesium carbonate ($MgCO_3$)	-
M	Magnetite (Fe_3O_4)	2.10
MG	Maghemite (γ-Fe_2O_3)	2.29

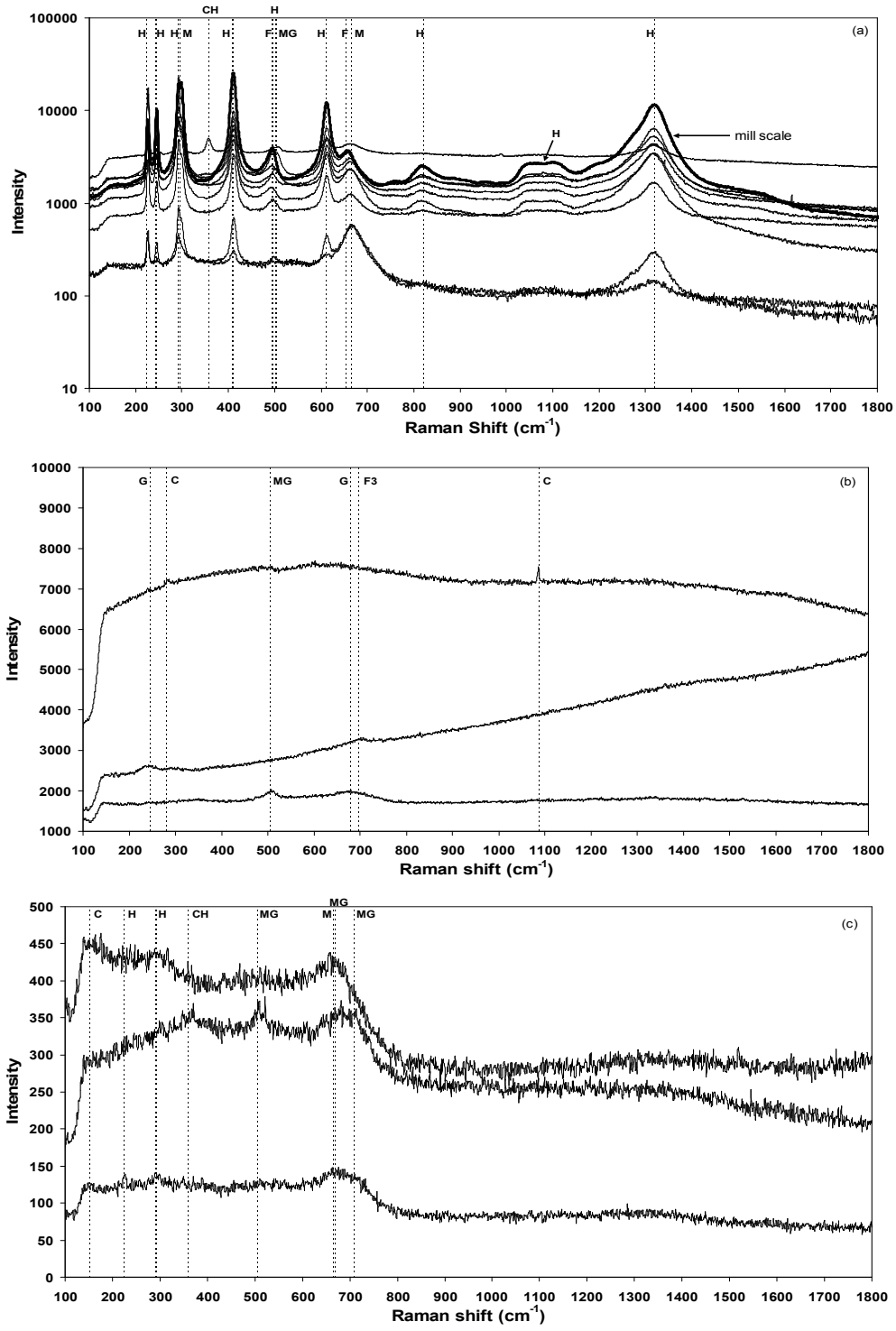

Figure 67: Raman spectra obtained from the rebar surface in the statically loaded OPCC beam. (a) is from a region on the bar with obvious corrosion products (including mill-scale); (b) is from a region with little corrosion and (c) is from a region with some cement paste adhered to the surface.

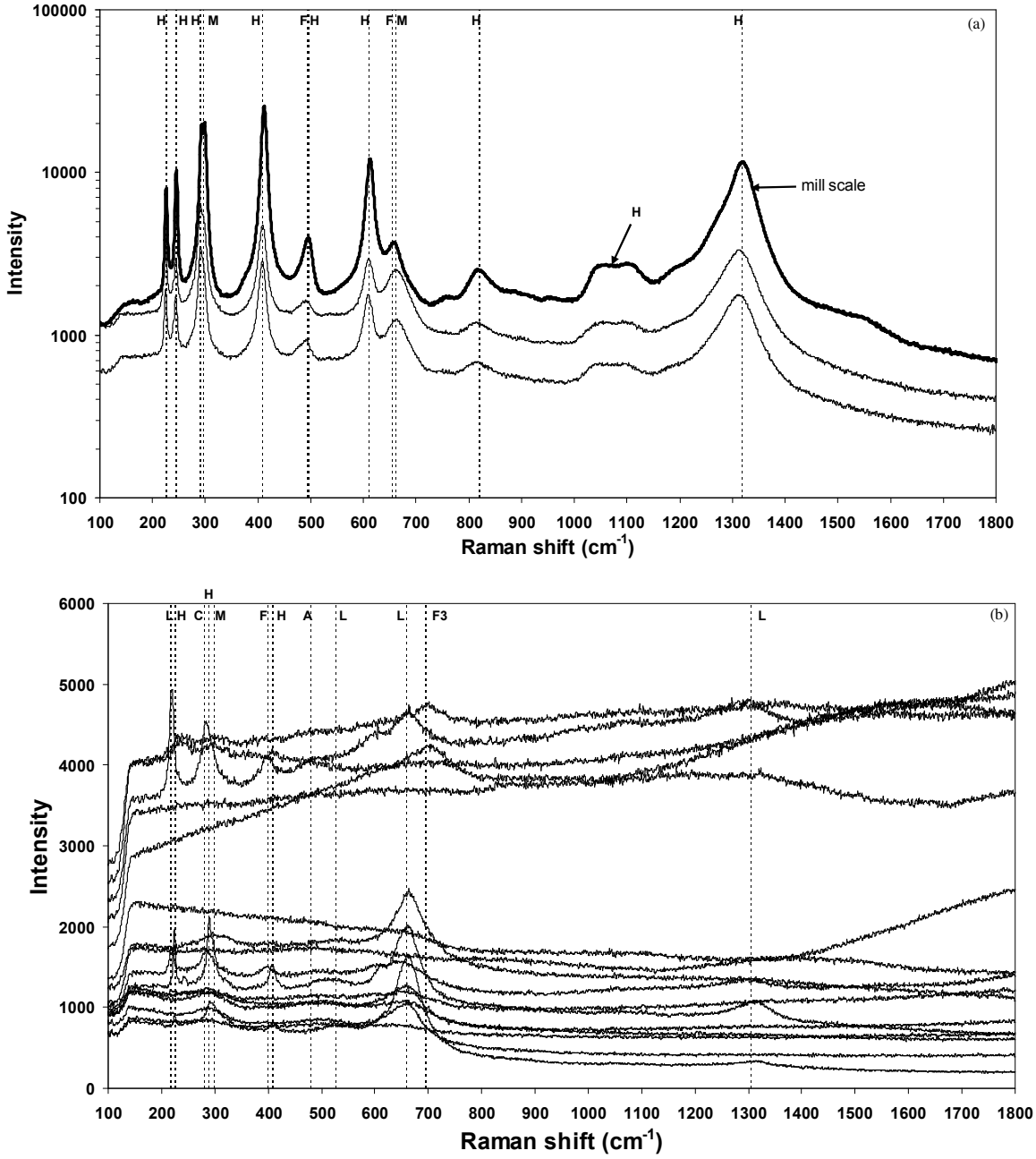

Figure 68: Raman spectra obtained from rebar surface in the dynamically loaded OPCC beam. (a) is from a region on the bar with obvious corrosion products (including mill-scale) and (b) is from a region with a corrosion products and some cement paste adhered to the surface of rebar.

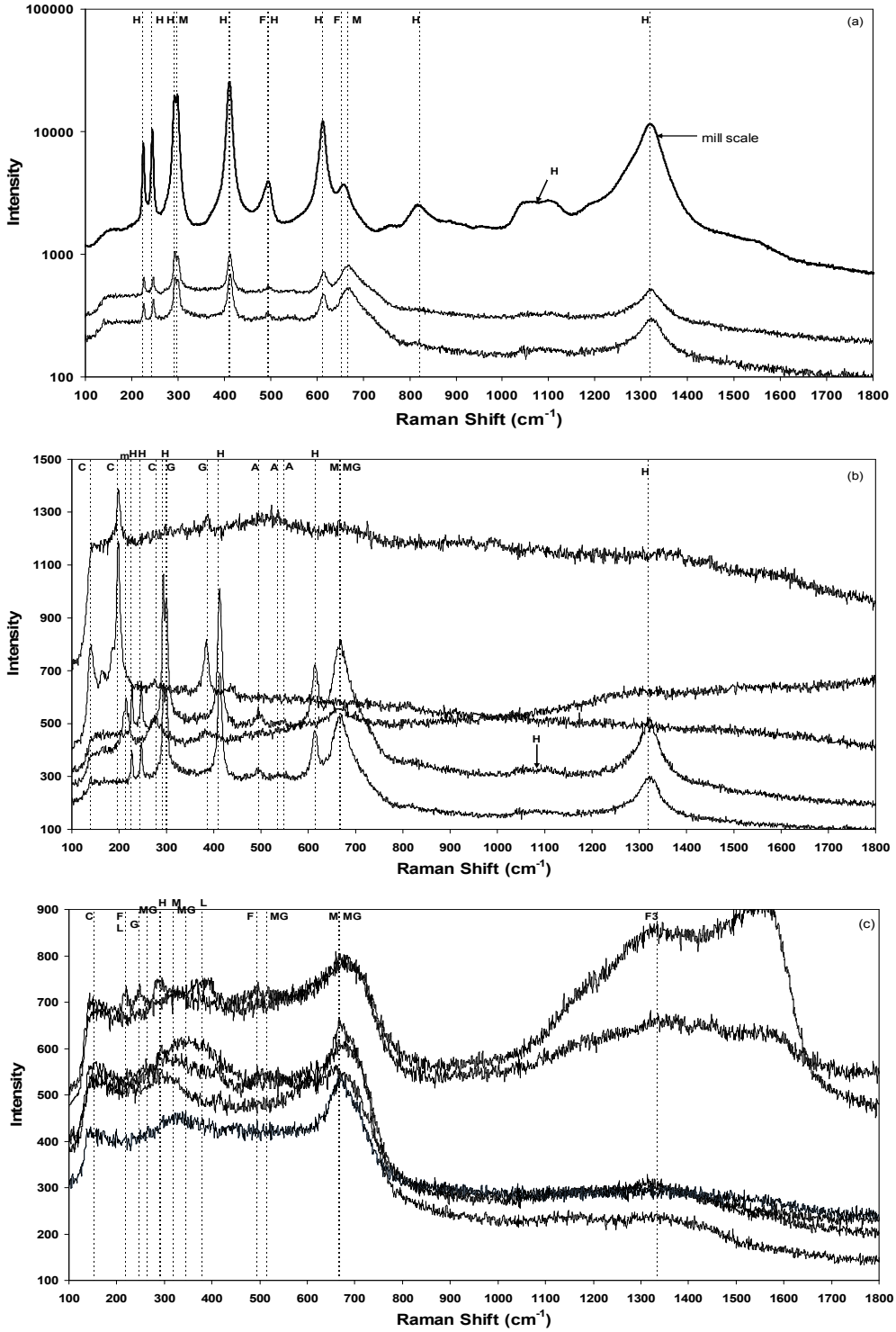

Figure 69: Raman spectra obtained from rebar surface in the statically loaded HPC beam. (a) is from a region on the bar with obvious corrosion products; (b) and (c) are from a region with corrosion products and some cement paste adhered to the surface of rebar.

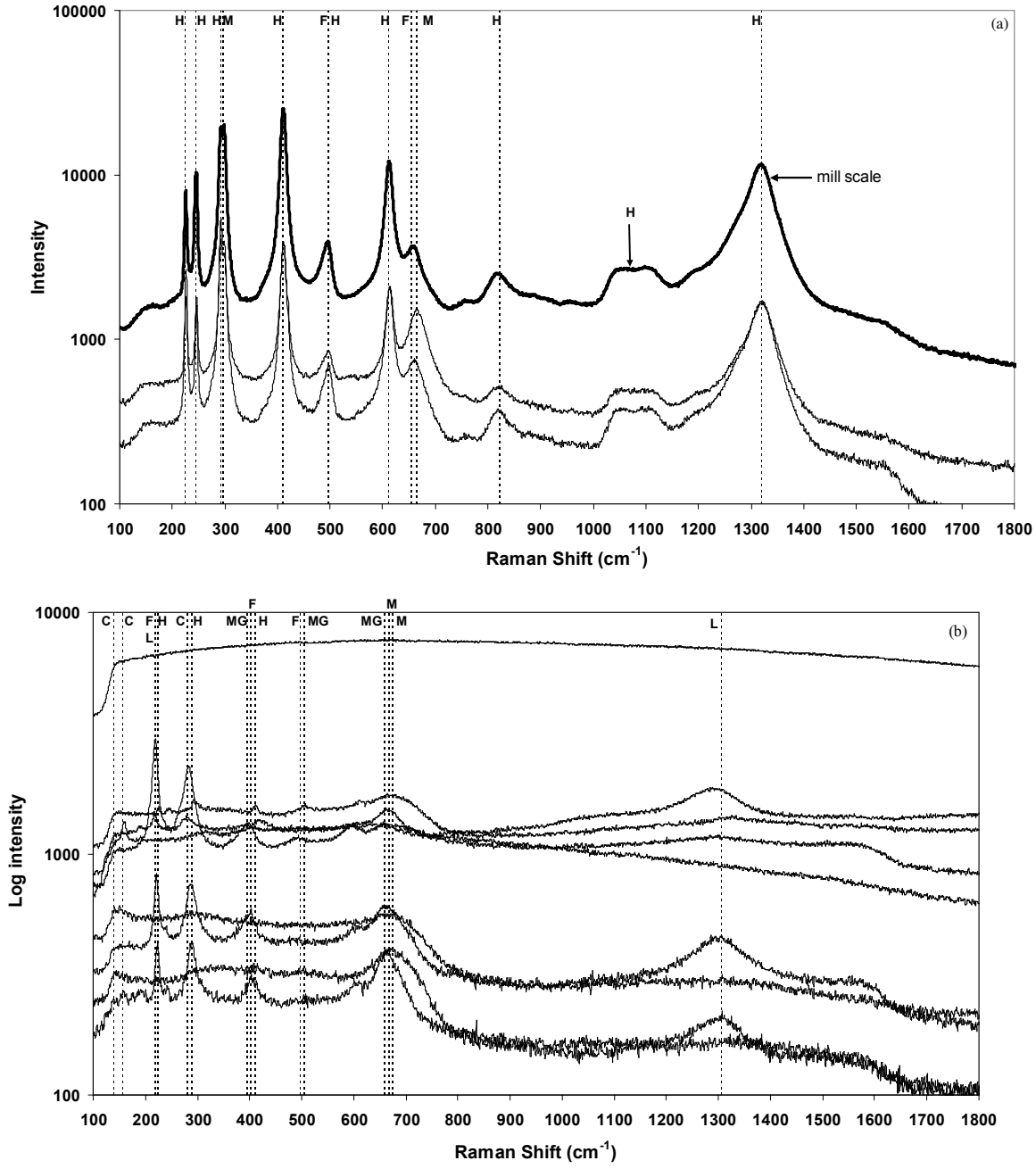

Figure 70: Raman spectra obtained from rebar surface in the dynamically loaded HPC beam. (a) is from a region with obvious corrosion products and (b) is from a region with a combination of corrosion products and some cement paste adhered to the surface of the rebar.

Table 15: Literature sources used in the identification of peaks in Figure 67-Figure 70.

Rebar in	Compound	Peak at (cm^{-1})	Peak in Literature Source (cm^{-1})
All beams (mill scale)	Feroxyhite	495	Unlabelled in [187]
		655	655 [188]
	Hæmatite	226	226 [189], 227 [190], 225 [186]
		245	245 [186, 189, 190]
		292	292 [189], 293 [190], 295 [186]
		411	411 [189], 414 [190], 415 [186]
		497	497 [189]
		612	612 [189], 612 [190], 615 [186]
		821	Unlabelled in [191]
		1050-1110 (hump)	Unlabelled in [191]
		1320	1320 [186]
	Magnetite	297	298 [192]
Statically Loaded OPCC	Calcium Carbonate	154	154 [193]
		1087	1087 [193]
	Calcium Hydroxide	360	360 [95]
	Ferric Hydroxide	697	696 [192]
	Goethite	245	245[186], 247 [189], 248 [192]
		680	680 [192], 685 [186]
	Hæmatite	225	225 [186], 226 [189], 227 [190]
		292	292 [189], 293 [190], 295 [186]
	Maghemite	505, 506	505 [188]
		670	670 [186, 189]
		710	710 [188]
Dynamically Loaded OPCC	Calcium Carbonate	282	283 [193]
	Feroxyhite	400	400 [188]
	Ferric Hydroxide	696	696 [192]
	Hæmatite	227	227 [190], 226 [189], 225 [186]
		290	292 [189], 293 [190], 295 [186]
		411	411 [189], 414 [190], 415 [186]
	Lepidocrocite	219	219 [189]
		528	528 [188, 189]
		660	660 [194]
		1307	1307 [188]
Statically Loaded HPC	Akaganeite	497	497 [188]
		535	unlabelled [187], 538[188]
		549	549 [189]
	Calcium Carbonate	140	140 [195]
		153	154 [193]
		199	199 [195]
		280	281 [193]
	Feroxyhite	220	unlabeled in [187]
		495	unlabeled in [187]
	Ferric Hydroxide	1335	1335 [192]
	Goethite	248	245[186], 247 [189], 248 [192]
		300	300 [186, 189], 303 [192]
		386	386 [189], 390 [186]

	Hæmatite	227	227 [190], 226 [189], 225 [186]
		245	245 [186, 189, 190]
		292/293	292 [189], 293 [190], 295 [186]
		411	411 [189], 414 [190], 415 [186]
		612	612 [189], 612 [190], 615 [186]
		1320	1320 [186]
	Lepidocrocite	219	219 [189]
		379	379 [189], 380 [194]
	Maghemite	265	265 [186]
		345	345 [186], 350 [188]
		515	515 [186]
		670	670 [186, 189]
	Magnesium Carbonate	216	216 [193]
	Magnetite	319	319 [192]
		667	667 [189], 663 [190]
Dynamically Loaded HPC	Calcium Carbonate	140	140 [195]
		158	158 [195]
	Feroxyhite	220	unlabelled in [187]
		403	400 [188]
		498	unlabelled in [187]
	Hæmatite	225	225 [186],227 [190], 226 [189]
		290	292 [189], 293 [190], 295 [186]
		411	411 [189], 414 [190], 415 [186]
	Lepidocrocite	219	219 [189]
		1307	1307 [188]
	Maghemite	395	395 [189]
		505	505 [188]
		660	660 [188]
	Magnetite	667/676	667 [189], 663 [190], 675 [186]

The photograph in Figure 71 exhibits the distribution of corrosion products on the concrete surface that formed the wall of a macrocrack in the statically loaded OPCC beam and Figure 72(a), (b) and (c) show the Raman spectra obtained from the locations identified in Figure 71. Figure 73-Figure 78 are similar illustrations for dynamically loaded OPCC, statically loaded HPC and dynamically loaded HPC beams, respectively. The nomenclature used in the Raman plots is the same as indicated in Table 14. The only missing products are 'f ' which denotes the $[Fe(H_2O)^6]^{3+}$ ion that was also observed by [196, 197] and 'D' which denotes dolomite aggregate ($CaMg(CO_3)_2$) [193]. The peaks in the Raman plots have been characterized using the references indicated in Table 16.

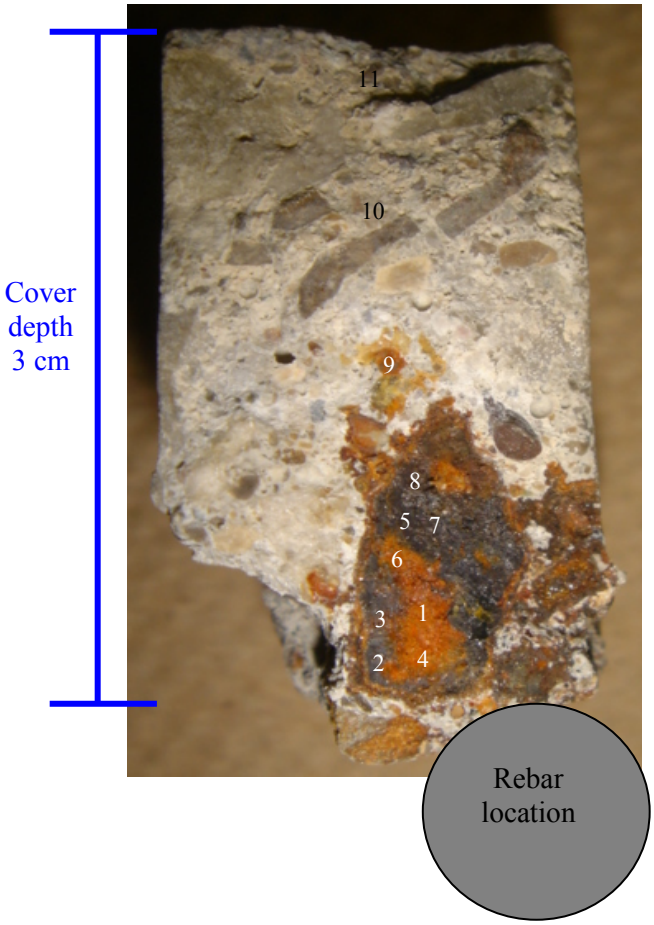

Figure 71: A photograph showing the distribution of corrosion products at a crack in the statically loaded OPCC beam. The Raman spectra from the locations indicated by numbers in this photograph are presented in Figure 72.

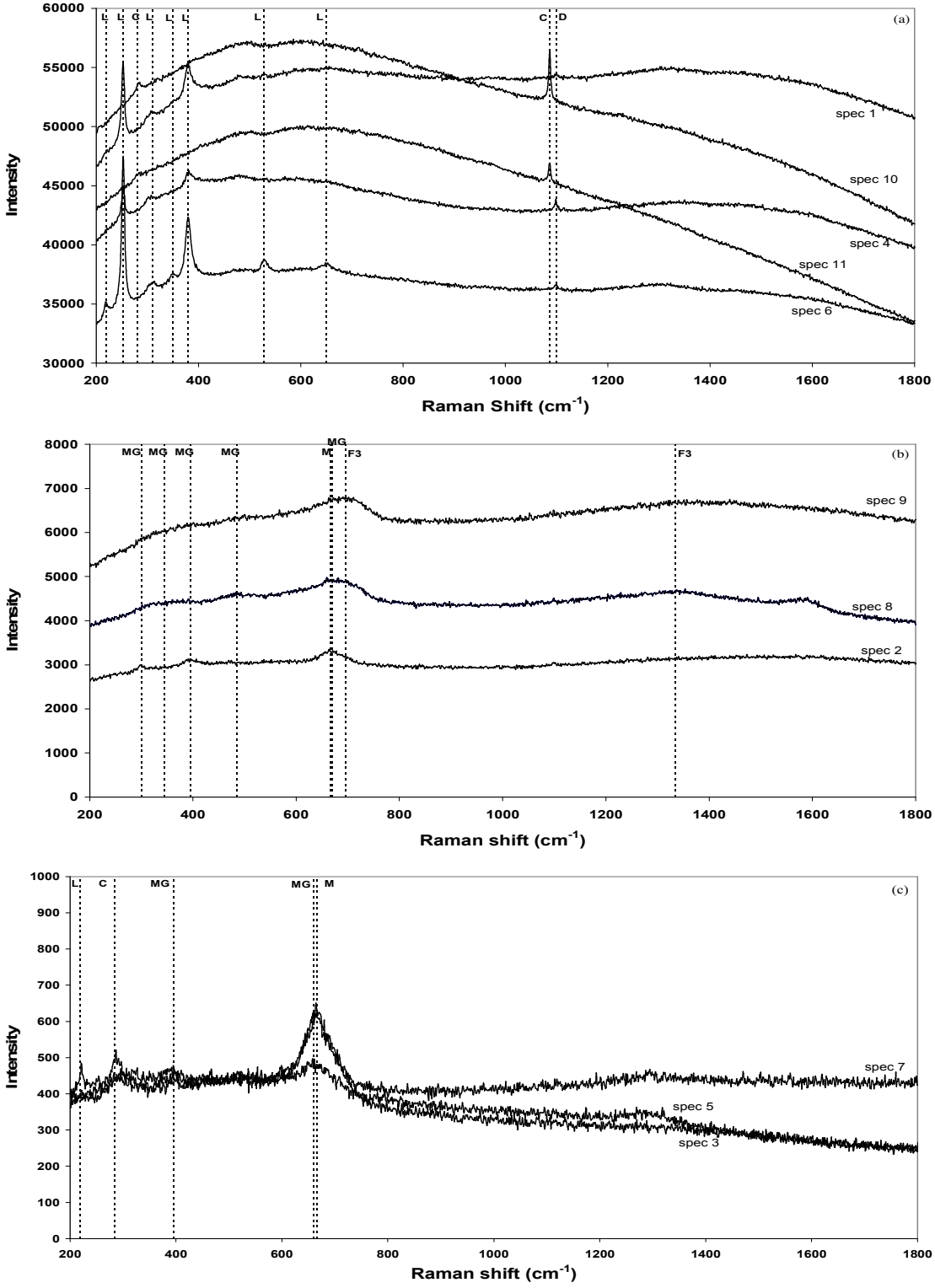

Figure 72: (a), (b) and (c) show the Raman spectra of the locations denoted by numbers in Figure 71.

Figure 73: A photograph showing the distribution of corrosion products at a crack in the dynamically loaded OPCC beam. The Raman spectra from the locations indicated by numbers in this photograph are presented in Figure 74.

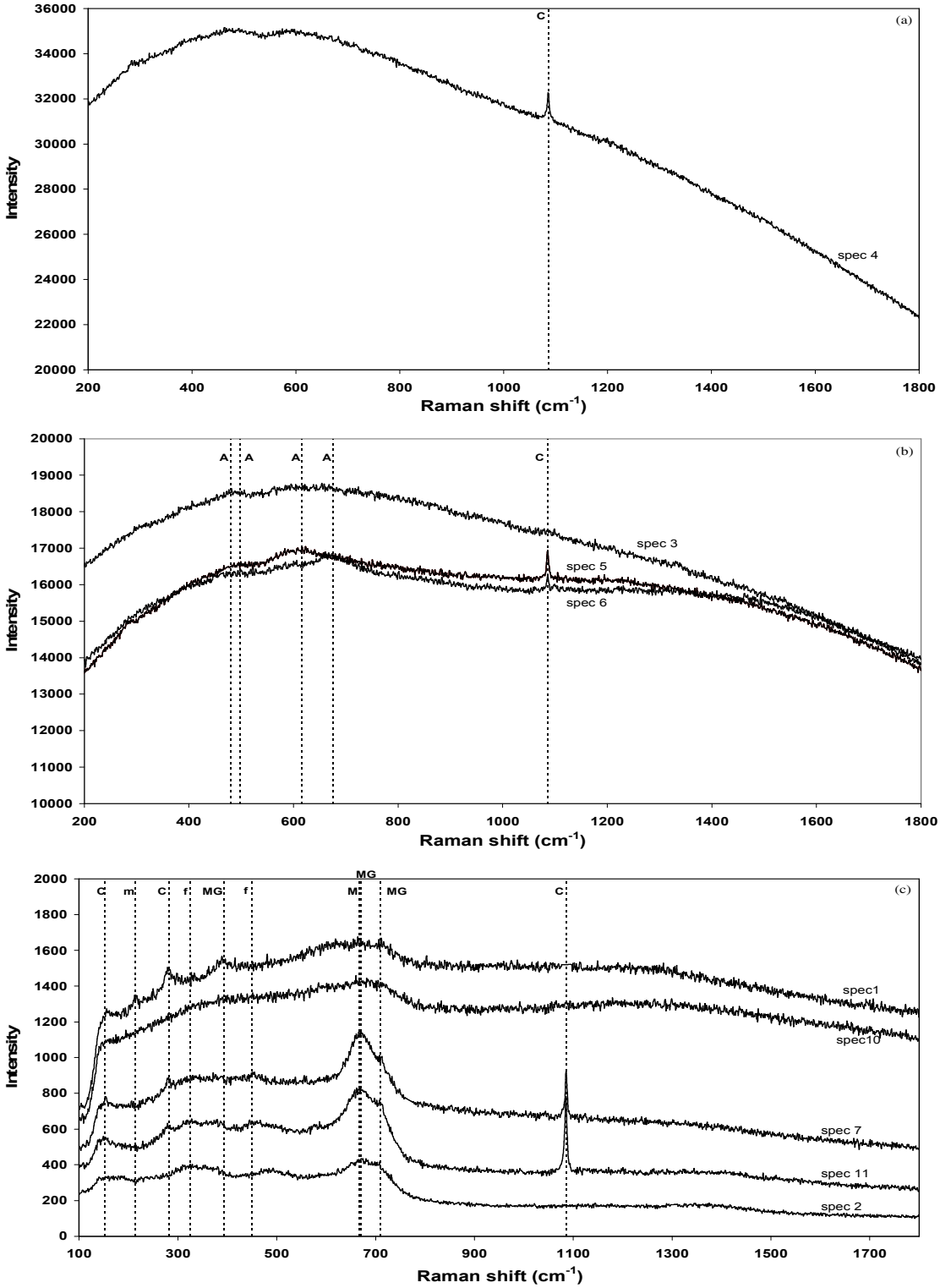

Figure 74: (a), (b) and (c) show the Raman spectra of the locations denoted by numbers in Figure 73.

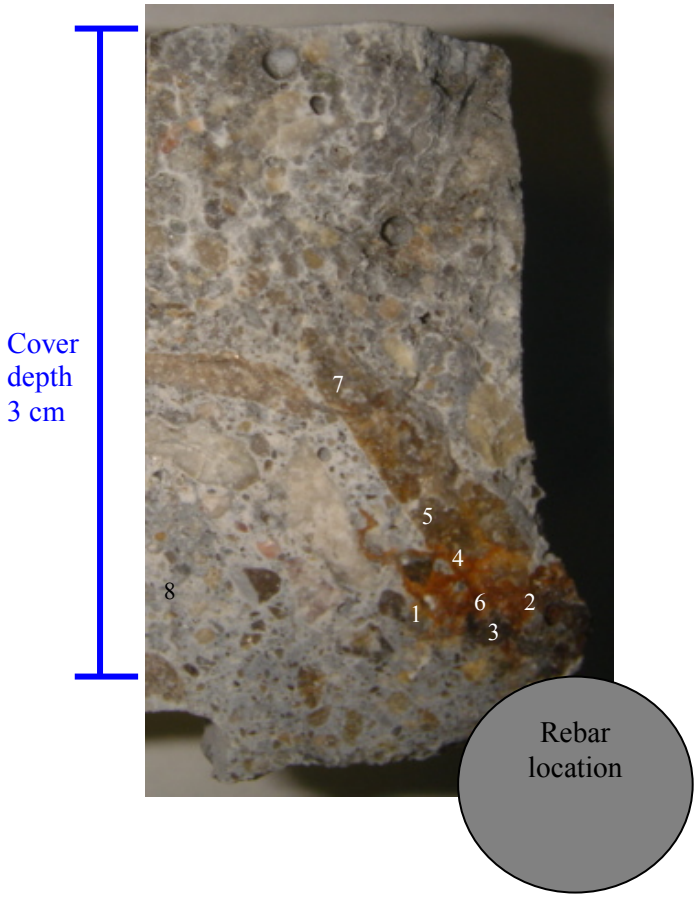

Figure 75: A photograph showing the distribution of corrosion products at a crack in the statically loaded HPC beam. The Raman spectra from the locations indicated by numbers in this photograph are presented in Figure 76.

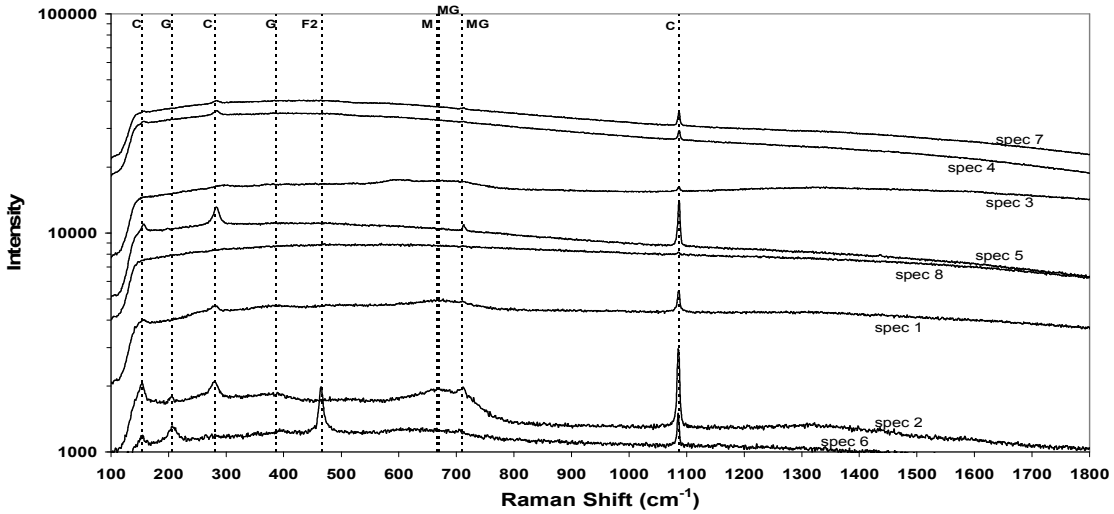

Figure 76: Shows the Raman spectra of the locations denoted by numbers in Figure 75.

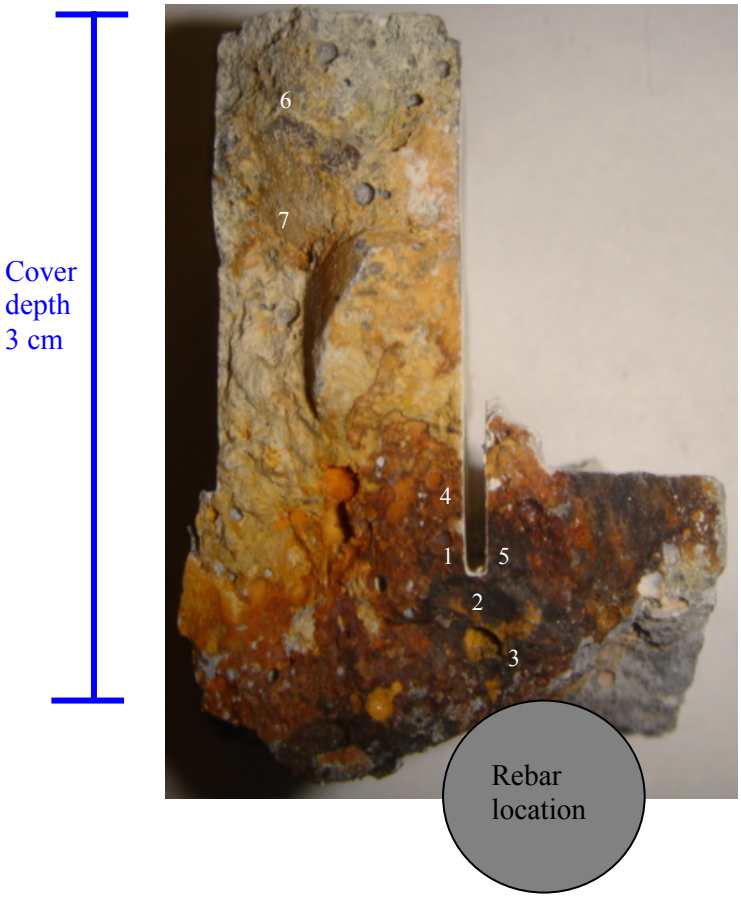

Figure 77: A photograph showing the distribution of corrosion products at a crack in the dynamically loaded HPC beam. The Raman spectra from the locations indicated by numbers in this photograph are presented in Figure 78.

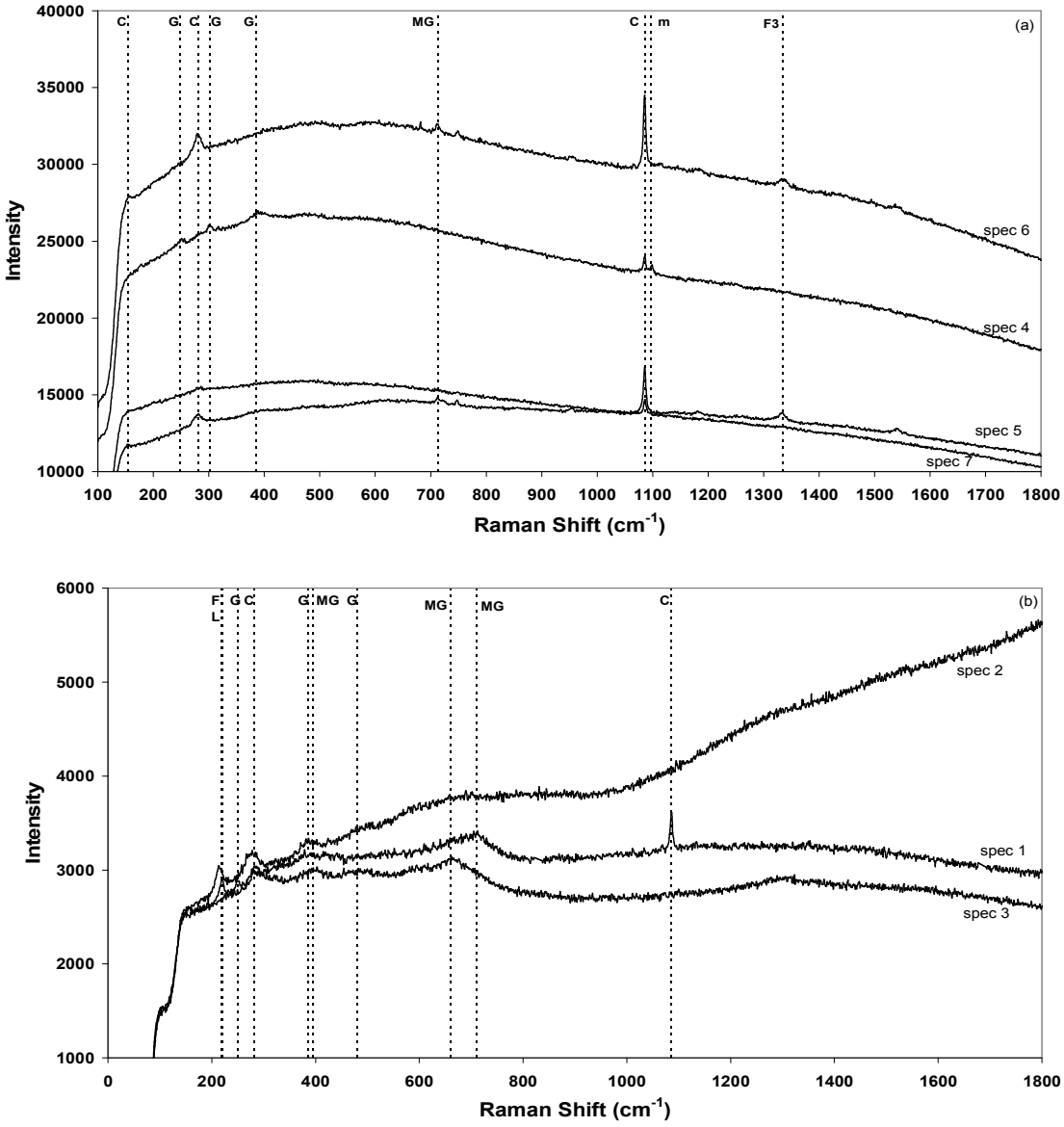

Figure 78: (a) and (b) show the Raman spectra of the locations denoted by numbers in Figure 77.

Table 16: Sources used for identification of Raman peaks in Figure 72-Figure 78.

Concrete	Compound	Peak at (cm^{-1})	Peak in Literature Source (cm^{-1})
OPCC Statically Loaded	Calcium Carbonate	281	283 [193]
		1086	1087 [193]
	Dolomite	1099	1099 [193]
	Ferric Hydroxide	696	696 [192]
	Lepidocrocite	219	219 [189]
		252	252[189, 194] 255 [188]
		311	311 [189]
		349	349 [189]
		379	379 [189], 380 [194]
		528	528 [188]
		650	648 [189]
	Maghemite	300	300 [186]
		345	345 [186], 350 [188]
		395 / 396	395 [186]
		486	486 [186]
		660	660 [188]
		670	670 [186, 189]
	Magnetite	667	667 [189], 663 [190]
OPCC Dynamically Loaded	Akaganeite	480	unlabelled in [187]
		497	497 [188]
		615	unlabelled in [187]
		675	unlabelled in [187]
	Calcium Carbonate	153	154 [193]
		281	283 [193]
		1086	1087 [193]
	$[Fe(H_2O)_6]^{3+}$ ion in solution	325	325 [196]
		450	450 [196]
	Maghemite	393	395 [186]
		670	670 [186, 189]
		710	710 [188]
	Magnesium Carbonate	214	216 [193]
	Magnetite	667	667 [189], 663 [190]
HPC Statically Loaded	Calcium Carbonate	154	154 [193]
		281	283 [193]
		1087	1087 [193]
	Ferrous Hydroxide	466	460 [198]
	Goethite	205	205 [189]
		386	386 [189], 390 [186]
	Maghemite	670	670 [186, 189]
		710	710 [188]
	Magnetite	667	667 [189], 663 [190]
HPC Dynamically Loaded	Calcium Carbonate	153	154 [193]
		281	283 [193]
		1086	1087 [193]
	Feroxyhite	220	unlabelled in [187]
	Ferric Hydroxide	1335	1335 [192]
	Goethite	248	248 [192], 245 [186] 247 [189]

		302	303 [192]
		386	386 [189], 390 [186]
		480	480 [186], 481 [189], 485 [192]
	Lepidocrocite	215	219 [189]
	Maghemite	395	395 [186]
		660	660 [188]
		710	710 [188]
	Magnesium Carbonate	1097	1096 [193]

Corrosion products identified on the rebar surfaces and on the crack walls in beams are summarized in Table 17. There is no discernable relationship between the products on the two surfaces. A possible reason for this is that, when corrosion products are formed on the rebar surface, they disperse into space that is available, be it in the rebar-concrete interface, in the pores of the concrete or in the crack. In the dynamically loaded beams, the larger spread of corrosion products on the surface of the crack walls is an indication that the combination of opening and closing of the crack and salt solution was aiding this distribution. Unlike the situation in sound concrete, the presence of an unblocked crack allows air to diffuse in during the drying cycle and, if the crack extends to the rebar, as in this case, this provides an unlimited supply of oxygen at the rebar. This causes further oxidation of diffused products on the crack walls and on the rebar.

Table 17: Corrosion products in the concrete beams. The products have been listed in order of increasing specific volume. * may be from mill scale.

Beam	**Corrosion products on rebar at a macro-crack**	**Corrosion products on the macro-crack walls in concrete**
Statically Loaded OPCC	Hæmatite* Maghemite Goethite Ferric Hydroxide	Magnetite Maghemite Lepidocrocite Ferric Hydroxide
Dynamically Loaded OPCC	Hæmatite* Feroxyhite Lepidocrocite Ferric Hydroxide	$[Fe(H_2O)_6]^{3+}$ Magnetite Maghemite Akaganeite
Statically Loaded HPC	Hæmatite* Maghemite Feroxyhite Goethite Lepidocrocite Akaganeite Ferric Hydroxide	Magnetite Maghemite Goethite Ferrous Hydroxide
Dynamically Loaded HPC	Magnetite* Hæmatite* Maghemite Feroxyhite Lepidocrocite	Maghemite Feroxyhite Goethite Lepidocrocite Ferric Hydroxide

The most voluminous (oxidized) corrosion product observed on the surface of the rebar in the dynamically loaded OPCC beams was ferric hydroxide, which was absent from the surface of the rebar in the dynamically loaded HPC beam. A comparison of corrosion products on the surface of the rebar in OPCC and HPC statically loaded beams revealed a larger variety of corrosion products in the latter. The HPC beam exhibited feroxyhite, lepidocrocite and akagneite, which were absent in the OPCC beams. According to [199, 200], goethite can be formed upon dissolution and re-precipitation of the other FeOOH compounds in alkaline solutions. The fact that OPCC was highly porous would enable it to continuously maintain moisture at the rebar-concrete interface (even in the dry cycle), which would account for only goethite being present at the rebar-crack interface. The absence of goethite at the rebar-concrete interface of the dynamically loaded OPCC beams is further evidence that, collectively, dynamic loading and salt solution enable corrosion products to diffuse away from rebar concrete interface. It should be noted that the FeOOH compounds are less expansive than ferric hydroxide; however, the absence of the latter does not imply that the FeOOH products will have a lesser impact on the durability of rebar-concrete bond. The most important factor influencing this durability is their amount, which was not determined in this project.

The types of corrosion products that were observed on the crack surface in the statically and dynamically loaded concretes were very similar. The crack walls in all the beams except dynamically loaded OPCC contained either ferrous or ferric hydroxide. The former can be converted to the latter when subjected to simultaneous processes of drying and oxidation [192]. These compounds were not present in the dynamically loaded OPCC beam either because (i) they had been washed out or (ii) they had not been able to precipitate because of the constant presence of moisture which was observed and is further confirmed by the presence of $[Fe(H_2O)_6]^{3+}$ ions. These ions (also known as the hexoaquoiron ions) are formed when the iron ions form covalent bonds with water molecules and are the "simplest iron ions in solution" [201]. The corresponding anions could be either chloride (Cl^-) or carbonate (CO_3^{2-}), which unfortunately, are not detectible by Raman spectroscopy when they are in solution [202]. The fact that the hexoaquoiron ions were detected close to the surface of the concrete as well as midway between the external concrete surface and the concrete/rebar interface implies that both water and iron ions were present in the crack at the time when Raman spectroscopy was performed. The presence of water can be explained by the high chloride concentration in OPCC dynamically loaded beams as seen in Section 4.3 (because NaCl is hygroscopic) while the iron ions may have been washed into the crack by the concurrent influence of dynamic loading and the salt solution.

It is interesting that hæmatite, which was observed at the rebar-concrete interface in all the concretes was not seen on the walls of the cracks; however, magnetite, which is a less oxidized corrosion product, was evident in all the concretes except HPC dynamically loaded. Dünnwald and Otto [192] propose that magnetite is formed from FeOOH or $Fe(OH)_2$ upon wetting if iron ions or FeOOH, respectively, are present, which explains its existence in the crack walls. Also, the hæmatite observed at the rebar-concrete interface was probably from the existing mill-scale on the surface of the rebar.

There was no particular order to the spatial distribution of corrosion products on the concrete surfaces. Magnetite and maghemite were observed at locations close to the rebar as well as close to the external surface of the beam in the dynamically loaded concretes. This spread could be caused by the opening and closing of the crack in the salt solution. Magnetite and maghemite were also seen wherever corrosion products were observed in the statically loaded concretes. The FeOOH compounds (e.g. akaganeite, goethite and feroxyhite), ferrous and ferric hydroxide were found in the vicinity of, or intermingled, with magnetite and maghemite. These expansive compounds could have been formed when magnetite or maghemite oxidized.

The most voluminous corrosion product observed in this study was ferric hydroxide while that observed by Marcotte and Hansson [142] was akaganeite. While akaganeite occupies about 3.5 times the volume of iron, ferric hydroxide occupies about 4 times the volume of iron [95]. Therefore, for the purpose of modelling the effect of cracking on the durability of concrete, it would be appropriate to adopt a conservative approach and assume that ferric hydroxide is the most expansive corrosion product formed.

4.5.4 Mill-Scale

Mill-scale is an oxide film formed on the surface of rebar when it is hot rolled. According to Cook [203], mill-scale on carbon steel is composed of wustite (FeO), magnetite (Fe_2O_3) and hæmatite (α-Fe_3O_4). The above oxides are formed in layers on the rebar surface, with wustite closest to the steel surface and hematite forming the outermost layer. In this project, magnetite and hæmatite were detected in the mill-scale by Raman spectroscopy; however, wustite was not observed probably because it did not exist in the region that was penetrated by the Raman laser. Feroxyhite was also observed in the mill-scale in this project.

The mill-scale on rebars used in this project had a thickness of between 20 and 50 μm. EDS analysis on a cross-section of rebar (Figure 79) that had not been embedded in concrete or exposed to chloride bearing environments (virgin bar) revealed that mill-scale was primarily composed of iron and oxygen. The oxygen content measured by the EDS analysis may not be accurate even though the EDS detector contained an ATW2 window which detected all elements higher than beryllium in the periodic table. The uncertainty is because the specimen chamber could have been contaminated with oxygen as the vacuum maintained in it was not high (10^{-6}-10^{-7} torr maintained by mechanical and diffusion pumps compared to 10^{-7}-10^{-9} torr in SEMs which contain an ion pump together with diffusion and mechanical pumps). However, based on a relative comparison of the data in Figure 79, there was very little variation in iron and oxygen contents within the mill-scale. This could be because of the sample preparation technique which involved using water as the lubricant while grinding / polishing and exposing the sample to atmospheric conditions.

Calcium, silicon and chlorine contents in the mill-scale were also included in this analysis in order to determine the base amounts of these elements so as to enable comparison with analyses of rebar embedded in concrete and exposed to chlorides. The steel substrate contained a small amount of silicon. The mill-scale, on the other hand, had negligible amounts of calcium, silicon and chlorine. There was one spot (#12) on the rebar in Figure 79 (b) which had higher amounts of these elements than the rest of the sample. This spot was adjacent to the mounting material and (a) could have been contaminated by the mounting material during sample preparation or (b) EDS could have detected the mounting material together with the mill-scale.

EDS analysis on a sample of rebar embedded in sound OPCC that was not exposed to chlorides (here after called concrete bar) is shown in Figure 80. The mill-scale of this bar appeared to be more porous / cracked and contained more calcium than that of the virgin bar. Typically, when surfaces are exposed to fresh concrete, calcium hydroxide precipitates on them [204]. However, because the mill-scale in the virgin bar was porous, calcium ions from the cement were able to penetrate into the mill-scale when it was embedded in fluid concrete. The calcium ions could have been accompanied by other ions (e.g. hydroxyl ions) which would allow products of cement hydration (e.g. calcium hydroxide) to form in the mill-scale. The formation of these hydration products could have induced further cracking in the mill-scale. The cracking could also have occurred when the rebar was removed from concrete.

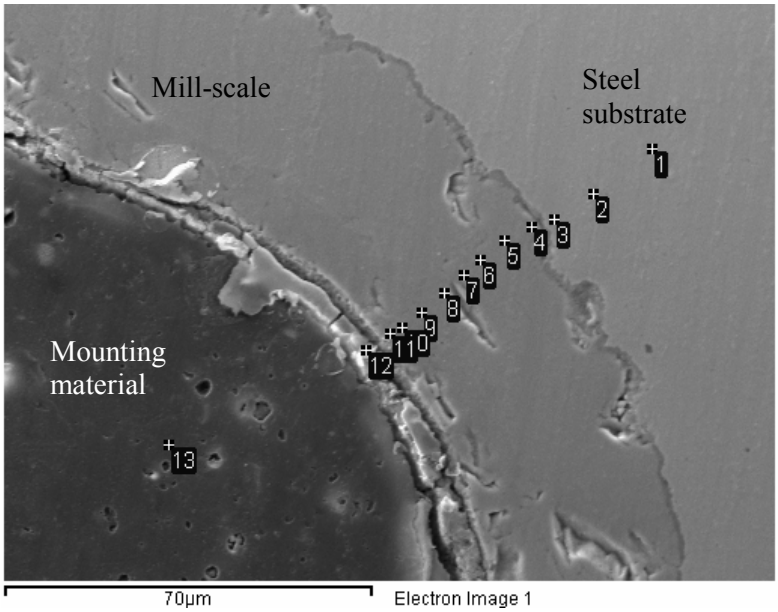

Spectrum	O	Si	Cl	Ca	Fe	Total
1	0.82	0.32	*0.05*	*-0.04*	98.84	100.00
2	0.93	0.29	*0.08*	*0.00*	98.70	100.00
3	0.40	0.50	*-0.06*	*0.10*	99.06	100.00
4	12.69	0.76	*0.02*	*0.07*	86.45	100.00
5	12.94	*0.00*	*0.06*	*0.07*	86.93	100.00
6	13.17	*-0.19*	*0.05*	*0.02*	86.95	100.00
7	14.06	*-0.09*	*0.13*	*0.17*	85.72	100.00
8	13.40	*-0.13*	*-0.12*	*0.00*	86.85	100.00
9	14.64	*-0.04*	*-0.02*	*0.02*	85.40	100.00
10	16.54	*0.07*	*-0.03*	*0.13*	83.29	100.00
11	16.63	*-0.07*	*0.17*	*0.18*	83.09	100.00
12	12.29	1.44	1.40	*0.57*	84.30	100.00
13	62.04	9.02	1.41	8.17	19.36	100.00

Figure 79: SE image and EDS analysis (weight %) of a cross-section of rebar not embedded in concrete or exposed to chlorides. Numbers in italics are values below the detectable limits.

The silicon content was also higher in the mill-scale of the concrete bar than in the virgin bar. In Figure 80, the silicon content decreased towards the surface of mill-scale, which could lead one to conclude that the steel substrate was the source of the silicon. However, this decrease was not observed in the other sections analysed. Hence, the source of silicon could also be the alite (C_3S) and belite (C_2S) phases in the cement. The mill-scale in the concrete bar contained lower amounts of silicon than calcium because (i) the cement components that react initially in water are tricalcium aluminate (C_3A) and gypsum ($C\overline{S}$) [205] and (ii) unhydrated phases (except gypsum) contain more calcium than any other elements. The silicon and calcium could combine to form calcium silicate hydrate (C-S-H) in the mill-scale, which would also induce cracking in the mill-scale.

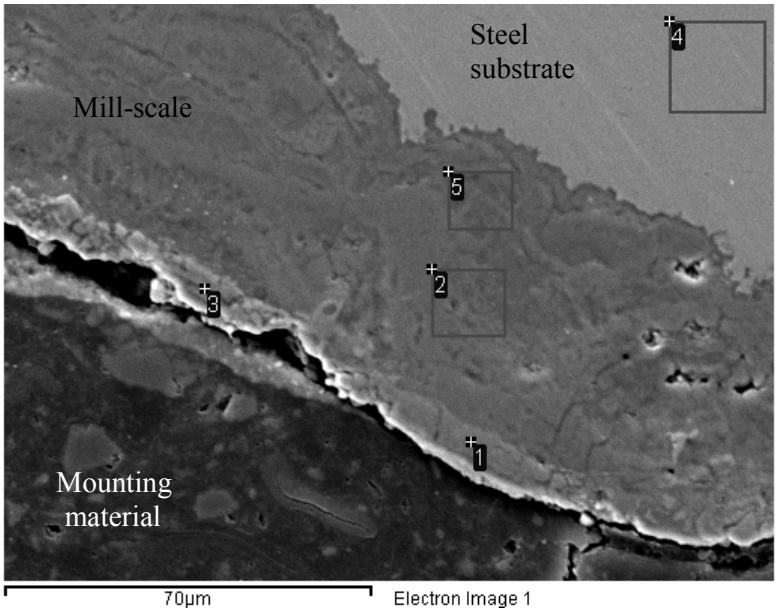

Spectrum	O	Si	Cl	Ca	Fe	Total
1	12.63	*0.08*	*0.05*	1.68	85.57	100.00
2	11.00	0.38	0.32	2.34	85.96	100.00
3	10.70	0.24	0.25	6.78	82.04	100.00
4	0.60	0.29	*0.08*	*0.07*	98.96	100.00
5	12.58	0.45	*0.11*	4.05	82.82	100.00

Figure 80: SE image and EDS analysis (weight %) of a cross-section of rebar embedded concrete but not exposed to chlorides. Numbers in italics are values below the detectable limits.

The chloride content at two locations in Figure 80 (# 2 and # 3) is higher than in the other locations. This locally high chloride content could be due to the contamination during sample preparation. Location # 3 was very close to the mounting material and could easily have been contaminated and location # 2 involved analysis of a large area that contained pores which could have trapped chlorides (e.g. from the mounting material).

Figure 81 illustrates an EDS analysis (weight percent) of a corroding section of rebar from the cracked region of OPCC (corroding bar) and the concrete adhered to it. Table 18 shows the EDS analysis in atomic percent which was used to identify the phases in the concrete. The sand particles in the concrete had negligible amounts of chloride. The cement paste, however, had chlorides and corrosion products as illustrated by the high chlorine and iron contents in the EDS analysis.

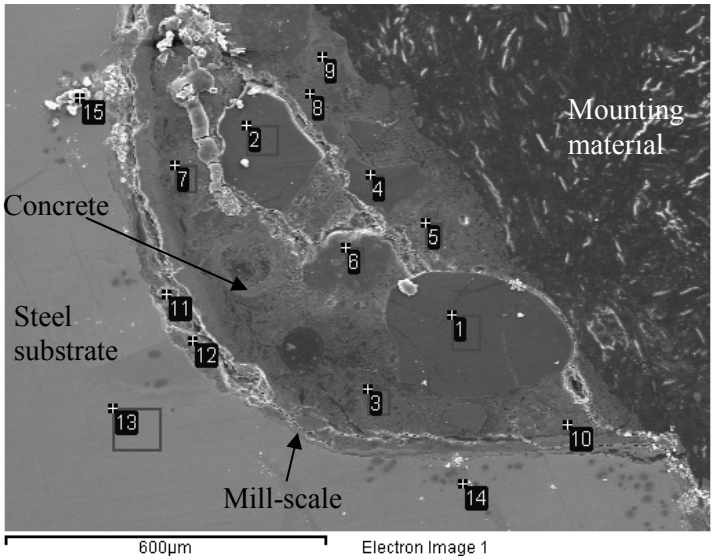

Spectrum	O	Si	Cl	Ca	Fe	Total
1	41.50	57.98	*0.10*	*0.06*	*0.36*	100.00
2	39.98	58.28	*0.10*	*0.17*	1.47	100.00
3	43.94	13.41	2.52	35.21	4.93	100.00
4	39.64	59.35	*0.11*	*0.12*	*0.79*	100.00
5	46.63	9.34	1.18	38.04	4.82	100.00
6	59.70	*0.00*	0.29	37.05	2.96	100.00
7	42.25	11.77	2.60	34.05	9.34	100.00
8	47.16	8.92	0.82	39.78	3.32	100.00
9	30.22	5.64	1.76	31.28	31.11	100.00
10	42.71	8.01	1.49	43.07	4.73	100.00
11	11.91	0.36	0.41	*0.63*	86.69	100.00
12	14.87	0.64	1.48	1.25	81.76	100.00
13	0.45	*0.11*	*0.12*	*0.12*	99.20	100.00
14	2.42	*0.13*	0.50	*-0.02*	96.98	100.00
15	3.30	0.32	4.26	0.49	91.63	100.00

Figure 81: SE image and EDS analysis (weight %) of a cross-section of corroding rebar at a crack in concrete and the concrete adhered to it. Numbers in italics are values below the detectible limits.

Table 18: EDS analysis in atomic % for SE image in Figure 81**.**

Spectrum	O	Si	Cl	Ca	Fe	Possible phases
1	55.56	44.21	0.06	0.03	0.14	Sand
2	54.24	45.04	0.06	0.09	0.57	Sand
3	64.45	11.20	1.67	20.61	2.07	Hydrated cement paste
4	53.73	45.83	0.07	0.07	0.30	Sand
5	67.54	7.71	0.77	21.99	2.00	Hydrated cement paste
6	79.11	0.00	0.17	19.60	1.12	Hydrated cement paste
7	63.63	10.10	1.77	20.47	4.03	Hydrated cement paste
8	67.92	7.31	0.53	22.87	1.37	Hydrated cement paste
9	54.33	5.77	1.42	22.45	16.03	Hydrated cement paste
10	64.23	6.86	1.01	25.86	2.04	Hydrated cement paste
11	31.85	0.55	0.50	0.68	66.43	Mill-scale
12	37.34	0.92	1.68	1.25	58.81	Mill-scale
13	1.54	0.22	0.19	0.16	97.89	Steel substrate
14	7.94	0.23	0.74	-0.03	91.11	Steel substrate with pits
15	10.37	0.58	6.03	0.62	82.41	Steel substrate with Cl deposit on surface

The interface between the corroding bar and the concrete is shown in Figure 82. An EDS analysis of this interface is presented in Figure 83. A comparison of this analysis with that of the virgin bar showed the surface of the corroding bar was covered by a layer of mill-scale. This mill-scale is indicated by points # 4 - # 8 in the SE image of Figure 83. The silicon content of this mill-scale was similar to that observed in the mill-scale of the concrete bar; however, the calcium content varied considerably in the former. Points # 9 - # 11 in Figure 83 had high iron, calcium and silicon contents which implied that a combination of cement paste and corrosion products was present. This was further justified by a BSE image (Figure 84), which revealed a combination of light (high atomic weight elements e.g. Fe) and dark (low atomic weight elements e.g. Ca) areas in the region indicated by points # 9 - # 11.

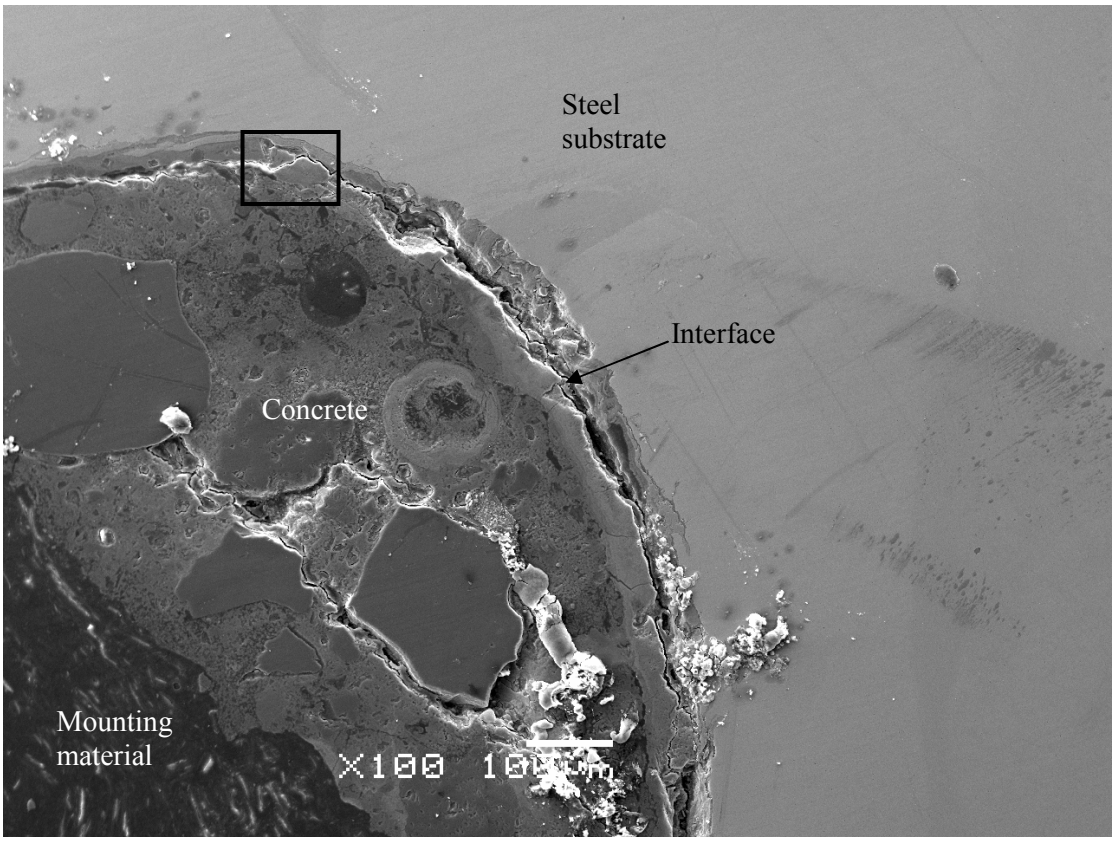

Figure 82: An SE image of mill-scale on a cross-section of corroding rebar at a crack in concrete. Area in the rectangle is presented in Figure 83.

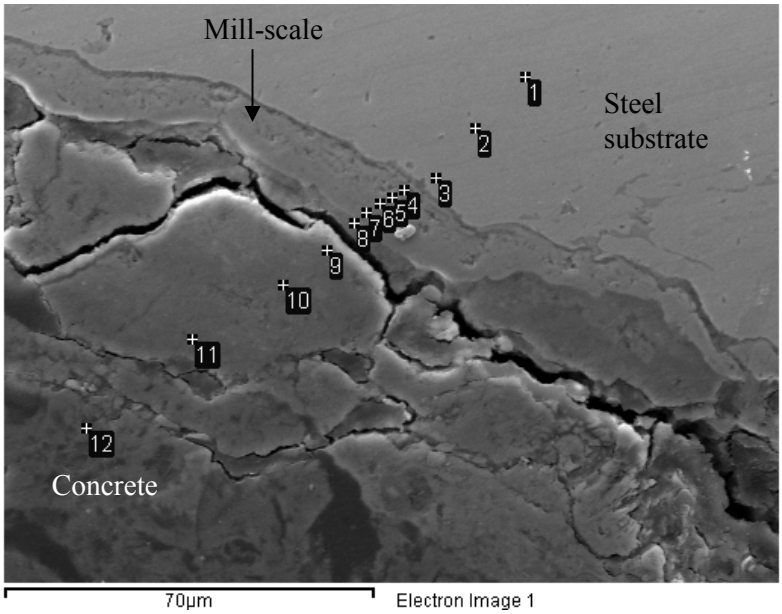

Spectrum	O	Si	Cl	Ca	Fe	Total
1	0.54	*0.17*	*0.14*	*0.10*	99.05	100.00
2	0.42	*0.15*	*0.09*	*0.02*	99.32	100.00
3	0.71	*0.17*	*0.00*	0.24	98.89	100.00
4	17.70	0.46	*0.08*	2.53	79.23	100.00
5	17.15	0.30	*0.07*	0.26	82.22	100.00
6	16.82	0.14	*0.15*	0.58	82.31	100.00
7	17.35	*0.06*	*0.00*	0.33	82.26	100.00
8	19.00	0.54	*0.17*	8.00	72.29	100.00
9	26.47	2.86	0.80	20.03	49.85	100.00
10	32.20	1.34	0.69	31.98	33.79	100.00
11	30.03	5.04	0.99	25.90	38.04	100.00
12	39.82	18.22	5.93	24.82	11.20	100.00

Figure 83: SE image and EDS analysis (weight %) of mill-scale in the corroding bar.

The BSE image clearly differentiates between the mill-scale and the corrosion products and shows a precipitated solid between the mill-scale and the substrate (in some areas). Under the BSE detection mode of the SEM, this solid has a similar colour to that of the cement paste containing corrosion products (indicated by points # 9 - # 11). There are two ways this solid could have precipitated between the mill-scale and the substrate. The first is that the ions (e.g. chloride, calcium and hydroxyl) diffused through the mill-scale and induced corrosion of the substrate. This is supported by the fact that variable amounts of calcium were detected in the mill-scale of the corroding bar (Figure 83). The second is that loading of the reinforced concrete beam to create cracks in the concrete could have induced cracks in the mill-scale which allowed chloride, calcium and other ions to penetrate to the substrate causing corrosion and cement hydration simultaneously. Regardless

of how the precipitated solid was formed, the growth of this solid could have induced further cracking in the mill-scale, thereby contributing to the corrosion.

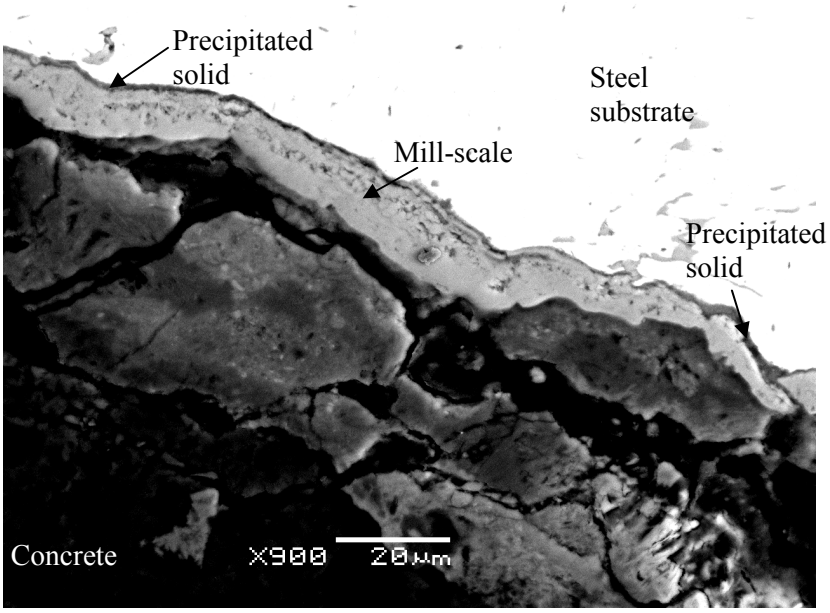

Figure 84: A BSE image of the image shown in Figure 83.

Chapter 5 - Conclusions

- Within the 18 months of exposure, corrosion occurred ONLY at cracks in the concrete, particularly at the submerged cracks which allowed the salt solution easy access to the rebar. Hence, greater emphasis should be placed on the influence of cracks on service-life evaluations of reinforced concrete structures.
- Corrosion initiated at cracks almost immediately upon exposure to salt solution and appeared to be independent of the chloride content in the concrete. Rebar corroded even at cracks that were not visible to the eye (e.g. in the unloaded OPCC beams). A significant amount of corrosion was observed in both OPCC and HPC beams after 18 months' exposure. However, in real structures, where the frequency of exposure to salt and the dilution of the salt by rain and snow would reduce the amount of salt at rebar, corrosion would occur much more slowly; nevertheless, it would occur.
- The type of loading (i.e. static, dynamic or no load) had a minor impact on the microcell corrosion rates of reinforcing steel; however, dynamically loaded beams illustrated higher macrocell currents than statically loaded ones. The microcell currents are more critical than macrocell currents because they are not as influenced by the concrete. The actual microcell current density (Table 5) for rebar at a crack in OPCC was approximately an order of magnitude higher than that in HPC, indicating that the latter was more protective towards the steel.
- It is extremely difficult to determine which areas of the steel in concrete are responsible for the corrosion currents observed. In this project, in the passive regions, the length of rebar which was polarized was considered to be influencing the measured corrosion currents; however, in the cracked region the polarized area of rebar was much larger than the actual corroding area leading to a significant underestimation of corrosion current densities.
- Macrocracks bifurcated at the rebar level and propagated parallel to the rebar in OPCC and HPC beams under both static and dynamic loading. This left large areas of steel devoid of direct protection from the concretes. However, corrosion was more localized in OPCC, but deeper (max 1.30 mm), than in HPC (max 0.37 mm). It could be that the variation in pH along the crack parallel to the rebar was influencing the extent of corrosion on the rebar.
- For both OPCC and HPC, the number and width of cracks in dynamically loaded beams increased over the period of the measurements more than those in the statically loaded beams. This had an impact on the concrete (e.g. high chloride content in dynamically loaded OPCC) but did not have

any observable effect on the corrosion current densities. It is reasonable that the increase in crack widths had no impact on the current density because, regardless of its size, a crack allows a direct path for chloride ions to reach the reinforcing steel and induce corrosion. However, the explanation for the lack of an effect of the increased number of cracks is not so obvious, in view of the fact that an area of active corrosion was observed at the intersection of almost all of the cracks in the submerged region of the bar. It is concluded, therefore, that that there is an upper limit to the area along the length of the rebar that can influence corrosion current densities at any location on the bar with the present experimental set-up.

- The build up of corrosion products at the rebar-concrete interface in HPC could act as a wedge and result in spalling of large pieces of concrete, with potentially catastrophic consequences. In contrast, because corrosion products can diffuse into the pores and aggregate-paste interface in OPCC, there is less likelihood of such spalling.

Chapter 6 - Recommendations

- In sound concrete, the cover-depth influences (i) the time it takes for corrosion to initiate on the rebar and (ii) the corrosion current density. Further investigation is needed to determine if the cover-depth has a similar influence on cracked concrete.
- It would be worthwhile to investigate the influence of different sizes of corroding areas on the distribution of corrosion potentials in reinforced concretes. A mathematical correlation taking into account current density, corrosion potential, corroding area and resistance of concrete would allow a more accurate interpretation of the potentials.
- In reinforced concrete structures, current densities based on polarized areas should be interpreted with caution. After measuring corrosion currents at several locations on a structure, cores (containing rebars) could be obtained from these locations. The relationship between corrosion currents and corroding areas could be determined. This would allow the estimation of the corroding areas based on the corrosion currents observed.
- Crevice corrosion occurred in the submerged regions of some of the beams where the rebars had been epoxy-coated and had no concrete cover over them. In future designs of reinforced concrete beams, the rebars should include a concrete cover over these ends to minimize the risk of corrosion.
- X-ray computed tomography (CT) could be calibrated to distinguish between the different corrosion products in concrete. This would enable the determination of the relative volumes of corrosion products for use in service-life prediction models.

Appendix A - Initial calculations for beam design

Calculations performed with the assistance of Dr. J. West of the Department of Civil Engineering. All equations contained herein are from "Reinforced Concrete Design: 3rd Edition" [206] by S. U. Pillai, D. W. Kirk and M. A. Erki.

Free body diagram of beam under three point bending:

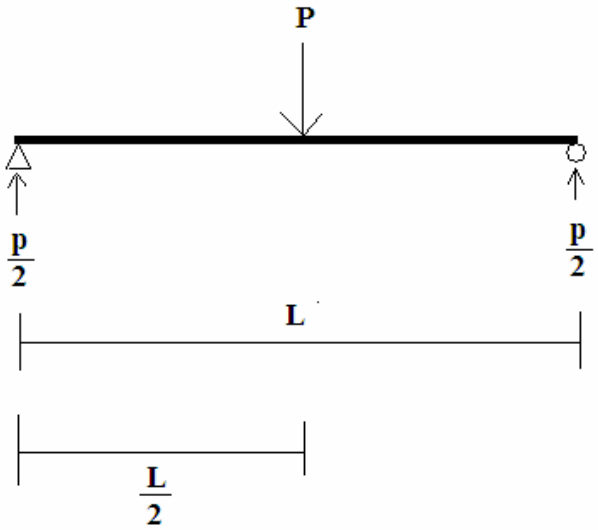

Cross section of the beam:

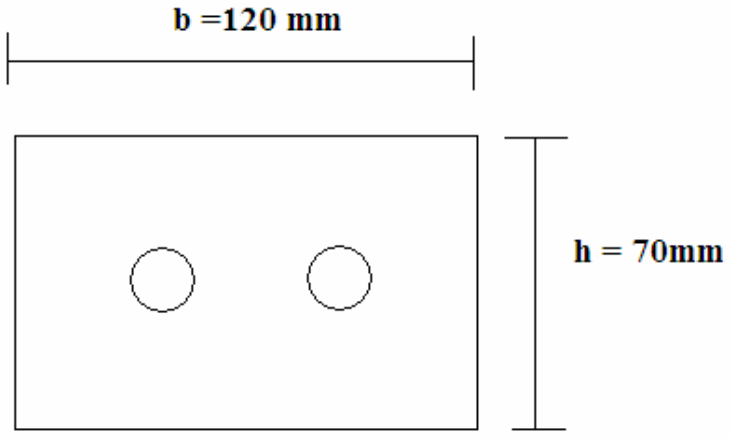

For the concrete in the beam (intended compressive strength at 28 days, f_c' = 35 MPa) not to develop any cracks under load, the moment applied ($M_{applied}$) should be less than 80 % of the cracking moment (M_{cr})

The cracking moment, $M_{cr} = \frac{f_{cr} I_g}{y_{tens}}$

Where:

$f_{cr} = 0.6\lambda\sqrt{f_c'} = (0.6)(1)(\sqrt{35}) = 3.55MPa$

$I_g = \frac{bh^3}{12} = \frac{(120)(70)^3}{12} = 3.430 * 10^6 mm^4$

$y_{tens} = \frac{h}{2} = \frac{70}{2} = 35mm$

Therefore,

$M_{cr} = \frac{(3.55MPa)(3.430 * 10^6 mm^4)}{(35mm)} = 0.348Nmm = 348Nm$

$0.8M_{cr} = \frac{PL}{4}$ **;** L is the portion of the length of the beam subjected to loading i.e. 1 m.

$P = \frac{(4)(0.8)(M_{cr})}{1} = 1113.6N = 113.6kg$

$\frac{P}{2} = 56.8kg$

Hence, the maximum load that can be applied without cracking the concrete is 56.8 kg.

Will this beam fail in shear under the above load?

Shear force diagram:

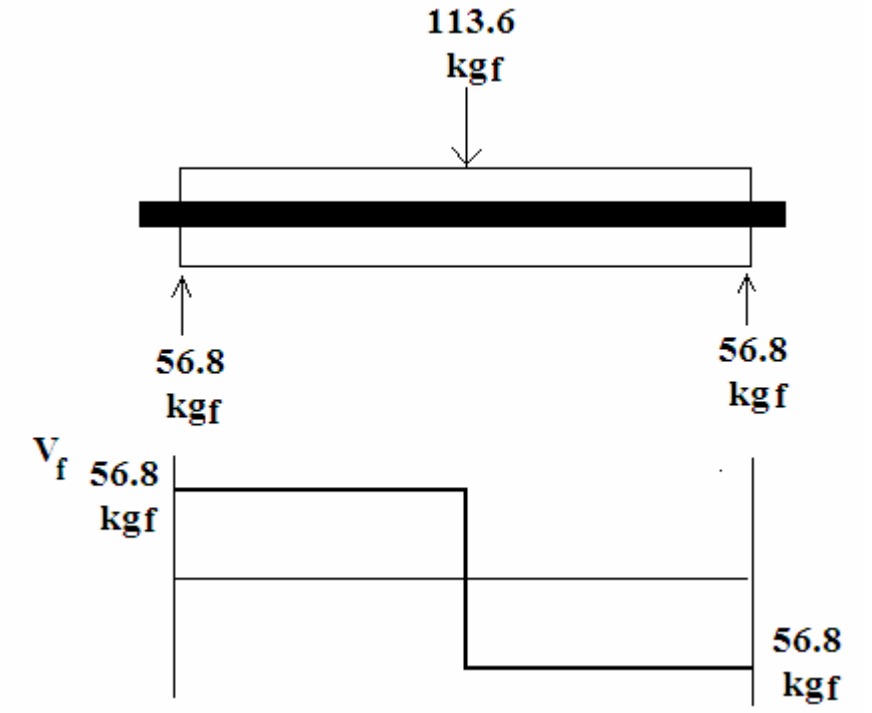

The shear force to cause beam to rupture:

$V_r = V_{concrete} + V_{steel}$;

However, to determine if the concrete (excluding the steel) will rupture

$V_r = V_{concrete}$

But $V_r \geq V_f \rightarrow V_c \geq V_f = 56.8kgf$

$$V_c = 0.2\lambda\phi_c\sqrt{f_c'}bd = 0.2\lambda\phi_c\sqrt{f_c'}b\frac{h}{2} = (0.2)(1)(0.60)(\sqrt{35})(120)(\frac{70}{2}) = 2981.7N$$

[Note: λ accounts for the effect of concrete density on the tensile strength (λ = 1 [135]), ϕ_c is the concrete resistance factor to account for variation in materials strength and cross-section dimension (ϕ_c = 0.60 [135]) and d is the effective depth.]

$V_f = 56.8kgf = 556.28N$

Increase by 25 % for safety factor $\rightarrow V_f = 695.28N$

$V_c > (V_f + 25\%V_f)$

Therefore, beam will not fail in shear.

Appendix B - Crack-widths in OPCC and HPC beams

Beams with final crack-widths measured after nine months have been denoted in italics while the crack-widths on the rest of the beams were measured after eighteen months of exposure. Also, cracks identified in bold in the final measurements were not witnessed during the initial measurements.

Table B1: Surface crack-widths in the OPCC beams.

Beam	**Initial number of visible cracks**	**Crack number (from top to bottom of beam)**	**Crack width (mm)**		**Final number of visible cracks**	**Crack number (from top to bottom of beam)**	**Crack width (mm)**	
			Crack open	**Crack closed**			**Crack open**	**Crack closed**
OPCC Dynamic1	2	1	0.1	0.05	4	1	0.15	0.1
		2	0.1	0.05		2	0.25	0.2
		-				**3**	0.3	0.2
		-				**4**	0.1	0
OPCC Dynamic2	2	1	0.1	0.05	4	1	0.2	0.1
		2	0.1	0.05		2	0.2	0.1
		-				**3**	0.2	0.1
		-				**4**	0.1	0.05
OPCC Dynamic 3	2	1	0.2	0.1	5	1	0.2	0.1
		2	0.2	0.1		2	0.2	0.1
		-				**3**	0.2	0.1
		-				**4**	0.2	0.15
		-				**5**	0.2	0.15
OPCC Dynamic 4	4	1	0.2	0	5	1	0.25	0.1
		2	0.3	0.1		2	0.3	0.1
		3	0.3	0.1		3	0.3	0.1
		4	0.2	0		4	0.25	0.15
		-				**5**	0.15	>0.05
OPCC Dynamic 5	5	1	0.1	0.05	5	1	0.25	0.2
		2	0.2	0.1		2	0.3	0.25
		3	0.2	0.1		3	0.3	0.2
		4	0.1	0.05		4	0.25	0.2
		-	0.2	0.1		5	0.25	0.2
OPCC Dynamic 6	2	1	0.2	0.1	4	1	0.35	0.3
		2	0.2	0.1		2	0.3	0.2
		-				**3**	0.2	0.1
		-				**4**	0.1	0.05
OPCC	4	1	0.1	0.05	4	1	0.2	0.1

Dynamic 7								
		2	0.2	0.1		2	0.2	0.1
		3	0.1	0.05		3	0.1	0.05
		4	0.05	>0.05		4	>0.05	>0.05
OPCC Dynamic 8	4	1	0.2	0.05	5	**1**	0.2	0.1
		2	0.2	0.05		2	0.2	0.1
		3	0.2	0.1		3	0.2	0.1
		4	0.2	0.1		4	0.2	0.1
		-				5	0.1	0
OPCC Static 1	3	1	0.1	N/A	3	1	0.1	N/A
		2	0.1	N/A		2	0.1	N/A
		3	0.1	N/A		3	0.1	N/A
OPCC Static 2	3	1	0.1	N/A	3	1	0.1	N/A
		2	0.15	N/A		2	0.15	N/A
		3	0.15	N/A		3	0.15	N/A
OPCC Static 3	3	1	0.1	N/A	3	1	0.1	N/A
		2	0.1	N/A		2	0.1	N/A
		3	0.1	N/A		3	0.1	N/A
OPCC Static 4	1	1	0.05	N/A	1	1	0.05	N/A
OPCC Static 5	4	1	0.15	N/A	5	1	0.15	N/A
		2	0.1	N/A		2	0.1	N/A
		3	0.05	N/A		3	0.05	N/A
		4	0.05	N/A		4	0.05	N/A
		-				**5**	>0.05	N/A
OPCC Static 6	2	1	0.2	N/A	2	1	0.2	N/A
		2	0.2	N/A		2	0.2	N/A
OPCC Static 7	5	1	0.1	N/A	5	1	0.1	N/A
		2	0.2	N/A		2	0.2	N/A
		3	0.2	N/A		3	0.2	N/A
		4	0.2	N/A		4	0.2	N/A
		5	0.1	N/A		5	0.1	N/A
OPCC Static 8	3	1	0.2	N/A	3	1	0.2	N/A
		2	0.1	N/A		2	0.1	N/A
		3	0.1	N/A		3	0.1	N/A
OPCC Unloaded 1	2	not visible			2	not visible		
OPCC Unloaded 2	4	not visible			4	not visible		

Table B2: Surface crack-widths in the HPC beams.

Beam	**Initial number of visible cracks**	**Crack number (from top to bottom of beam)**	**Crack width (mm)**		**Final number of visible cracks**	**Crack Number (from top to bottom of beam)**	**Crack width (mm)**	
			Crack open	**Crack closed**			**Crack open**	**Crack closed**
HPC Dynamic 1	4	1	0.1	0	6	1	0.2	0.1
		2	0.1	0.05		2	0.1	0.05
		3	0.25	0.2		**3**	0.25	0.2
		4	0.05	0.05		4	0.1	0.05
						5	0.15	0.1
						6	>0.05	>0.05
HPC Dynamic 2	1	1	0.1	0	5	**1**	0.15	0.05
						2	0.15	0.05
						3	0.1	0
						4	0.1	0.05
						5	0.15	0.1
HPC Dynamic 3	1	1	0.1	0	2	1	0.15	0.1
		-				**2**	0.1	0.05
HPC Dynamic 4	2	1	0.1	0.05	2	1	0.15	0.1
		2	0.05	0		2	0.1	0.05
HPC Dynamic 5	4	1	0.1	0	4	1	0.2	0.1
		2	0.15	0.05		2	0.3	0.2
		3	0.3	0.2		3	0.3	0.2
		4	0.2	0.1		4	0.25	0.2
HPC Dynamic 6	6	1	0.3	0.2	6	1	0.3	0.2
		2	0.3	0.1		2	0.3	0.2
		3	0.25	0.1		3	0.3	0.15
		4	0.2	0.1		4	0.3	0.1
		5	0.05	0		5	0.05	0
		6	0.05	0		6	0.05	0
HPC Dynamic 7	4	1	0.1	0.05	5	1	0.15	0.1
		2	0.2	0.1		2	0.2	0.1
		3	0.1	0.05		3	0.1	0.05
		4	0.05	0		4	0.05	0
		-				**5**	>0.05	>0.05
HPC Dynamic 8	4	1	0.1	0.05	5	1	0.1	0.05
		2	0.2	0.1		2	0.1	0.05
		3	0.2	0.1		3	0.1	0.05
		4	0.1	0.05		4	0.1	0

						5	0.1	0
HPC Static 1	3	1	0.1	N/A	3	1	0.1	N/A
		2	0.1	N/A		2	0.2	N/A
		3	0.1	N/A		3	0.1	N/A
HPC Static 2	3	1	0.15	N/A	4	1	0.15	N/A
		2	0.2	N/A		2	0.2	N/A
		3	0.1	N/A		3	0.1	N/A
						4	>0.05	N/A
HPC Static 3	4	1	0.2	N/A	4	1	0.2	N/A
		2	0.2	N/A		2	0.2	N/A
		3	0.2	N/A		3	0.2	N/A
		4	0.2	N/A		4	0.2	N/A
HPC Static 4	3	1	0.2	N/A	3	1	0.2	N/A
		2	0.2	N/A		2	0.2	N/A
		3	0.2	N/A		3	0.2	N/A
HPC Static 5	7	1	0.1	N/A	8	1	0.1	N/A
		2	0.15	N/A		2	0.15	N/A
		3	0.15	N/A		3	0.15	N/A
		4	0.15	N/A		4	0.15	N/A
		5	0.15	N/A		5	0.15	N/A
		6	0.2	N/A		6	0.2	N/A
		7	0.1	N/A		7	0.1	N/A
						8	**>0.05**	N/A
HPC Static 6	5	1	0.1	N/A	5	1	0.1	N/A
		2	0.1	N/A		2	0.1	N/A
		3	0.1	N/A		3	0.1	N/A
		4	0.15	N/A		4	0.2	N/A
		5	0.15	N/A		5	0.15	N/A
HPC Static 7	5	1	0.15	N/A	5	1	0.15	N/A
		2	0.2	N/A		2	0.2	N/A
		3	0.2	N/A		3	0.2	N/A
		4	0.15	N/A		4	0.15	N/A
		5	0.15	N/A		5	0.15	N/A
HPC Static 8	3	1	0.25	N/A	4	1	0.25	N/A
		2	0.2	N/A		**2**	0.05	N/A
		3	0.25	N/A		3	0.2	N/A
						4	0.25	N/A
HPC Unloaded 1	5	not visible			6	1	not visible	
						2	not	

							visible	
						3	>0.05	
						4	>0.05	
						5	0.05	
						6	0.05	
HPC Unloaded 2	6	not visible			6	1	not visible	
						2	not visible	
						3	0.05	
						4	0.05	
						5	>0.05	
						6	0.05	

Appendix C - Current density data from LPR and galvanostatic pulse techniques

The number format on the y-axis of the plots is of the form 1.00E-02 which translates to $1x10^{-2}$.

(a)

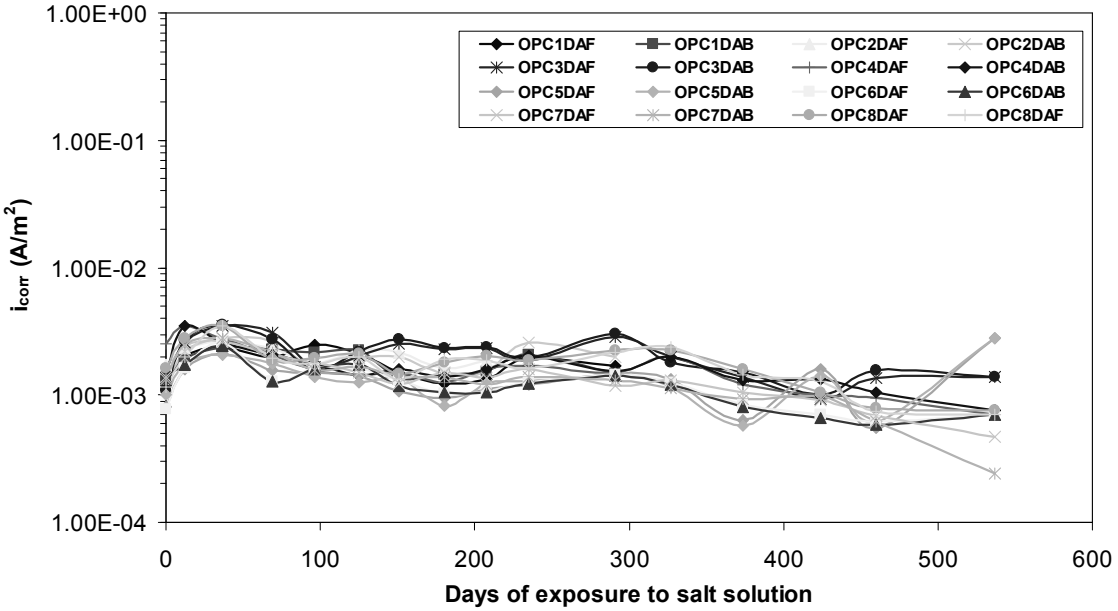

(b)

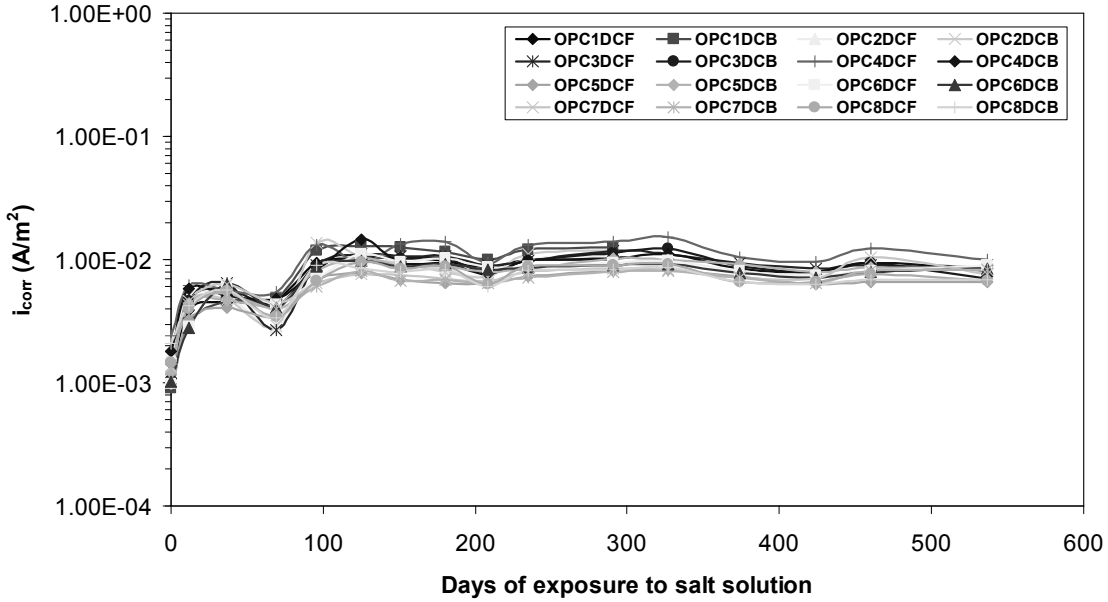

(c)

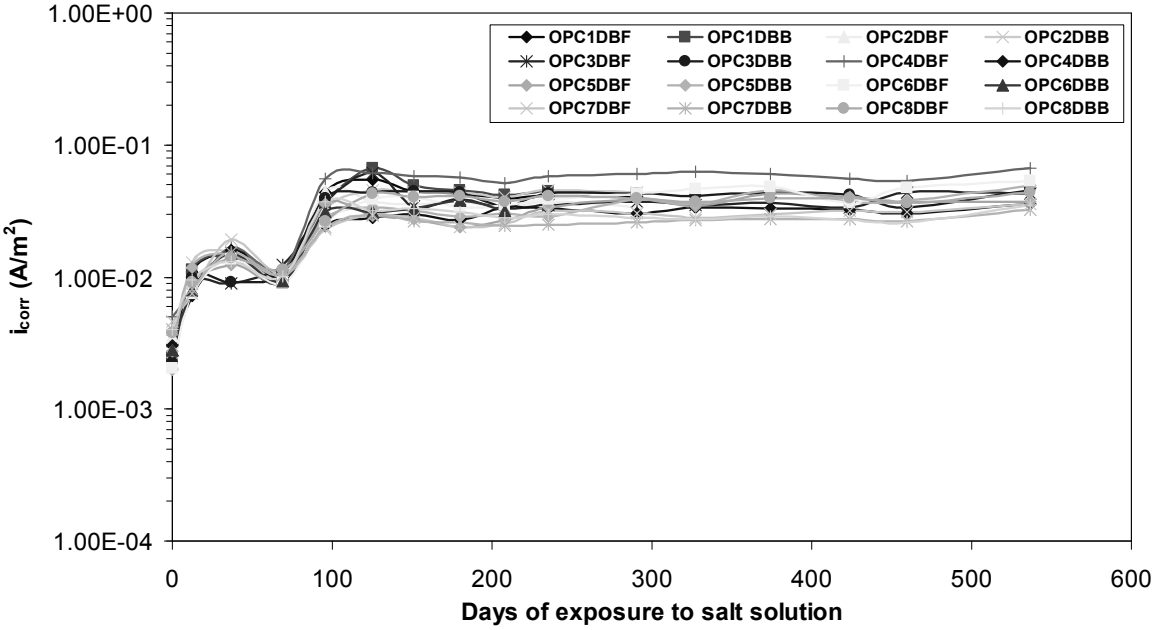

Figure C1: Corrosion current density obtained in the (a) non-submerged, (b) submerged and (c) cracked regions of the dynamically loaded OPCC beams using LPR technique.

(a)

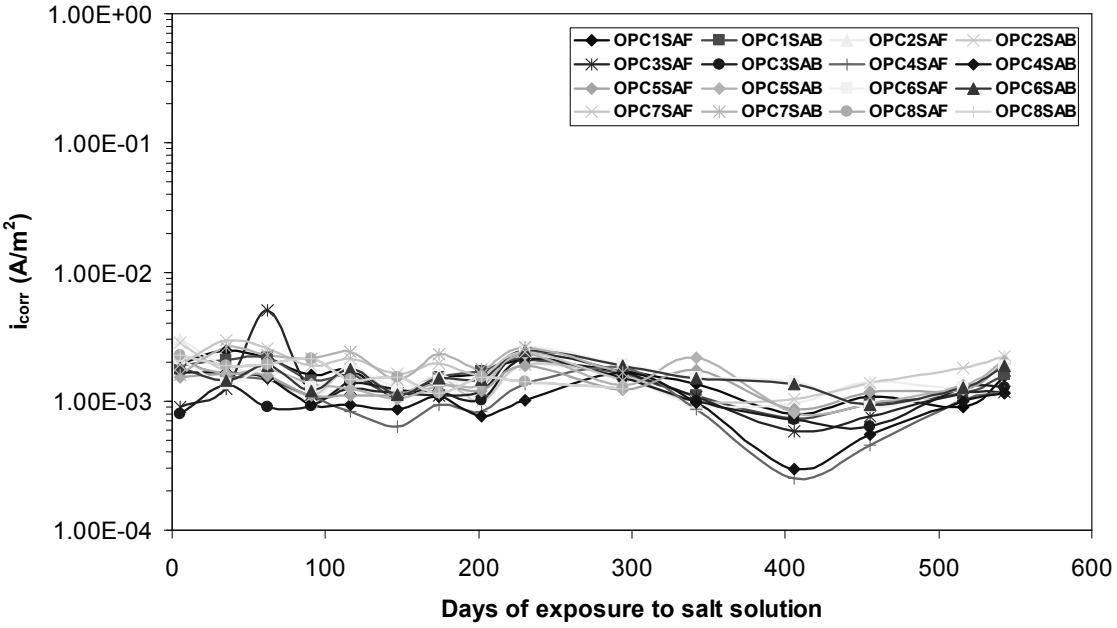

(b)

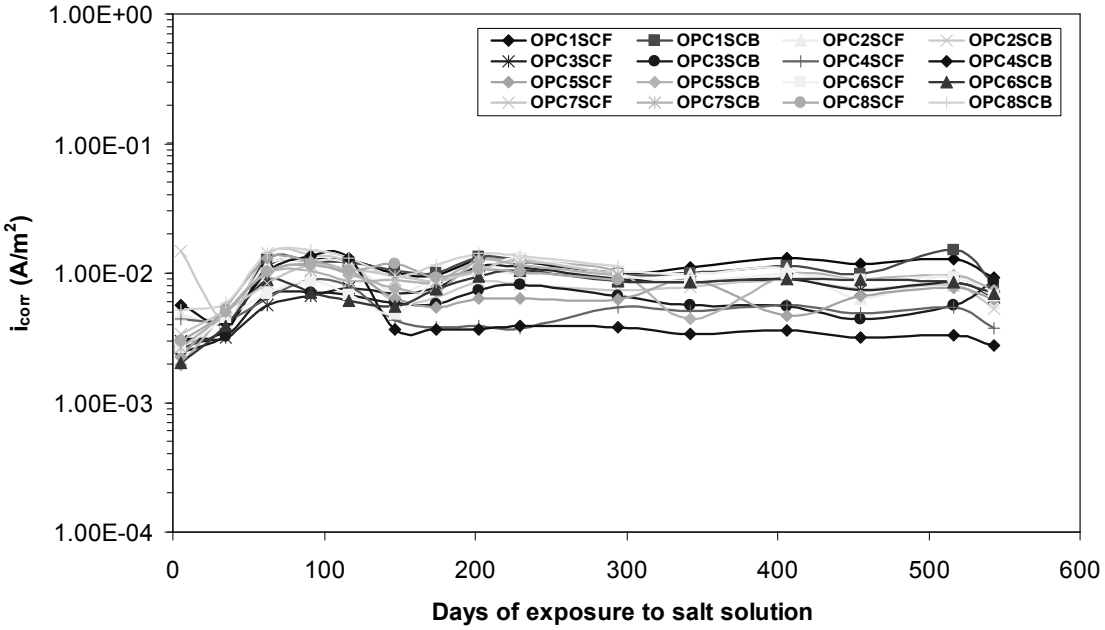

(c)

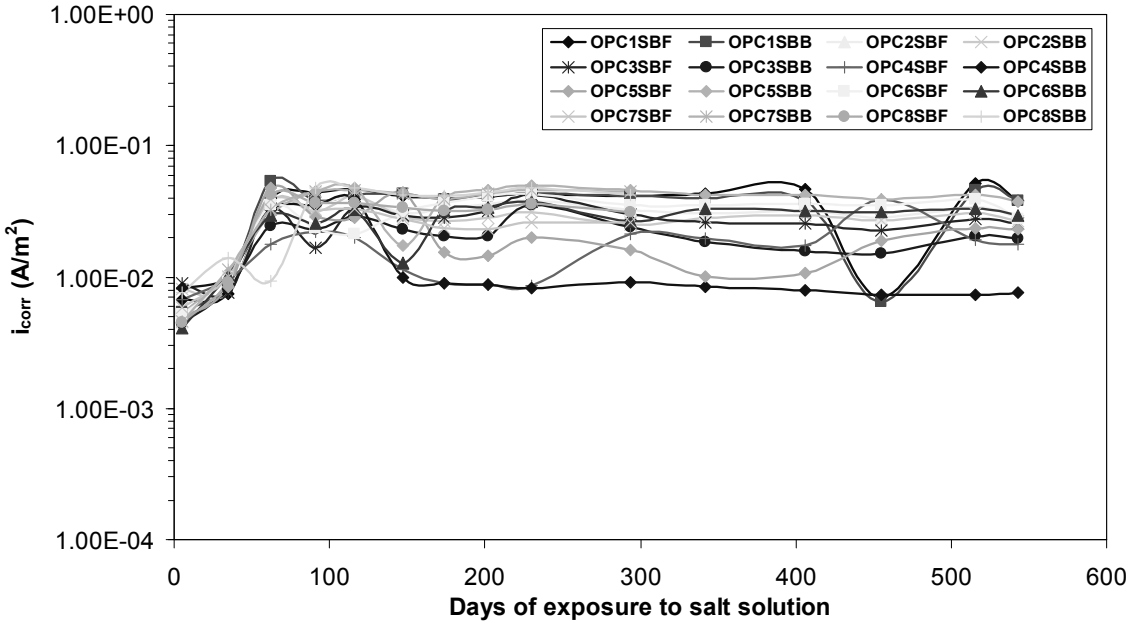

Figure C2: Corrosion current density obtained in the (a) non-submerged, (b) submerged and (c) cracked regions of the statically loaded OPCC beams using LPR technique.

(a)

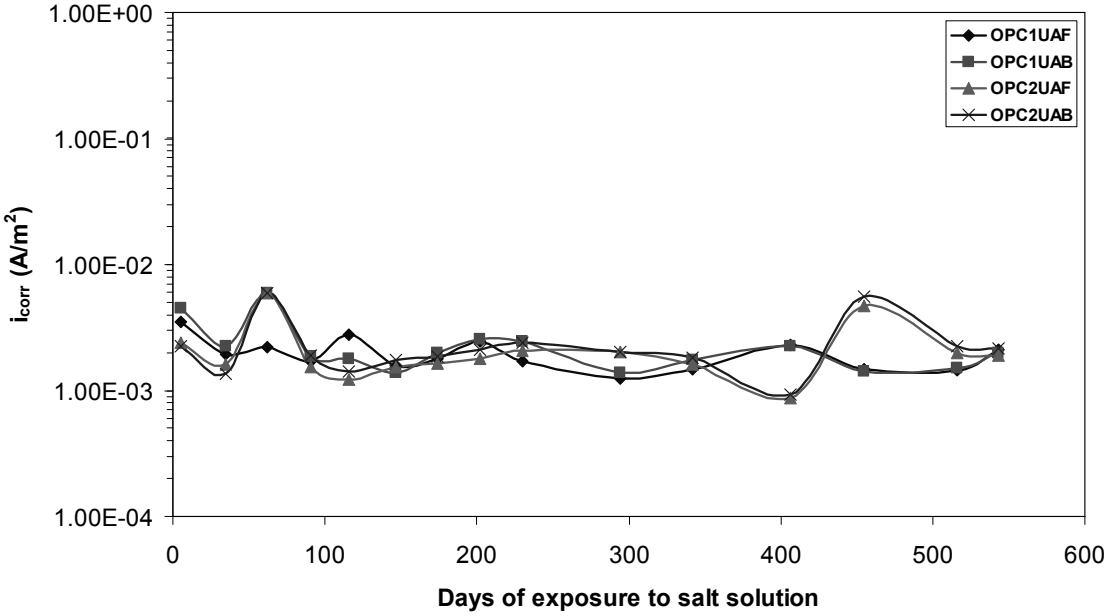
1.00E+00
1.00E-01
1.00E-02
1.00E-03
1.00E-04
i_{corr} (A/m^2)
0
100
200
300
400
500
600
Days of exposure to salt solution
OPC1UAF
OPC1UAB
OPC2UAF
OPC2UAB

(b)

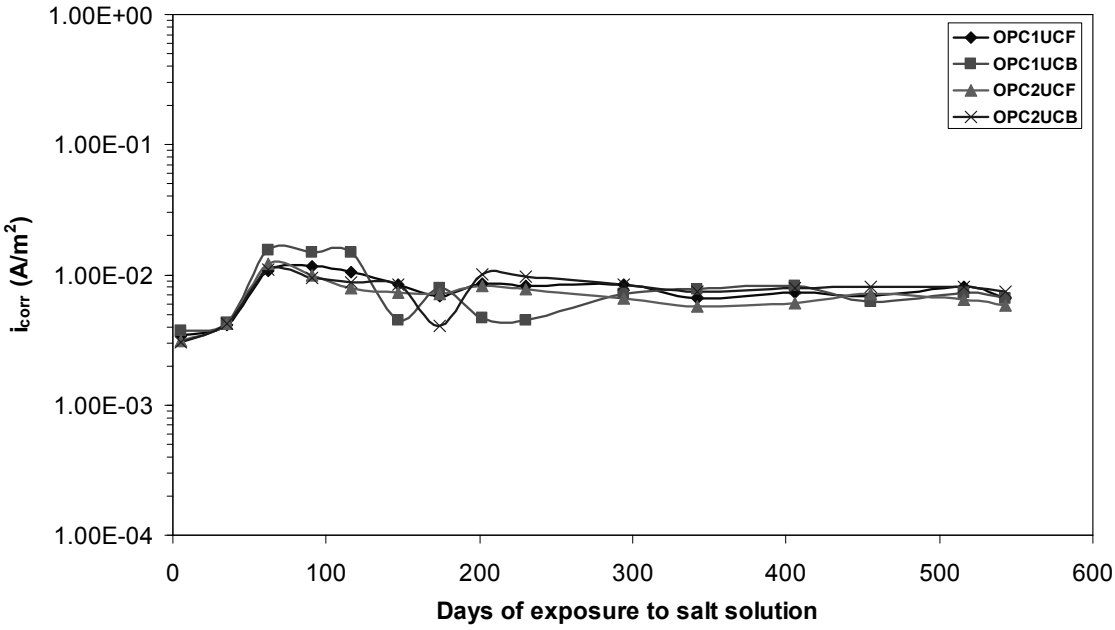
1.00E+00
1.00E-01
1.00E-02
1.00E-03
1.00E-04
i_{corr} (A/m^2)
0
100
200
300
400
500
600
Days of exposure to salt solution
OPC1UCF
OPC1UCB
OPC2UCF
OPC2UCB

(c)

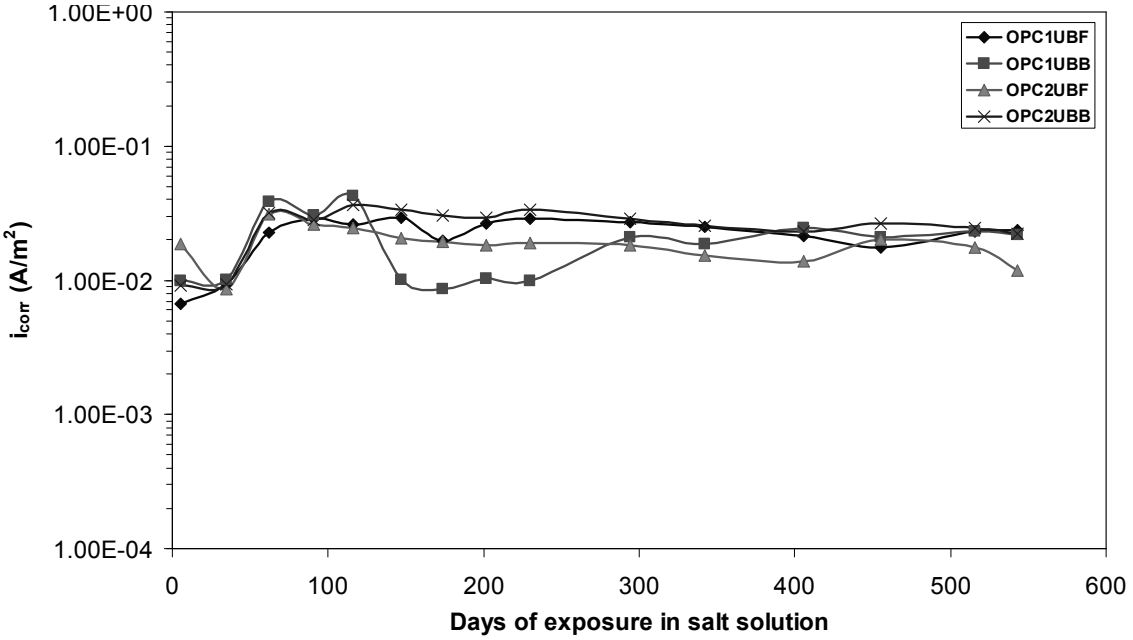

Figure C3: Corrosion current density obtained in the (a) non-submerged, (b) submerged and (c) cracked regions of the unloaded OPCC beams using LPR technique.

(a)

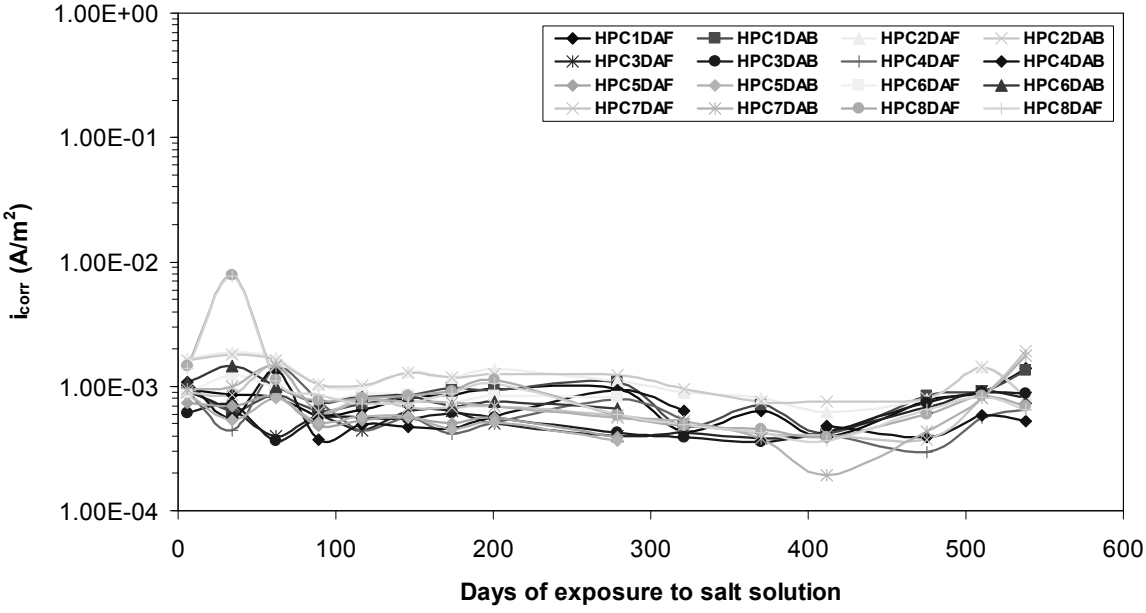

(b)

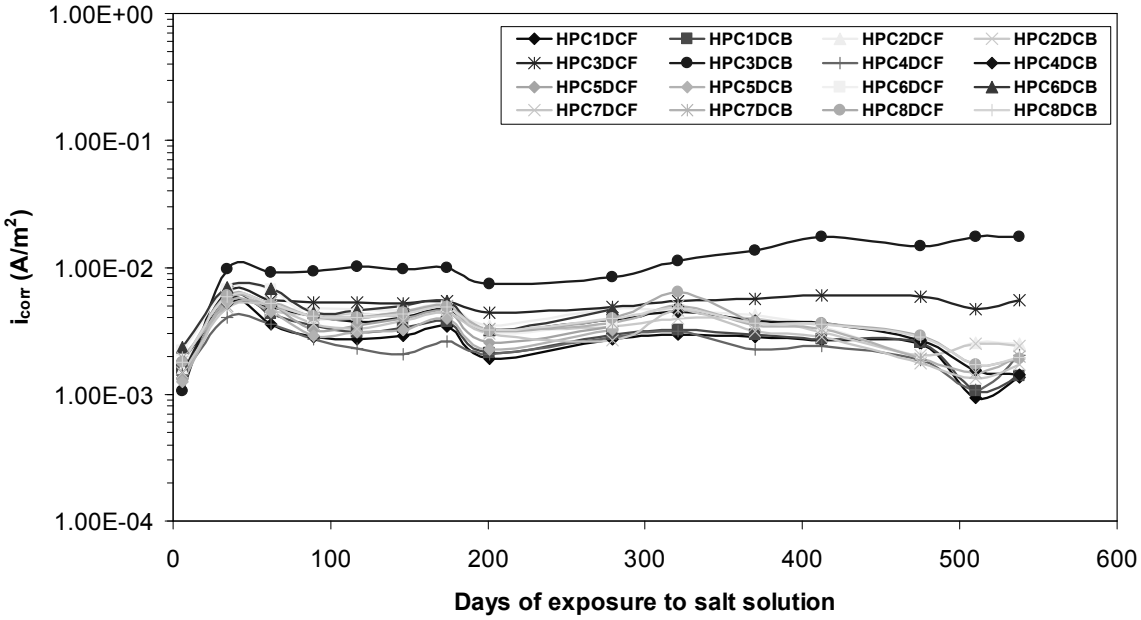

(c)

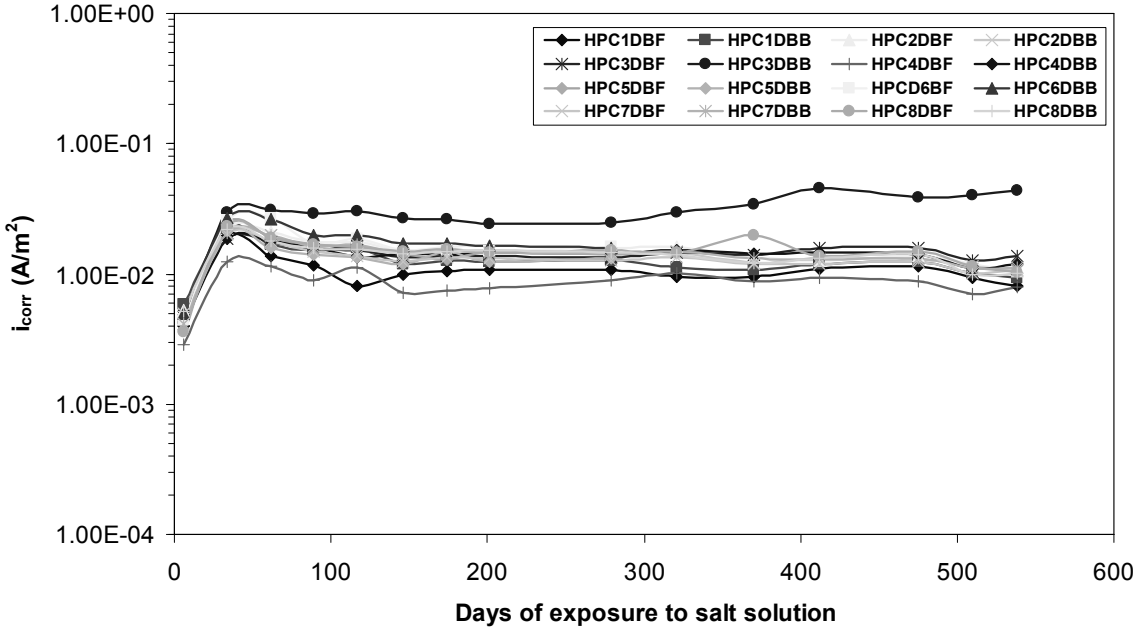

Figure C4: Corrosion current density obtained in the (a) non-submerged, (b) submerged and (c) cracked regions of the dynamically loaded HPC beams using LPR technique.

(a)

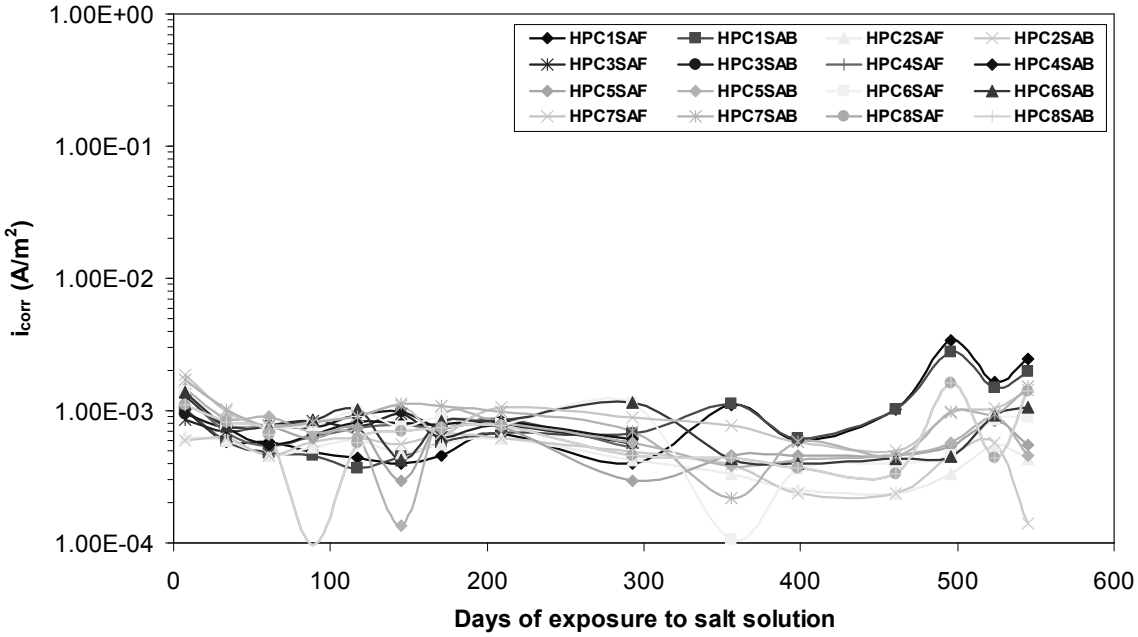
1.00E+00
1.00E-01
1.00E-02
1.00E-03
1.00E-04
i_{corr} (A/m^2)
0
100
200
300
400
500
600
Days of exposure to salt solution
HPC1SAF
HPC1SAB
HPC2SAF
HPC2SAB
HPC3SAF
HPC3SAB
HPC4SAF
HPC4SAB
HPC5SAF
HPC5SAB
HPC6SAF
HPC6SAB
HPC7SAF
HPC7SAB
HPC8SAF
HPC8SAB

(b)

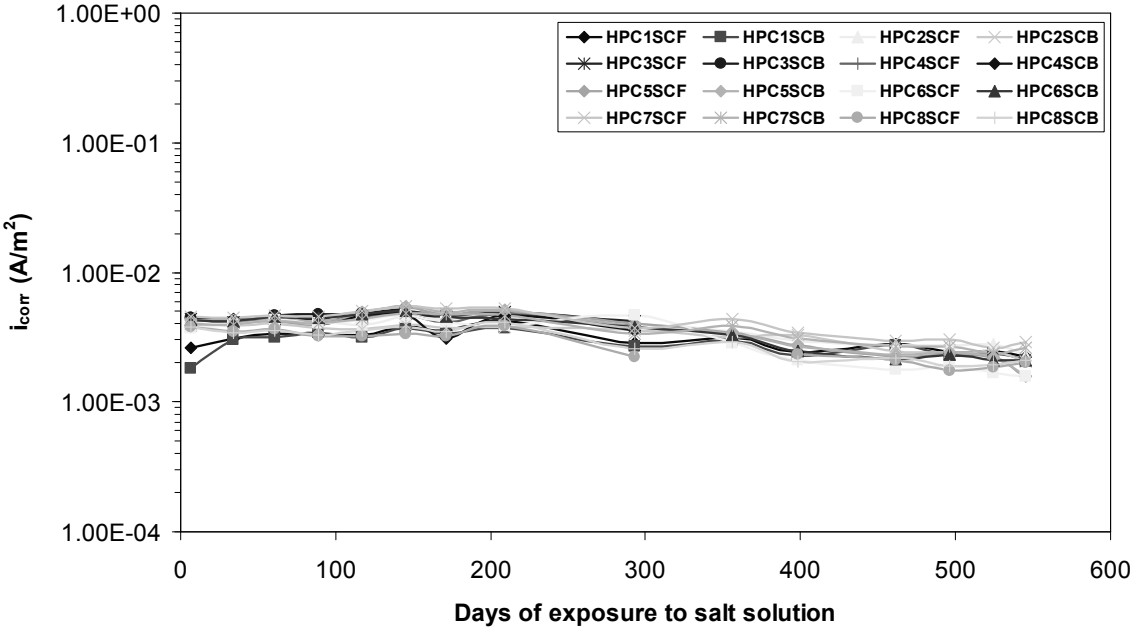
1.00E+00
1.00E-01
1.00E-02
1.00E-03
1.00E-04
i_{corr} (A/m^2)
0
100
200
300
400
500
600
Days of exposure to salt solution
HPC1SCF
HPC1SCB
HPC2SCF
HPC2SCB
HPC3SCF
HPC3SCB
HPC4SCF
HPC4SCB
HPC5SCF
HPC5SCB
HPC6SCF
HPC6SCB
HPC7SCF
HPC7SCB
HPC8SCF
HPC8SCB

(c)

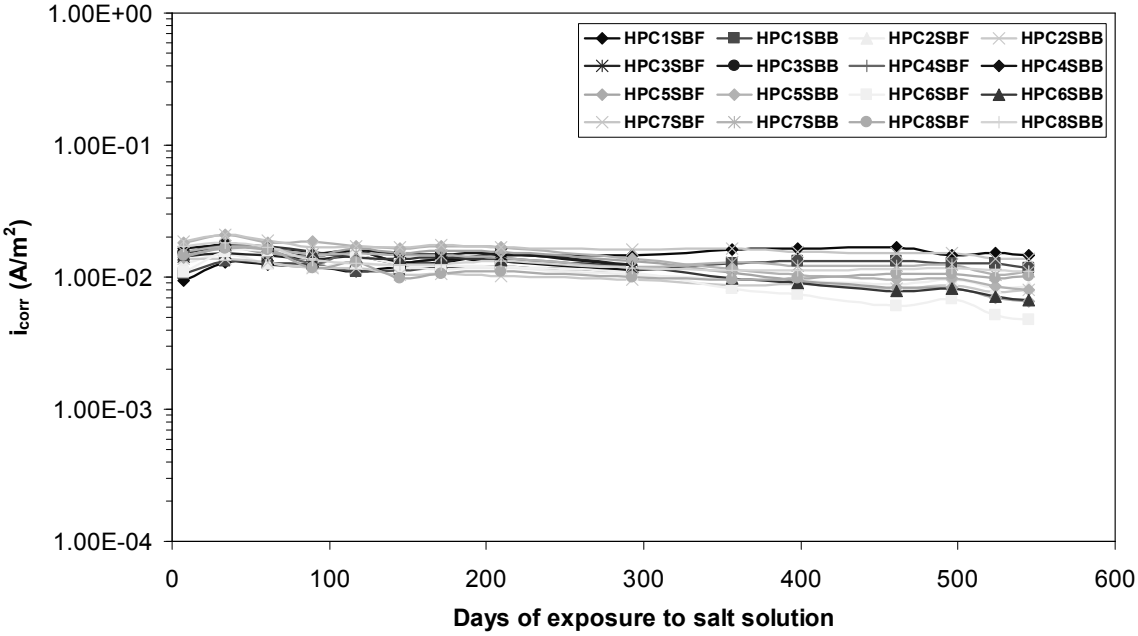

Figure C5: current density obtained in the (a) non-submerged, (b) submerged and (c) cracked regions of the statically loaded HPC beams using LPR technique.

(a)

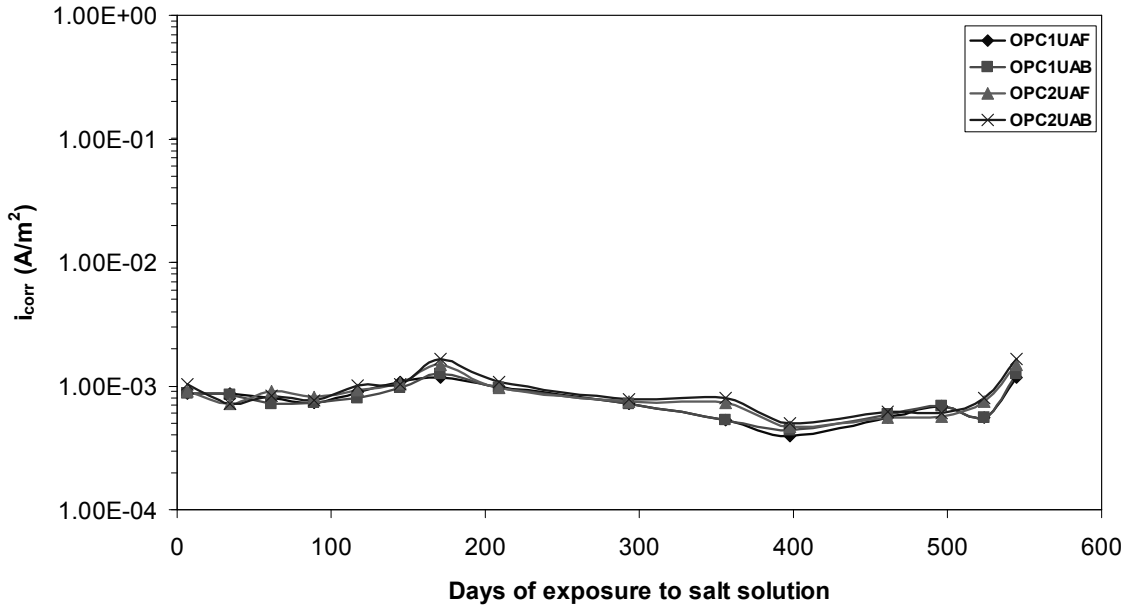

(b)

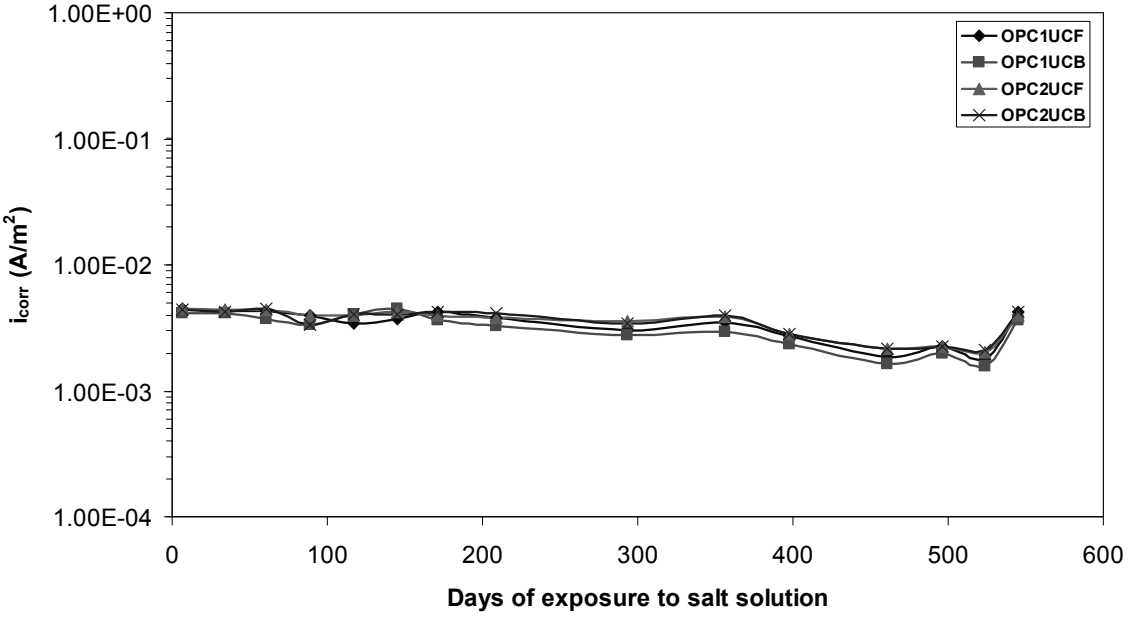

(c)

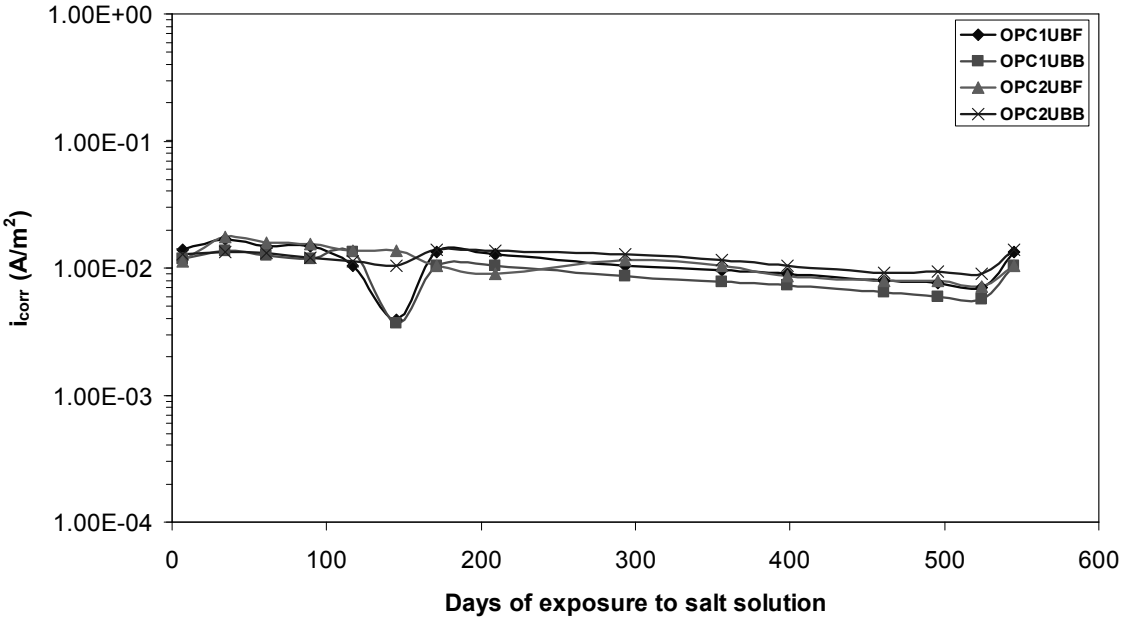

Figure C6: current density obtained in the (a) non-submerged, (b) submerged and (c) cracked regions of the unloaded HPC beams using LPR technique.

(a)

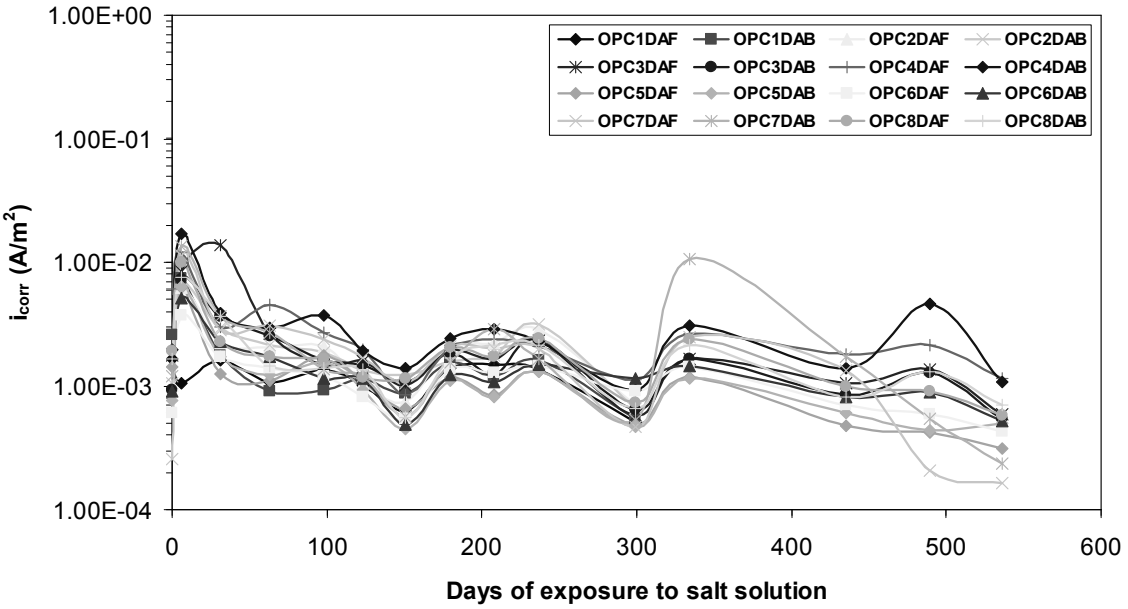
1.00E+00
1.00E-01
1.00E-02
1.00E-03
1.00E-04
icorr (A/m2)
0
100
200
300
400
500
600
Days of exposure to salt solution
OPC1DAF
OPC1DAB
OPC2DAF
OPC2DAB
OPC3DAF
OPC3DAB
OPC4DAF
OPC4DAB
OPC5DAF
OPC5DAB
OPC6DAF
OPC6DAB
OPC7DAF
OPC7DAB
OPC8DAF
OPC8DAB

(b)

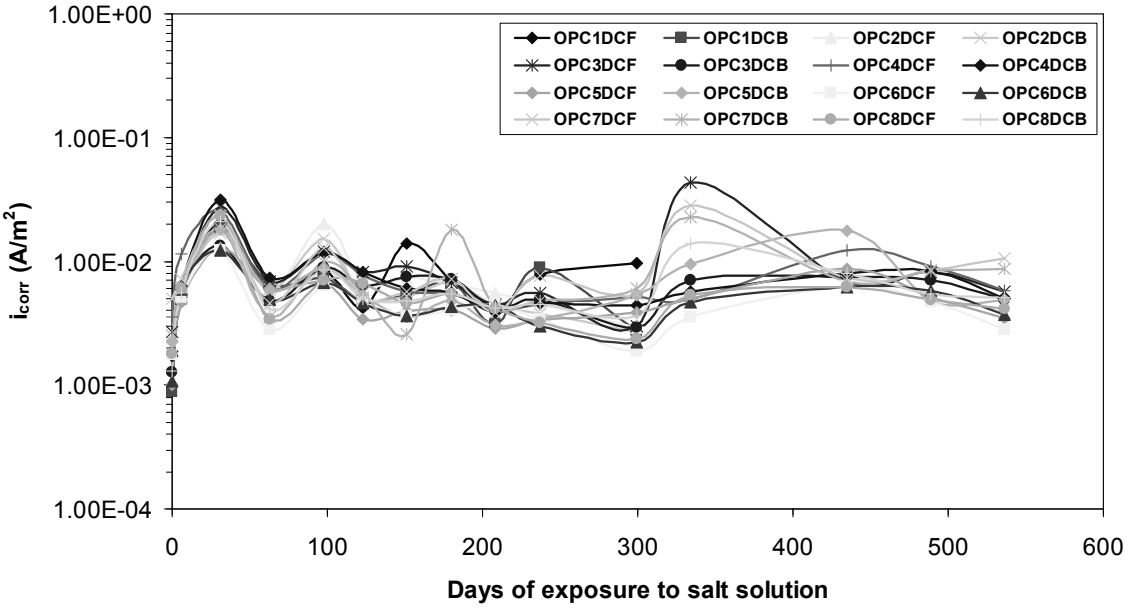
1.00E+00
1.00E-01
1.00E-02
1.00E-03
1.00E-04
icorr (A/m2)
0
100
200
300
400
500
600
Days of exposure to salt solution
OPC1DCF
OPC1DCB
OPC2DCF
OPC2DCB
OPC3DCF
OPC3DCB
OPC4DCF
OPC4DCB
OPC5DCF
OPC5DCB
OPC6DCF
OPC6DCB
OPC7DCF
OPC7DCB
OPC8DCF
OPC8DCB

(c)

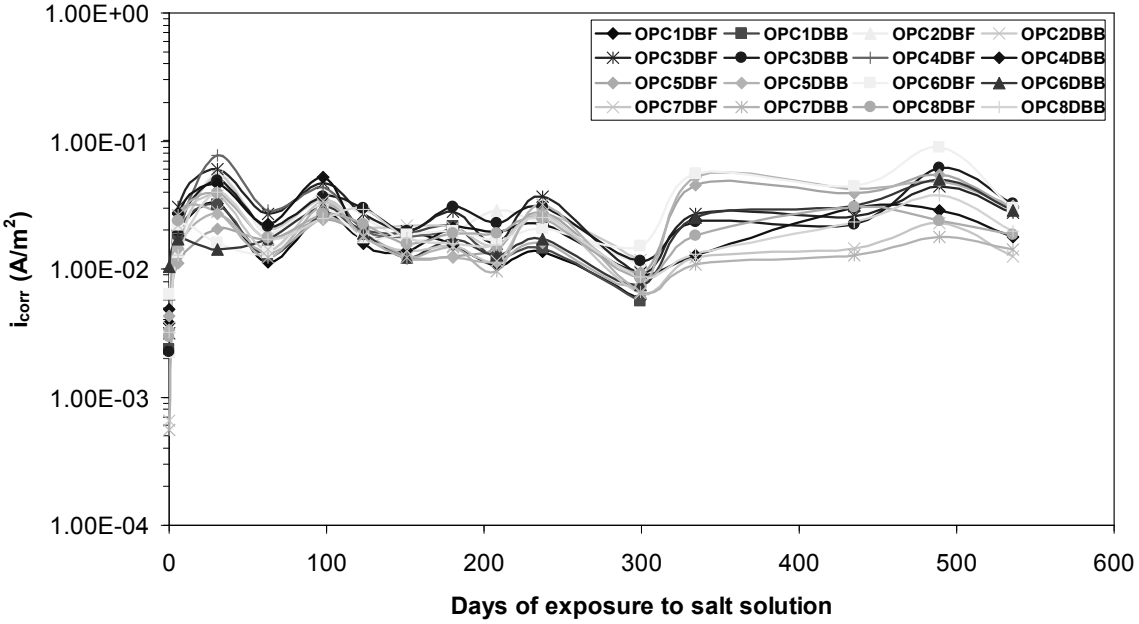

Figure C7: Corrosion current density obtained in the (a) non-submerged, (b) submerged and (c) cracked regions of the dynamically loaded OPCC beams using galvanostatic pulse technique.

(a)

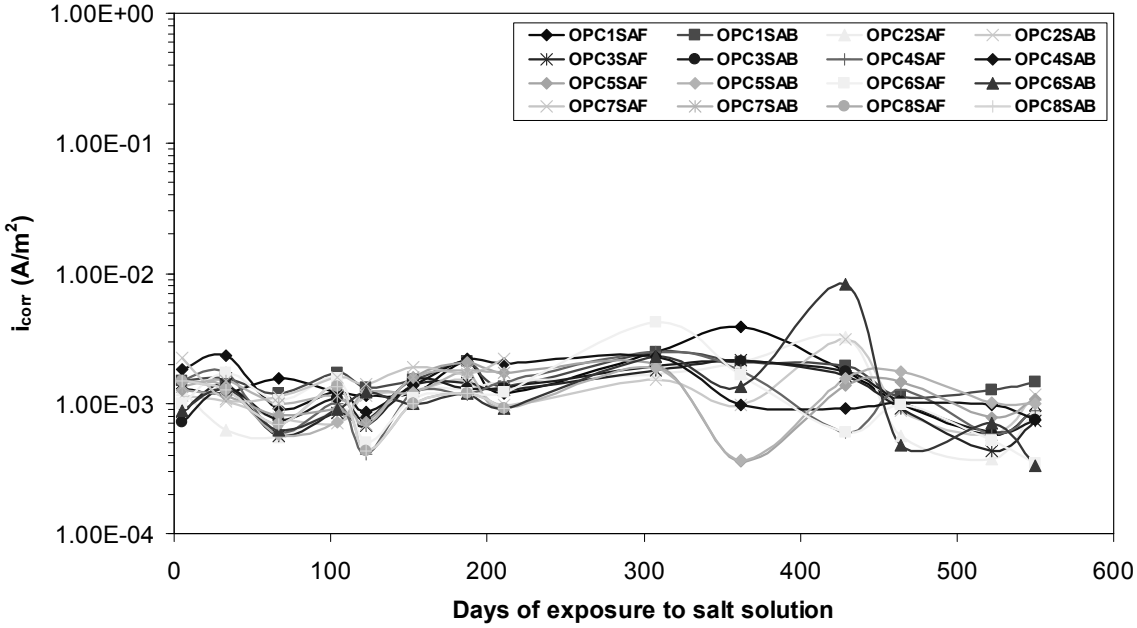

(b)

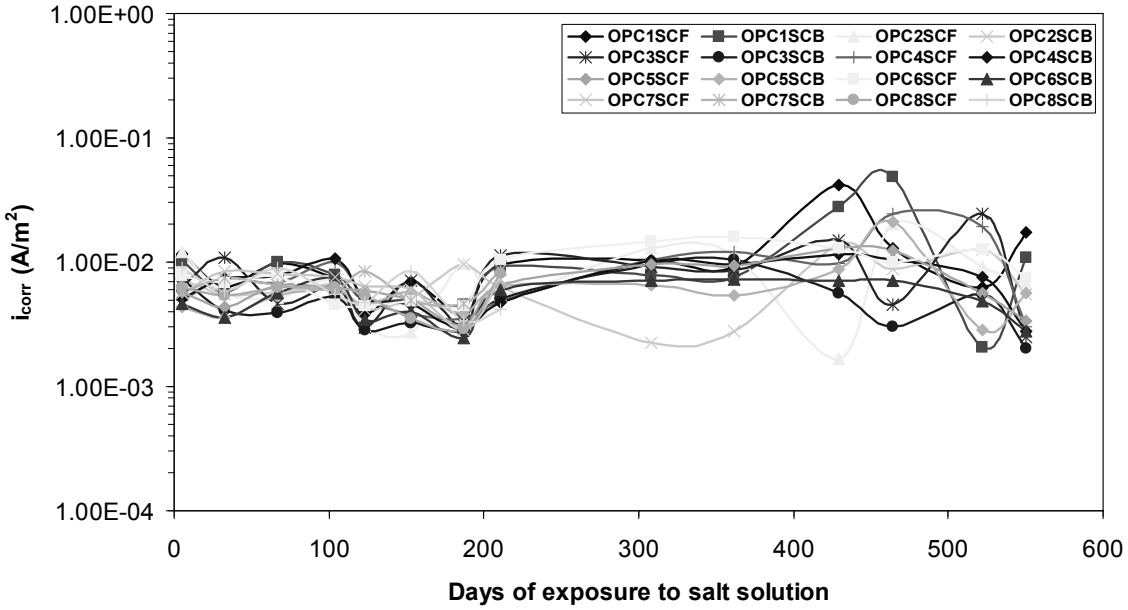

(c)

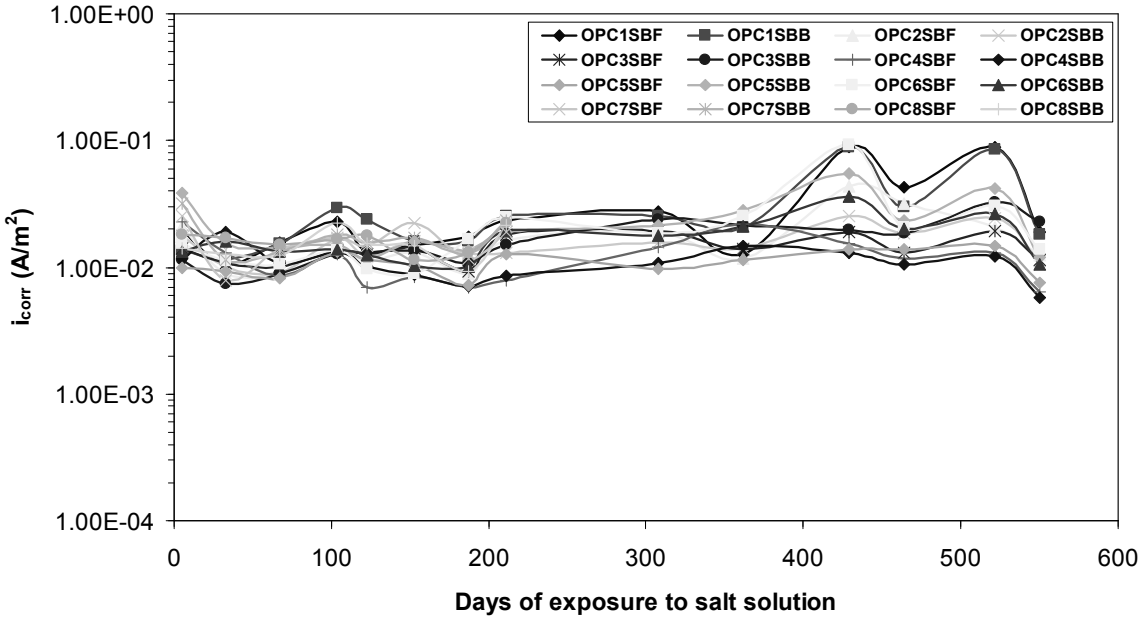

Figure C8: Corrosion current density obtained in the (a) non-submerged, (b) submerged and (c) cracked regions of the statically loaded OPCC beams using galvanostatic pulse technique.

(a)

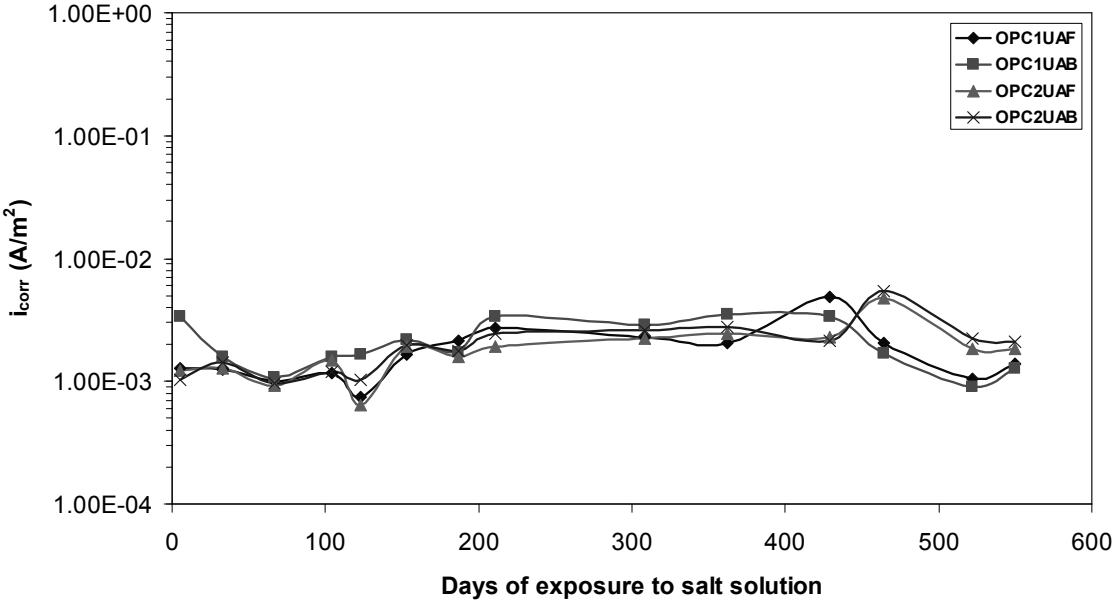
1.00E+00
1.00E-01
1.00E-02
1.00E-03
1.00E-04
i_{corr} (A/m^2)
0
100
200
300
400
500
600
Days of exposure to salt solution
OPC1UAF
OPC1UAB
OPC2UAF
OPC2UAB

(b)

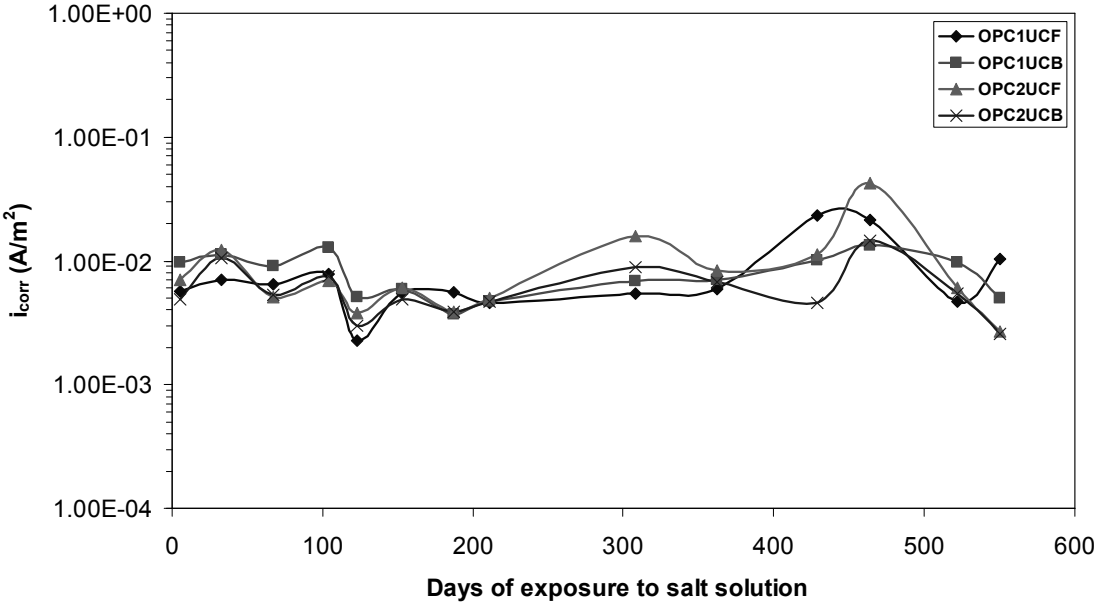
1.00E+00
1.00E-01
1.00E-02
1.00E-03
1.00E-04
i_{corr} (A/m^2)
0
100
200
300
400
500
600
Days of exposure to salt solution
OPC1UCF
OPC1UCB
OPC2UCF
OPC2UCB

(c)

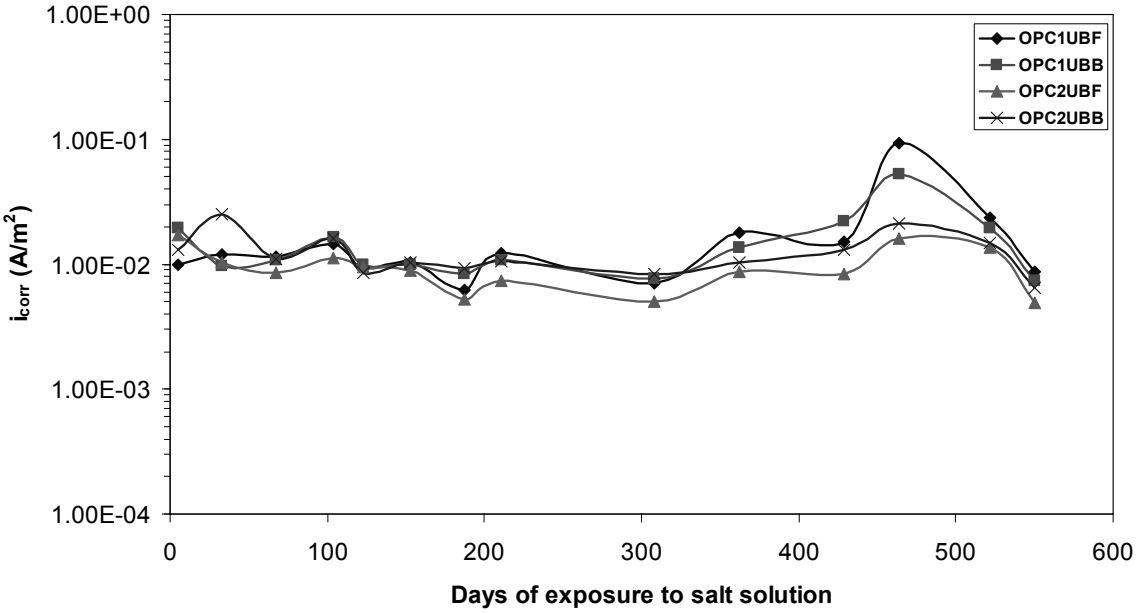

Figure C9: Corrosion current density obtained in the (a) non-submerged, (b) submerged and (c) cracked regions of the unloaded OPCC beams using galvanostatic pulse technique.

(a)

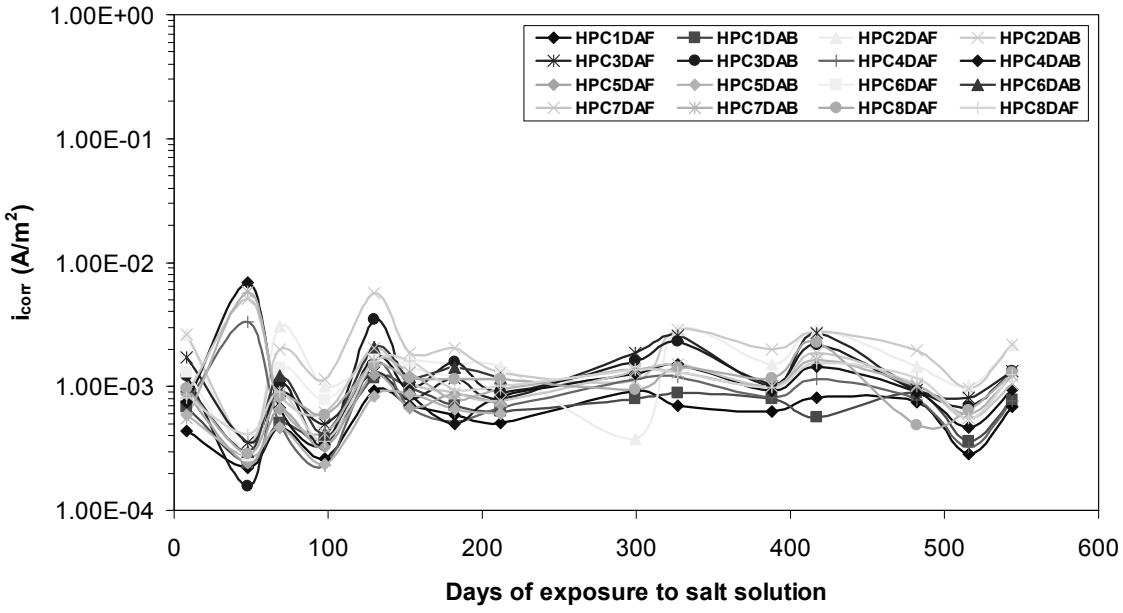

(b)

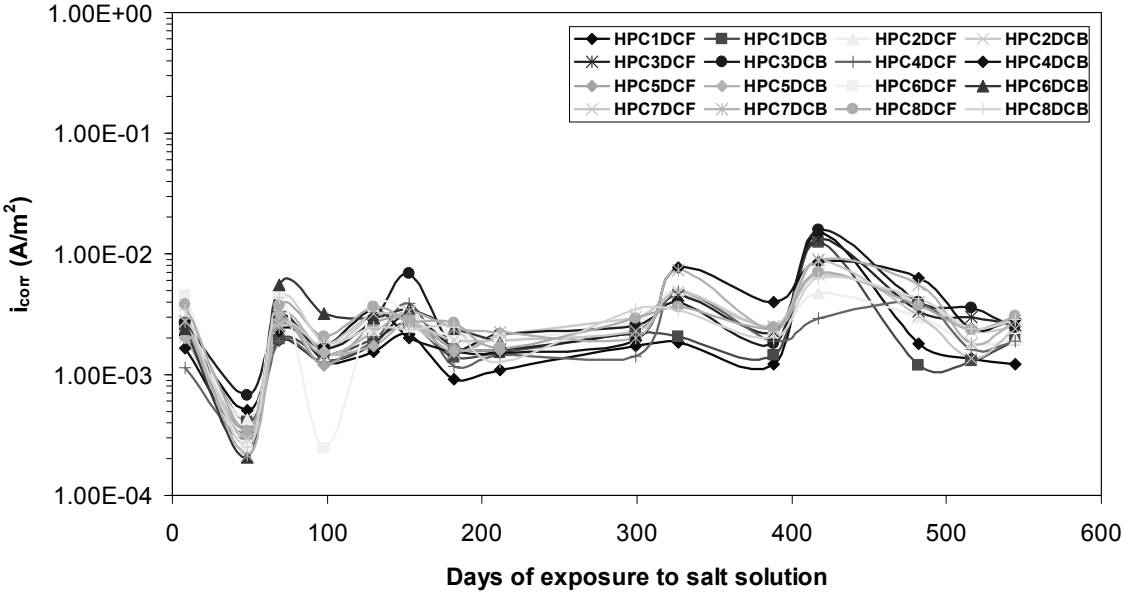

(c)

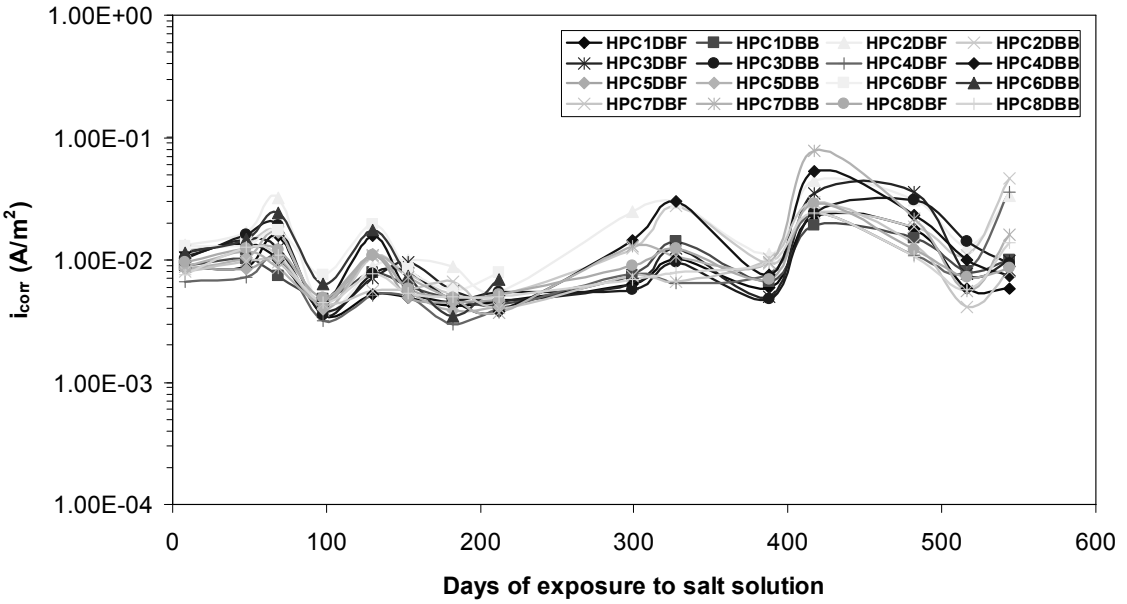

Figure C10: Corrosion current density obtained in the (a) non-submerged, (b) submerged and (c) cracked regions of the dynamically loaded HPC beams using galvanostatic pulse technique.

(a)

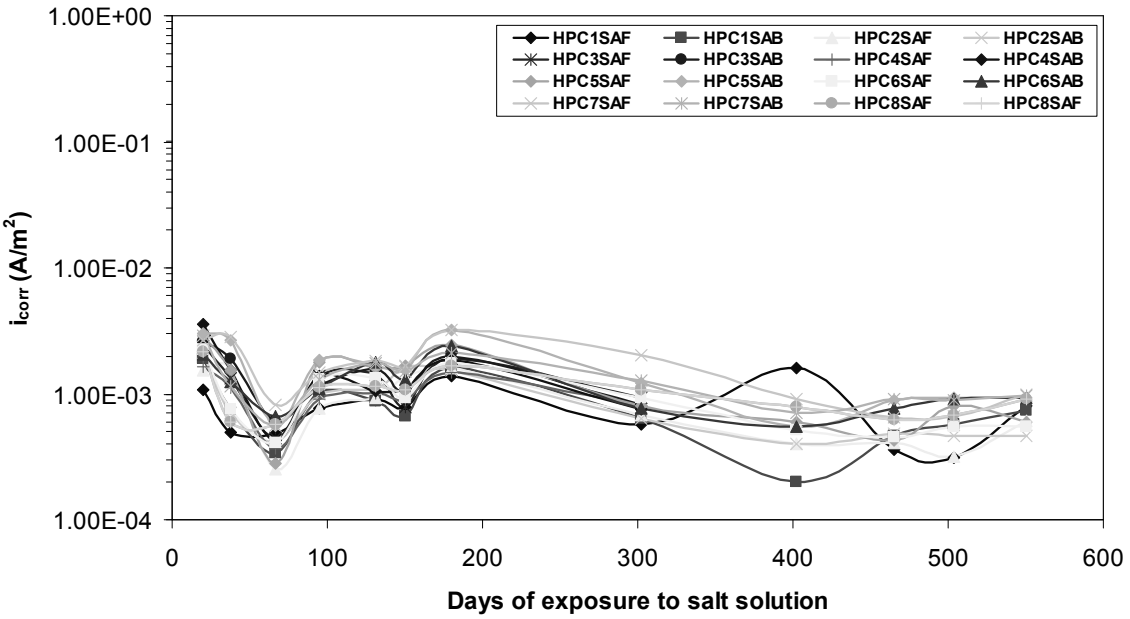
1.00E+00
1.00E-01
1.00E-02
1.00E-03
1.00E-04
icorr (A/m2)
0
100
200
300
400
500
600
Days of exposure to salt solution
HPC1SAF
HPC1SAB
HPC2SAF
HPC2SAB
HPC3SAF
HPC3SAB
HPC4SAF
HPC4SAB
HPC5SAF
HPC5SAB
HPC6SAF
HPC6SAB
HPC7SAF
HPC7SAB
HPC8SAF
HPC8SAF

(b)

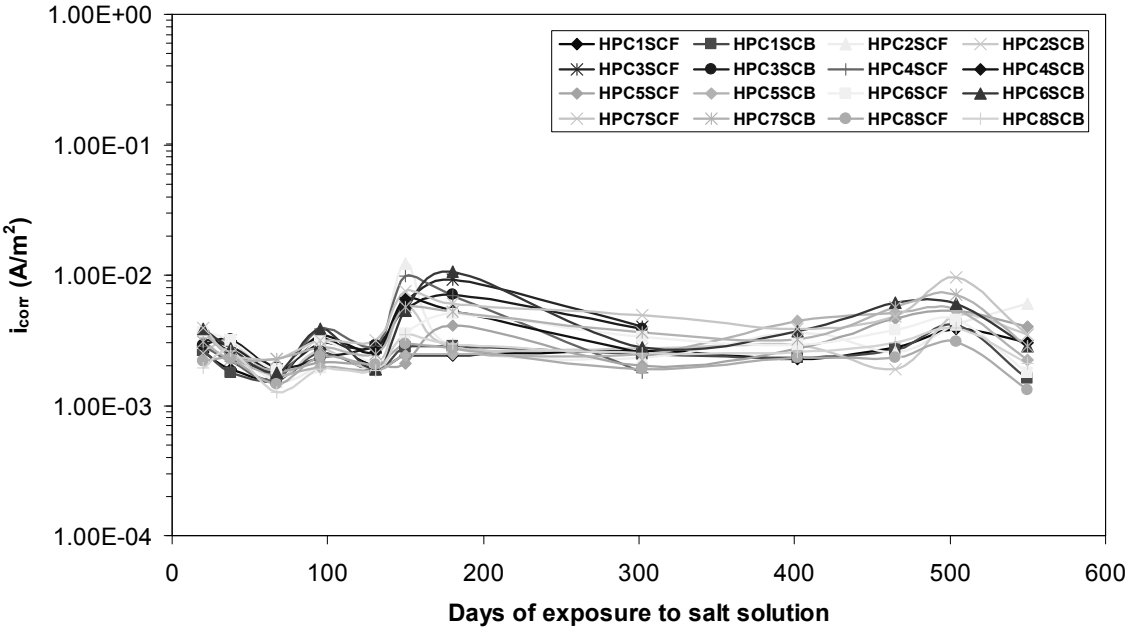
1.00E+00
1.00E-01
1.00E-02
1.00E-03
1.00E-04
icorr (A/m2)
0
100
200
300
400
500
600
Days of exposure to salt solution
HPC1SCF
HPC1SCB
HPC2SCF
HPC2SCB
HPC3SCF
HPC3SCB
HPC4SCF
HPC4SCB
HPC5SCF
HPC5SCB
HPC6SCF
HPC6SCB
HPC7SCF
HPC7SCB
HPC8SCF
HPC8SCB

(c)

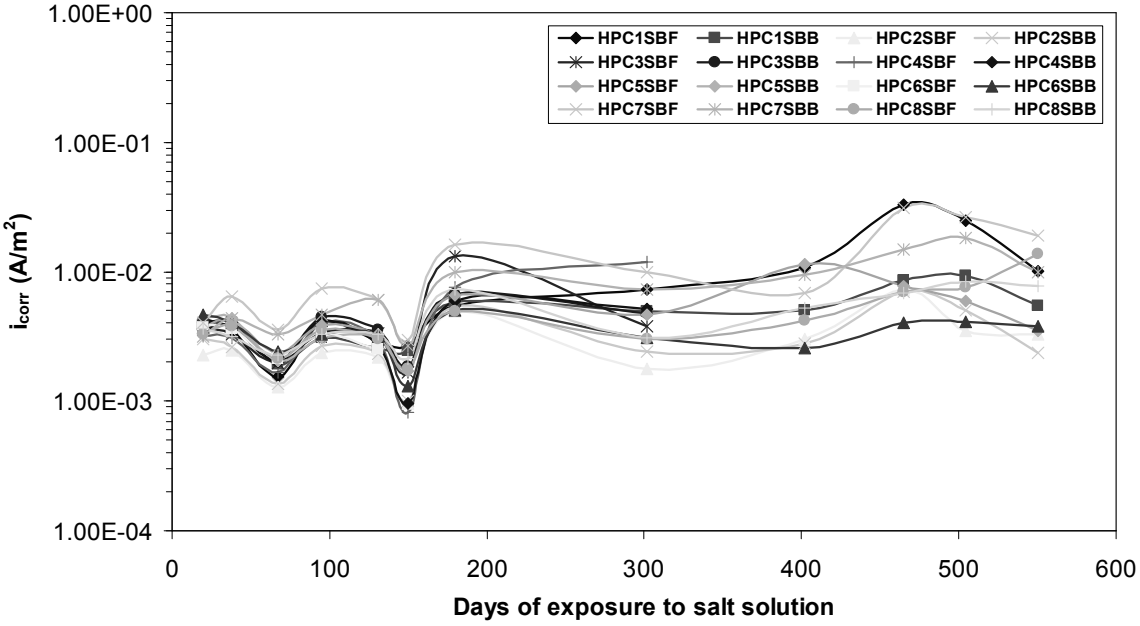

Figure C11: current density obtained in the (a) non-submerged, (b) submerged and (c) cracked regions of the statically loaded HPC beams using galvanostatic pulse technique.

(a)

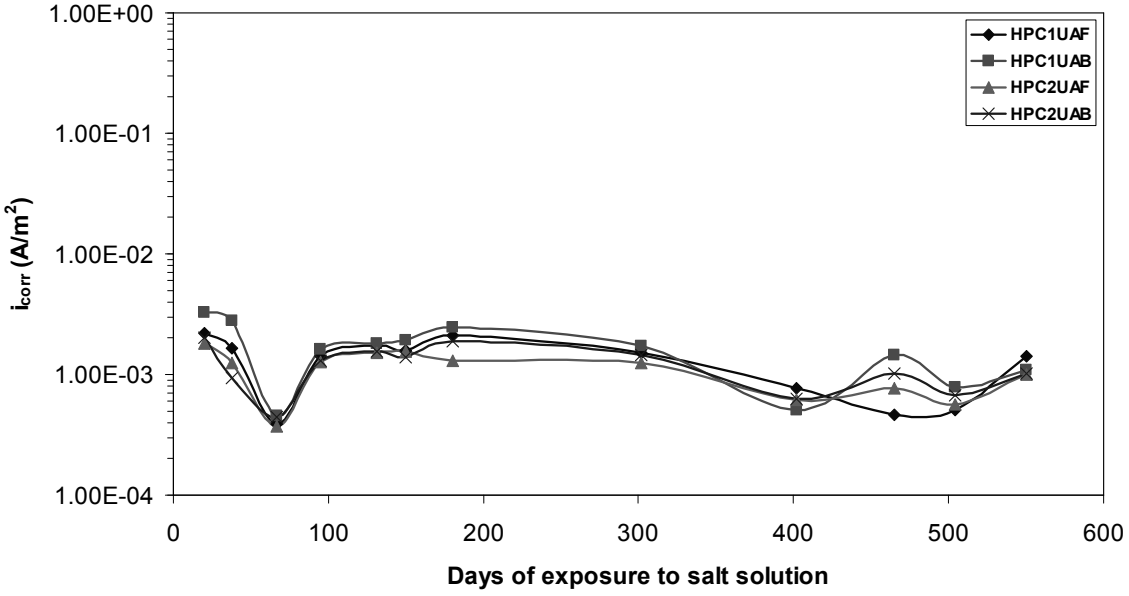

(b)

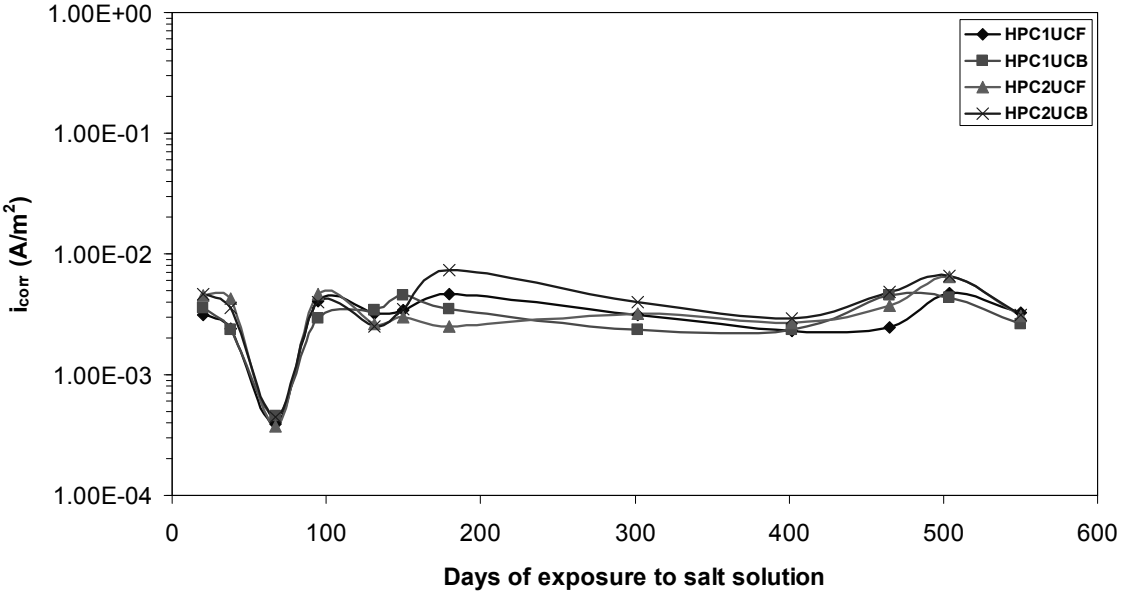

(c)

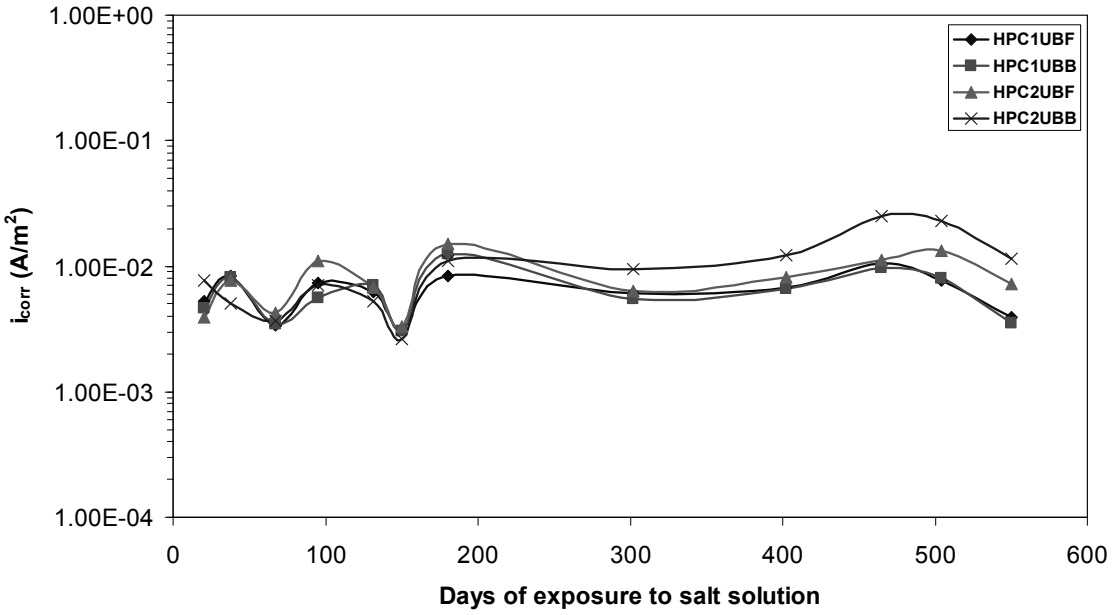

Figure C12: current density obtained in the (a) non-submerged, (b) submerged and (c) cracked regions of the unloaded HPC beams using galvanostatic pulse technique.

Appendix D - Corroding areas on rebar matched with cracks in the concrete

OPCC dynamic beam 3

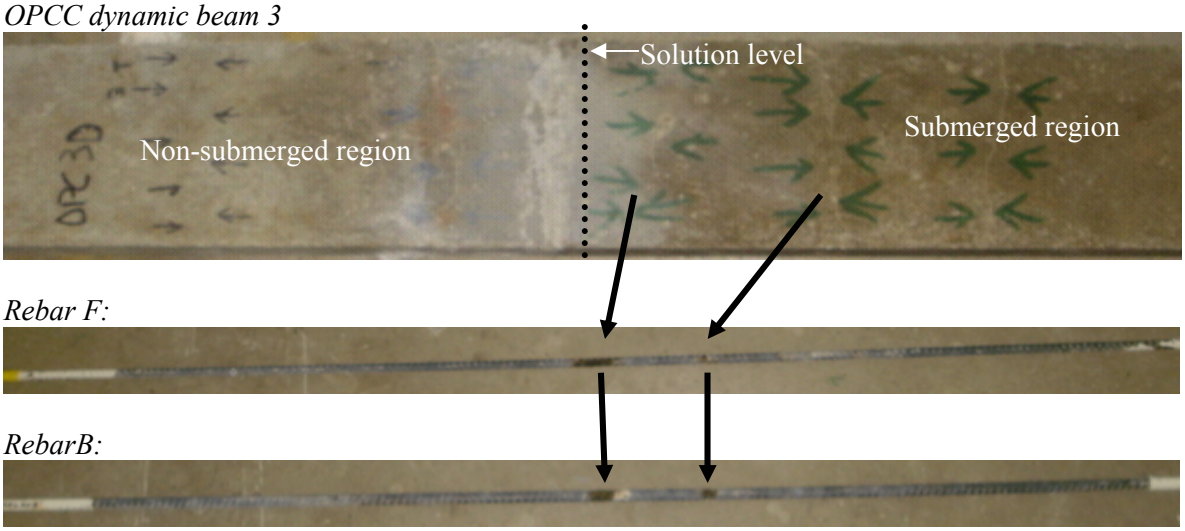

OPCC dynamic beam 4:

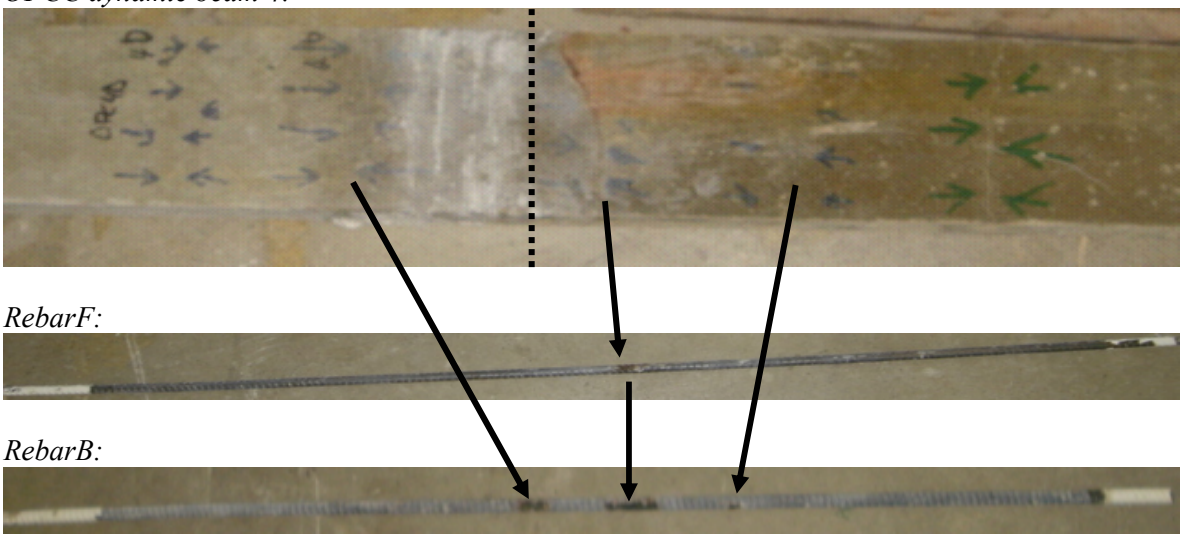

OPCC dynamic beam 7

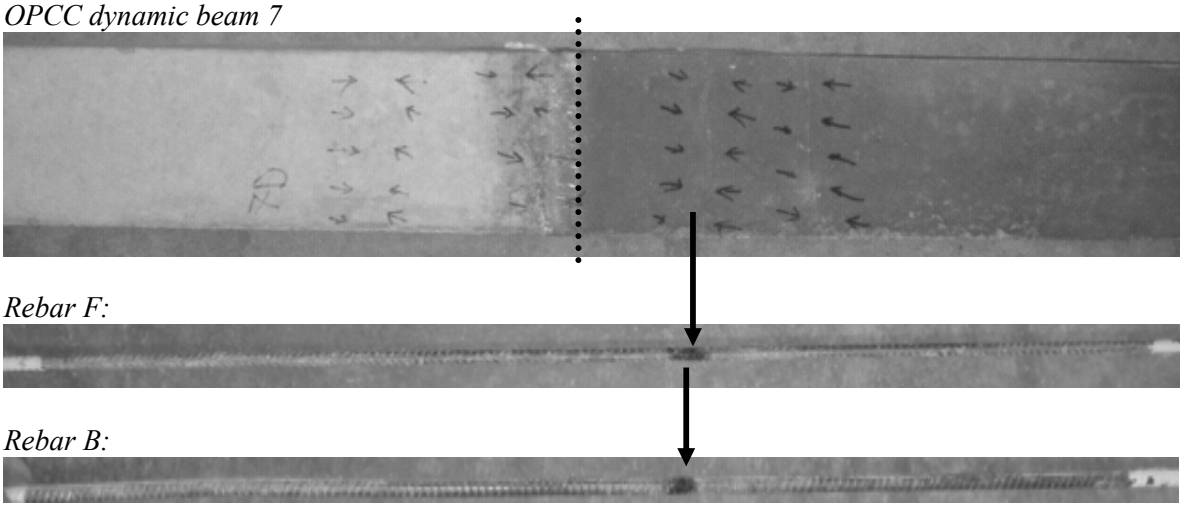

Rebar F:

Rebar B:

OPCC dynamic beam 8

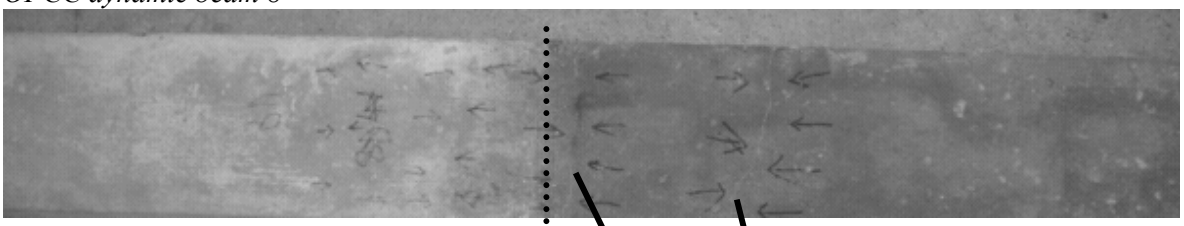

Rebar F:

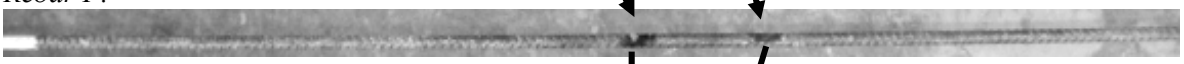

RebarB:

OPCC Static beam 3:

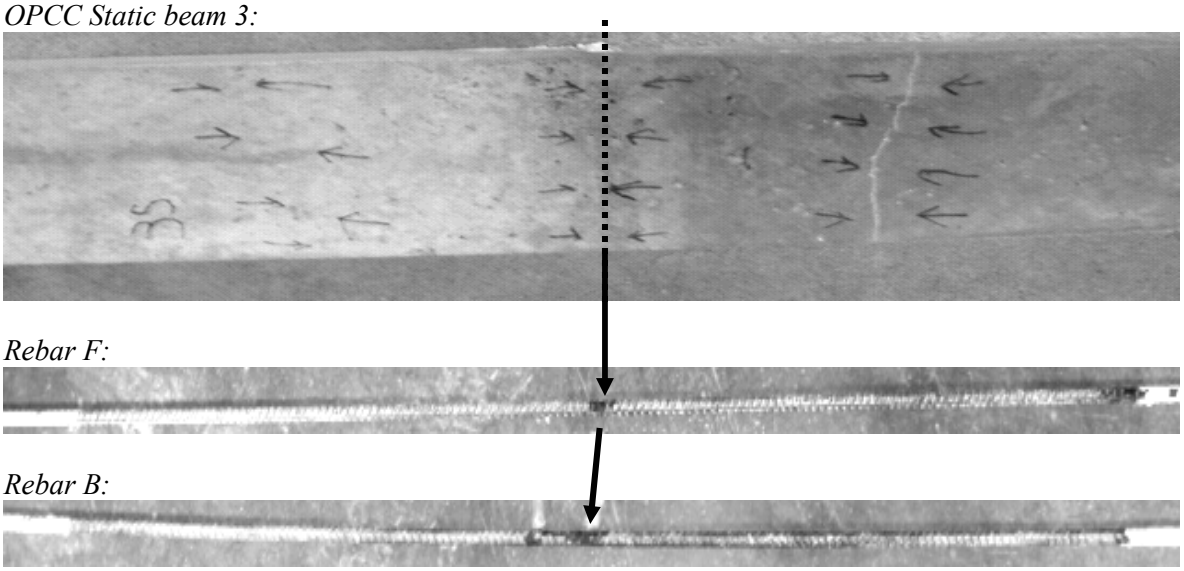

Rebar F:

Rebar B:

OPCC Static beam 4:

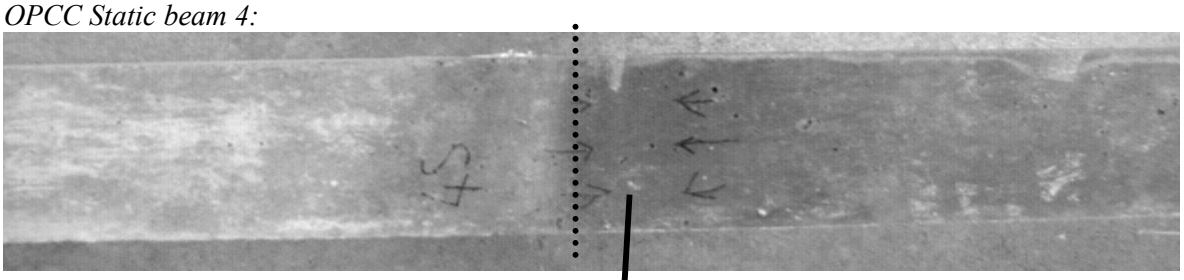

Rebar F:

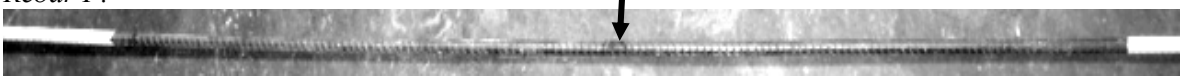

Rebar B:

OPCC Static beam 5:

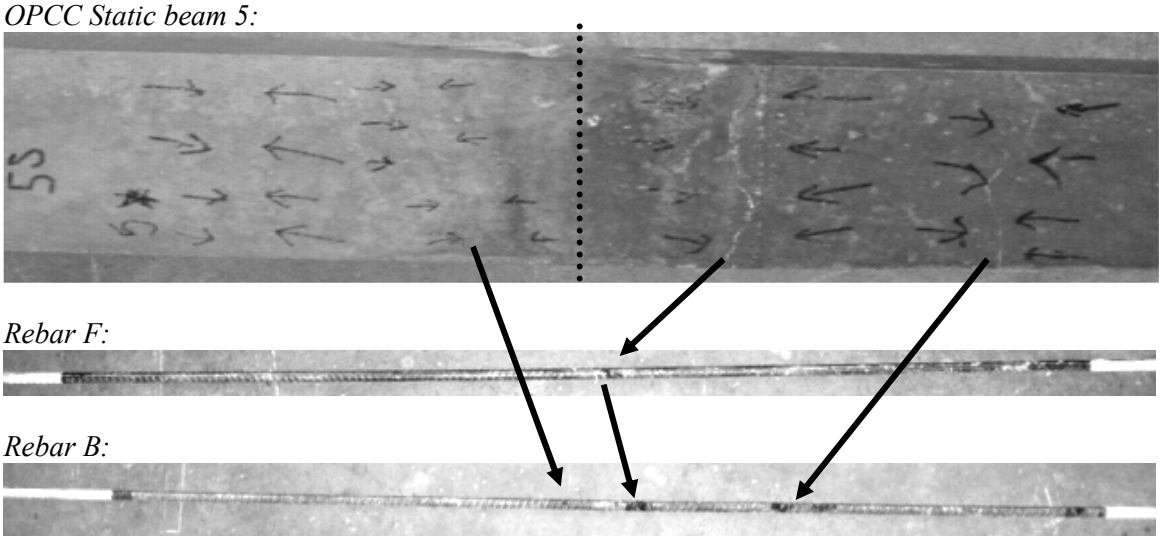

Rebar F:

Rebar B:

OPCC Static beam 6:

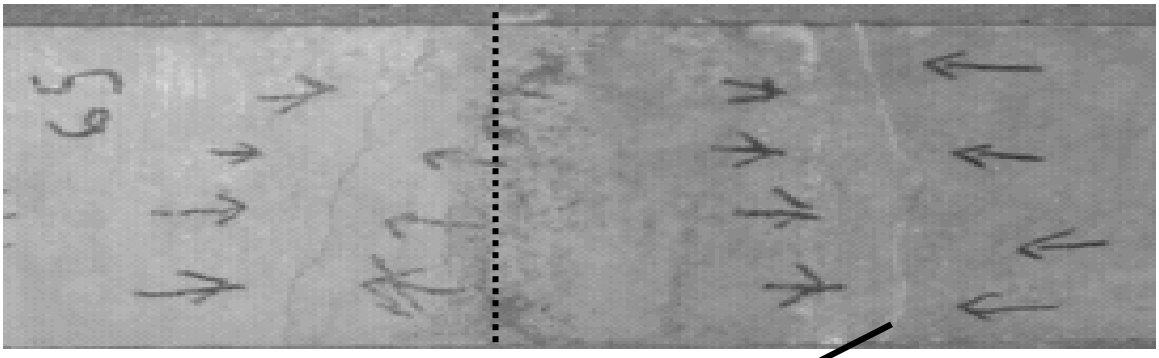

Rebar F:

Rebar B:

OPCC unloaded beam 1:

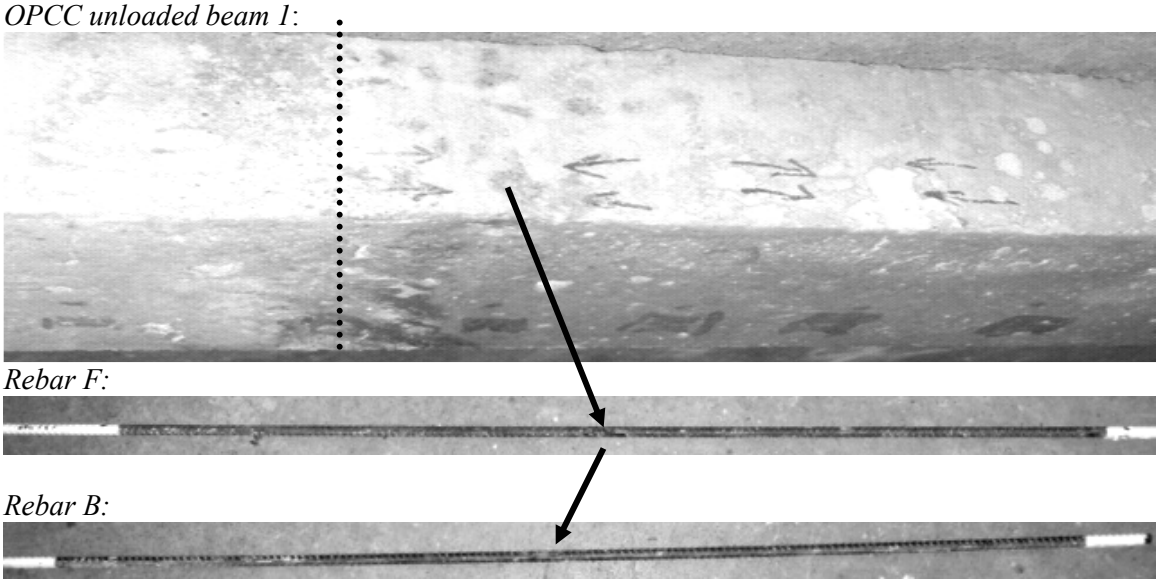

Rebar F:

Rebar B:

OPCC unloaded beam 2:

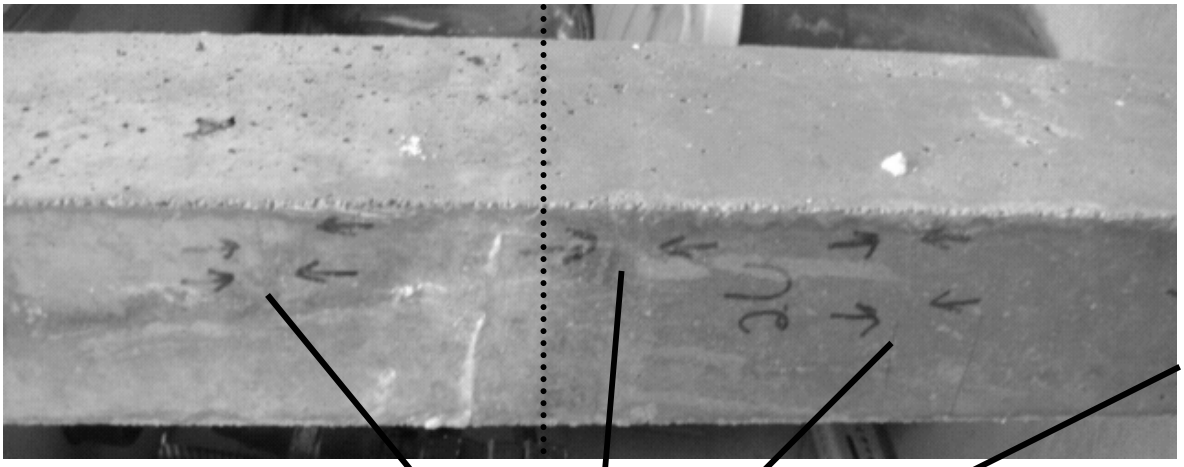

Rebar F:

Rebar B:

HPC Dynamic Beam 3:

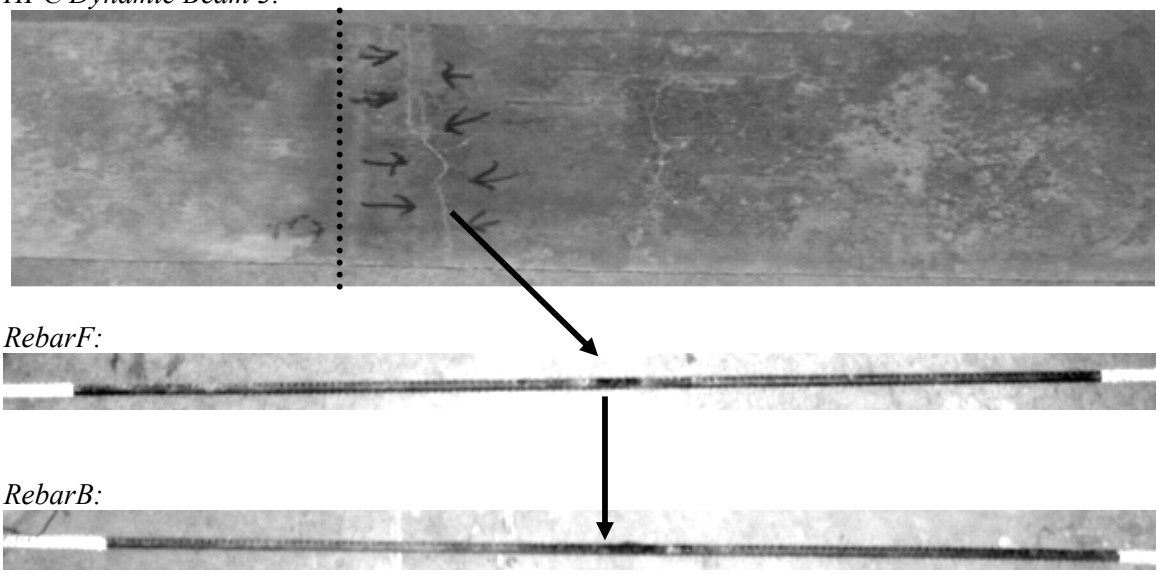

RebarF:

RebarB:

HPC Dynamic Beam 4:

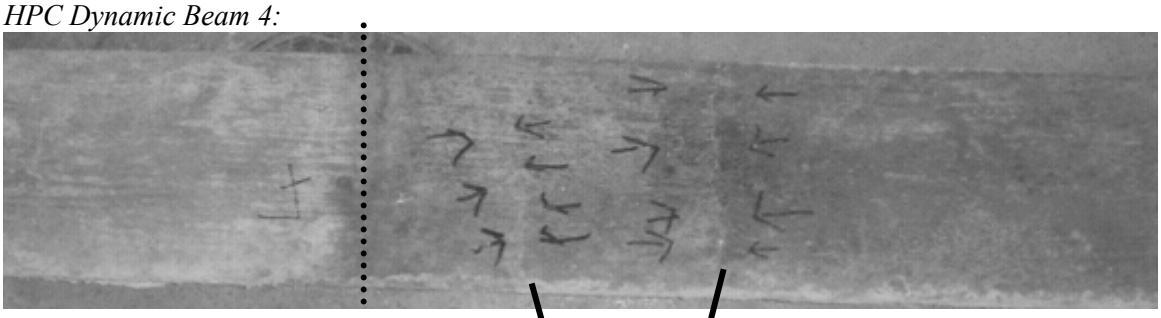

Rebar F:

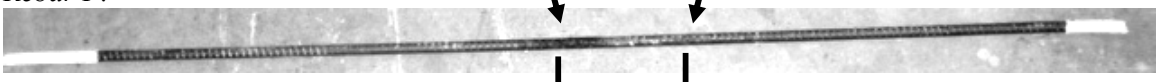

Rebar B:

HPC Dynamic Beam 7:

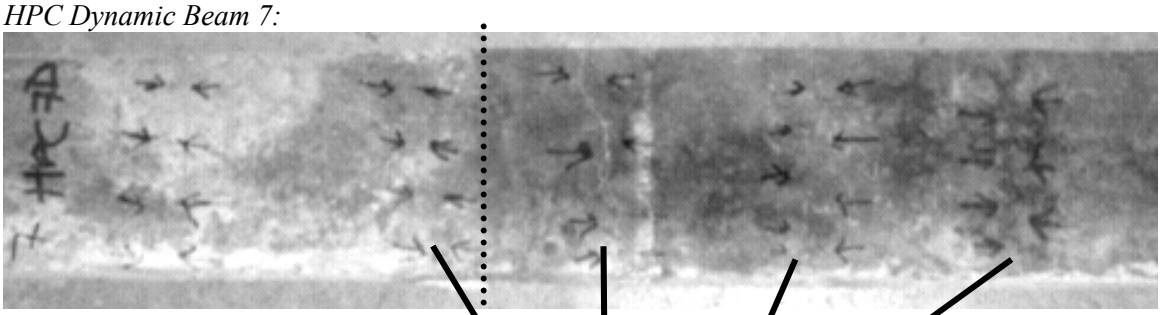

Rebar F:

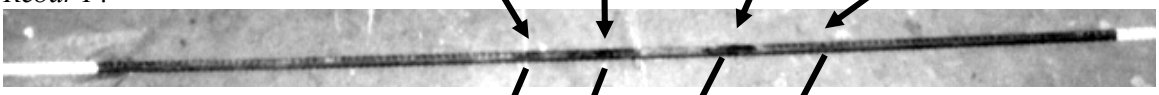

Rebar B:

HPC Dynamic Beam 8:

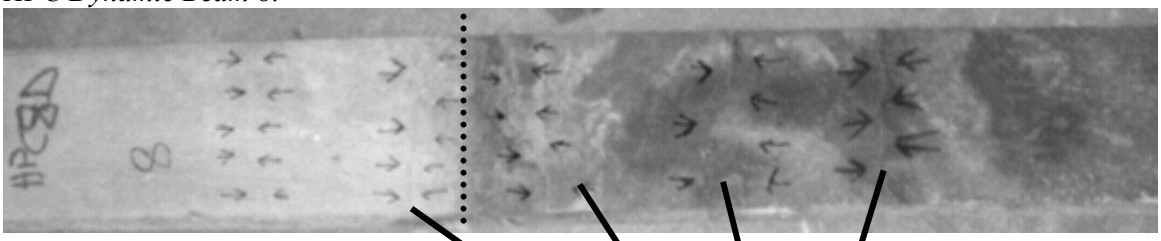

Rebar F:

Rebar B:

HPC Static Beam 1:

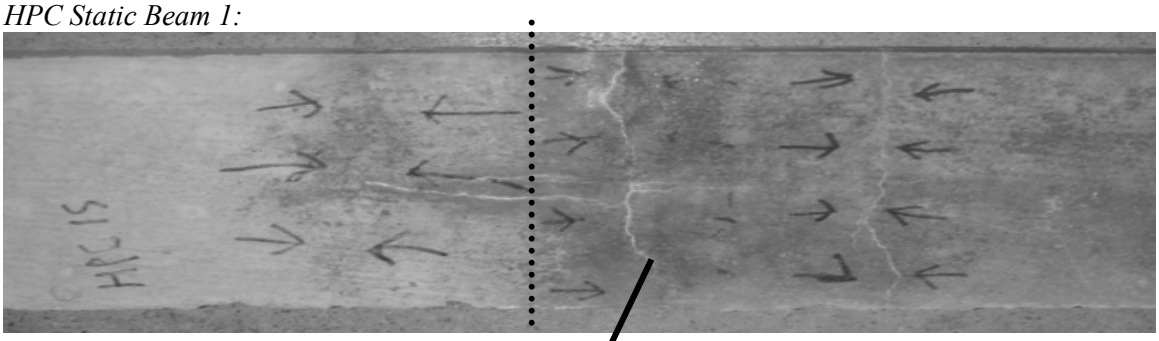

Rebar F:

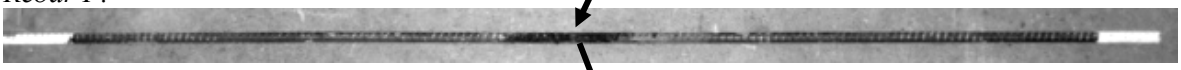

Rebar B:

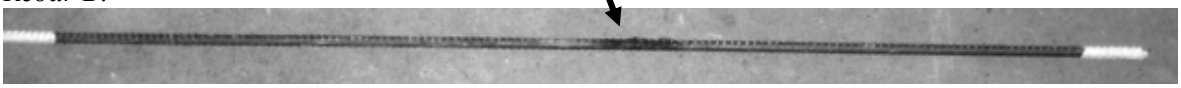

HPC Static Beam 2:

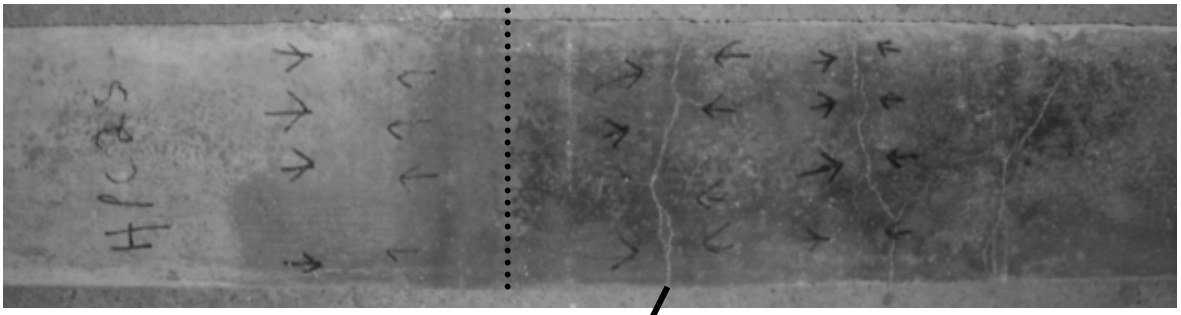

Rebar F:

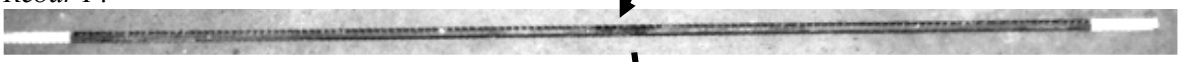

Rebar B:

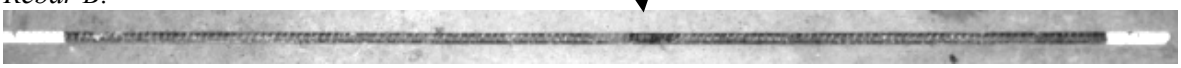

HPC Static Beam 5:

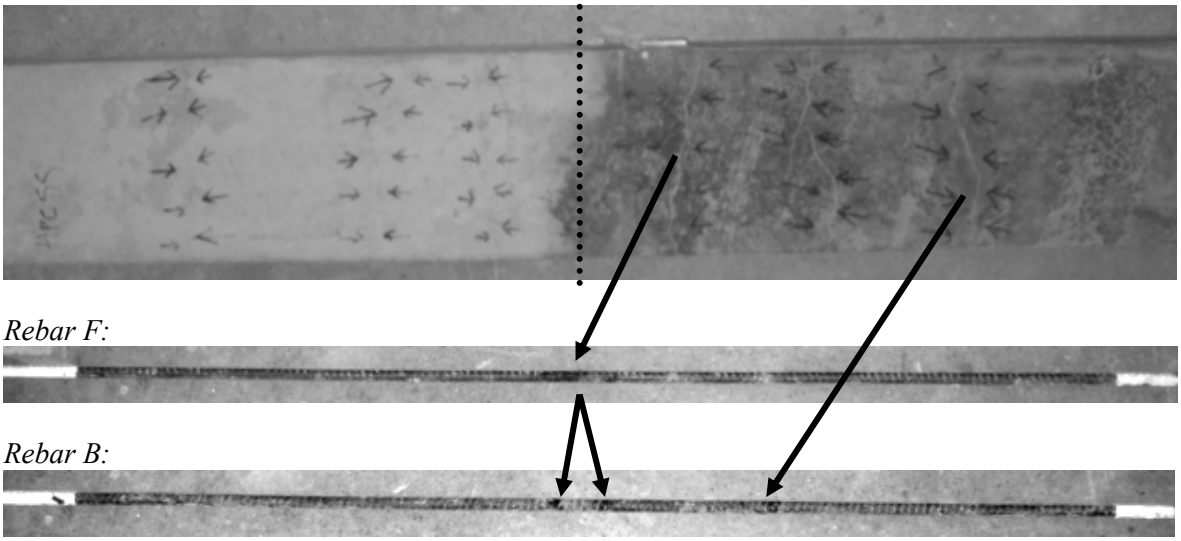

Rebar F:

Rebar B:

HPC Static Beam 6:

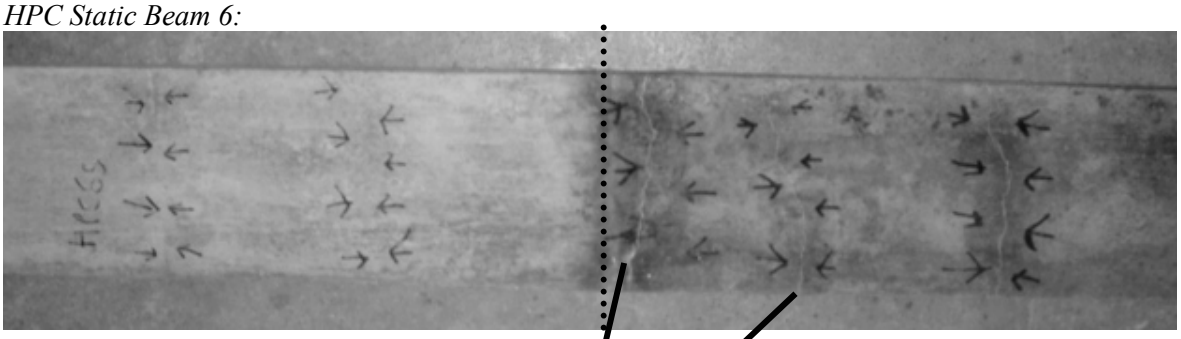

Rebar F:

Rebar B:

HPC Unloaded Beam 1:

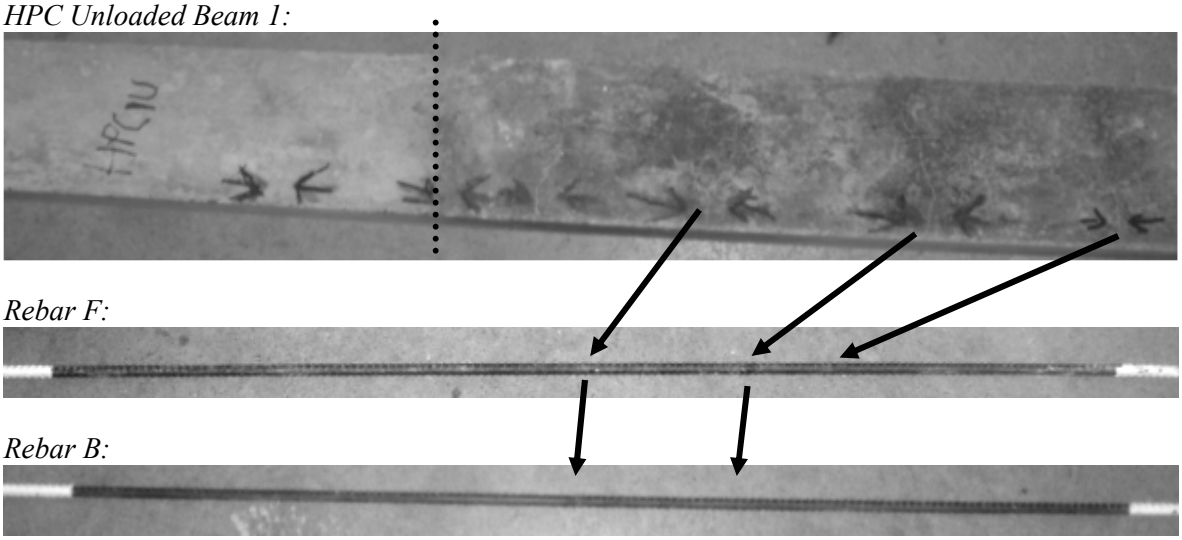

Rebar F:

Rebar B:

HPC Unloaded Beam 2:

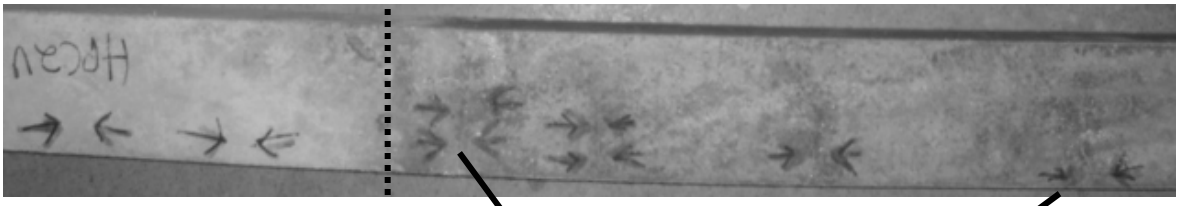

Rebar F:

Rebar B:

References

1. Concrete Canada - Networks of Centres of Excellence Annual Report, *Meeting Challenges of the Third Millenium - High Performance Concrete Structures*. 1997.
2. M. Pourbaix, *Atlas of Electrochemical Equilibria in Aqueous Solutions*. 1974, Houston, Texas: National Association of Corrosion Engineers.
3. M.F. Montemor, A.M.P. Simoes, M.G.S. Ferreira, *Chloride-induced corrosion on reinforcing steel: from fundamentals to the monitoring techniques.* Cement and Concrete composites, 2003. 25(4-5): p. 491-502.
4. A. Rosenberg, W.R. Grace, C.M. Hansson, C. Andrade, *Mechanisms of Corrosion of Steel in Concrete*. Materials Science of Concrete, ed. J.P. Skalny. Vol. 1. 1989, Westerville, OH, USA: The American Ceramic Society. 285-313.
5. M. Richardson, *Carbonation of Reinforced Concrete*. 1988, New York, New York, USA: CITIS Ltd.
6. V.G. Papadakis, M.N. Fardis, C.G. Vayenas, *Effect of Composition, Environmental Factors and Cement-Lime Mortar Coating on Concrete Carbonation.* Materials and Structures, 1992. 25(5): p. 293-304.
7. G.J. Verbeck, *Carbonation of Hydrated Portland Cement.* ASTM Special Technical Publication, 1958. 205: p. 17-36.
8. C.M. Hansson, *Comments on Electrochemical Measurements of the Rate of Corrosion of Steel in Concrete.* Cement and Concrete Research, 1984. 14(4): p. 574-584.
9. M. Santhanam, M.D. Cohen, J. Olek, *Mechanism of Sulphate Attack: A Fresh Look Part 1: Summary of Experimental Results.* Cement and Concrete Research, 2002. 32(6): p. 915-921.
10. S. Chatterji, *Mechanism of the $CaCl_2$ Attack on Portland Cement Concrete.* Cement and Concrete Research, 1978. 8(4): p. 461-468.
11. R.D. Cody, A.M. Cody, P.G. Spry, G.,-L. Gan. *Concrete Deterioration by De-icing Salts: An Experimental Study*. in *Semisesquicentennial Transportation Conference Proceedings*. 1996. Ames, Iowa, USA: Centre for Transportation Research and Education.
12. L. Sutter, T. Van Dam., K. R. Peterson, D.P. Johnston, *Long-Term Effects of Magnesium Chloride and Other Concentrated Salt Solutions on Pavement and Structural Portland Cement Concrete: Phase I Results.* Transportation Research Board of the National Academies, 2006. 1979: p. 60-68.
13. Rasheeduzzafar, *Influence of Cement Composition on Concrete Durability.* ACI Materials Journal, 1992. 89(6): p. 574 - 586
14. A. K. Suryavanshi, J.D. Scantlebury, S.B. Lyon, *Mechanism of Friedel's Salt Formation in Cements Rich in Tri-Calcium Aluminate.* Cement and Concrete Research, 1996. 26(5): p. 717-727.
15. P. Brown, J. Bothe Jr., *The System $CaO-Al_2O_3-CaCl_2-H_2O$ at 23±2 ^oC and The Mechanism of Chloride Binding in Concrete.* Cement and Concrete Research, 2004. 34(9): p. 1549-1553.
16. E.P. Nielsen, D. Herfort, M.R. Geiker, *Binding of Chloride and Alkalis in Portland Cement Systems.* Cement and Concrete Research, 2005. 35(1): p. 117-123.
17. J.J. Beaudoin, V.S. Ramachandran, R.F. Feldman, *Interaction of Chloride and C-S-H.* Cement and Concrete Research, 1990. 20(6): p. 875-883.
18. V.S. Ramachandran, *Possible States of Chloride in the Hydration of Tricalcium Silicate in the Presence of Calcium Chloride.* Materials and Structures, 1971. 4(19): p. 3-12.
19. ACI Committee 222, *Protection of Metals in Concrete Against Corrosion*.
20. T.C. Powers, *Properties of Cement Paste and Concrete*. in *Chemistry of Cement : Fourth International Symposium*. 1960. Washington, D.C. USA: National Bureau of Standards, U.S. Department of Commerce.

21. J.Y. Jehng, D.T. Sprague, W.P. Halperin, *Pore Structure of Hydrating Cement Paste by Magnetic Resonance Relaxation analysis and freezing.* Magnetic Resonance Imaging, 1996. 14(7/8): p. 785-791
22. P.C. Aïtcin, A.M. Neville, P. Acker, *Integrated View of Shrinkage Deformation*, in *Concrete International*. 1997. p. 35-41.
23. I. Soroka, *Portland Cement Paste and Concrete*. 1979, Surrey, England: The Macmillan Press Ltd.
24. S. Diamond, *Pores in Concrete- Is it Time to Reconsider the Paradigm*. 2004: West Lafayette, IN, USA.
25. R.D. Hooton, *Permeability and Pore Structure of Cement Pastes Containing Fly Ash, Slag, and Silica Fume.* ASTM Special Technical Publication 1986. 897: p. 128-143.
26. ASTM C 595, *Standard Specifications for Blend Hydraulic Cements*.
27. P.K. Mehta, O.E. Gjørv, *Properties of Portland Cement Concrete Containing Fly Ash and Condensed Silica Fume.* Cement and Concrete Research, 1982. 12(5): p. 587-595.
28. V.G. Papadakis, S. Tsimas, *Supplementary Cementing Materials in Concrete Part 1: Efficiency and design.* Cement and Concrete Research, 2002. 32(10): p. 1525-1532.
29. Silica Fume Association, *Building a Durable Future into Our Nation's Infrastructure*. 2007; Available from: www.silicafume.org.
30. M. Nehdi, S. Mindess, P.C. Aïtcin, *Rheology of High-Performance Concrete: Effect of Ultrafine Particles.* Cement and Concrete Research, 1998. 28(5): p. 687-697.
31. R.P. Khatri, V. Sirivivatnanon, W. Gross, *Effect of Different Supplementary Cementitious Materials on Mechanical Properties of High Performance Concrete.* Cement and Concrete Research, 1995. 25(1): p. 209-220.
32. V. Lilkov, E. Dimitrova, O.E. Petrov, *Hydration Process of Cement Containing Fly Ash and Silica Fume: The First 24 Hours.* Cement and Concrete Research, 1997. 27(4): p. 577-588.
33. M.D.A. Thomas, M.H. Shehata, S.G. Shashiprakash, D.S. Hopkins, K. Cail, *Use of Ternary Cementitious Systems Containing Silica Fume and Fly Ash in Concrete.* Cement and Concrete Research, 1999. 29(8): p. 1207-1214
34. R.F. Feldman, H. Cheng-Yi, *Properties of Portland Cement-Silica Fume Pastes II. Mechanical Properties.* Cement and Concrete Research, 1985. 15(6): p. 943-952.
35. S. Igarashi, H.R. Kubo, M. Kawamura, *Long-term Volume Changes and Microcracks Formation in High Strength Mortars.* Cement and Concrete Research, 2000. 30(6): p. 943-951.
36. C. L. Page, O. Vennesland., *Pore Solution Composition and Chloride Binding Capacity of Silica Fume Cement Pastes.* Materials and Structures, 1983. 16(1): p. 19-25.
37. R.J. Detwiler, P.K. Mehta, *Chemical and Physical Effects of Silica Fume on the Mechanical Behaviour of Concrete.* ACI Materials Journal, 1989. 86(6): p. 609-614.
38. S. Igarashi, A. Watanabe, M. Kawamura, *Evaluation of Capillary Pore Size Characteristics in High-Strength Concrete at Early Ages.* Cement and Concrete Research, 2005. 35(3): p. 513-519.
39. ASTM C 1240, *Standard Specification for Silica Fume Used in Cementitious Mixtures*.
40. AASHTO M 307, *Standard Specification for Microsilica for Use in Concrete and Mortar*.
41. ACI 234, *Guide for the Use of Silica Fume in Concrete*.
42. S. Song, H.M. Jennings, *Pore Solution Chemistry of Alkali-Activated Ground Granulated Blast furnace Slag.* Cement and Concrete Research, 1999. 29(2): p. 159-170.
43. R.N. Swamy, *Design for Durability and Strength Through the Use of Fly Ash and Slag*. in *Third CANMET / ACI International Symposioum Advances in Concrete Technology*. 1997. Auckland, New Zealand: American Concrete Institute.

44. C.-M. Aldea, F. Young, K. Wang, S.P. Shah, *Effects of Curing Conditions on Properties of Concretes Using Slag Replacement.* Cement and Concrete Research, 2000. 30(3): p. 465-472.
45. W.-C. Jau, D.-S. Tsay, *A Study of the Basic Engineering Properties of Slag Cement Concrete and its Resistance to Seawater Corrosion.* Cement and Concrete Research, 1998. 28(10): p. 1363-1371.
46. F. Leng, N. Feng, X. Lu, *An Experimental Study on the Properties of Resistance to Diffusion of Chloride Ions of Fly Ash and Blast Furnace Slag Concrete.* Cement and Concrete Research, 2000. 30(6): p. 989-992.
47. G.J. Osborne, *Durability of Portland Blast-Furnace Slag Cement and Concrete.* Cement and Concrete Composites, 1999. 21(1): p. 11-21.
48. K.Y. Yeau, E. Kyum, *An Experimental Study on Corrosion Resistance of Concrete with Ground Granulated Blast Furnace Slag.* Cement and Concrete Research, 2005. 35(7): p. 1391-1399.
49. P.C. Aïtcin, *The Durability Characteristics of High Performance Concrete: A Review.* Cement and Concrete Composites, 2003. 25(4-5): p. 409-420.
50. B.H. Oh, S.W. Cha., B.S. Jang, S.Y. Jang, *Development of High-Performance Concrete Having High Resistance to Chloride Penetration.* Nuclear Engineering and Design, 2002. 212: p. 221-231.
51. M. Collepardi, *Admixtures Used to Enhance Placing Characteristics of Concrete.* Cement and Concrete Composites, 1998. 20(1998): p. 103-112.
52. S.A. Okulaja, *Effects of Structural Cracks on the Durability of Reinforced High Performance Concretes and Ordinary Portland Cement Concretes Exposed to De-icing Salts*, *MASc Thesis in Mechanical Engineering*. 2003, University of Waterloo: Waterloo. p. 150.
53. P. Balaguru, R. Narahari, M. Patel, *Flexural Toughness of Steel Fibre Reinforced Concrete.* ACI Materials Journal, 1989. 89(6): p. 541-546.
54. A. Neville, P.C. Aïtcin, *High Performance Concrete-An Overview.* Materials and Structures, 1998. 31(2): p. 111-117.
55. J. Bisschop, J.G.M. Van Mier, *How to Study Drying Shrinkage Microcracking in Cement-Based Materials Using Optical and Scanning Electron Microscopy?* Cement and Concrete Research, 2002. 32(2): p. 279-287.
56. T. Shiotani, J.Bisschop, J.G.M. Van Mier, *Temporal and Spatial Development of Drying Shrinkage Cracking in Cement-Based Materials.* Engineering Fracture Mechanics, 2003. 30: p. 1509-1525.
57. F.O. Slate, K.C. Hover, *Microcracking in Concrete*, in *Fracture Mechanics of Concrete: Material Characterization and Testing*, A. Carpinteri and A.R. Ingraffea, Editors. 1984, Martinus Nijhoff Publishers: The Hague, Netherlands.
58. K.O. Kjellsen, H.M. Jennings, *Observations of Microcracking in Cement Paste upon Drying and Rewetting by Environmental Scanning Electron Microscopy.* Advanced Cement Based Materials, 1996. 3: p. 14-19.
59. P.K. Mehta, *Durability of Concrete-: The Zigzag Course of Progress.* Indian Concrete Journal, 2006. 80(8): p. 9-16.
60. A. Van Hauwaert, F. Delannay, J.-F. Thimus, *Cracking Behaviour of Steel Fibre Reinforced Concrete Revealed by Means of Acoustic Emission and Ultrasonic Wave Propagation.* ACI Materials Journal, 1999. 96(3): p. 291-296.
61. R.W. Burrows, *The Visible and Invisible Cracking of Concrete*. 1998, Farmington Hill, Michigan, USA: American Concrete Institute.
62. B.C. Gerwick, Jr. *A Holistic Approach to Concrete Technology for Major Bridges*. in *V. Mohan Malhotra Symposium*. 1994. Detroit, Michigan, USA: American Concrete Institute.

63. E. Holt, M. Leivo, *Cracking Risks Associated With Early Age Shrinkage.* Cement and Concrete Composites, 2004. 26(5): p. 521-530.
64. S. Igarashi, A. Bentur, K. Kovler, *Autogenous Shrinkage and Induced Restraining Stresses in High-Strength Concretes.* Cement and Concrete Research, 2000. 30(11): p. 1701-1707.
65. B. Barr, S.B. Hoseinian, M.A. Beygi, *Shrinkage of Concrete Stored in Natural Environments.* Cement and Concrete Composites, 2003. 25: p. 19-29.
66. F.H. Wittmann, *On the Action of Capillary Pressure in Fresh Concrete.* Cement and Concrete Research, 1976. 6(1): p. 49-56.
67. A.A. Almusallam, M. Maslehuddin, M. Abdul-Waris, M.M. Khan, *Effect of Mix Proportions on Plastic Shrinkage Cracking of Concrete in Hot Environments.* Construction and Building Materials, 1998. 12(1998): p. 353-358.
68. O.S.B. Al-Amoudi, M. Maslehuddin, and T. Abiola, *Effect of Type and Dosage of Silica Fume on Plastic Shrinkage in Concrete Exposed to Hot Weather.* Construction and Building Materials, 2004. 18(10): p. 737-743.
69. D. P. Bentz, O.M. Jensen, *Mitigation Strategies for Autogenous Shrinkage Cracking.* Cement and Concrete Composites, 2004. 26(6): p. 677-685.
70. N. Setter, D.M. Roy, *Mechanical Features of Chemical Shrinkage of Cement Paste.* Cement and Concrete Research, 1978. 8: p. 623-634.
71. P.C. Aïtcin, *Does Concrete Shrink or Does it Swell?* in *Concrete International*. 1999. p. 77 - 80.
72. W. Hansen, *Drying Shrinkage Mechanisms in Portland Cement Paste.* Journal of the American Ceramic Society, 1987. 70(5): p. 323-328.
73. P. Soroushian, M. Elzafraney, A. Nossoni, *Specimen Preparation and Image Processing and Analysis Techniques for Automated Quantification of Concrete Microcracks and Voids.* Cement and Concrete Research, 2003. 33: p. 1949-1962.
74. H.C. Gran, *Fluorescent Liquid Replacement Technique. A Means of Crack Detection and Water:Binder Ratio Determination in High Strength Concretes.* Cement and concrete research, 1995. 25(5): p. 1063-1074.
75. J.J. Chen, J.J. Thomas, H.M. Jennings, *Decalcification Shrinkage of Cement Paste.* Cement and Concrete Research, 2006. 36(5): p. 801-809.
76. K. Kobayashi, K. Suzuki, Y. Uno, *Carbonation of Concrete Structures and Decomposition of C-S-H.* Cement and Concrete Research, 1993. 25(5): p. 55-61.
77. G. W. Groves, A. Brough, I.G. Richardson, C.M. Dobson, *Progressive Changes in the Structure of Hardened C_3S Cement Pastes due to Carbonation.* Journal of the American Ceramic Society, 1991. 74(11): p. 2891-2896.
78. T.C. Powers, *A Hypothesis on Carbonation Shrinkage.* Journal of PCA Research and Development Labs, 1962. 4(2): p. 40-50.
79. R.W. Carlson, D.L. Houghton, M. Polivka, *Causes and Control of Cracking in Unreinforced Mass Concrete.* ACI Journal, 1979. 76(7): p. 821-837.
80. M. Prezzi, P.J.M. Monteiro, G. Sposito, *Alkali-Silica Reaction, Part 1: Use of the Double-Layer Theory to Explain the Behaviour of Reaction-Product Gels.* ACI Materials Journal, 1997. 94(1): p. 10-17.
81. B. Fournier, M.-A.Bérubé, *Alkali-Aggregate Reaction in Concrete: A Review of Basic Concepts and Engineering Implication.* Canadian Journal of Civil Engineering, 2000. 27(2): p. 167-191.
82. E. G. Swenson, J.E. Gillott, *Alkali-Carbonate Rock Reaction*, in *Highway Research Record, no 45*. 1964. p. 21-40.

83. ACI committee 224, *Cause, Evaluation and Repair of Cracks in Concrete Structures*. 1998, American Concrete Institute.
84. P. Nerenst, *Frost Action in Concrete*. in *Chemistry of Cement Proceedings of the Fourth International Symposium*. 1960. Washington, D.C., USA: U.S. Department of Commerce National Bureau of Standards.
85. T.C. Powers, *A Working Hypothesis for Further Studies of Frost Resistance of Concrete*. in *Proceedings of American Concrete Institute*. 1945. Detroit, Michigan, USA: American Concrete Institute.
86. M.R. Geiker, P. Laugesen, *On the Effect of Laboratory Conditioning and Freeze / Thaw Exposure on the Moisture Profiles in HPC.* Cement and Concrete Research, 2001. 31(12): p. 1831-1836.
87. S. Jacobsen, H.C. Gran, E.J. Sellevold, J.A. Bakke, *High Strength Concrete - Freeze/Thaw Testing and Cracking.* Cement and Concrete Research, 1995. 25(8): p. 1775-1780.
88. S. Jacobsen, J. Marchand, H. Hormain, *SEM Observations of Microstructure of Frost Deteriorated and Self-Healed Concretes.* Cement and Concrete Research, 1995. 25(8): p. 1781-1790.
89. P. Montes, T.W. Bremner, D.H. Lister, *Influence of Calcium Nitrite Inhibitor and Crack Width on Corrosion of Steel in High Performance Concrete Subjected to Simulated Marine Environment.* Cement and Concrete Composites, 2004. 26(3): p. 243-253.
90. R.B Polder, W.H.A. Peelen, *Characteristic of Chloride Transport and Reinforcement Corrosion in Concrete Under Cyclic Wetting and Drying by Electrical Resistivity.* Cement and Concrete Composites, 2002. 24(5): p. 427-435.
91. G.W. Scherer, *Stress From Crystallization of Salt.* Cement and Concrete Research, 2004. 34(9): p. 1613 - 1624.
92. J.G. Cabrera, *Deterioration of Concrete Due to Reinforcement Steel Corrosion.* Cement and Concrete Composites, 1996. 18(1): p. 47-59.
93. C. Andrade, C. Alonso, F.J. Molina, *Cover Cracking as a Function of Bar Corrosion: Part I - Experimental Test.* Materials and Structures, 1993. 26: p. 453-464.
94. C.M. Hansson, *Discussion of Corrosion Effects on Bond Strength in Reinforced Concrete. Paper by Kyle Stanish, R. D. Hooton, S. J. Pantazopoulou.* ACI Structural Journal 2000. 97(5): p. 789-790.
95. T.D. Marcotte, *Characterization of Chloride-Induced Corrosion Products that Form in Steel-Reinforced Cementitious Materials*, *PhD Thesis in Department of Mechanical Engineering*. 2001, University of Waterloo: Waterloo, Canada. p. 330.
96. M.L. Allan, *Probability of Corrosion Induced Cracking in Reinforced Concrete.* Cement and Concrete Research, 1995. 25(6): p. 1179-1190.
97. F.A.K.M. Uddin, K. Numata, J. Shimasaki, S. Mitsuhiro, M. Ohtsu, *Mechanisms of Crack Propagation due to Corrosion of Reinforcement in Concrete by AE-SiGMA and BEM.* Construction and Building Materials, 2004. 18(3): p. 181-188.
98. M. Ohtsu, Y. Shinichi, *Analysis of Crack Propagation and Crack Initiation Due to Corrosion of Reinforcement.* Construction and Building Materials, 1997. 11(7-8): p. 437-442.
99. K.M. Nemati, P.J.M. Monteiro, K.L. Scrivener, *Analysis of Compressive Induced Stress in Concrete.* ACI Materials Journal, 1998. 95(5): p. 617-630.
100. Z. Li, S.P. Shah, *Localization of Microcracking Under Uniaxial Tension.* ACI Materials Journal, 1994. 91(4): p. 372 - 381.
101. V.S. Gopalaratnam, S.P. Shah, *Softening Response of Plain Concrete in Direct Tension.* ACI Journal, 1985. 82(3): p. 310-323.

102. K. Otsuka, H. Date, *Fracture Process Zone in Concrete Tension Specimen.* Engineering Fracture Mechanics, 2000. 65(2-3): p. 111-131.
103. Y. Goto, *Cracks Formed in Concrete Around Deformed Tension Bars.* ACI Journal, 1971. 68(4): p. 244-252.
104. N.K. Raju, *Microcracking in Concrete Under Repeated Compressive Loads.* Building Science, 1970. 5(1): p. 51-56.
105. S.P. Shah, S. Chandra, *Critical Stress, Volume Change and Microcracking of Concrete.* ACI Journal, 1968. 65(9): p. 770-780.
106. J.M. Torrenti, E.H. Benaija, C. Boulay, *Influence of Boundary Conditions on Strain Softening in Concrete Compression Tests.* Journal of Engineering Mechanics, 1993. 119(12): p. 2369-2384.
107. D.C. Jansen, S.P. Shah, *Effect of Length on Compressive Strain Softening of Concrete.* Journal of Engineering Mechanics, 1997. 123(1): p. 1997.
108. S. Puri, J. Weiss, *Assessment of Localized Damage in Concrete Under Compression Using Acoustic Emission.* Journal of Materials in Civil Engineering, 2006. 18(3): p. 325-333.
109. S.P. Shah, S. Chandra, *Fracture of Concrete Subjected to Cyclic Sustained Loading.* ACI Journal, 1970. 67(10): p. 816-827.
110. O.M. Jensen, P.F. Hansen, A.M. Coats, F.P. Glasser, *Chloride Ingress in Cement Paste and Mortar.* Cement and Concrete Research, 1999. 29(9): p. 1497-1504.
111. P. Sandberg, L. Tang, A. Andersen, *Recurrent Studies of Chloride Ingress in Uncracked Marine Concrete at Various Exposure Times and Elevations.* Cement and Concrete Research, 1998. 28(10): p. 1489-1503.
112. O.M. Jensen, A.M. Coats, F.P. Glasser, *Chloride Ingress Profiles Measured by Electron Probe Micro Analysis.* Cement and Concrete Research, 1996. 26(11): p. 1695-1705.
113. C.M. Hansson, S.A Okulaja, *Corrosion of Reinforcing Steel in Cracked High Performance Concrete*. in *Advances in Cement and Concrete*. 2003. Copper Mountain, CO, USA: University of Illinois at Urbana - Champaign.
114. D.W. Hobbs, *Aggregates Influence on Chloride Ion Diffusion into Concrete.* Cement and Concrete Research, 1999. 29(12): p. 1995-1998.
115. T. Sugiyama, T.W. Bremner, Y. Tsuji, *Determination of Chloride Diffusion Coefficient and Gas Permeability of Concrete and Their Relationship.* Cement and Concrete Research, 1996. 26(5): p. 781-790.
116. K.O. Ampadu, K. Torii, M. Kawamura, *Beneficial Effect of Fly Ash on Chloride Diffusivity of Hardened Cement Paste.* Cement and Concrete Research, 1999. 29(4): p. 585-590.
117. ASTM C 1202, *Standard Test Method for Electrical Indication of Concrete's Ability to Resist Chloride Ion Penetration*.
118. K. Hong, R.D. Hooton, *Effects of Cyclic Chloride Exposure on Penetration of Concrete Cover.* Cement and Concrete Research, 1999. 29(9): p. 1379-1386.
119. M. Castellote, C. Alonso, C. Andrade, G.A. Cadbourn, C.L. Page, *Oxygen and Chloride Diffusion in Cement Pastes as a Validation of Chloride Diffusion Coefficients Obtained by Steady-State Migration Tests.* Cement and Concrete Research, 2001. 31(4): p. 621-625.
120. R.F. Feldman, G.W. Chan, R.J. Brousseau, P.J. Tumidajski, *Investigation of the Rapid Chloride Permeability Test.* ACI Materials Journal, 1994. 91(3): p. 246-255.
121. S.E. Hussain, Rasheeduzzafar, A. Al-Musallam, A.S. Al-Gahtani, *Factors Affecting Threshold Chloride for Reinforcement Corrosion in Concrete.* Cement and Concrete Research, 1995. 25(7): p. 1543 - 1555.
122. M. Thomas, *Chloride Thresholds in Marine Concrete.* Cement and Concrete Research, 1996. 26(4): p. 513-519.

123. N. Thangavel, N.S. Rengaswamy, *Relationship Between Chloride/Hydroxide Ratio and Corrosion of Steel in Concrete.* Cement and Concrete Composites, 1998. 20(4): p. 283-292.
124. G.K. Glass, N.R. Buenfeld, *The Presentation of the Chloride Threshold Level for Corrosion of Steel in Concrete.* Corrosion Science, 1997. 39(5): p. 1001-1013.
125. G.K. Glass, B. Reddy, N.R. Buenfeld, *The Participation of Bound Chloride in Passive Film Breakdown on Steel in Concrete.* Corrosion Science, 2000. 42(11): p. 2013-2021.
126. C. Alonso, C. Andrade, M. Castellote, P. Castro, *Chloride Threshold Values to Depassivate Reinforcing Bars Embedded in Standardized OPC Mortar.* Cement and Concrete Research, 2000. 30(7): p. 1047-1055.
127. B. Gerard, J. Marchand, *Influence of Crack on the Diffusion Properties of Cement-Based Materials Part 1: Influence of Continuous Cracks on the Steady-State Regime.* Cement and Concrete Research, 2000. 30(1): p. 37-43.
128. S. Jacobsen, J. Marchand, L. Boisvert, *Effect of Cracking and Healing on Chloride Transport in OPC Concrete.* Cement and Concrete Research, 1996. 26(6): p. 869-881.
129. K. Wang, D.C. Jensen, S.P. Shah, A.F. Karr, *Permeability Study of Cracked Concrete.* Cement and Concrete Research, 1997. 27(3): p. 381-393.
130. M. Ismail, A. Toumi, R. François, R. Gagné, *Effect of Crack Opening on the Local Diffusion of Chloride in Inert Materials.* Cement and Concrete Research, 2004. 34(4): p. 711-716.
131. N. Gowripalan, V. Sirivivtnanon, and C.C. Lim, *Chloride Diffusivity of Concrete Cracked in Flexure.* Cement and Concrete Research, 2000. 30(5): p. 725-730.
132. P.P. Win, M. Watanabe, A. Machida, *Penetration Profile of Chloride Ion in Cracked Reinforced Concrete.* Cement and Concrete Research, 2004. 34(7): p. 1073-1079.
133. R. Gagné, R. François, P. Masse. *Chloride Penetration Testing of Cracked Mortar Samples*. in *Concrete Under Severe Conditions: Environment and Loading*. 2001. Vancouver, BC, Canada: University of British Columbia.
134. CSA S6, *Canadian Highway Bridge Design Code*.
135. CSA A23.3, *Design of Concrete Structures*
136. ACI 224, *Control of Cracking in Concrete Structures*.
137. K. Suzuki, Y. Ohno, S. Praparntanatorn, H. Tamura. *Mechanism of Steel Corrosion in Cracked Concrete*. in *International Symposium on Corrosion of Reinforcement in Concrete Construction (3rd)*. 1990. Wishaw, England: Elsevier Applied Science.
138. C. Arya, F.K. Ofori-Darko, *Influence of Crack Frequency on Reinforcement Corrosion in Concrete.* Cement and Concrete Research, 1996. 26(3): p. 345-353.
139. R. Weiermair, C.M. Hansson, P.T. Seabrook, M. Tullmin, *Corrosion Measurements on Steel Embedded in High Performance Concrete Exposed to a Marine Environment*. in *Third CANMET/ ACI International Conference on Concrete in Marine Environment*. 1996. St. Andrews by the Sea, New Brunswick, Canada: American Concrete Institute.
140. P. Schiessl, M. Raupach, *Laboratory Studies and Calculations on the Influence of Crack Width on Chloride-Induced Corrosion of Steel in Concrete.* ACI Materials Journal, 1997. 94(1): p. 56 - 62.
141. F. Belaïd, G. Arliguie, R. François, *Corrosion Products of Galvanized Rebars Embedded in Chloride-Contaminated Concrete.* Corrosion, 2000. 56(9): p. 960-965.
142. T.D. Marcotte, C.M. Hansson, *The Influence of Silica Fume on the Corrosion Resistance of Steel in High Performance Concrete Exposed to Simulated Seawater.* Journal of Materials Science, 2003. 38(23): p. 4765 - 4776.
143. T.D. Marcotte, C.M. Hansson. *A Comparison of the Chloride-Induced Corrosion Products from Steel Reinforced Industrial Standard versus High Performance Concrete Exposed to*

Simulated Sea Water. in *International Symposium on High-Performance and Reactive Powder Concretes*. 1998. Sherbrooke, Québec, Canada: University of Sherbrooke.
144. B. Espelid, N. Nielsen, *A Field Study of the Corrosion Behaviour on Dynamically Loaded Marine Concrete Structures*. in *Concrete in Marine Environment - Second International Conference*. 1988. St. Andrews by the Sea, Canada: American Concrete Institute.
145. W. Ahn, D.V. Reddy, *Galvanostatic Testing for the Durability of Marine Concrete Under Fatigue Loading.* Cement and Concrete Research, 2001. 31(3): p. 343 - 349.
146. A. Esmaeilpoursaee, *An Analysis of the Factors Influencing Electrochemical Measurements of the Conditions of Reinforcing Steel in Concrete Structures*, *PhD Thesis in Mechanical Engineering*. 2007, University of Waterloo: Waterloo, Ontario. p. 269.
147. R.F. Stratfull, *The Corrosion of Steel in a Reinforced Concrete Bridge.* Corrosion, 1957. 13: p. 43-48.
148. ASTM C 876, *Standard Test Method for Half-Cell Potentials of Uncoated Reinforcing Steel in Concrete.*
149. B. Elsener, C. Andrade, J. Gulikers, R. Polder, M. Raupach, *Half-Cell Potential Measurements - Potential Mapping on Reinforced Concrete Structures.* Materials and Structures, 2003. 36(7): p. 461-471.
150. B. Elsener, *Half-Cell Potential Mapping to Assess Repair Work on RC Structures.* Construction and Building Materials, 2001. 15(2-3): p. 133-139.
151. J. Mietz, B. Isecke, *Monitoring of Concrete Structures with Respect to Rebar Corrosion.* Construction and Building Materials, 1996. 10(5): p. 367-373.
152. C. Alonso, C. Andrade, J. A. González, *Relation Between Resistivity and Corrosion Rate of Reinforcements in Carbonated Mortar Made With Several Cement Types.* Cement and concrete Composites, 1988. 8(5): p. 687-698.
153. P. Gu, J.J. Beaudoin, M.-H. Zhang, V.M. Malhotra, *Performance of Steel Reinforcement in Portland Cement and High-Volume Fly Ash Concretes Exposed to Chloride Solution.* ACI Materials Journal, 1999. 96(5): p. 551-558.
154. A. Poursaee, C.M. Hansson, *Reinforcing Steel Passivation in Mortar and Pore Solution.* Cement and Concrete Research, 2007. 37(7): p. 1127-1133.
155. C.M. Hansson, A. Poursaee, A. Laurent, *Macrocell and Microcell Corrosion of Steel in Ordinary Portland Cement Concrete and High Performance Concretes.* Cement and Concrete Research, 2006. 36(11): p. 2098-2102.
156. K.R. Gowers, S.G. Millard, *On-Site Linear Polarization Resistance Mapping of Reinforced Concrete Structures.* Corrosion Science, 1993. 35(5-8): p. 1593-1600.
157. M. Stern, A.L. Geary, *Electrochemical Polarization I. A Theoretical Analysis of the Shape of Polarization Curves*. Journal of The Electrochemical Society, 1957. 104(1): p. 56-63.
158. C. Andrade, J.A. González, *Quantitative Measurements of Corrosion Rate of Reinforcing Steel Embedded in Concrete Using Polarization Resistance Measurements.* Werkstoffe und Korrosion, 1978. 29: p. 515-519.
159. K.R. Gowers, S.G. Millard, *Electrochemical Techniques for Corrosion Assessment of Reinforced Concrete Structures.* Proceedings of the Institution of Civil Engineers. Structures and Buildings 1999. 134(2): p. 129-137.
160. O.K. Gepraegs, *Comparison and Evaluation of Electrochemical Techniques and Monitoring Instruments to Determine the Corrosion Rate of Steel in Concrete*, *MASc Thesis in Mechanical Engineering*. 2002, University of Waterloo: Waterloo. p. 1-187.
161. C. Andrade, C. Alonso, *Corrosion Rate Monitoring in the Laboratory and On-site.* Construction and Building Materials, 1996. 10(5): p. 315-328.

162. C.J. Newton, J.M. Sykes, *A Galvanostatic Pulse Technique for Investigation of Steel Corrosion in Concrete.* Corrosion Science, 1988. 28(11): p. 1051-1074.
163. B. Elsener, H. Wojtas, H. Boehni, *Galvanostatic Pulse Measurements-Rapid on Site Corrosion Monitoring*, in *Corrosion and Corrosion Protection of Steel in Concrete*. 1994, 236-246: Sheffield, UK.
164. A. Legat, V. Dolecek,, *Corrosion Monitoring System Based on Measurement and Analysis of Electrochemical Noise.* Corrosion, 1995. 51(4): p. 295-300.
165. J. M. Smulko, K. Darowicki, A. Zieliński, *Evaluation of Reinforcement Corrosion Rate in Concrete Structures by Electrochemical Noise Measurements.* Russian Journal of Electrochemistry, 2006. 42(5): p. 546-550.
166. R.G. Hardon, P. Lambert, C.L. Page, *Relationship between Electrochemical Noise and Corrosion Rate of Steel in Salt Contaminated Concrete.* British Corrosion Journal, 1988. 23(4): p. 225-228.
167. L. Mariaca, A. Bautista, P. Rodríguez, J. A. González, *Use of Electrochemical Noise for Studying the Rate of Corrosion of Reinforcements Embedded in Concrete.* Materials and Structures, 1997. 30(10): p. 613-617.
168. M.J. Katwan, T. Hodgkiess, P.D. Arthur, *Electrochemical Noise Technique for the Prediction of Corrosion Rate of Steel in Concrete.* Materials and Structures, 1996. 29(5): p. 286-294.
169. M. Saremi, E. Mahallati, *A Study on Chloride-Induced Depassivation of Mild Steel in Simulated Concrete Pore Solution.* Cement and Concrete Research, 2002. 32(12): p. 1915-1912.
170. E. Mahallati, M. Saremi, *An Assessment on the Mill Scale Effects on the Electrochemical Characteristics of Steel Bars in Concrete Under DC-Polarization.* Cement and Concrete Research, 2006. 36(7): p. 1324-1329.
171. D.C. Silverman, *Tutorial on Polexpert™ and the Cyclic Potentiodynamic Polarization Technique*.2007; Available from: www.argentumsolutions.com.
172. CSA A23.1/A23.2, *Concrete Materials and Methods of Concrete Construction*.
173. Ministry of Transportation of Ontario, *OPSS 1350: Materials Specification for Concrete - Materials and Production*.
174. Ministry of Transportation of Ontario, *OPSS 904 S13 High Performance Concrete.*
175. ASTM C 39, *Standard Test Method for Compressive Strength of Cylindrical Concrete Specimens*.
176. ASTM C 617, *Standard Method of Capping Cylindrical Concrete Specimens*.
177. Force Technology, *GalvaPulse™*. 2007; Available from: www.forcetechnology.com.
178. V. Feliu, J.A. Gonzalez, C. Andrade, S. Feliu, *Equivalent Circuit for Modelling the Steel Concrete Interface. 1. Experimental Evidence and Theoretical Predictions.* Corrosion Science, 1998. 40(6): p. 975-993.
179. R.A Cottis, *Interpretation of Electrochemical Noise Data.* Corrosion, 2001. 57(3): p. 265 - 285.
180. P. Gu, Z. Xu, X. Ping, J.J. Beaudoin, *Application of A.C. Impedance Techniques in Studies of Porous Cementitous Materials.* Cement and Concrete Research, 1993. 23(3): p. 531-540.
181. ASTM C 116, *Standard Test Methods for Chemical Analysis of Hydraulic Cement*.
182. ASTM C 1152, *Standard Test Method for Acid-Soluble Chloride in Mortar and Concrete*.
183. A.R. Spurr, *A Low-Viscosity Epoxy Resin Embedding Medium For Electron Microscopy.* J. Ultrastructure Research, 1969. 26: p. 31-43.
184. ASTM G 1, *Standard Practice for Preparing, Cleaning, and Evaluating Corrosion Test Specimens*.

185. K. Ritter, M.S. Odziemkowski, R.W. Gillham, *An In situ Study of the Role of Surface Films on Granular Iron in the Permeable Iron Wall Technology.* Journal of Contaminant Hydrology, 2002. 55: p. 87-111.
186. T. Ohtsuka, K. Kubo, N. Sato, *Raman Spectroscopy of Thin Corrosion Films on Iron at 100 to 150 deg C in Air.* Corrosion 1986. 42(8): p. 476-481.
187. T. Ohtsuka, *Raman Spectra of Passive Films of Iron in Neutral Borate Solution.* Materials Transactions, JIM, 1996. 37(1): p. 67-69.
188. N. Boucherit, P. Delichere, S. Joiret, A. Hugot-Le Goff, *Passivity of Iron and Iron Alloys Studied by Voltammetry and Raman Spectroscopy.* Materials Science Forum, 1989. 44&45: p. 51-52.
189. S. J. Oh, D.C. Cook, H.E. Townsend, *Characterization of Iron Oxides Commonly Formed as Corrosion Products on Steel.* Hyperfine Interactions, 1998. 112(1-4): p. 59-66.
190. R. J. Thibeau, C.W. Brown, R. H. Heidersbach, *Raman Spectra of Possible Corrosion Products of Iron.* Applied Spectroscopy, 1978. 32(6): p. 532-535.
191. R.K. Singh Raman, *Characterisation of 'Rolled-in', 'Fragmented' and 'Red' Scale Formation During Secondary Processing of Steels.* Engineering Failure Analysis, 2006. 13(7): p. 1044-1050.
192. J. Dünnwald, A. Otto, *An Investigation of Phase Transitions in Rust Layers Using Raman Spectroscopy.* Corrosion Science, 1989. 29(9): p. 1167-1176.
193. R.G. Herman, C.E. Bogdan, A.J. Sommer, D.R. Simpson, *Discrimination Among Carbonate Minerals by Raman Spectroscopy Using the Laser Microprobe.* Applied Spectroscopy, 1987. 41(3): p. 437-440.
194. D. Thierry, D. Persson, C. Leygraf, N. Boucherit, A. Hogot-Le Goff, *Raman Spectroscopy and XPS Investigations of Anodic Corrosion Films Formed on Fe-Mo Alloys in Alkaline Solutions.* Corrosion Science, 1991. 32(3): p. 273-284.
195. National Institute of Advanced Science and Technology (AIST), *Raman Spectra Database of Minerals and Inorganic Materials*. 2007.
196. H. Kanno, J.Hiraishi, *A Raman Study of Aqueous Solution of Ferric Nitrate, Ferrous Chloride and Ferric Chloride in Glassy State.* Journal of Raman Spectroscopy, 1982. 12(3): p. 224-227.
197. P. M. L. Bonin, W. Jedral, M. S. Odziemkowski, R.W. Gillham, *Electrochemical and Raman Spectroscopic Studies of the Influence of Chlorinated Solvents on the Corrosion Behaviour of Iron in Borate Buffer and in Simulated Groundwater.* Corrosion Science, 2000. 42(11): p. 1921-1939.
198. I.C.G. Thanos, *In Situ Raman and Other Studies of Electrochemically Oxidized Iron and Iron-9% Chromium Alloy.* Electrochimica Acta, 1986. 31(7): p. 811-820.
199. R. M. Cornell, U. Schwertmann, *The Iron Oxides: Structure, Properties, Reactions, Occurrences, and Uses*. 2nd ed. 2003, Weinheim, Germany: Wiley-VCH. 664.
200. U. Schwertmann, R.M. Taylor, *The Transformation of Lepidocrocite to Goethite.* Clay and Clay Minerals, 1972. 20(3): p. 151-158.
201. J. Clark, *Chemguide-Helping You Understand Chemistry*. 2007; Available from www.chemguide.co.uk.
202. M. Odziemkowski, Email to S.J. Jaffer. 13th October 2007.
203. D.C. Cook, *Spectroscopic Identification of Protective and Non-protective Corrosion Coatings on Steel Structures in Marine Environments.* Corrosion Science, 2005. 47(10): p. 2550-2570.
204. C.L. Page, K.W.J. Treadaway, *Aspects of the Electrochemistry of Steel in Concrete.* Nature, 1982. 297(5862): p. 109-115.

205. K.L. Scrivener, *The Microstructure of Concrete*, in *Materials Science of Concrete*, J. Skalny, Editor. 1989, The American Ceramic Society: Westerville, OH, USA.
206. S.U. Pillai, D.W. Kirk, M.A. Erki, *Reinforced Concrete Design*. Third Edition ed. 1999: McGraw-Hill.